

Design and synthesis of nano- catalysts for catalytic transformation of biomass derivatives

By
Haimei Xu

A THESIS SUBMITTED TO MACQUARIE UNIVERSITY

FOR THE DEGREE OF

DOCTOR OF PHILOSOPHY

SCHOOL OF ENGINEERING

December 2020



MACQUARIE
University

I certify that the work in this thesis has not previously been submitted for a degree nor has it been submitted as part of requirements for a degree to any other university or institution other than Macquarie University.

Haimei Xu 31-December-2020

Copyright © 2020 Haimei Xu
All Rights Reserve

Acknowledgments

The dissertation was carried out at the School of Engineering, Macquarie University, Australia. I am greatly indebted to Macquarie University for the financial support of my research and my living allowance through iMQRES scholarship. Also, I would like to express my gratitude to the Postgraduate Research Fund that has provided me an opportunity to present my research work at an international conference in Spain, attend a workshop in Germany and visit two research groups in France and Poland.

I would like to give particular thanks to my principal supervisor, Associate Professor Yijiao Jiang, for allowing me to join her research group and for her excellent guidance in my research and career development throughout my years at Macquarie University and also for her constant encouragement and insightful guidance in preparing this dissertation. I am also very fortunate and thankful to my co-supervisor, Professor Jun Huang from the University of Sydney, for his excellent supervision and trustworthy discussions throughout my PhD research. His passionate attitude and knowledge about this research field are inspirational and have opened my eyes to how research needs to be approached and conducted.

This dissertation would not have been possible without the help from my colleagues. I would like to thank all the members in my research group for their help and support throughout these years: Dr. Zichun Wang, Amanj Kheradmand, Dr. Aleksei N. Marianov, Shengshen Gu, Alena Kochubei, Wenwen Zhang, Xiaoxia Yang, Yutong

Zhao for their scientific insights, support of my work and friendships.

I am also grateful to Lizhuo Wang and Wenjie Yang from the University of Sydney for TEM, XPS and Diffuse Reflectance UV-Vis measurements. I would like to thank Dr. Patrice Castignolles and Dr. Marion Gaborieau at the Western Sydney University for their help in conducting solid-state NMR measurements. Sincere thanks to Zhichao Miao from Shandong University of Technology for his help in the guidance of mesoporous catalyst synthesis.

Many thanks go to Mark Tran, Dr. Alf Garcia-Bennett, Dr. Tao Kan, Dr. Chao Shen, Dr. Remi Rouquette, Jane Yang, Susan Law, Wendy Tao, Walter Adendorff, Joe Gatt, Tom Lawson, Tony Wang, Dr. Nicole Cordina in Macquarie University for their technical assistance and support. Sincerest thanks are also given to the HDR team, Engineering Administrative team for their support and help during my scientific research. I am also thankful for the Department of Molecular Sciences at Macquarie University for the instrumental support.

I would also like to give thanks to my dear husband Yunzhao Fan, my son Wenjia Fan, my parents as well as my siblings for their continuous encouragement and support throughout my PhD work. Their unconditional support and endless love and encouragement allow me to stay on track and keep the high spirit during numerous setbacks.

Finally, I express my sincere gratitude to the examiners for reviewing my thesis and for their valuable comments.

List of publications

Journal publications included in the thesis:

[1] **Xu, H.**; Wang, Z.; Huang, J.; and Jiang, Y., Thermal catalytic conversion of biomass-derived glucose to fine chemicals. *Energy & Fuels* **2021**, Accepted. (Part of Chapter 2)

[2] **Xu, H.**; Wang, Z.; Miao, Z.; Zhu, Y.; Marianov, A.; Wang, L.; Castignolles, P.; Gaborieau, M.; Huang, J.; and Jiang, Y., Correlation between acidity and catalytic performance of mesoporous zirconium oxophosphate in phenylglyoxal conversion. *ACS Sustainable Chemistry & Engineering* **2019**, 7 (9), 8931-8942. (Chapter 4)

[3] **Xu, H.**, Zhang, W., Zhao, J., Kheradmand, A., Yang, X., Huang, J. and Jiang, Y., Tin exchanged phosphotungstic acid supported on [Si]MCM-41: An effective catalyst for glucose conversion into 5-hydroxymethylfurfural. Submitted to the Journal of Catalysis. (Chapter 3)

[4] **Xu, H.**, Wang, L., Kheradmand, A., Yang, W., Huang, J. and Jiang, Y., TiO₂ anchored Pt single atoms co-catalyst and Bi promoter for highly selective photocatalytic alcohol oxidation into aldehydes. Pending for submission. (Chapter 5)

[5] **Xu, H.**, Gu, S., Kheradmand, A., Marianov, A., Huang, J. and Jiang, Y., Enhanced photocatalytic activity of hierarchical flower-like Bi₂WO₆ microspheres with Pt nanoparticles as co-catalyst for the selective benzyl alcohol oxidation. Pending for submission. (Chapter 6)

Other publications:

- [6] Zhu, Y.; Marianov, A.; **Xu, H.**; Lang, C.; and Jiang, Y., Bimetallic Ag–Cu supported on graphitic carbon nitride nanotubes for improved visible-light photocatalytic hydrogen production. *ACS Applied Materials & Interfaces* **2018**, 10 (11), 9468-9477.
- [7] Zhang, W.; Zhu, Y.; **Xu, H.**; Gaborieau, M.; Huang, J.; and Jiang, Y., Glucose conversion to 5-hydroxymethylfurfural on zirconia: Tuning surface sites by calcination temperatures. *Catalysis Today* **2020**, 351, 133-140.
- [8] Yang, X.; Kan, T.; Kheradmand, A.; **Xu, H.**; Strezov, V.; Yu, A.; and Jiang, Y., Tunable syngas production from two-stage sorption-enhanced steam gasification of sewage sludge. *Chemical Engineering Journal* **2021**, 404, 126069.
- [9] Gu, S.; Marianov, A.; **Xu, H.**; and Jiang, Y., Effect of TiO₂ Support on immobilization of cobalt porphyrin for electrochemical CO₂ reduction. *Journal of Materials Science & Technology* **2021**, 55, 219-227.
- [10] Wang, Z.; Buechel, R.; Jiang, Y.; Wang, L.; **Xu, H.**; Castignolles, P.; Gaborieau, M.; Lafon, O.; Amoureux J.; Hunger, M.; Baiker A.; and Huang J., Engineering the Distinct Structure Interface of Subnano-alumina Domains on Silica for Acidic Amorphous Silica–Alumina toward Biorefining. *Journal of the American Chemical Society Au* **2021**, 1, 3, 262–271.
- [11] Zhao, Y.; Wang, L.; Kochubei, A.; Yang, W.; **Xu, H.**; Luo, Y.; Baiker, A.; Huang, J.; Wang, Z.; and Jiang, Y., Formation and location of Pt single sites induced by penta-coordinated Al species on amorphous silica–alumina. *The Journal of Physical Chemistry Letters* **2021**, 12, 10, 2536-2546.

Conference papers

- [1] **Xu, H.**, Huang, J. and Jiang, Y., Tin exchanged phosphotungstic acid supported on [Si]MCM-41: An effectual catalyst for glucose conversion into 5-hydroxymethylfurfural. International Conference on Catalysis, *Advanced Chemical Engineering and Technology*, Valencia, Spain, Sep 05-07, **2019**. (Oral Presentation)
- [2] **Xu, H.** and Jiang, Y., Mesoporous zirconium oxophosphate catalyzed phenylglyoxal conversion. *School of Engineering HDR conference*, Macquarie University, Australia, June 20, **2019**. (Oral Presentation).
- [3] **Xu, H.**, Huang, J. and Jiang, Y., Correlation between Acidity and Catalytic Performance of Mesoporous Zirconium Oxophosphate in Phenylglyoxal Conversion. *International Conference on Emerging Advanced Nanomaterials 2018*, Newcastle NSW, Australia, 30th Oct-2nd Nov, **2018**. (Poster Presentation)

List of acronyms

LAS	Lewis acid sites
BAS	Brønsted acid sites
HMF	5-hydroxymethylfurfural
MPW	Metal exchanged Keggin-structure phosphotungstic acids
HPW	Keggin-structure phosphotungstic acids
MCM-41	Mesoporous silica
ZrPO	Zirconium oxophosphate
EISA	One-pot evaporation-induced self-assembly
PG	Phenylglyoxal
EM	Ethyl mandelate
NMR	Nuclear magnetic resonance
TiO ₂	Titanium dioxide
TOF	Turnover frequency
BiOW	Bismuth tungstate composite
VB	Valence band
CB	Conduction band
HPAs	Heteropoly acids

Abstract

The energy crisis is a major challenge for the 21st century due to fossil fuel depletion. Biomass, the waste material from plants or animals containing renewable and abundant carbon resources, is considered as an ideal alternative for fossil fuels. However, the biomass utilization is limited by the lack of cost-effective technology for biomass valorization. Therefore, the objectives of this dissertation are to rationally design novel nanocatalysts to selectively convert biomass-derived carbohydrates into value-added chemicals and fuels and to understand the catalyst structure-property relationship and the underlying reaction mechanisms.

5-hydroxymethylfurfural (HMF) derived from biomass is considered as a renewable chemical platform to produce liquid fuels and fine chemicals, which could be produced from glucose, the main unit of cellulose, via Lewis and Brønsted acid sites (LAS and BAS). In Chapter 3, the stable solid acid catalysts with Lewis-Brønsted acidity were designed for efficient catalytic conversion of glucose to HMF. A series of metal (Fe^{3+} , Cu^{2+} , Zn^{2+} and Sn^{4+}) exchanged Keggin-structure phosphotungstic acids (MPW), were confined in mesopores of siliceous MCM-41 for efficient glucose conversion. The selectivity to HMF decreases with the reducing Lewis acid strength of metal ions in the order: $\text{Sn}^{4+} > \text{Fe}^{3+} > \text{Zn}^{2+} > \text{Cu}^{2+}$. The LAS dominated Sn(IV)PW/MCM provides twice higher HMF selectivity than that obtained with HPW/MCM containing mainly BAS. Increasing the density and strength of LAS on Sn(IV)PW/MCM catalyst by elevating pretreatment temperature promote the glucose conversion and HMF selectivity.

Moreover, the confinement effect of mesoporous MCM-41 affords high resistance of leaching and dissolving for Sn(IV)PW in polar dimethyl sulfoxide (DMSO) solvent, therefore resulting in an outstanding stability of Sn(IV)PW/MCM catalyst.

The production of another kind of important platform chemicals in biomass utilization, α -hydroxycarboxylic acids or their derivatives, from α -keto aldehydes conversion using solid acids was studied and addressed in Chapter 4. The ordered mesoporous zirconium oxophosphate (ZrPO) catalysts with tunable acidity were prepared using one-pot evaporation-induced self-assembly (EISA) method and their catalytic performance in α -hydroxycarboxylic acid production was evaluated using phenylglyoxal (PG) conversion to ethyl mandelate (EM) as a model reaction. The roles of LAS and BAS of ZrPO were investigated by kinetic studies of PG conversion combined with temperature-programmed desorption of ammonia (NH₃-TPD) and solid-state nuclear magnetic resonance (NMR) characterizations. It is found that the ratio of LAS to strong BAS on the ZrPO plays a dominant role in this reaction. ZrPO-0.75-500, with a LAS/strong BAS ratio of 2.1, is found to be the best catalyst. The reaction pathways, i.e., direct isomerization of PG to EM by LAS via the formation of an intermediate hemiacetal by strong BAS, are therefore proposed. Moreover, the effect of water on catalytic activity was studied. A moderate content of water-induced either by catalyst pre-treatment at the proper temperature or deliberately dosed on the ZrPO materials achieved a maximum catalytic activity. The highest catalytic activity, i.e., 82 % of PG conversion and 92 % of EM yield, was obtained on ZrPO-0.75-500 dosed by 15 μ mol water per 50 mg of the catalyst. It is concluded that ZrPO with a suitable combination of LAS and BAS is required to catalyze the conversion of α -keto aldehydes efficiently and selectively to α -hydroxycarboxylic acid derivatives. It is feasible, from a practical point of view, to tune the density of LAS and BAS on the catalysts for achieving a better

catalytic performance.

For a better and cleaner environment, scientists have turned to make use of solar energy to satisfy the demands of modern society aiming at reaching the dual Holy Grail of energy: harvesting solar energy via artificial photosynthesis and achieving low-temperature biomass conversion. The combination of biomass utilization and the green and cost-effective photocatalysis is considered as a promising approach to achieve sustainable chemical transformation processes. In Chapters 5 and 6, photocatalytic process under sunlight irradiation is applied instead of the thermal catalytic process for the oxidation of biomass-derived alcohols.

In Chapter 5, platinum (Pt) and bismuth (Bi) bimetallic modified mesoporous titanium dioxide (TiO₂) was successfully prepared via EISA synthetic method. It was used as a highly active and selective catalyst for the photooxidation of alcohols using O₂ as oxidant. Remarkably, the Pt single sites and Bi promoter co-modified TiO₂ catalyst exhibited a good activity on benzyl alcohol oxidation, giving a turnover frequency (TOF) of 372.2 h⁻¹, about 1.2 and 3.9 times higher than that of Pt subnano clusters (300 h⁻¹) and nanoparticles (95.9 h⁻¹) stabilized catalysts. The selectivity to benzaldehyde was up to 100% for all catalysts. The superior performance can be attributed to the strong interaction between Pt single sites, promoter Bi and mesoporous TiO₂, which favors the formation of a high density of positively charged Pt even at a high reduction temperature. Positively charged Pt could play an important role in promoting the charge carrier transition and separation as well as improving the absorption of visible light. The optimized catalyst can perform various light-driven alcohol oxidation leading to the selective formation of aldehyde.

Considering the limited practical application of TiO₂ due to low quantum efficiency and

large bandgap, various novel visible light-responsive semiconductor photocatalysts have been developed. The naturally abundant and non-toxic bismuth-based oxide (BiOX, X=Cl, Br, I, W or Mo), has emerged as a potential visible-light-driven photocatalyst in various photocatalytic reactions due to its narrow gap (~ 2.8 eV) and better visible light absorption ($\lambda > 400$ nm). In Chapter 6, various BiOW composites with different morphologies and Bi/W ratios were synthesized via a facile hydrothermal precipitation process and applied in photocatalytic benzyl oxidation to produce benzaldehyde. The systematic research has explored how the morphologies of Bi_2WO_6 and the components of BiOW composites affect the photocatalytic activity. The UV/Vis absorption spectra and photoelectrochemical performance showed that the bandgap of BiOW composites is mainly governed by the components of catalysts. However, the efficiency in the separation and transfer of photo-generated electron-hole pairs is dominated by the morphology of the nanostructure. As a result, the photocatalytic activities of BiOW composites are strongly dependent on their morphologies and structures. It is found that the flower-like Bi_2WO_6 exhibited superior performance in benzyl alcohol oxidation to benzaldehyde, achieving ca. 2.2- and 2.7-times higher activity compared to Bi_2WO_6 in nanosheet and nanoplate structure. In contrast, the Bi-rich $\text{Bi}_2\text{WO}_6/\text{Bi}_{3.84}\text{O}_{6.24}\text{W}_{0.16}$ composite and Bi_2O_3 in block-like structure were almost inactive in this reaction. Besides, the light absorption and the separation and transfer of photogenerated charge carriers could be further enhanced via loading of co-catalyst Pt nanoparticles on the surface of the flower-like Bi_2WO_6 , thus resulting in highly efficient photocatalytic oxidation. This study provides structural optimization strategies for bismuth tungstate photocatalysts which can be applied in fine chemicals synthesis.

Table of Contents

Acknowledgments	V
List of publications.....	VII
List of acronyms.....	X
Abstract.....	XI
Table of Contents	XV
Chapter 1 Introduction.....	1
1.1 Background.....	1
1.2 Scope and objectives	7
1.3 Organization of this dissertation.....	8
References	9
Chapter 2 Literature review	11
2.1 Biomass introduction.....	11
2.1.1 Biomass components.....	11
2.1.2 Biomass utilization.....	12
2.2 Thermal-catalytic transformations of biomass-derived substrates	14
2.2.1 Acid-catalyzed transformation	15
2.2.2 Catalytic oxidation of biomass-derived glucose	36
2.3 Photocatalytic transformations of biomass-derived substrates.....	43
2.3.1 Semiconductor.....	44
2.3.2 Photocatalytic oxidation of biomass derivatives.....	45
Reference	56
Chapter 3. Lewis-promoted glucose conversion into HMF catalyzed by metal exchanged phosphotungstic acid confined into MCM-41	70
3.1 Introduction	70
3.2 Experimental.....	72
3.2.1 Materials and reagents.....	72

3.2.2 Catalyst preparation.....	73
3.2.3 Catalyst characterization	74
3.2.4 Catalytic reaction.....	75
3.2.5 Recycling experiment of catalyst	76
3.2.6 Dehydration experiments	77
3.3 Results and discussion	77
3.3.1 Textural and morphological characteristics.....	77
3.3.2 Effect of Lewis acid metals of MPW/MCM catalysts on glucose conversion	82
3.3.3 Acidity characterization.....	84
3.3.4 Catalytic performance of HPW/MCM and Sn(IV)PW/MCM in glucose conversion	87
3.3.5 Tuning Lewis acidity via dehydration of Sn(IV)PW/MCM for glucose conversion	92
3.3.6 LAS accelerates fructose production at a lower temperature.....	94
3.3.7 Stability and reusability.....	97
3.4 Conclusions	99
References	100
Chapter 4. Correlation between acidity and catalytic performance of mesoporous zirconium oxophosphate in phenylglyoxal conversion	105
4.1 Introduction	105
4.2 Experimental section	108
4.2.1 Chemicals.....	108
4.2.2 Catalyst synthesis	108
4.2.3 Characterizations	109
4.2.4 Catalytic activity testing.....	110
4.2.5 Dehydration and rehydration experiments	111
4.3 Results and discussion	111
4.3.1 Textural and morphological properties.....	111
4.3.2 Coordination states of phosphate	117

4.3.3 Acidic properties	118
4.3.4 Catalytic performance in PG conversion to EM	123
4.3.5 Reaction pathways of PG conversion on ZrPO.....	125
4.3.6 Effect of water content on catalytic activity.....	127
4.3.7 Stability and Recyclability Evaluation.....	128
4.4 Conclusions	129
References	130
Chapter 5. Pt single sites on Bi-TiO₂ for selective photocatalytic oxidation of alcohols into aldehydes	135
5.1 Introduction	135
5.2 Experimental section	138
5.2.1 Catalyst fabrication	138
5.2.2 Characterization	140
5.2.3 Photocatalytic oxidation of alcohols	142
5.3 Results and discussion	143
5.3.1 Characterization	143
5.3.2 Photocatalytic performance.....	165
5.4 Conclusion	172
Reference	172
Chapter 6. Pt-deposited hierarchical flower-like Bi₂WO₆ microspheres for the selective photooxidation of benzyl alcohol.....	176
6.1 Introduction	176
6.2 Experimental.....	178
6.2.1 Preparation of samples	178
6.2.2 Characterization	179
6.2.3 Photocatalytic oxidation of benzyl alcohol	179
6.3 Results and discussion	179
6.3.1 Structure characterization.....	179
6.3.2 Photocatalytic performance.....	183
6.3.3 Photoelectrochemical performance	185

6.3.4 The proposed mechanism.....	190
6.4 Conclusions	191
References	192
Chapter 7 Conclusions and further work.....	196
7.1 Conclusions	196
7.2 Future work.....	197

Chapter 1 Introduction

1.1 Background

Our global society's energy demand is increasing at a high rate. However, more than 80% of worldwide energy is mainly from non-renewable fossil fuels, which results in the highest growth rate of greenhouse gas emissions, as a consequence, leading to the climate change.¹ Extensive investigations on the development of cost-effective systems for harnessing energy from a carbon-neutral renewable resource and carbon-free renewable sources such as solar, wind, geothermal, tidal, nuclear and hydroelectric energy are being undertaken to seek alternatives to fossil fuels.²

As a sustainable source of organic carbon, biomass, mostly referring to plants or plant-based materials, can be used as alternative for fossil fuels.³ Biomass comes from living organisms, such as animals and plants. Plant-derived biomass is a renewable and low environmental-loading resource, produced from water (H₂O) and carbon dioxide (CO₂) via photosynthesis using sunlight. For example, crops and forests capture around 1 % of the incoming solar energy into biomass. These energies are stored as complex molecules, such as lignin, carbohydrates, terpenes, glycerides, proteins and others.⁴ Thus, biomass as an abundant renewable carbon source could be utilized to produce bioenergy and biomaterials. The enhanced utilization of biomass would address various societal needs. Biorefinery,⁵ identified in Figure 1.1, the transformation of biomass to sustainable biochemicals and biofuels, is important under the situation of the rising cost

and decreasing supply of oil. The integration of biorefinery manufacturing technologies and renewable plant-based biomass offers potentials for the development of renewable biochemicals and biofuels.^{6,7}

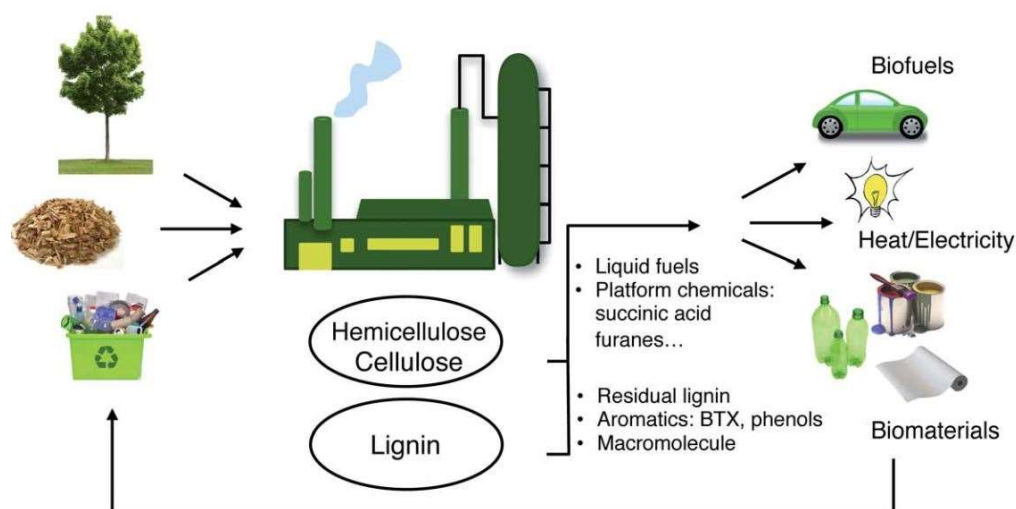


Figure 1.1 Biorefinery Concept.⁵ Reproduced from [Strassberger Z.; Tanase S. and Rothenberg G., The Pros and Cons of Lignin Valorisation in an Integrated Biorefinery. RSC Adv. 2014, 4 (48), 25310-25318.]. Published by The Royal Society of Chemistry.

The most common biomass used as renewable energy are plant-based biomass feedstocks such as plants, wood, and wastes, which are called plant-based lignocellulose. Lignocellulose is the most abundant biomass on earth, with billions of tons produced annually. This composition of plant-based biomass feedstocks varies significantly with the type of the plants. The primary products formed in lignocellulose are C5- and C6- sugars-based chemicals including cellulose formed by glucose polymerization and hemicellulose built from glucose and xylose (Figure 1.2). Another main component is lignin which is a highly cross-linked polymer of substituted phenols, giving strength to plants.⁸ Besides these main components, plants also include energy storage products like starches and lipids as well as some products relatively rich in hydrogen and carbon such as terpenes.⁴ However, lignin and carbohydrates including

cellulose and hemicellulose represent the two largest fractions of lignocellulose and the transformation of lignocellulose plays major roles in the industrial utilization of biomass.⁴ As an energy source, lignocellulosic biomass can be used either directly to produce heat via combustion or indirectly being converted into various forms of biofuels and biochemicals. Various transformation processes have been used in the valorization of lignocellulose. However, only a small proportion of the global lignocellulosic biomass are cultivated and employed in biorefinery processes.⁹ Extensive research has been conducted to produce important platform chemicals from lignocellulose.

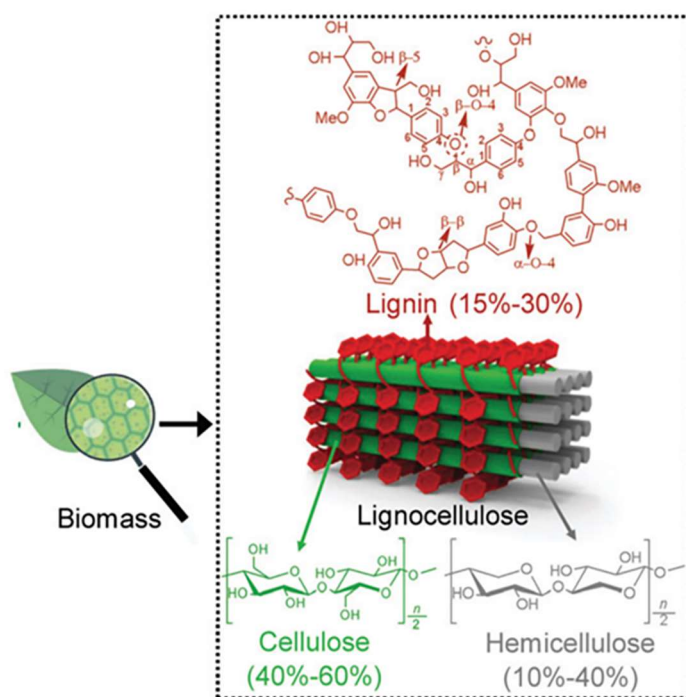


Figure 1.2 The major components of lignocellulosic biomass and their chemical structures. This figure was reproduced with permission from the literature.⁸

Currently, various technologies including thermochemical, catalytic and enzymatic conversion processes have been developed. These conversion reactions may occur in

the gas and liquid phases, involving low-temperature conversion of biomass-derived carbohydrates as well as high-temperature transformation of biomass raw materials. However, biomass-derived carbohydrates are mainly converted at mild temperatures due to their high reactivity and low volatility under high temperatures.¹⁰ Various conversion reactions of biomass-derived carbohydrates including aldol condensation, dehydration, hydrolysis, isomerization, hydrogenolysis, hydrogenation and oxidation are often conducted at temperatures near or below 200 °C.¹⁰ Thus the conversion processes of most of carbohydrates are typically carried out in the liquid phase. From the view of the development of green transformation processes, heterogeneous catalysis where the phase of catalysts differs from that of the reactants or products seems more promising for practical applications, which could be a more energy-saving chemical process with less wastes as well as less toxics than homogeneous catalysis.¹¹ Thus, in liquid-phase biomass-derived carbohydrates conversion processes, solid catalysts are the preferred option considering that heterogeneous catalysis for industrial processes enables catalyst separation and recovery. The use of renewable feedstock and heterogeneous catalytic processes are making a significant contribution to accomplish the goal of sustainability and environmental friendliness.

Dehydration reactions of biomass and biomass-derived carbohydrates comprise an important class of reactions in the field of biomass valorization. Biomass-derived carbohydrates such as glucose and fructose generally can be dehydrated to form furan-based compounds such as furfural and HMF that can subsequently be converted into various chemicals such as levulinic acid, tetrahydrofurfuryl alcohol, furfuryl alcohol,

2,5-diformylfuran, 2,5-furandicarboxylic acid and so on. Among these compounds, HMF is identified as a high potential biomass-based platform for the production of pharmaceuticals, polymers, fragrances, agrochemicals, biofuel as well as macro- and heterocycles.¹² And, HMF is called a “sleeping giant” showing a growing industrial demand.¹³ The current price of HMF is estimated 500-1500 USD/kg, which is far higher than that of other platform chemicals, such as furfural (500–1500 USD/metric ton) and levulinic acid (1000–3000 USD/ton).¹⁴ Therefore, developing efficient catalytic processes for HMF production to lower its prices is promising and encouraging. Now, the most effective approach to produce HMF is the acid-catalyzed biomass-derived cellulose hydrolysis and carbohydrates dehydration, preferably glucose, representing the main C6 fraction of lignocellulose.

Except for HMF, α -hydroxycarboxylic acids including lactic acid (LA) and mandelic acid are a class of chemical compounds that consist of a carboxylic group and a hydroxyl group at the adjacent carbon. They can be used to remove the dead cells on our skin, to reduce bacteria and photo-corrosion. Besides, they could also be applied to prepare food additives, plastic products, pharmaceuticals, and other chemicals.⁴ Up to now, numerous studies on the dehydration of biomass-derived carbohydrates using various solid acids such as heteropolyacids, cation exchanged clay, metal oxidants and sulfonated active carbons have been conducted. It has been revealed that the activity is dependent on the type (Brønsted and Lewis), amount, and strength of acid sites.

Except for dehydration reaction, a large number of transformations in biomass valorization are redox reactions, where stoichiometric reductant and/or oxidant as well

as high temperature are usually required in thermal catalysis. Compared with thermal catalysis using thermal energy, photocatalysis is based on the use of photon solar energy to drive chemical reactions. By using photon solar energy rather than thermal energy, the reaction can be carried out at ambient or lower temperatures. In addition, photoexcitation of catalysts, referring to semiconductors, can produce charge carriers (e^-/h^+ pairs) or reactive species with high redox ability, which could replace the stoichiometric reductant and/or oxidant, thus efficiently driving a number of redox reactions. Furthermore, the chemoselective transformation of biomass-derived compounds via photocatalysis emerged as a promising approach to obtain desired biomass-based products because of the mild reaction conditions as well as its unique reaction patterns induced by photo-generated reactive species and/or photo-excited charge carriers, which may selectively act specific functional groups of substrates or enable the precise cleave target chemical bonds.⁸ More importantly, from the perspective of sustainability, maximum use of solar energy for the transformation of biomass-derived feedstock to value-added chemicals is a viable green process. Thus, catalytic transformations of biomass using solar energy have been extensively investigated at present.^{8, 15, 16}

Semiconductor materials are the most applied catalysts in photocatalytic reactions. It is apparent that the major types of catalysts used in the oxidation reaction of biomass-derived feedstocks are noble metals and alloys deposited solid catalysts.^{17, 18} Nonprecious metal-based materials were also explored as active catalysts for the oxidation of biomass derivatives during the past decade. Making use of nonprecious

metal-based catalysts for oxidation reactions would result in a more cost-efficient reaction process. Many morphological and microscopic structural factors of semiconductor-based photocatalysts, such as crystal facet, size, shape, or promoter have significant and even synergistic impacts on the catalytic performance of photocatalysts, including tuning the activity and selectivity to target products in photocatalytic oxidation of alcohols.¹⁹ The control of selectivity to specific products with targeted functional groups or chemical bonds activation and cleavage is challenging.

1.2 Scope and objectives

The overall aim of this thesis is to improve the economic potential of biomass-derived feedstocks by designing efficient catalysts and developing efficient heterogeneous catalytic transformation processes. This research explored the conversion of various biomass-based feedstocks including glucose, α -keto aldehydes and aromatic alcohols into value-added chemicals such as HMF, α -hydroxycarboxylic acids and aromatic aldehydes via thermal catalytic and photocatalytic processes. The specific objectives of the dissertation are as follows:

- (1) To synthesis of value-added HMF from the abundant biomass-derived resource (glucose) using solid acid catalysts; Investigate the effect of acidity on glucose conversion and understand the reaction pathways of glucose conversion.
- (2) To synthesis α -hydroxycarboxylic acids and their derivatives from biomass-derived α -keto aldehydes using solid acid catalysts; Investigate the effect of acidity on α -keto aldehydes conversion and the underlying reaction mechanisms.

(3) To develop efficient chemoselective TiO₂-based photocatalysts for the oxidation of biomass-derived benzyl alcohol; Investigate the size effect of Pt co-catalyst on photocatalytic oxidation activity.

(4) To develop novel visible light-responsive photocatalysts, such as BiOW composites. Investigate the effect of catalyst morphologies on photocatalytic oxidation activity.

1.3 Organization of this dissertation

This dissertation starts with a general introduction in Chapter 1 that includes background, objectives, thesis organization. Chapter 2 is an introduction to biomass and chemical transformations from biomass-derived substrates through conventional thermal catalysis and sustainable photocatalytic process. Chapter 3 addresses the Lewis-promoted glucose conversion into HMF catalyzed by metal exchanged phosphotungstic acid confined into MCM-41. The roles of the total acid sites, BAS and LAS (density and strength) on HMF catalytic production were studied. Chapter 4 focuses on the catalytic conversion of PG to EM over mesoporous ZrPO solid acids. The roles of LAS and BAS of ZrPO were investigated by kinetic studies of PG conversion combined with NH₃-TPD and solid-state NMR characterizations of these catalysts.

In the photocatalysis part, Chapter 5, a facile synthetic strategy was developed to disperse co-catalyst Pt (single sites, subnano-clusters and nanoparticles) into a mesoporous Bi-TiO₂. Their activities were applied in the model reaction of benzyl alcohol oxidation. The effect of Pt particle size on photoelectrochemical properties and

photocatalytic activities were explored. Chapter 6 presents a facile hydrothermal approach to prepare BiOW composites with different morphology structures and different components via changing the pH value of precursor suspension. The effects of the morphological structure and components of BiOW composites on photoelectrochemical properties and photocatalytic activities were explored. Chapter 7 provides concluding remarking and a discussion of future work on improving the biomass utilization, and the challenges and prospects of heterogeneous catalysis in this field.

References

- [1]. Global Energy & CO₂ Status Report 2019. Paris: International Energy Agency; **2019** March.
- [2]. Koohi-Fayegh, S., and Rosen, M. A., A review of renewable energy options, applications, facilitating technologies and recent developments. *European Journal of Sustainable Development Research* **2020**, 4 (4).
- [3]. McKendry P., Energy production from biomass (part 1): Overview of biomass. *Bioresource Technology* **2002**, 83 (1), 37-46.
- [4]. Corma A., Iborra S., and Velty A., Chemical routes for the transformation of biomass into chemicals. *Chemical Reviews* **2007**, 107 (6), 2411-2502.
- [5]. Strassberger Z., Tanase S. and Rothenberg G., The pros and cons of lignin valorisation in an integrated biorefinery. *RSC Advance* **2014**, 4 (48), 25310-25318.
- [6]. Roman-Leshkov Y., Barrett C.J., and Liu Z.Y. et al., Production of dimethylfuran for liquid fuels from biomass-derived carbohydrates. *Nature* **2007**, 447 (7147), 982-U5.
- [7]. Ragauskas A.J., Williams C.K., and Davison B.H. et al., The path forward for biofuels and biomaterials. *Science* **2006**, 311 (5760), 484-489.
- [8]. Wu X., Luo N., and Xie S. et al., Photocatalytic transformations of lignocellulosic biomass into chemicals. *Chemical Society Reviews* **2020**, 49 (17), 6198-6223.
- [9]. Dahmen N., Lewandowski I., Zibek S. and Weidtmann A., Integrated lignocellulosic value chains in a growing bioeconomy: Status quo and perspectives. *GCB Bioenergy* **2019**, 11 (1), 107-117.
- Chheda J.N., Huber G.W., Dumesic J.A., Liquid-phase catalytic processing of biomass-derived oxygenated hydrocarbons to fuels and chemicals. *Angewandte Chemie International Edition* **2007**, 46 (38), 7164-7183.

- [10]. Klemm D., Heublein B., Fink H.P. and Bohn A., Cellulose: Fascinating biopolymer and sustainable raw material. *Angewandte Chemie-International Edition* **2005**, 44 (22), 3358-3393.
- [11]. Huber G.W., Iborra S. and Corma A., Synthesis of transportation fuels from biomass: Chemistry, catalysts, and engineering. *Chemical Reviews* **2006**, 106 (9), 4044-4098.
- [12]. van Dam H.E., Kieboom A.P.G. and van Bekkum H., The conversion of fructose and glucose in acidic media: Formation of hydroxymethylfurfural. *Starch - Stärke* **1986**, 38 (3), 95-101.
- [13]. Galkin K.I. and Ananikov V.P., When will 5-hydroxymethylfurfural, the "sleeping giant" of sustainable chemistry, awaken? *Chemsuschem* **2019**, 12 (13), 2976-2982.
- [14]. Mika L.T., Cséfalvay E. and Németh Á., Catalytic conversion of carbohydrates to initial platform chemicals: Chemistry and sustainability. *Chemical Reviews* **2018**, 118 (2), 505-613.
- [15]. Ibhaden A.O. and Fitzpatrick P., Heterogeneous photocatalysis: Recent advances and applications. *Catalysts* **2013**, 3 (1), 189-218.
- [16]. Lanzafame P., Centi G. and Perathoner S., Catalysis for biomass and CO₂ use through solar energy: Opening new scenarios for a sustainable and low-carbon chemical production. *Chemical Society Reviews* **2014**, 43 (22), 7562-7580.
- [17]. Davis S.E., Ide M.S. and Davis R.J., Selective oxidation of alcohols and aldehydes over supported metal nanoparticles. *Green Chemistry* **2013**, 15 (1), 17-45.
- [18]. Granone L.I., Sieland F., Zheng N., Dillert R. and Bahnemann D.W., Photocatalytic conversion of biomass into valuable products: A meaningful approach? *Green Chemistry* **2018**, 20 (6), 1169-1192.
- [19]. Ravelli D., Dondi D., Fagnoni M. and Albini A., Photocatalysis. A multi-faceted concept for green chemistry. *Chemical Society Reviews* **2009**, 38 (7), 1999.

Chapter 2 Literature review

2.1 Biomass introduction

2.1.1 Biomass components

Biomass comes from living organisms, such as animals and plants. The most common biomass used as renewable energy are plants, wood, and wastes which are called plant-based biomass feedstock. Biomass feedstocks contain energy that is derived from the sun. For example, plants convert photons into chemical bonds via photosynthesis which combines carbon dioxide and water into carbohydrates. This composition of plant-based biomass feedstock varies significantly with the type of the plants. However, carbohydrates and lignin represent the two largest fractions of plant-based biomass and their transformations play major roles in the industrial utilization of biomass.¹ For example, in crops, carbohydrates and lignin account for 75% and 10-20% of the dry weight, respectively, while the rest part is mainly represented by triglycerides, namely lipids, and proteins.²

There are two major types of carbohydrates in plant-based biomass: structural polysaccharides including cellulose and hemicellulose, and those for energy storage such as inulin and starch. Cellulose, indigestible for most animals and humans, is the main carbohydrate in plant-based biomass. Hence, it is considered as a promising candidate for chemicals and biofuel production. Currently, cellulose could be converted into sugars, alcohols and various fine chemicals using chemical and biotechnological

processes.³ Lignin, a kind of biopolymer consisting of a three-dimensional polyphenolic framework, form the cell walls of plants. Lignin is particularly important in wood and bark since they lend rigidity and do not rot easily.⁴ The natural structure of lignin is very complex, and its composition and molecular mass vary with the source of biomass. Triglycerides could be transferred to fatty acid methyl esters which is known as biodiesel.⁵ Biodiesel production on a large scale is another important example of biomass utilization, which could satisfy the world's growing demand for liquid fuels.⁶ The main by-product during biodiesel production process is glycerol, as the production of 1 Kg biodiesel resulting in the production of 100 g glycerol. The obtained glycerol with high purity can be applied for the biochemical production directly.⁷

2.1.2 Biomass utilization

The energy stored in plant-based biomass can be transformed into usable energy through either direct or indirect routes.⁶ For example, biomass can be converted directly into electricity, burned to create heat, or processed indirectly into biofuels and bioproducts. Lignocellulosic biomass could be converted to biofuels via gasification and pyrolysis or to well-identified platform molecules via fermentation and thermal catalytic routes. These platform molecules can be then used for the production of biochemicals.⁸ The process of biomass conversion to produce biofuels and chemicals is called biorefinery.^{9, 10} Simplified biorefinery operations of lignocellulosic biomass are given in Figure 2.1.¹¹

The operations can be divided into thermo-chemical (gasification and pyrolysis), biochemical processes as well as hydrolysis routes. During the gasification process, lignocellulosic biomass feedstock is heated to higher than 700 °C with a controlled

amount of O_2 .⁶ The molecules break down and produce syngas and slag. Syngas can be converted into fuels, such as synthetic natural gas, which is used as an alternative for natural gas. Pyrolysis is a process that biomass is thermally treated without the presence of oxygen.¹² Pyrolysis produces syngas, bio-oil and biochar. All these components as energy source or biofuels can be applied for power stations as. For example, bio-oil can either be combusted to generate electricity or can be used as a component in fuels and plastics, which has emerged as a possible alternative to petroleum.

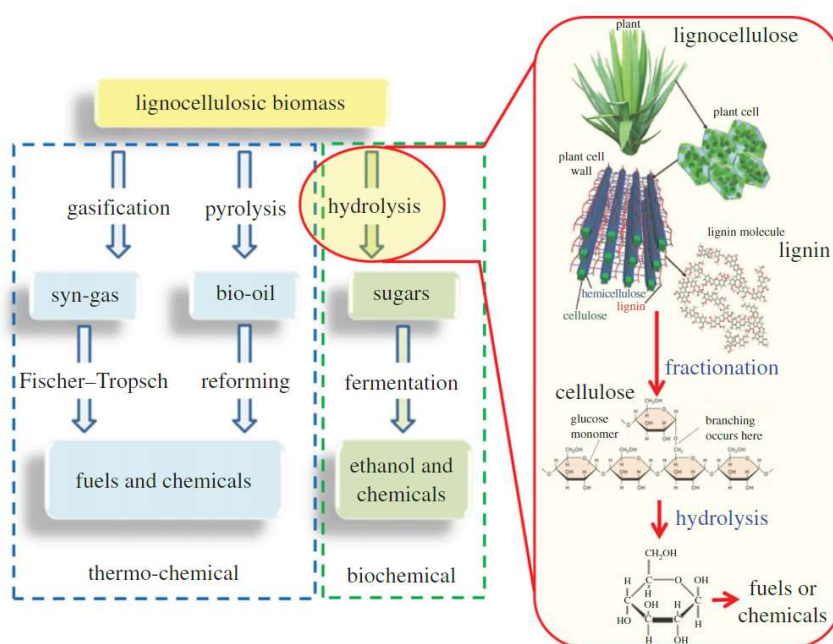


Figure 2.1 Strategies to produce biofuels and chemicals from plant-based lignocellulosic biomass. This figure was reproduced with permission from the literature.¹¹

Hydrolysis pathways are also feasible for lignocellulosic biomass utilization in the production of biofuels and value-added chemicals. Sugars are natural intermediates in the hydrolysis of lignocellulose,^{13, 14} which can be further converted into chemicals or biofuels efficiently via biological and chemical processes as shown in Figure 2.1.¹¹

However, the isolation of sugar monomers from lignocellulosic feedstock is complex and expensive because accessing to sugars from lignocellulosic biomass is hindered by the of plant cell walls.¹⁵ Various technologies including steam explosion,¹⁶ organosolv¹⁷ treatments and acid/base hydrolysis have been applied to separate and isolate hemicellulose and cellulose from lignin components. After separation, the hemicellulose can be typically hydrolyzed into sugars, like glucose and xylose, while cellulose fractions can be converted into glucose via chemical (acid/base),¹⁸ ionic liquid-based,¹⁹ supercritical water²⁰ or enzymatic²¹ treatment processes. Whereas the hydrolysis of lignin remains a challenge, although it is a suitable feedstock to produce phenolic resins bio-oil and aromatic chemicals.²² Consequently, lignin and humins as the solid residues are usually left during the hydrolysis processes of lignocellulose. And the solid residues can be used to produce aromatic bio-oil or heat generation.^{23, 24} Further, A range of industrially important chemicals including acids, alcohols hydrocarbons and the platform chemicals for polymers could be produced from these biomass-derived sugars via various reaction processed, such as hydrolysis, oxidation and hydrogenation.¹ Furthermore, these biomass-derived chemicals can also be further conversion into biofuels or biofuel additives.^{23, 24} In the following sections, various catalytic strategies for converting lignocellulose -derived carbohydrates to yield value-added chemicals are presented.

2.2 Thermal-catalytic transformations of biomass-derived substrates

Plant-based lignocellulose is the most abundant biomass on earth, with billions of tons of biomass produced annually. However, only a few percent of the global lignocellulosic biomass are cultivated and employed in biorefinery processes.²⁵

Extensive research has been conducted to produce important platform chemicals from

lignocellulose biomass. The conversion of biomass-derived carbohydrates has become a major and multidisciplinary field of research. Various catalytic transformation processes have been used in the thermochemical conversion of carbohydrates.

2.2.1 Acid-catalyzed transformation

2.2.1.1 Introduction of acids

In acid-catalyzed reactions, both Brønsted and Lewis acids are commonly used. Brønsted acids are the substances which can act as a proton donor, and Lewis acids are substances having incomplete electron groups which can accept electrons pairs to form a coordination bond. Consequently, the corresponding active sites are defined as Brønsted acid sites (BAS) and Lewis acid sites (LAS). Reactants and acid catalysts presented in the same phase are classified as homogeneous acid-catalyzed reactions, while in heterogeneous acid-catalyzed reaction, acid catalyst and reactant are in different phases. In general, the homogeneous acid catalysts are often referred to the liquid acids and the heterogeneous acid catalysts are referred to solid acids. The inherent disadvantages of liquid acids compared to solid acids are as follows: (1) the difficult catalyst separation and recovery;²⁶ (2) safety problems related to their corrosion;²⁷ (3) issues connected with the environment and sustainable development.²⁸ Thus, solid acids with favorable characteristics including efficient activity, ease in recovery and reuse, and long catalytic life, can substitute conventional liquid acids for catalyzing biomass-derived carbohydrates conversion. And they have great potential for transformation of biomass efficiently.

2.2.1.2 Acid-catalyzed hexose conversion to HMF

Hexoses, mainly glucose and fructose, which are the building units of cellulose, are the most widely used monosaccharides that have wide applications ranging from the pharmaceutical and food industries. Thermal catalytic dehydration of hexoses over acid catalysts leads to the formation of an important platform chemical: 5-hydroxymethylfurfural (HMF). HMF is a key biorefining intermediate from carbohydrate feedstock. It can subsequently be converted into various chemicals including levulinic acid, 5-hydroxymethylfuran-2-carboxylic acid, 2,5-furandicarboxaldehyde, 2,5-bis(hydroxymethyl)furan, 2,5-furandicarboxylic acid, as shown in Figure 2.2.¹¹ HMF was identified as a high potential biomass-based platform for the production of pharmaceuticals, polymers, fragrances, agrochemicals, biofuel as well as macro- and heterocycles.²⁹ Thus, HMF is called a “sleeping giant” showing a growing industrial demand.³⁰ Recently, various types of solid acid catalysts including zeolites,³¹ cation-exchange resins,³² carbonaceous solid acid,³³ transition-metal oxides,³⁴ catalysts supported solid acids³⁵ and heteropoly compounds³⁶ have been applied in glucose conversion. The mechanism of HMF formation from glucose as well as recent achievements in one-pot glucose conversion into HMF are reviewed in this section.

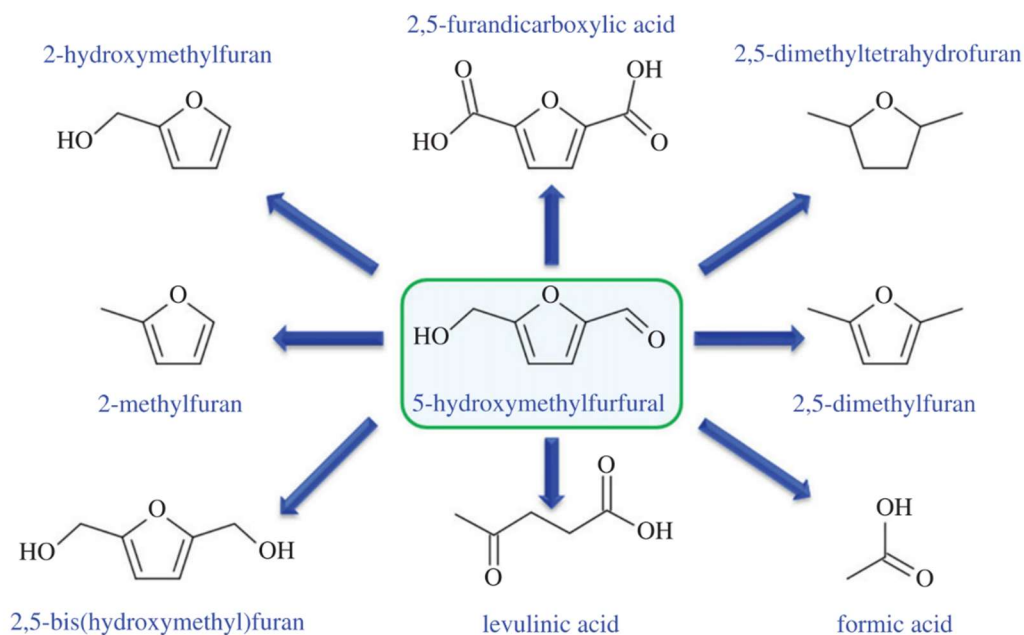


Figure 2.2 The potential uses of HMF. This figure was reproduced with permission from the literature.¹¹

2.2.1.2.1 Mechanism of glucose dehydration into HMF

Recently, the dehydration reaction of glucose to HMF has been extensively studied, however no clear conclusions about the mechanism have been proposed yet. Now, the most widely studied reaction of glucose-to-HMF may occur through two pathways: (1) based on the acyclic intermediates^{37, 38} and (2) based on the transformation of cyclic intermediates.^{1, 39} The proposed acyclic pathway generally initiated by the glucose isomerization via a key species 1,2-enediol, which then undergoes three consecutive dehydration steps to produce HMF as shown in Figure 2.3 (Route 1). It is called as “enediol mechanism.”

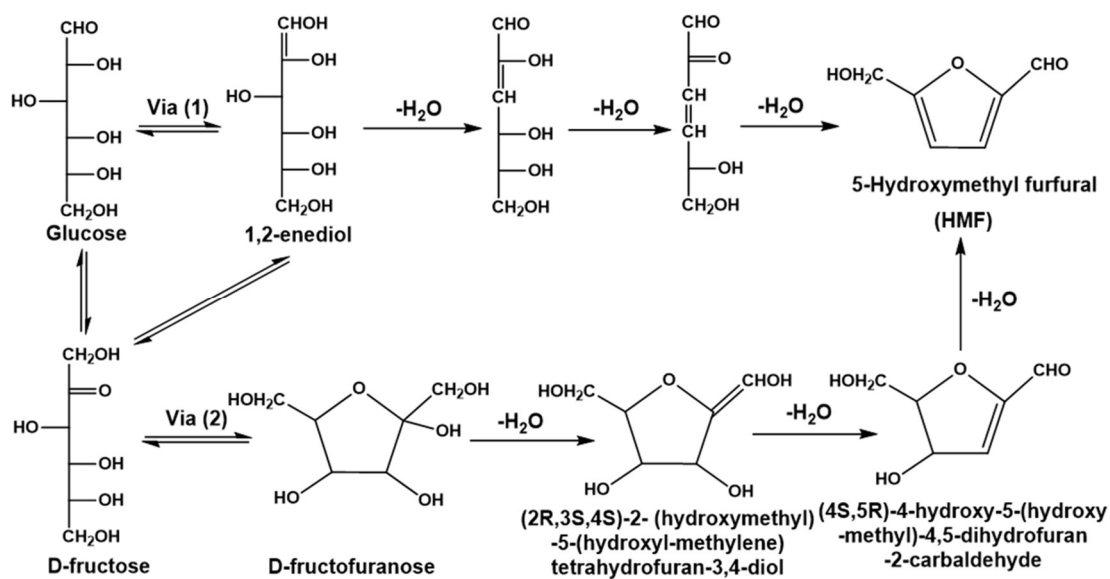


Figure 2.3 Pathways of glucose dehydration into HMF.

The cyclic conversion pathway involves glucose isomerization into fructose, which further is converted into HMF. Various studies investigated the mechanisms of fructose production from glucose isomerization in various reaction media.⁴⁰⁻⁴² And, Mika et al⁴³ has reviewed the recent achievements of the mechanistic investigations of glucose isomerization. The proposed “1,2-hydride-shift” mechanism of glucose isomerization has been widely accepted and is showed in Figure 2.4. Besides, DFT studies showed that the “1,2-hydride-shift” step is proposed as the rate-limiting step in the catalytic system under both acidic and basic conditions.⁴⁴ The proposed fructose dehydration (Figure 2.3 (Route 2)) started with the D-fructofuranose dehydration, forming (2R,3S,4S)-2-(hydroxymethyl)-5-(hydroxyl-methylene) tetrahydrofuran-3,4-diol, referring to 3,4-DIOL. 3,4-DIOL is further dehydrated into (4S,5R)-4-hydroxy-5-(hydroxymethyl)-4,5-dihydrofuran-2-carbaldehyde, followed by dehydration to HMF.^{37, 39}

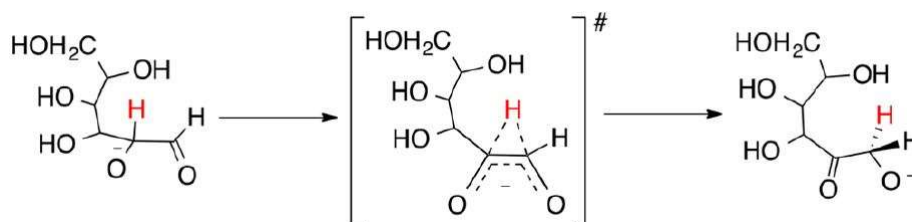


Figure 2.4 Proposed mechanism of glucose isomerization to fructose. This figure was reproduced with permission from the literature.⁴²

2.2.1.2.2 One-pot conversion of glucose into HMF

Currently, the fructose dehydration is the most common route to produce HMF. And fructose can be obtained by selective glucose isomerization or acid-catalyzed sucrose and inulin hydrolysis. Various catalysts have been used for the fructose dehydration including various organic and/or inorganic acids⁴⁵ and salts,⁴⁶ as well as various solid acids, i.e. ion-exchange resins⁴⁷ and zeolites⁴⁸. Although the production of HMF from fructose dehydration is more selective and efficient compared to that from glucose. HMF production from glucose is much more economical than that from fructose since glucose is one of most abundant monosaccharides as the basic unit of cellulose. Thus, glucose has a great potential as a feedstock in the industry production of HMF.¹ The dehydration of glucose requires two consecutive steps involving in glucose isomerization into fructose and fructose dehydration into HMF.⁴⁹ The glucose isomerization reaction as the prior step in glucose conversion to produce HMF can be catalyzed by Lewis acids, Brønsted bases, as well as immobilized enzymes. Palkovits and Bai et al⁵⁰ reviewed the heterogeneous and homogeneous catalytic glucose isomerization, with the application of various catalysts including organic bases, anion

exchange resins, hydrotalcites, zeolites and so on. In addition, Mika et al⁴³ focused on the recent achievements of the mechanistic investigations in glucose isomerization. In this thesis, we focus on the one-pot glucose transformation into HMF. And recent some achievements of one-pot glucose dehydration into HMF are summarized in Table 2.1.

Acid-base system. It is commonly accepted that the glucose isomerization is promoted by Brønsted base or Lewis acid and the subsequent fructose dehydration into HMF is favored by BAS or LAS.⁴⁹ Takagaki et al.^{51, 52} performed the one-pot glucose transformation into HMF combining various solid acids and basic Mg-Al hydrotalcite catalysts. This study⁵¹ demonstrated that the basic Mg-Al hydrotalcite ($\text{Mg}_6\text{Al}_2\text{CO}_3(\text{OH})_{16}\cdot 4(\text{H}_2\text{O})$) catalyzed the glucose isomerization with 38% of fructose yield obtained at 100 °C after 3 h in DMF. Combining the Mg-Al hydrotalcite and Amberlyst-15, 58% of HMF selectivity was obtained directly from glucose at 73% of conversion at 80 °C after 9 h. This catalytic system was also applied for disaccharides dehydration into HMF. Besides, the basic zirconium silicate ($\text{Na}_2\text{ZrSi}_4\text{O}_{11}$) also showed a good activity in the reaction of glucose isomerization to fructose.⁵³ Combining $\text{Na}_2\text{ZrSi}_4\text{O}_{11}$ and Amberlyst-15, 45% of HMF selectivity and 87% of glucose conversion were obtained at 180 °C after 1.5 h in the THF/ H_2O biphasic system. Study also showed that the basic NaAlO_2 catalyst could also promote glucose isomerization effectively, providing 72% of fructose selectivity at 68% of glucose conversion using a multiphasic system of H_2O , propylene glycol and DMSO.⁵⁴ And up to 82% yield of HMF was achieved from the sequent fructose dehydration over HCl.

The combination of base-catalyzed glucose isomerization and subsequent acid-

catalyzed fructose dehydration can produce HMF in relatively high yield, however, the reaction system has several drawbacks.⁵⁵ Firstly, the environment for the co-existence of base and acid catalysts is required. To isolate the active sites of bases and acids, organic aprotic solvents are the preferred reaction mediums because they can minimize the possible acid-base pairs interaction. However, using organic solvents has the main drawbacks about their subsequent purification from products. In addition, the byproduct water obtained from the glucose dehydration could cause the mutual destruction of acid and base moieties even if in the organic reaction system.

Lewis-Brønsted acid system. Combined BAS and LAS could provide an integrated approach for the direct glucose conversion into HMF. For example, the combination of HCl with BAS and Sn-beta catalyst with LAS for HMF production from glucose was explored in a biphasic system.⁴⁸ 70% of HMF selectivity and 79% of glucose conversion were obtained at 180 °C in the H₂O/n-butanol biphasic system. Besides, it was also found that 26% of glucose conversion was achieved with only HCl and 18% of HMF selectivity obtained with only Sn-beta, suggesting that BAS and LAS have a synergistic effect for glucose conversion into HMF. In contrast to the combined Brønsted base and acid catalytic system, combining BAS and LAS could provide a more easily integrated “one-step” conversion process, especially in an H₂O media.⁵⁶

Table 2.1 Dehydration performance of glucose into HMF over various catalysts.

Catalysts	conditions	Glucose conversion (%)	HMF yield (%)	HMF selectivity (%)	Ref.
Sn-beta /HCl	180 °C;70 min; pH = 1; THF/H ₂ O (1:3); 35% NaCl in H ₂ O; Glucose/ Sn molar ratio of 200.	79	55.3	70	48
Mg–Al hydrotalcite/ Amberlyst-15	80 °C, 9 h; DMF 3 ml, Glucose 0.1 g, Amberlyst- 15 0.1g, HT 0.2g	73	42.4	58	51
Na ₂ ZrSi ₄ O ₁₁ /Amberlyst- 15	180 °C; 1.5 h; 1.5 mL THF/H ₂ O; 75 mg glucose; 50 mg Amberlyst-15; 200 mg Na ₂ ZrSi ₄ O ₁₁ .	87	39	45	53
H-BEA-25	130 °C; 30 min; 125 g/L H- BEA-25; 10wt% glucose.	/	60	/	57
H-ZSM-5	195°C; 30min; 20wt% of NaCl in MIBK/H ₂ O solvent; 150 mg glucose, 50 mg catalyst; 3.5 mL solvent.	80	42	52.5	31
ZrO ₂	200 °C; 3 min. microwave heating; 2 wt.% glucose in H ₂ O; glucose/catalyst weight ratio of 2.	48.4	2.2	4.6	58
ZrPO (P/Zr = 2)	160 °C; 1h; 800 psi He; 10 wt.% glucose in H ₂ O; 5 wt%. catalysts.	38	14.4	38	60
SnPO	160 °C; 1h; 800 psi He; 10 wt.% glucose in H ₂ O; 5 wt%. catalysts.	80	30.4	38	60
NbPO/Si	135 °C; 2 g catalyst; 40 mL H ₂ O; 4 g MIBK.	<10%	/	60	61
15wt%P-TiO ₂	175 °C; 3 h; 2 g glucose; 0.6 g catalyst; 30 mL H ₂ O; 70 mL n-butanol.	97	78.6	81	62
SAPO-34	170 °C; 40 min; 10 mg glucose; 20 mg SAPO-34; 1.6 g GVL.	100	93.6	93.6	63
TaOPO ₄	170 °C; 1h; 50 mg catalyst; water/MIBK solvent; 100g glucose	56.3	32.8	58.3	64

FePO ₄	140 °C; 15 min; 1 g glucose; 0.5 g catalyst, 3.5 g NaCl, 30 mL THF, 10 mL H ₂ O.	97.8	23.1	23.6	65
SO ₄ -ZrO ₂ /SBA-15	100 °C; 6h; 0.1 g glucose; 0.1 g catalyst; 20 mL of H ₂ O.	9.5	1.3	13.5	70

2.2.1.2.3 Bifunctional catalysts for glucose conversion into HMF

Multifunctional catalysts possessing acid-base sites or LAS-BAS have also been developed to facilitate the glucose transformation into HMF. The amphoteric catalysts containing acidity-basicity or BAS-LAS were employed in the glucose conversion. Metal oxides are of the common bifunctional catalysts for converting glucose into HMF. Swift and co-workers⁵⁷ found that H-BEA-25 zeolite with both BAS and LAS could be used for the HMF production from glucose. 60% of HMF yield was obtained at 130 °C after 30 min in H₂O. Other silica-aluminate materials were also applied for glucose conversion. For example, the acidic H-ZSM-5 zeolites prepared by ion-exchange method is catalytically active for glucose-to-HMF transformation.³¹ 42% of HMF yield at 80% of glucose conversion was obtained at 195°C after 30 min in MIBK/H₂O biphasic system containing 20 wt% of NaCl. The authors pointed that the good catalytic performance of H-ZSM-5 could be due to the higher BAS/LAS ratio. Zirconia (ZrO₂) and titanium (TiO₂) as the efficient catalysts for glucose isomerization to fructose have also been reported.⁵⁸ Studies showed that ZrO₂ promoted the glucose isomerization reaction, while TiO₂ could not only promote the glucose isomerization but also improve the HMF production from glucose. Besides, the study showed that microwave heating could improve the activity. Higher fructose conversion and HMF yields (73% and 35%,

respectively) were obtained. Thus, sulfated zirconia (SZ) bearing BAS and LAS is considered as an attractive solid acid catalyst for HMF production from glucose dehydration. Initial studies on the catalytic performance of SZ in H₂O media were somewhat disappointing ascribed to the instabilities of the SO₄²⁻ under high-temperature.⁵⁹ However, zirconium phosphates^{60, 61} exhibited good catalytic performance and stability in glucose conversion. Besides, Beltramini and co-workers⁶² found that titanium phosphates (TiPO) also showed excellent catalytic activity in glucose-to-HMF transformation. 81% of HMF yield at 97% of glucose conversion was achieved at 175 °C after 3 h in the n-butanol/ H₂O biphasic system. Meanwhile, the catalyst could be reused for several times, showing a good stability. Zhang and co-workers⁶³ prepared silicoaluminophosphates (SAPO-34) catalysts with BAS and LAS for the dehydration of glucose in γ -valerolactone. 93.6 % of HMF yield and almost 100 % of glucose conversion were obtained after 40 min at 170 °C. Various metal phosphates such as aluminum (Al),⁶³ titanium (Ti),⁶² zirconium (Zr),²⁹ tin (Sn),²⁹ tantalum (Ta),⁶⁴ iron (Fe),⁶⁵ and niobium (Nb)⁶¹ phosphates showed the activity in HMF formation from glucose.

Although acidic metal oxides are promising, their efficiency still need to be improved significantly in the HMF production. One of the possible methods is to deposit the catalyst on highly porous supports achieving both high dispersion and stabilization. Nanostructured silica, e.g., MCM-41⁶⁶ and SBA-15⁶⁷, with well-defined mesoporous configuration are attractive supports due to their high surface area and stability. To maintain the internal pore network and make the reactant accessible, it is critical to

control the immobilization of acidic metal oxides to minimize the formation of crystallite which leads to pore blockage.⁶⁸ Various synthesis methods including incipient wetness impregnation,⁶⁹ direct synthesis method,⁶⁷ solution-phase atomic layer deposition⁷⁰ and vapor-induced hydrolysis⁷¹ have been explored. For example, Wilson's group⁷⁰ reported hydrothermally stable SZ monolayer supported on mesoporous SBA-15 ($\text{SO}_4\text{-ZrO}_2/\text{SBA-15}$) prepared using a solution-phase atomic layer deposition method. For the catalyst, LAS are ascribed to the metal atoms, while the BAS is from the protons of the surface hydroxyl groups. The ratio of BAS/LAS increased with the sulfate loading. The ordered mesoporous material $\text{SO}_4\text{-ZrO}_2/\text{SBA-15}$ catalyst with bilayer structure showed high density of acid sites and exhibited a 3-times enhancement in HMF production from glucose than the non-porous counterparts. However, there are several challenges in designing the bifunctional solid acid catalysts for glucose conversion. (1) Controlling the density of different acid sites as well as the total acid sites is crucial for the design of catalysts. The density of total acid sites is a key factor in controlling the glucose conversion rate, while the ratio of LAS/BAS is critical in maximizing HMF yield since BAS can retard isomerization of glucose, promote HMF rehydration and facilitate humins formation.⁷² In addition, the LAS can induce more pronounced polymerization despite its enhancement on glucose isomerization rate.¹¹ (2) Improving the water-tolerance of catalysts is also important. Water, one of the by-products of hexose dehydration, poisons solid acids catalysts, because of its strong adsorption on the active sites, leading to site-blocking and active sites leaching.^{73, 74} The water-tolerant phosphate-immobilized TiO_2 solid acid was

reported by Noma et al.,⁷⁵ where phosphate/TiO₂ was used for glucose conversion. 34% of HMF yield at 49% of glucose conversion was achieved at 120 °C after 4 h. Besides, they suggested that the continuous extraction of HMF increased the HMF selectivity, even using a high concentration of glucose solution (40 wt%) as the substrate since the side reactions occurred between HMF and intermediates could be prevented.

In conclusion, the production of HMF is not only governed by the acidity, i.e. the density and strength of acids, the LAS/BAS ratio, and the total acid density, but also related to any synergistic functional groups existed on catalysts, the accessibility of active sites, the surface area and wettability of solid acids. Therefore, numerous attempts to tailor the textural properties and surface chemistry of solid acids have been made to maximize their catalytic activity in glucose transformation to HMF.

Besides, from the viewpoint of green chemistry, H₂O is an ideal solvent because of its cheap, non-toxic, and non-flammable characteristics.⁷⁶ In a heterogeneous catalytic process, glucose could also be converted directly into HMF in aqueous system. Until now, there are several examples for solid acid-catalyzed glucose dehydration in H₂O, but the yields of HMF are generally disappointing since the rehydration of HMF to levulinic acid and/or formic acid occurs easily in H₂O with the existence of acidic catalysts.^{77,78} To improve HMF yield, aprotic solvents such as DMF,⁵⁷ GVL,⁶³ acetonitrile, and DMSO have been used in the HMF production. And the high yield of HMF has been achieved under the moderate operating conditions in DMSO. DMSO as solvent could prevent the formation of LA and humin;⁷⁷ however, the main drawbacks of using DMSO involve in the difficulty of separating products from DMSO as well as the possibility

of DMSO decomposition forming the toxic S-containing byproducts.¹ Besides, the biphasic solvents (H₂O -organic) are also widely used in HMF production from glucose. The adding of H₂O could improve the solubility of glucose in organic solvents. In addition, the using of biphasic system, like H₂O/butanol,⁶² H₂O/MIBK,³¹ and H₂O/THF^{61, 64} reduced the formation of byproduct LA. Therefore, extensive studies aiming at searching for both most suitable reaction medium and the catalytic system are still required.

2.2.1.3 Acid-catalyzed α -ketoaldehyde conversion to α -hydroxycarboxylic acids

2.2.1.3.1 α -Hydroxycarboxylic acids

α -Hydroxycarboxylic acids including lactic acid (LA) and mandelic acid are a class of chemicals that consist of a hydroxyl group and a carboxylic group at the adjacent carbon. They can be used to remove the dead cells on our skin, to reduce bacteria and photodamage. Besides, they could also be applied to prepare food additives, plastic products, pharmaceuticals and other chemicals.¹

Lactic acid (LA)

As a bifunctional compound bearing carboxylic and hydroxyl groups, LA can be used in numerous chemical conversions to produce useful products in the chemical, food, cosmetic and pharmaceutical industries. These important platform compounds derived from LA are presented in Figure 2.5.¹ LA as a monomer could be applied for the synthesis of biodegradable polylactic-acid polymers, which could be an environmentally friendly alternative to petrochemicals-derived plastics.⁷⁹

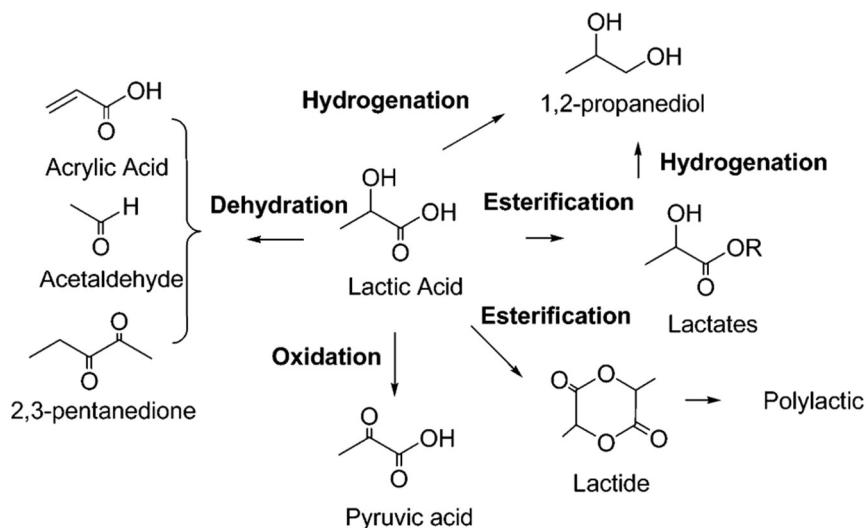


Figure 2.5 Summary of these important chemicals derived from lactic acid. This figure was reproduced with permission from the literature.¹

Mandelic acid

Lignin, the second most abundant terrestrial biopolymer, is the product of the biologically regulated radical coupling of three compounds: coniferyl alcohol, coumaryl alcohol and sinapyl alcohol.⁸⁰ Conceptualizations of lignin structures and surrogate compounds used in the lignin chemistry are included in Figure 2.6. β -O-4 linkages, whose oxygens are found at positions both α - and β -carbons relative to benzene rings,⁸¹ are readily transformed via the chemical reaction to the α -hydroxycarboxylic acids. Fungal decomposition of lignin generates methoxy-, hydroxy-substituted mandelic acids, and substituted phenylglyoxylic acids, phenylpyruvic acids, and aromatic aldehydes during industrial chemical processes that are part of pulp and paper manufacture.^{82, 83}

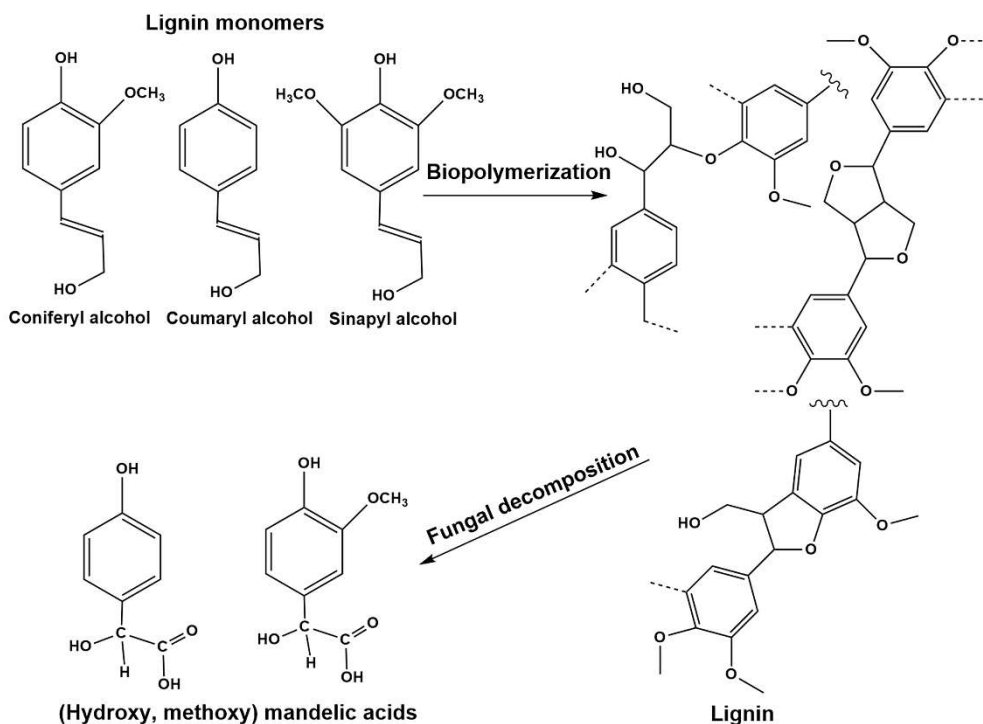


Figure 2.6 The production of mandelic acid- and phenylglyoxylic acid-like structures from Lignin. This figure was reproduced with permission from the literature.⁸⁰

2.2.1.3.2 Conversion of trioses to LA

LA can be produced by fermentation and/or chemical routes from various biomass-derived carbohydrates such as sucrose from syrups, juices, and molasses, as well as maltose from enzymatic starch conversion, glucose from starch, and lactose from whey.⁸⁴ The current manufacture route for LA, based on the fermentation of carbohydrate sources, seems unable to develop in a large market, due to the low productivity of LA and the stoichiometric amount of waste (gypsum) generated.⁸⁵ Therefore, novel methods to produce LA from carbohydrates through non-fermentative chemical routes have attracted great interest in both academic and industrial fields. Various feedstock such as C6 sugars⁸⁶⁻⁸⁸ (glucose and fructose) and C6 sugars

precursors (cellulose⁸⁹) and C6 sugars derivatives (glycerol,⁹⁰ dihydroxyacetone (DHA) and glyceraldehyde (GLY)⁹¹⁻⁹³ were investigated for the LA production. Interestingly, these studies demonstrated that when converting C6 sugars and glycerol into LA, trioses, such as DHA, GLY, as well as pyruvaldehyde (PRV), are intermediates. Therefore, it is concluded that one of the most promising strategies could be the conversion of trioses, i.e. DHA and GLY, into LA through PRV intramolecular Cannizzaro reaction as shown in Figure 2.7.⁹⁰

The conversion of trioses into LA is typically performed in subcritical H₂O in the presence of homogenous catalysts, such as strong basic media (NaOH and Ca(OH)₂)⁸⁷ or metal salts⁹⁴. Hence, developing alternative processes enabling a large-scale, environmentally friendly, and cost-effective production of LA is demanded. The two trioses, i.e. DHA and GLY, can be obtained either catalytically or biochemically from glycerol,^{95, 96} which could be obtained as a byproduct in the biodiesel production. The very low price of glycerol with a high purity provides its potential to serve as feedstock for industrial LA synthesis.⁹⁷

The oxidation of glycerol to LA is a classic reaction which involves the combined oxidation of glycerol to DHA and GLY, the dehydration of GLY or DHA to PRA, and the dehydration of PRA into LA.⁹⁸ The glycerol oxidation to DHA and GLY is an essential step in the LA production from glycerol. For this reason, redox-acid-base trifunctional catalysts are considered and have been reported towards the target production of LA. For example, Pt/ZrO₂,⁹⁹ Ru-Zn-Cu/hydroxyapatite,¹⁰⁰ CuO/ZrO₂,¹⁰¹ Au-Pt/ CeO₂¹⁰² et al. showed a high catalytic activity in the presence of a base.

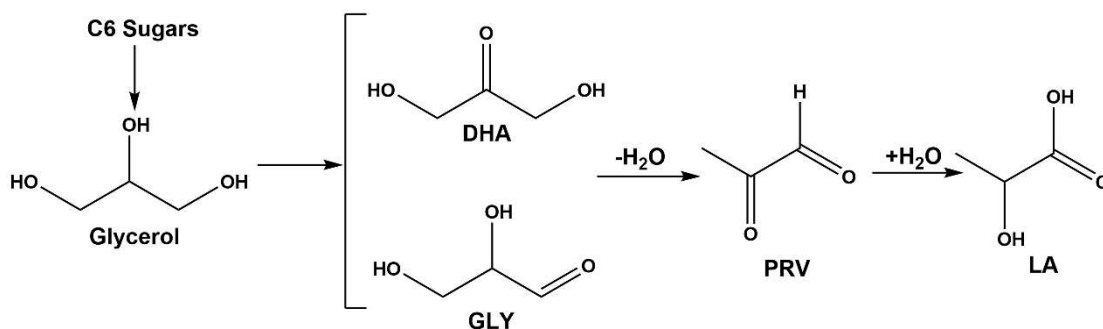


Figure 2.7 LA production from C6 sugars conversion.

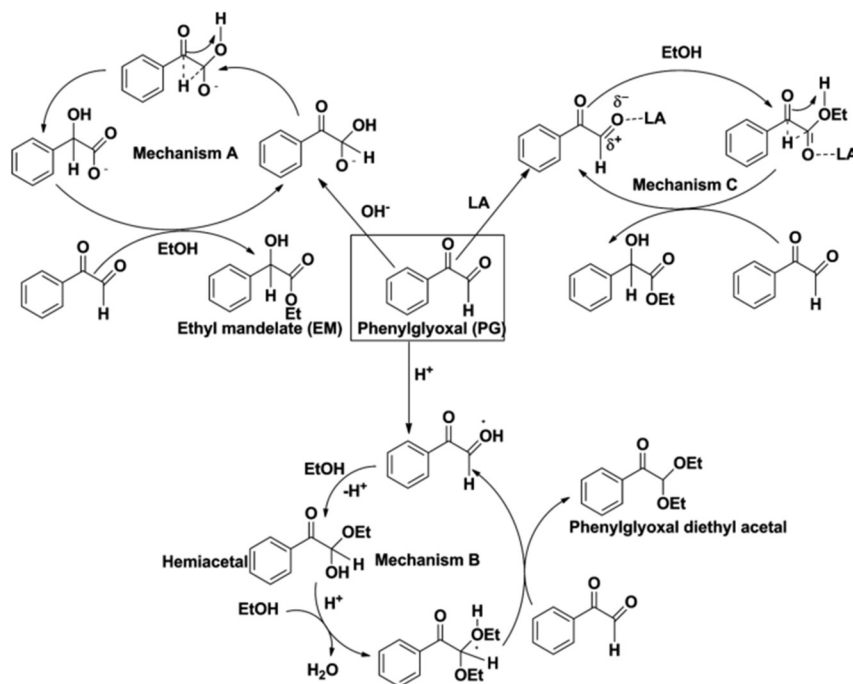
Moreover, the conversion of trioses (DHA and GLY) into LA has been conducted either as two separate steps or in one pot over bifunctional catalysts with LAS and BAS¹⁰³ which involves the dehydration of DHA and/or GLY to PRV, followed by PRV intramolecular Cannizzaro reaction into LA. For example, the ultra-stable zeolite (H-USY) has been reported to be an efficient catalyst in DHA dehydration reaction, with 90 mol% of LA obtained at 125 °C in aqueous system.⁹³ Moreover, tin (Sn) modified materials, such as Sn-MFI zeolites,⁹³ Sn-Beta,¹⁰⁴ Sn-MONT,¹⁰⁵ Sn-doped MCM-41,¹⁰⁶ ¹⁰⁷ SnO₂/NbOPO₄¹⁰⁸ and Sn-MWW zeolites¹⁰⁹ also have been proved to be effective catalysts for the trioses conversion into LA. 85% of LA yield from DHA at 97% conversion was obtained over Lewis-acidic Sn-MFI zeolites as highly active catalysts.¹¹⁰ SnPO catalysts were also used in the conversion of triose sugars; 96.1% of LA yield was achieved at 140 °C after 4 h.¹¹¹ In addition, other metals (such as Cr, Al, Zr, and Ti) supported on zeolites were also demonstrated to be catalytically active components in the reaction of DHA conversion to methyl lactate.^{110, 112, 113} Bifunctional Fe-doping SnO₂ catalysts with both BAS and LAS also exhibited high efficiency and selectivity for the sugars conversion to LA and showed good reusability.¹¹⁴ However, it was found that the dehydration of DHA and GLY into PRA can be catalyzed by a basic

catalyst better than by an acid or a neutral medium.¹¹⁵ Alkaline-treated ZSM-5 zeolites⁹³ afforded an exceeding 90% of LA selectivity. The combination of commercial Pt/Al₂O₃ with alkali metal hydroxides¹¹⁶ attained up to 96% of LA selectivity. Furthermore, a remarkable 100% of LA selectivity from DHA could be reached on bifunctional metal/base catalysts.¹¹⁶

2.2.1.3.3 Acid catalyzed phenylglyoxal conversion to mandelic acid

The production of mandelic acid and its derivatives is of great interest due to their important applications as discussed in Section 2.2.1.3.1. The conversion of PG provides a one-step method for the production of mandelic acid and its derivatives. Considerable efforts have been attempted to produce mandelic acid and its derivatives from PG.¹¹⁷⁻¹²⁰ Similar to the reaction pathway of LA production from PRA, the intramolecular Cannizzaro reaction is the key step in this reaction. Homogeneous acids and bases were originally used. The mechanisms of the reaction catalyzed by homogeneous acids and base is shown in Scheme 2.1. However, these catalysts have inherent disadvantages arising from their toxic and corrosive nature, problems related to catalyst separation, regeneration, as well as the occurrence of competitive side reactions. Recently, the PG conversion to produce mandelic acid and its derivatives by employing suitable solid acids has attracted extensive attention.¹²⁰⁻¹²² Various catalysts including zeolites, nanoporous silica/alumina materials^{120, 121} have been applied for the catalytic conversion of PG. It is concluded that the reaction pathway of PG conversion into mandelic acid and its derivatives on solid acids is similar to the reaction of the α -keto

aldehydes and alcohols in homogeneous catalytic systems.^{118, 123} Pescarmona et al.⁹² reported that the high activity of zeolite USY CBV 600 catalyst on the production of desired ethyl mandelate (97% of selectivity) was due to the presence of LAS induced from extra-framework Al species. However, it was also reported that the BAS on solid-acid catalysts showed a beneficial effect on this reaction. Si/Zr materials with both BAS and LAS showed higher activity in PG conversion into ethyl mandelate than ZrO_2 with only LAS.¹²⁴ Moreover, ethyl mandelate could be produced even if the catalyst has only BAS.¹²¹



Scheme 2.1 Proposed reaction mechanisms of PG conversion in EtOH in the homogeneous base catalytic system(A), homogeneous BAS catalytic system (B), and LAS catalytic system (C). This scheme was reproduced with permission from the

literature.¹²⁰

2.2.1.4 Conclusions

Selective conversion of biomass-derived carbohydrates to value-added chemicals over solid acids is an important topic in the field of biomass valorization. This sub-section provides a recent development of heterogeneous catalysts for HMF and α -hydroxycarboxylic acids production from glucose and α -ketoaldehyde.

In HMF production from glucose, the BAS and LAS play different roles in the glucose-to-HMF transformation. Generally, it is accepted that BAS promotes the dehydration of fructose, whereas LAS plays an important role in the two steps of glucose conversion, especially in the glucose-to-fructose isomerization, which is the determining step in the conversion of glucose to HMF. More importantly, it has been found that suitable BAS/LAS ratio is crucial to achieve higher yield and selectivity towards HMF. Therefore, extensive research should be carried out to determining the detail roles of BAS and LAS in the glucose-to-HMF conversion.

In the α -ketoaldehyde conversion to α -hydroxycarboxylic acids, where the intramolecular Cannizzaro reaction is the key step, the solid acids with LAS were widely reported as efficient catalysts. However, there are studies demonstrated that the BAS shows a beneficial effect on this reaction. BAS can also promote the PG conversion to mandelic acid and its derivatives mandelate. Besides, it is pointed that LAS and BAS collaborate to promote the reaction process. Therefore, the individual role of BAS and LAS in this reaction remains a matter of debate. The role of BAS and

LAS in this reaction should be investigated. In addition, there are also many challenges that need to be addressed, and this thesis specifically aims to address the following challenges.

(1) Although various efficient heterogeneous catalysts have been developed for biomass-derived carbohydrates, some of these catalysts are not stable, especially under high reaction temperatures. Thus, design and synthesis of novel stable heterogeneous catalysts with high catalytic activity is very crucial.

(2) More efforts should be devoted to understanding the molecular interactions between the catalysts, feedstock, and solvents to understand the reaction mechanisms of biomass-derived carbohydrates conversion over different catalysts. And it is meaningful to clarify their specific roles in reaction routes to achieve high activity of catalysts and selectivity of target products, which could in turn guide the design of novel catalytic systems.

Thus, in this thesis, multi-functional solid acid catalysts with LAS and BAS are developed for the tandem dehydration of biomass-derived carbohydrates to value-added chemicals. Additionally, the density and strength of acids in solid acids are examined and controlled since the acid-catalytic processes and the selectivity of target products could be affected significantly by their density, strength, and ratio. Furthermore, the roles of LAS and BAS in the conversion of biomass-derived carbohydrates are clarified and the mechanism of reactions is investigated.

2.2.2 Catalytic oxidation of biomass-derived glucose

Oxidation reactions are widely used to produce high value chemicals from biomass-derived carbohydrates.^{4, 125} Glucose oxidation reactions have been extensively studied recently. Figure 2.8 presents these compounds produced from glucose oxidation reactions. Different functional groups of glucose can be oxidized into value-added oxidation compounds via the oxidation of the anomeric center (C1), the secondary alcohols at (C2 and C4) as well as the primary alcohol (C6). Besides, the over-oxidation of glucose or product, and the cleavage of the vicinal diol producing degradation products could also occur.¹ The chemo- and regio-selectivity are most important features of the catalytic glucose oxidation due to the multifunctionality of glucose. The oxidation of glucose at anomeric center position is easier than that at primary and secondary -OH groups.¹²⁶ Thus glucose oxidation generally produces high yield of gluconic acid especially when the reaction is catalyzed by supported metal catalysts, mainly noble metals.¹²⁷ There, herein we focus on the gluconic acid production from glucose via supported metal catalysts and the recent achievements were summarized in Table 2.2. In addition, the proposed mechanism of glucose oxidation on Au particles, the commonly used catalysts, is also discussed.

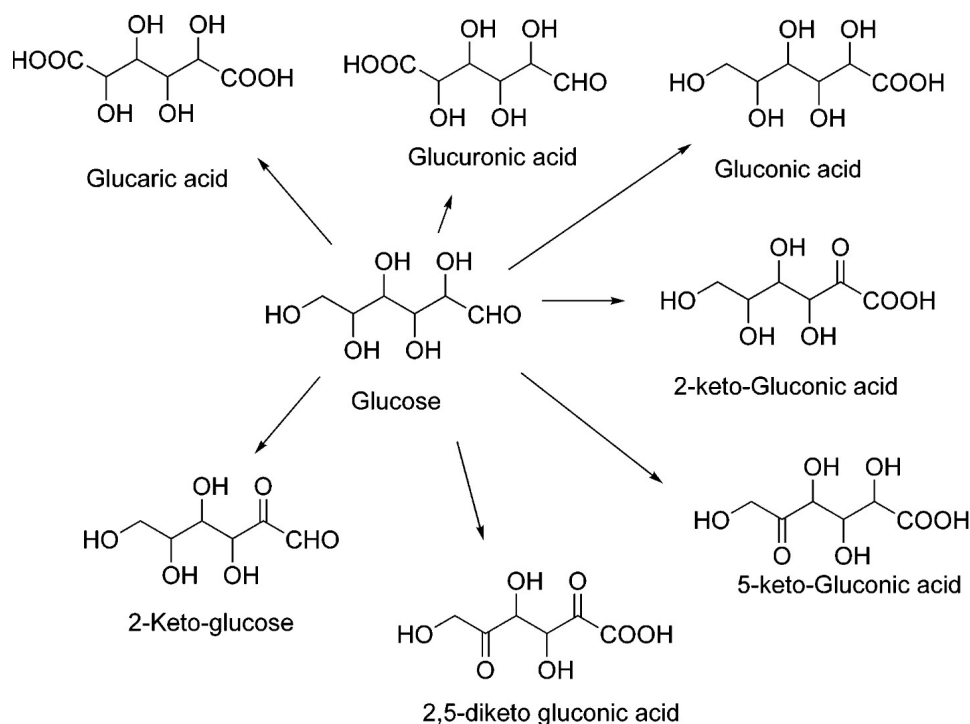


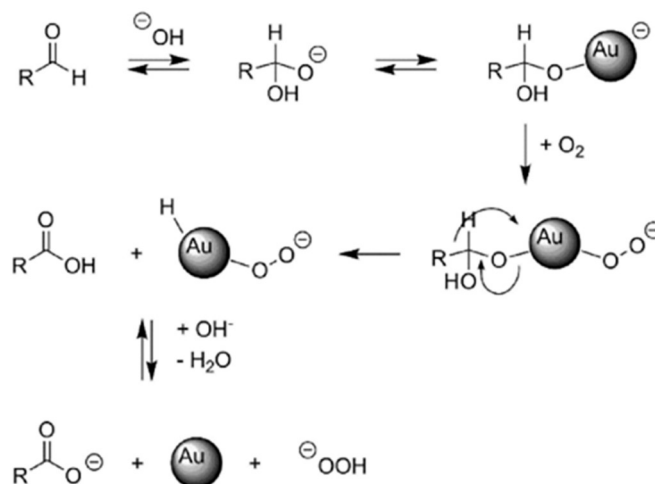
Figure 2.8 Summary of chemicals obtained via glucose oxidation. This figure was reproduced with permission from the literature. This figure was reproduced with permission from the literature.¹

2.2.2.1 Mono-metallic catalysts

The oxidation reactions of glucose catalyzed by metal supported catalysts has been reported widely.¹²⁸ Until now, gold (Au) as an efficient catalyst has been extensively studied for biomass-derived glucose oxidation. 99% of gluconic acid yield was achieved from glucose oxidation over Au particles (2-5 nm) deposited on activated carbon at 50 °C under basic condition.¹²⁹ However, the deactivation of catalysts was observed, which could be due to the metal leaching and sintering.

The Langmuir-Hinshelwood mechanism (Scheme 2.2) is proposed for glucose oxidation on the Au surface in the basic medium where a deprotonated germinal diol is formed from glucose which undergoes the nucleophilic attack of hydroxide ions.

Subsequently, diol and O_2 adsorbed on the Au particle surface form $O^{\bullet-}$ species and a metal alkoxide. Finally, a gluconate ion is formed due to diol decomposition by hydrogen transfer, and the remaining hydrogen atom reacts with $O_2^{\bullet-}$ species to produce $HOO^{\bullet-}$ species which will be desorbed subsequently. A high oxidation rate can be obtained in an alkaline condition. Besides, Biella et al reported that the turnover frequency (TOF) value could be improved almost four times with the increase of pH value from 7 to 9.5.¹²⁹ A similar conclusion using Au catalyst was also drawn by Comotti et al.¹³⁰



Scheme 2.2 Mechanism of gluconic acid formation from glucose oxidation over Au particles under basic condition. This scheme was reproduced with permission from the literature.¹³¹

Molecular oxygen (O_2) as the preferred oxidant has been widely used in glucose oxidation. In addition, hydrogen peroxide (H_2O_2) as the common oxidation agent has also been used widely in this reaction because of its good solubility in H_2O . A high activity with $8300 \text{ mmol min}^{-1} \text{ g}_{Au}^{-1}$ and high selectivity of gluconic acid ($> 99 \%$) were obtained over $0.3 \text{ wt}\% \text{ Au/Al}_2\text{O}_3$ at 40°C in basic medium ($\text{pH}=9$) using H_2O_2 as

the oxidant.¹³² The high oxidation activity could be attribute to Au/Al₂O₃ efficiently decomposing H₂O₂ to O₂. In addition, studies showed that the Au particle size could affect the activity of glucose oxidation.¹³³ The activity could be improved with the increase of the Au particle size from 1.2 nm to 1.9 nm and the best activity with TOF of 2.3 s⁻¹ was observed. Besides, Ishida et al.¹³⁴ also studied the influence of the support on catalytic activity. And they concluded that even if the support could affect the stability of catalyst and even the size of Au particles but could not affect the catalytic activity considerably. Also, Rossi group¹³⁵ reported that particle agglomeration and sintering are the main reason of catalyst deactivation. The agglomeration or sintering of Au particles reduced the specific surface area of catalysts and consequently reduced the catalytic activity. Irreversible deactivation arising from metal leaching and particle sintering in base-free conditions was observed using ceria-supported Au nanoparticles.¹³⁶ The stability of catalysts against the metal sintering could be improved by reducing the Au loading amount. Moreover, the study showed that the deactivation of catalysts arising from the adsorption of reactive species is reversible and the catalysts could be regenerated by simply calcination process. An extensive study about catalyst deactivation was conducted using Au colloids immobilized with carbon by Odriozola and co-workers.¹³⁷ The regeneration procedure via calcination treatment was proved to be non-effective. This showed that the adsorption of some intermediates or products is not the main reason in the deactivation of catalysts. The main reason for catalytic deactivation could be due to the metal leaching. Besides, the formation of particle sintering was also observed.

Table 2.2 Oxidation performance of glucose into gluconic acid over different catalytic systems.

Catalyst	Conditions	TOF or Activity	Conversion of glucose (%)	Selectivity of gluconic acid (%)	Ref.
1%Au/ACC	50 °C; 6h; 4 wt% glucose; glucose/M = 1000; P_{O_2} = 300 kPa; pH=9.5	3000 h ⁻¹	100	/	129
0.3 wt% Au/Al ₂ O ₃	40 °C; H ₂ O ₂ ; pH=9 30wt.% glucose; 1.6 g catalyst; H ₂ O ₂ /glucose = 1.1 mol/mol.	8300 mmol min ⁻¹ g _{Au} ⁻¹	99	/	132
Au/ZrO ₂	50°C; pH =9.0; 5 wt% glucose solution (175 mL), 30 mg catalyst; 120 ml/min O ₂	45 s ⁻¹	/	98	134
2 % Pd/C (3 nm Pd)	60 °C; 7h; pH = 9, glucose/Pd molar ratio of 750; 0.6 M Glucose, 10 mL/min O ₂ .	0.5 s ⁻¹	/	95	138
5 % Pt/C	60 °C; 7h; pH = 9, glucose/Pt molar ratio of 750; 0.6 M Glucose, 10 mL/min O ₂ .	0.05 s ⁻¹	/	77	138
Pd-Bi/C	40 °C; 155min; pH = 9; glucose/Pd molar ratio of 787, Bi/Pd =0.1; 1.5 L/min O ₂ .	/	99.6	99.8	145
5%Pd-5%Te/SiO ₂	60 °C; pH = 9; 1 g catalyst; glucose concentration of 1 mol/L; 0.9 L/min O ₂ .	48.1 s ⁻¹	76.1	97.4	147
5% Pd-8%Bi/SiO ₂	60 °C; pH = 9; 1h; 1 L/min O ₂ .	/	/	>90	149

Similar to the Au supported catalysts, the major challenge of the supported Pt or Pd catalysts used in glucose oxidation is also the rapid deactivation. Delidovich et al.¹³⁸ reported that 5% Pt/C catalyst showed a good activity on glucose oxidation with a high

TOF of 0.05 s^{-1} at $60\text{ }^{\circ}\text{C}$. It is found that the catalytic activity was independent on the Pt size when the size of Pt particles was between 1.1 and 4.5 nm. And the 2% Pd/C catalyst with 3 nm of Pd particle showed the TOF value of approximately 0.5 s^{-1} under the same reaction conditions, while a similar catalyst with high Pd particles size (6.3 nm) showed a significantly high activity with the TOF of 1.3 s^{-1} . Nevertheless, although the high selectivity towards gluconic acid (over 95%) was obtained both in these two catalytic systems, the deactivation of catalysts was also observed due to the excessive oxidation of metals. Therefore, extensive research on the promotion of Pt and Pd based catalysts has been carried out to enhance their resistance to deactivation. Besides, due to the strong adsorption of byproducts on Pt and Pd and the occurrence of metal over-oxidation, many studies were deliberately undertaken under these conditions which can limit the O_2 transportation to the catalyst and avoid the formation of metal oxides.

2.2.2.2 Bimetallic or trimetallic catalysts

Although the excellent selectivity towards gluconic acid (nearly 100 %) achieved on monometallic catalysts for glucose oxidation at a relatively low temperature and moderate basic conditions, a major challenge of glucose oxidation via supported monometallic catalysts originates from the rapid deactivation of catalysts. Bimetallic catalysts modified with Pt and Pd have been investigated to inhibit the rapid deactivation.¹³⁸⁻¹⁴⁰ However, noble metal-supported catalysts are easy poisoned by oxygen molecule, generally showing low reusability. It was found that the addition of Bi as the promoter can not only help delay the deactivation of catalysts but also help to prevent the excessive oxidation of Pd particles partially and enhance the reusability of

catalyst.¹⁴¹⁻¹⁴⁴ Due to the excessive oxidation of Pd particles, the reaction rate was low over the unpromoted Pd based catalyst although it was active in glucose oxidation to gluconic acid. Besides the occurrence of side reactions ascribing to the excessive oxidation of Pd particles also decreased the selectivity of desired gluconic acid. However, the high selectivity of gluconic acid were observed using Bi-doping Pd/C and Bi-doping Pt-Pd/C as the catalysts. The reaction rate of glucose oxidation over Pd-Bi/C catalysts was 20 times higher than that on Pd/C. And the high catalytic activity of Pd-Bi/C could be obtained on both the fresh and recycled catalysts.¹⁴⁵ Bi was assumed to act as a promoter, which can protect Pd from over-oxidation due to strong affinity of Bi to O₂. The addition of Bi promoter in bimetallic Pt-Pd catalysts also increased the TOF of glucose oxidation.¹⁴⁶ The Bi-Pt-Pd trimetallic catalyst also demonstrated less deactivation.

Te is also proven to be a promoter for Pd-based catalysts and showed a significant increase in glucose oxidation. The 5%Pd–5%Te/SiO₂ catalyst showed increased catalytic activity with a TOF of 48.1 s⁻¹ in gluconic acid production from glucose at 333 K than that on 5% Pd/SiO₂ catalyst (0.79 s⁻¹).¹⁴⁷ Karsi et al.^{148, 149} studied the effect of various promoters (like Co, Bi, Sn and Tl) on Pd-based catalysts and developed the use of various oxophilic promoters. The results showed that the Bi doping catalysts exhibited the highest activity, followed by Tl, Sn and then Co. Bi promoter not only prevents excessive oxidation of metal Pd to PdO but also hinders the adsorption of acid by-products.¹⁴⁹

2.3 Photocatalytic transformations of biomass-derived substrates

As discussed above, biomass-derived carbohydrates are promising platforms for sustainable production of organic oxygenates due to their high oxygen/carbon molar ratios.¹⁵⁰ However, in the thermo-catalytic approaches of biomass-derived carbohydrates conversion, high temperature is generally required to overcome the activation barrier of reaction. For example, hydrogenolysis mostly occurs at a temperature higher than 150 °C¹⁵¹ and pyrolysis at the temperature of higher than 300 °C.¹⁵² In addition, thermal treatment is generally unselective towards target product since biomass-derived carbohydrates typically have multiple-functional groups. And the heat could not be transferred precisely to the targeted chemical bonds and reactant, which leads to the production of by-products, such as humins. Consequently, the considerable selectivity towards target products is difficult to achieve under high reaction temperatures, especially for these valuable but reactive products, such as aldehydes and/or acids.

Unlike the conventional catalysis using thermal energy, photocatalysis is based on the use of solar energy to drive chemical transformations.² As illustrated in Figure 2.9, photocatalysis is generally induced by light absorption of photocatalyst which then is activated to the excited state. The excited photocatalyst can then activate the reactant to overcome the energy barrier, giving target products. By using photons, the reaction can occur at low temperatures.^{153, 154} Therefore, photocatalysis has emerged as a promising approach for selective transformations of biomass-derived feedstock under mild conditions via harnessing solar energy.

An increasingly growing research focus on the selective production of fine chemicals from biomass conversion with solar energy. This sub-section mainly focuses on the recent work about heterogeneous photocatalytic conversion of biomass-derived alcohols into high value chemicals over metal oxide-based photocatalysts.

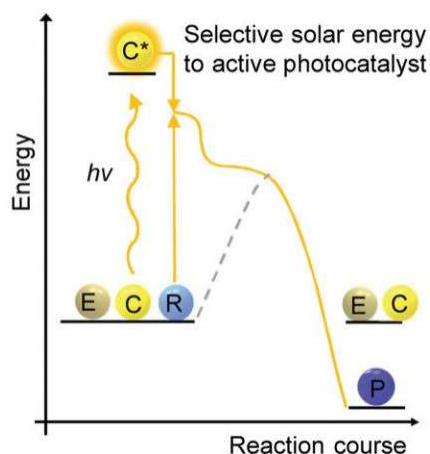


Figure 2.9 Energy diagram of photocatalytic reaction. R, P, C, E refer to the reactant, product, catalyst and molecules in the environment. Reproduced with permission from the literature.⁴

2.3.1 Semiconductor

Semiconductors are between conductors and insulators, which are defined by their unique electric conductive behavior.¹⁵⁵ The differences between these materials can be understood in terms of the quantum states of electrons. The electronic state is associated with the band structure of these materials.

Semiconductors can be organic and inorganic, crystalline and amorphous, solids and liquids. Even though they are different forms of substance, they all change their

properties dramatically in an electromagnetic field. There are two basic classifications of different semiconductors:

Intrinsic semiconductors: an intrinsic semiconductor refers to a pure semiconductor crystal which contains only one compound or one element. In this type of semiconductors, there are equal numbers of holes and electrons. Meanwhile the Fermi level of materials is located midway between the valence and conduction bands.

Extrinsic semiconductors: extrinsic semiconductors refer to those where a small amount of impurity has been doped to the basic intrinsic material. An excess or shortage of electrons are therefore created, and the band structure is modified. According to the different of charge carriers, semiconductors could further be classified to two types: (1) *p*-type: *p*-type semiconductor materials have a shortage of electrons, i.e., there are positively charged carriers (holes) in the crystal lattices. (2) *n*-type: *n*-type semiconductors have an excess of electrons. As a result, negatively charged carriers (free electrons) are available within the lattices. The Fermi level of a *p*-type semiconductors shifts closer to the valence band, while it shifts near to the conduction band for *n*-type semiconductors.¹⁵⁶

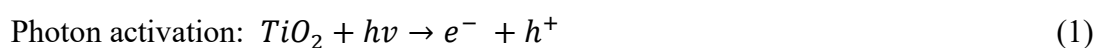
2.3.2 Photocatalytic oxidation of biomass derivatives

Conventional catalytic oxidation of biomass commonly occurs at high temperature and high pressures as well as employing stoichiometric amounts of oxidants as oxygen donors. These reactions are generally costly and toxic due to large amounts of hazardous waste produced. Therefore, it urges to develop more environmentally

friendly systems. From a sustainability point of view, the development of selective photocatalytic routes for the biomass-derived carbohydrates transformation into value-added platform molecules and chemicals at low temperature is of great significance.¹⁵⁷

2.3.2.1 Fundamental principles of photo-oxidation

The heterogeneous photocatalysis has been extensively studied and the fundamental principles have also been developed.^{158, 159} When the absorbed photon energy ($h\nu$) equals or exceeds the bandgap of the semiconductor photocatalysts, a photoexcited electron from the filled valence band (VB) is excited to the empty conduction band (CB) of the semiconductor. As a consequence, an electron and hole pair (e^-h^+) is formed as shown in equation (1).¹⁶⁰ Redox reactions then can occur at the surface of the photoexcited photocatalyst. Meanwhile, a very fast recombination of excited electrons and holes could take place unless O_2 as the electron acceptor scavenges the photoexcited electrons to produce superoxides ($O_2^{\bullet-}$) (equation (2)). Subsequently, hydroperoxyl radicals (HO_2^{\bullet} , HO_2^- and H_2O_2) are formed (equation 4-6). HO_2^{\bullet} radicals (equation (5)) also have scavenging electrons properties, thus prolonging the photo-hole lifetime. The generated h^+ have high potential to oxidize water into OH^{\bullet} (equation (7)) or to oxidize organic species directly. The abundant OH^{\bullet} species in water solution could further oxidate organic species to corresponding chemicals via the combination with generated h^+ (equation 8-9).^{157, 161} The mineral acid could be formed as the by-products.





2.3.2.2 Selective photo-oxidation of glucose

Photo-oxidation of biomass-derived sugars was developed using TiO_2 semiconductor as the catalyst initially, owing to its non-toxicity, low cost, thermal stability as well as photocorrosion resistance. Glucose as the main unit of cellulose remains the most studied model system. Photocatalytic oxidation of glucose can produce a wide range of high-value chemicals including gluconic acid (GA), glucaric acid (GUA), succinic, levulinic acids, 2,5-furan dicarboxylic, 3-hydroxy propionic and 3-hydroxybutyrolactone, which are important platform chemicals in pharmaceutical, food, perfume and fuel industries.¹⁶² The photocatalytic oxidation of glucose (Figure 2.10) was found to be highly selective towards GUA and GA, which are two important organic carboxylic acids. Particularly, GUA is a promising alternative for adipic acid production, which is widely used in the textile and polymers industries.¹⁶³ In addition, traces of light hydrocarbon products were also detected in this reaction.¹⁶⁴

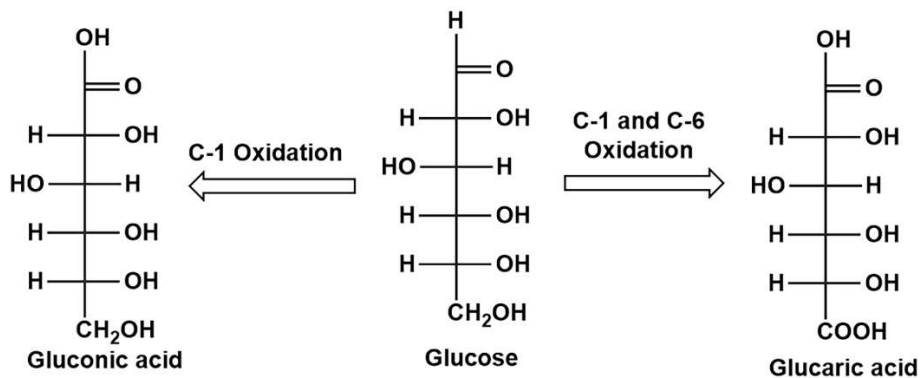


Figure 2.10 The scheme of glucose oxidation into gluconic and glucaric acids.

TiO₂ catalysts synthesized by an ultrasound-assisted sol-gel protocol (TiO₂ (US)) and by a reflux method (TiO₂ (R)) were initially reported for the photocatalytic oxidation of glucose using O₂ as the oxidant.¹⁶⁵ The best product selectivity was achieved with the TiO₂ (US) photocatalyst, with 71.3% total selectivity towards GUA and GA but low glucose conversion (11%) in an H₂O/acetonitrile (1:1) solvent. In an attempt to improve selectivity of GUA and GA, TiO₂ nanoparticles supported on a zeolite Y have been synthesized.¹⁶⁶ They found that the zeolite Y added to TiO₂ provided an improved activity. 15.5% of glucose conversion and 68.1% of GUA and GA selectivity were achieved on TiO₂/zeolite Y after 10 min illumination time, which is comparably superior to those over commercially P-25 and unsupported TiO₂ photocatalysts. Importantly, P-25 and unsupported TiO₂ photocatalysts may lead to the higher selectivity towards by-product carboxylic acids. In addition, it was suggested that the negatively charged zeolite framework not only improved the charge separation minimizing electron-hole recombination but also favored the desorption of acids because of electrostatic repulsion, improving the selectivity. Further development of advanced photocatalytic systems via incorporating transition-metal (Fe or Cr) on TiO₂ materials has improved

the selectivity to carboxylic acids.¹⁶⁷ Fe–TiO₂ systems showed a high selectivity towards to the acid (94%) after 20 min of illumination.¹⁶⁸ Besides, no metal leaching (Ti, Fe and Cr) was observed after photoreaction. Nevertheless, the low conversion of glucose (only 7%) was achieved. The strategy of aliovalent doping anatase TiO₂ with transition metals has not enhanced the photocatalytic glucose conversion significantly into gluconic and/or glucaric acids.

Similar to the thermo-catalytic oxidation of glucose, noble metals (such as Ag, Pt, and Au) supported materials also have been developed in photocatalytic oxidation of glucose. The addition of plasmonic metals on the TiO₂ surface extended visible-light-harvesting due to the concomitant surface plasmon resonance effect.¹⁶⁹ Ag/TiO₂ photocatalysts prepared by a deposition-precipitation method was reported for the photocatalytic oxidation of glucose under visible light conditions where the mineralization pathway was suppressed.¹⁷⁰ The Ag/TiO₂ with 0.5 wt% Ag loading is the most selective, showing 20% selectivity to gluconic acid after 2 h illumination in H₂O/CH₃CN (1:1) solvent under air condition. The remaining 80% by-products included various organic degradation products, such as glyceraldehyde, erythrose, arabinose and formic acid. Nevertheless, the yield was below 7%. Recently, Zhou et al.¹⁷¹ reported that glucose could be totally and selectively oxidized into corresponding aldinate derivatives on Au/TiO₂ photocatalysts in aqueous alkaline conditions (Na₂CO₃) with 94% and 99% of selectivity under visible and UV light, respectively. It was suggested that the base played a crucial role in the selectivity of the photocatalytic reaction. Moreover, they argued that under UV light, the base served as a sacrificial

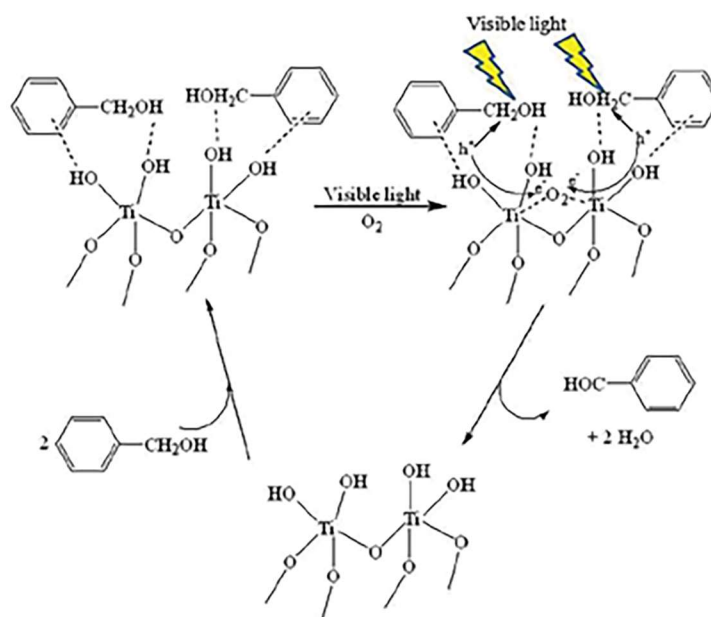
agent to avoid the formation of highly oxidizing oxygen species, whereas under visible light it could act as an effective promoter. In addition, Omri et al. reported¹⁷² efficient glucose oxidation with selective sodium aldonates obtained over three photocatalysts including Au/Al₂O₃, Au/TiO₂ and Au/CeO₂ under alkaline condition. Compared to Au/Al₂O₃ and Au/TiO₂, Au/CeO₂ photocatalyst showed the best performance with a TOF of around 750,000 h⁻¹ using H₂O₂ as the oxidant. The H₂O₂ was an electron scavenger to enhance the photogenerated-hole activity towards sugar oxidation. It could also play the role of a UV filter inhibiting the formation of excessive radicals induced by photoexcited holes. The solvent composition has a considerable effect on photocatalytic activity/selectivity. Studies showed that the introduction of acetonitrile into H₂O solvent has a beneficial influence on selective photo-oxidation.¹⁷³

2.3.2.3 Selective photo-oxidation of benzyl alcohol

Aromatic alcohols, considered as model compounds of lignin, have been converted into various value-added chemicals via photocatalytic oxidation. Benzyl alcohol as the simplest aromatic alcohol represents an essential structure of lignin.¹⁷⁴ Benzaldehyde as the second most important aromatic chemical has been widely used in the food, perfumery, cosmetics, flavor, and pharmaceutical industries.¹⁵⁷ Extensive studies have focused on the photocatalytic conversion of benzyl alcohol to benzaldehyde as a model reaction of lignin valorization.^{157, 174}

Recently, the efficiency of TiO₂ semiconductor materials in the photocatalytic oxidation of benzyl alcohol has been reported by the Colmenares group.^{157, 175-180}

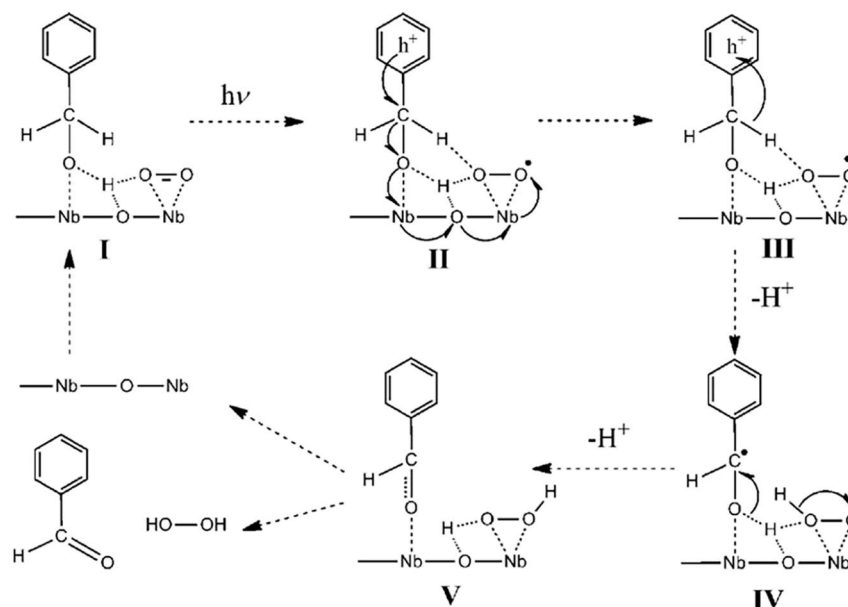
TiO₂/maghemite-silica composite reached 90% of benzyl aldehyde selectivity at 50% of benzyl alcohol conversion. Besides, the magnetic property of the composite allowed the easy separation of the catalyst from the CH₃CN solution. Higashimoto et al studied the photocatalytic oxidation of benzyl alcohol under visible-light irradiation.¹⁸¹ Over 99% of benzyl aldehyde selectivity at 99% of benzyl alcohol conversion was obtained on TiO₂ using O₂ as the oxidant. Besides, they revealed that a surface complex is formed due to the interaction between the surface OH groups of TiO₂ and the alcohol group of aromatic alcohol as shown in Scheme 2.3. The photo-generated holes react with hydrogen atoms connected to the carbon of the CH₂OH group of benzyl alcohol, whereas the photo-generated electrons react with O₂.



Scheme 2.3 The proposed reaction mechanism of selective photocatalytic oxidation of benzyl alcohol on TiO₂ in the presence of O₂. This scheme was reproduced with permission from the literature.¹⁸¹

Another mechanism (Scheme 2.4) of photocatalytic oxidation of benzyl alcohol was

proposed by Wu's group.¹⁸² In the study, monolayer HNb_3O_8 nanosheet was proven to be a highly chemoselective and active photocatalyst in benzyl alcohol oxidation under visible light irradiation. They suggested that the surface complexes formed between the LAS on the catalyst and the -OH group of benzyl alcohol play a key role in the activity of the material. Under light irradiation, the photogenerated charges transfer from metal to ligands due to the adsorption of O_2 molecular and benzyl alcohol on the surface of catalysts. The adsorbed O_2 is then reduced into superoxide radicals (O_2^\bullet) and the photogenerated holes induce the deprotonation of benzyl alcohol with the assistance of the O_2^\bullet . Next, the O_2^\bullet species further induce the deprotonation of intermediate complex to produce the corresponding aldehyde and H_2O_2 . In addition, some novel catalysts with nanosheets such as monolayer C_3N_4 ¹⁸³ and monolayer Bi_2MoO_6 ¹⁸⁴ were applied in this reaction under visible-light irradiation and showed enhanced activity and good selectivity towards benzaldehyde. The increase of activity might be related to the low molecular thickness of the monolayer catalysts with the high surface area, leading to the ultrafast charge separation and transferring, and the high capacity for O_2 activation. It was demonstrated that these catalysts employed on selective benzyl alcohol oxidation into benzaldehyde can be extended for the oxidation of other alcohols as well.¹⁸¹



Scheme 2.4 Reaction mechanism of alcohol photooxidation over HNb₃O₈ nanosheets with molecular oxygen. This scheme was reproduced with permission from the literature.¹⁸²

A similar advantage of the plasmonic effect of noble metals, like Au,^{185, 186} Pd¹⁸⁷ and Pt,¹⁸⁸ can be extended to photocatalytic oxidation of aromatic alcohols. The Au/TiO₂ catalyst showed a plasmon phenomenon where the Au particles were activated by visible light followed by consecutive electrons transferring at the Au/TiO₂ interphase contact.¹⁸⁶ Next, the positively charged Au particles facilitated the oxidation process of aromatic alcohols. Metal core-shell semiconductor composites (Pt@CeO₂ and Pd@CeO₂) were proven to be efficient visible light driven photocatalysts for the selective oxidation of benzyl alcohol into benzaldehyde.¹⁸⁹ Pt and Pd served as the cores of the hybrid system while the semiconductor CeO₂ as the shell.¹⁸⁹ Electrons produced from the CeO₂ shell under visible light irradiation were trapped by the noble metal cores and the adsorbed benzyl alcohol molecules interacted with the photogenerated holes to

form the corresponding radical cation. Notably, the photocatalytic activity of core-shell-structure Pt@CeO₂ in term of the benzaldehyde yield was around 9, 27, and 39 times higher than that of nanosized CeO₂, bulk CeO₂ and supported Pt/CeO₂, respectively.¹⁸⁸

2.3.2.4 Conclusions

In conclusion, photocatalytic transformations of biomass-derived substrates mainly focus on the redox reactions, where the photo-generated reactive species or photo-excited charge carriers are as the reductants or oxidants. Compared to thermal catalysis, photocatalysis has various advantages considered from the following aspects. First, the photo-generated reactive species and/or photo-excited charge carriers as the reductants and/or oxidants can drive redox reactions without consuming additional reductants or oxidants, enabling the transformations being environmentally benign. Second, photocatalysis could perform kinetically difficult reactions with high energy barrier under relatively mild conditions. In contrast the conventional thermal catalysis typically requires high temperatures or the addition of hazardous/toxic additives.¹⁹⁰ Further, photocatalysis has the potential to carry out selective functionalization of specific functional groups or selective cleavage of targeted chemical bonds whereas other functional groups may remain intact.^{153, 154}

Therefore, with the growing demand for energy and a cleaner environment, scientists have turned to solar energy to satisfy the needs of modern society.² Photocatalytic conversion of biomass-derived carbohydrates is considered as a promising approach to achieve high sustainability in chemical transformation processes. However, the main

drawback of heterogeneous photocatalysis is the inherent low quantum efficiency, only ca. 1% achieved under optimized conditions. That means only one out of one hundred incident photons can participate in an oxidation/reduction step. Only ca. 5% of sunlight can be used by TiO₂ currently, and these values are realistically insufficient.

There exist several main challenges in heterogeneous photocatalysis to understand what factors govern photochemical processes in heterogeneous catalytic systems. The first challenge is to identify these factors governing the performance of photocatalysts, and subsequent understanding how these factors influence their activity. For example, photocatalytic conversion of biomass-derived carbohydrates under anaerobic conditions generally leads to C–C bond cleavage. Main products along with small molecules, like formic acid, CO₂, CO and H₂ could be obtained^{191, 192} The selective activation of targeted functional groups or selective cleavage of specific chemical bonds is challenging. Many morphological and microscopic structural factors of photocatalysts, such as crystal facet, size, shape, or promoter have significant and even synergistic impacts on the performance of catalysts, including tuning the activity and selectivity to target products.¹⁹³ High selectivity to desired high-value chemicals is expected to be achieved via heterogeneous photocatalytic process. Another challenge is about how to improve the light absorption of semiconductor photocatalysts so that they can absorb solar energy significantly, thus improving their quantum efficiencies. Besides, photocatalysts also suffer from deactivation attributed from the aggregation of the molecular complexes as well as the oxidative degradation of the organic moiety.⁴ Thus to improve the stability of photocatalysts, effective strategies to reduce the

aggregation of molecular complexes and to suppress the generation of too reactive species should be developed. Developing the efficient photocatalytic system to improving the selectivity of main products in photocatalytic reactions is of great importance.

In this thesis, efficient visible light-responsive photocatalysts for chemoselective oxidation of biomass-derived alcohols into value-added aldehydes are developed; The effect of metal-particle size and catalyst morphologies on photocatalytic oxidation activity is investigated.

Reference

- [1]. Corma A., Iborra S. and Velty A., Chemical routes for the transformation of biomass into chemicals. *Chemical Reviews* **2007**, *107* (6), 2411-2502.
- [2]. Granone L.I., Sieland F., Zheng N., Dillert R. and Bahnemann D.W., Photocatalytic conversion of biomass into valuable products: A meaningful approach? *Green Chemistry* **2018**, *20* (6), 1169-1192.
- [3]. Klemm D., Heublein B., Fink H.P. and Bohn A., Cellulose: Fascinating biopolymer and sustainable raw material. *Angewandte Chemie-International Edition* **2005**, *44* (22), 3358-3393.
- [4]. Wu X., Luo N., Xie S., Zhang H., Zhang Q., Wang F. and Wang Y., Photocatalytic transformations of lignocellulosic biomass into chemicals. *Chemical Society Reviews* **2020**, *49* (17), 6198-6223.
- [5]. Atabani A.E., Silitonga A.S., Badruddin I.A., Mahlia T.M.I., Masjuki H.H. and Mekhilef S., A comprehensive review on biodiesel as an alternative energy resource and its characteristics. *Renewable and Sustainable Energy Reviews* **2012**, *16* (4), 2070-2093.
- [6]. Huber G.W., Iborra S. and Corma A., Synthesis of transportation fuels from biomass: chemistry, catalysts, and engineering. *Chemical Reviews* **2006**, *106* (9), 4044-4098.
- [7]. Dodekatos G., Schunemann S. and Tuysuz H., Recent advances in thermo-, photo-, and electrocatalytic glycerol oxidation. *ACS Catalysis* **2018**, *8* (7), 6301-6333.
- [8]. Huber G.W. and Dumesic J.A., An overview of aqueous-phase catalytic processes for production of hydrogen and alkanes in a biorefinery. *Catalysis Today* **2006**, *111* (1-2), 119-132.
- [9]. Karinen R., Vilonen K. and Niemela M., Biorefining: Heterogeneously catalyzed

reactions of carbohydrates for the production of furfural and hydroxymethylfurfural. *Chemsuschem* **2011**, 4 (8), 1002-1016.

[10]. Cherubini F., The biorefinery concept: Using biomass instead of oil for producing energy and chemicals. *Energy Conversion and Management* **2010**, 51 (7), 1412-1421.

[11]. Wilson K. and Lee A.F., Catalyst design for biorefining. *Philosophical Transactions of the Royal Society A: Mathematical, Physical and Engineering Sciences* **2016**, 374 (2061), 20150081.

[12]. Kim J.-S. and Choi G.-G., Chapter 11 - pyrolysis of lignocellulosic biomass for biochemical production. In *Waste biorefinery*, Bhaskar T., Pandey A., Mohan S.V. et al., Eds. Elsevier: 2018; pp 323-348.

[13]. Lange J.-P., Lignocellulose conversion: An introduction to chemistry, process and economics. *Biofuels, Bioproducts and Biorefining* **2007**, 1 (1), 39-48.

[14]. Binder J.B. and Raines R.T., Simple chemical transformation of lignocellulosic biomass into furans for fuels and chemicals. *Journal of the American Chemical Society* **2009**, 131 (5), 1979-1985.

[15]. Himmel M.E., Ding S.-Y., Johnson D.K., Adney W.S., Nimlos M.R., Brady J.W. and Foust T.D., Biomass recalcitrance: Engineering plants and enzymes for biofuels production. **2007**, 315 (5813), 804-807.

[16]. Glasser W.G. and Wright R.S., Steam-assisted biomass fractionation. II. Fractionation behavior of various biomass resources. *Biomass and Bioenergy* **1998**, 14 (3), 219-235.

[17]. Zhao X., Cheng K. and Liu D., Organosolv pretreatment of lignocellulosic biomass for enzymatic hydrolysis. *Applied Microbiology and Biotechnology* **2009**, 82 (5), 815-827.

[18]. Rinaldi R. and Schüth F., Acid hydrolysis of cellulose as the entry point into biorefinery schemes. *ChemSusChem* **2010**, 3 (3), 296-296.

[19]. Binder J.B. and Raines R.T., Fermentable sugars by chemical hydrolysis of biomass. *Proceedings of the National Academy of Sciences* **2010**, 107 (10), 4516-4521.

[20]. Sasaki M., Kabyemela B., Malaluan R., Hirose S., Takeda N., Adschiri T. and Arai K., Cellulose hydrolysis in subcritical and supercritical water. *The Journal of Supercritical Fluids* **1998**, 13 (1-3), 261-268.

[21]. Alvira P., Tomás-Pejó E., Ballesteros M. and Negro M.J., Pretreatment technologies for an efficient bioethanol production process based on enzymatic hydrolysis: A review. *Bioresource Technology* **2010**, 101 (13), 4851-4861.

[22]. Alonso D.M., Bond J.Q. and Dumesic J.A., Catalytic conversion of biomass to biofuels. *Green Chemistry* **2010**, 12 (9), 1493-1513.

[23]. Kang S., Fu J. and Zhang G., From lignocellulosic biomass to levulinic acid: A review on acid-catalyzed hydrolysis. *Renewable and Sustainable Energy Reviews* **2018**, 94, 340-362.

[24]. Hahn-Hägerdal B., Galbe M., Gorwa-Grauslund M.F., Lidén G. and Zacchi G., Bio-ethanol - the fuel of tomorrow from the residues of today. *Trends in Biotechnology* **2006**, 24 (12), 549-556.

[25]. Dahmen N., Lewandowski I., Zibek S. and Weidtmann A., Integrated

lignocellulosic value chains in a growing bioeconomy: Status quo and perspectives. *GCB Bioenergy* **2018**.

[26]. Hara M., Biomass conversion by a solid acid catalyst. *Energy & Environmental Science* **2010**, 3 (5), 601.

[27]. Delbecq F., Wang Y., Muralidhara A., El Ouardi K., Marlair G. and Len C., Hydrolysis of hemicellulose and derivatives-A review of recent advances in the production of furfural. *Frontiers in Chemistry* **2018**, 6.

[28]. Guo F., Fang Z., Xu C.C. and Smith R.L., Solid acid mediated hydrolysis of biomass for producing biofuels. *Progress in Energy and Combustion Science* **2012**, 38 (5), 672-690.

[29]. van Dam H.E., Kieboom A.P.G. and van Bekkum H., The conversion of fructose and glucose in acidic media: Formation of hydroxymethylfurfural. *Starch - Stärke* **1986**, 38 (3), 95-101.

[30]. Galkin K.I. and Ananikov V.P., When will 5-hydroxymethylfurfural, the "sleeping giant" of sustainable chemistry, awaken? *Chemsuschem* **2019**, 12 (13), 2976-2982.

[31]. Moreno-Recio M., Santamaría-González J. and Maireles-Torres P., Brönsted and lewis acid ZSM-5 zeolites for the catalytic dehydration of glucose into 5-hydroxymethylfurfural. *Chemical Engineering Journal* **2016**, 303, 22-30.

[32]. Pumrod S., Kaewchada A., Roddecha S. and Jaree A., 5-HMF production from glucose using ion exchange resin and alumina as a dual catalyst in a biphasic system. *RSC Advances* **2020**, 10 (16), 9492-9498.

[33]. Nahavandi M., Kasanneni T., Yuan Z.S., Xu C.C. and Rohani S., Efficient conversion of glucose into 5-hydroxymethylfurfural using a sulfonated carbon-based solid acid catalyst: An experimental and numerical study. *ACS Sustainable Chemistry & Engineering* **2019**, 7 (14), 11970-11984.

[34]. Takagaki A., Production of 5-hydroxymethylfurfural from glucose in water by using transition metal-oxide nanosheet aggregates. *Japan Catalysts* **2019**, 9 (10), 818.

[35]. Han B., Zhao P., He R., Wu T. and Wu Y., Catalytic conversion of glucose to 5-hydroxymethylfurfural over B₂O₃ supported solid acids catalysts. *Waste and Biomass Valorization* **2018**, 9 (11), 2181-2190.

[36]. Zhao P., Zhang Y., Wang Y., Cui H., Song F., Sun X. and Zhang L., Conversion of glucose into 5-hydroxymethylfurfural catalyzed by acid-base bifunctional heteropolyacid-based ionic hybrids. *Green Chemistry* **2018**, 20 (7), 1551-1559.

[37]. Newth F.H., The formation of furan compounds from hexoses. *Advances in Carbohydrate Chemistry and Biochemistry* **1951**, 6, 83-106.

[38]. Anet E.F., 3-deoxyglycosuloses (3-deoxyglycosones) and the degradation of carbohydrates. *Advances in Carbohydrate Chemistry and Biochemistry* **1964**, 19, 181-218.

[39]. Antal M.J., Jr., Mok W.S. and Richards G.N., Mechanism of formation of 5-(hydroxymethyl)-2-furaldehyde from d-fructose and sucrose. *Carbohydrate Research* **1990**, 199 (1), 91-109.

[40]. Pidko E.A., Degirmenci V., van Santen R.A. and Hensen E.J.M., Coordination properties of ionic liquid-mediated chromium(ii) and copper(ii) chlorides and their complexes with glucose. *Inorganic Chemistry* **2010**, 49 (21), 10081-10091.

- [41]. Zhang Y., Pidko E.A. and Hensen E.J.M., Molecular aspects of glucose dehydration by chromium chlorides in ionic liquids. *Chemistry - A European Journal* **2011**, *17* (19), 5281-5288.
- [42]. Pidko E.A., Degirmenci V., van Santen R.A. and Hensen E.J., Glucose activation by transient Cr^{2+} dimers. *Angewandte Chemie International Edition* **2010**, *49* (14), 2530-4.
- [43]. Mika L.T., Cséfalvay E. and Németh Á., Catalytic conversion of carbohydrates to initial platform chemicals: Chemistry and sustainability. *Chemical Reviews* **2018**, *118* (2), 505-613.
- [44]. Daorattanachai P., Namuangruk S., Viriya-empikul N., Laosiripojana N. and Faungnawakij K., 5-hydroxymethylfurfural production from sugars and cellulose in acid- and base-catalyzed conditions under hot compressed water. *Journal of Industrial and Engineering Chemistry* **2012**, *18* (6), 1893-1901.
- [45]. Asghari F.S. and Yoshida H., Kinetics of the decomposition of fructose catalyzed by hydrochloric acid in subcritical water: Formation of 5-hydroxymethylfurfural, levulinic, and formic acids. *Industrial & Engineering Chemistry Research* **2007**, *46* (23), 7703-7710.
- [46]. Zhao H.B., Holladay J.E., Brown H. and Zhang Z.C., Metal chlorides in ionic liquid solvents convert sugars to 5-hydroxymethylfurfural. *Science* **2007**, *316* (5831), 1597-1600.
- [47]. Qi X.H., Watanabe M., Aida T.M. and Smith R.L., Catalytic dehydration of fructose into 5-hydroxymethylfurfural by ion-exchange resin in mixed-aqueous system by microwave heating. *Green Chemistry* **2008**, *10* (7), 799-805.
- [48]. Nikolla E., Roman-Leshkov Y., Moliner M. and Davis M.E., "One-pot" synthesis of 5-(hydroxymethyl)furfural from carbohydrates using tin-beta zeolite. *ACS Catalysis* **2011**, *1* (4), 408-410.
- [49]. Choudhary V., Mushrif S.H., Ho C., Anderko A., Nikolakis V., Marinkovic N.S., Frenkel A.I., Sandler S.I. and Vlachos D.G., Insights into the interplay of lewis and bronsted acid catalysts in glucose and fructose conversion to 5-(hydroxymethyl)furfural and levulinic acid in aqueous media. *Journal of the American Chemical Society* **2013**, *135* (10), 3997-4006.
- [50]. Delidovich I. and Palkovits R., Catalytic isomerization of biomass-derived aldoses: A review. *ChemSusChem* **2016**, *9* (6), 547-561.
- [51]. Takagaki A., Ohara M., Nishimura S. and Ebitani K., A one-pot reaction for biorefinery: Combination of solid acid and base catalysts for direct production of 5-hydroxymethylfurfural from saccharides. *Chemical Communications* **2009**, (41), 6276.
- [52]. Tuteja J., Nishimura S. and Ebitani K., One-pot synthesis of furans from various saccharides using a combination of solid acid and base catalysts. *Bulletin of the Chemical Society of Japan* **2012**, *85* (3), 275-281.
- [53]. Yue C.C., Rigutto M.S. and Hensen E.J.M., Glucose dehydration to 5-hydroxymethylfurfural by a combination of a basic zirconsilicate and a solid acid. *Catalysis Letters* **2014**, *144* (12), 2121-2128.
- [54]. Despax S., Estrine B., Hoffmann N., Le Bras J., Marinkovic S. and Muzart J., Isomerization of D-glucose into D-fructose with a heterogeneous catalyst in organic

solvents. *Catalysis Communications* **2013**, 39, 35-38.

[55]. Wang T., Nolte M.W. and Shanks B.H., Catalytic dehydration of C6 carbohydrates for the production of hydroxymethylfurfural (HMF) as a versatile platform chemical. *Green Chemistry* **2014**, 16 (2), 548-572.

[56]. Román-Leshkov Y. and Davis M.E., Activation of carbonyl-containing molecules with solid lewis acids in aqueous media. *ACS Catalysis* **2011**, 1 (11), 1566-1580.

[57]. Swift T.D., Nguyen H., Erdman Z., Kruger J.S., Nikolakis V. and Vlachos D.G., Tandem Lewis acid/Brønsted acid-catalyzed conversion of carbohydrates to 5-hydroxymethylfurfural using zeolite beta. *Journal of Catalysis* **2016**, 333, 149-161.

[58]. Qi X., Watanabe M., Aida T.M. and Smith Jr R.L., Catalytical conversion of fructose and glucose into 5-hydroxymethylfurfural in hot compressed water by microwave heating. *Catalysis Communications* **2008**, 9 (13), 2244-2249.

[59]. Qi X., Watanabe M., Aida T.M. and L. Smith Jr R., Sulfated zirconia as a solid acid catalyst for the dehydration of fructose to 5-hydroxymethylfurfural. *Catalysis Communications* **2009**, 10 (13), 1771-1775.

[60]. Weingarten R., Kim Y.T., Tompsett G.A., Fernández A., Han K.S., Hagaman E.W., Conner W.C., Dumesic J.A. and Huber G.W., Conversion of glucose into levulinic acid with solid metal(IV) phosphate catalysts. *Journal of Catalysis* **2013**, 304, 123-134.

[61]. Ordonsky V.V., Sushkevich V.L., Schouten J.C., Van Der Schaaf J. and Nijhuis T.A., Glucose dehydration to 5-hydroxymethylfurfural over phosphate catalysts. *Journal of Catalysis* **2013**, 300, 37-46.

[62]. Atanda L., Mukundan S., Shrotri A., Ma Q. and Beltramini J., Catalytic conversion of glucose to 5-hydroxymethyl-furfural with a phosphated TiO₂ catalyst. *ChemCatChem* **2015**, 7 (5), 781-790.

[63]. Zhang L., Xi G., Chen Z., Qi Z. and Wang X., Enhanced formation of 5-HMF from glucose using a highly selective and stable SAPO-34 catalyst. *Chemical Engineering Journal* **2017**, 307, 877-883.

[64]. Jiménez-Morales I., Teckchandani-Ortiz A., Santamaría-González J., Maireles-Torres P. and Jiménez-López A., Selective dehydration of glucose to 5-hydroxymethylfurfural on acidic mesoporous tantalum phosphate. **2014**, 144, 22-28.

[65]. Yang L., Yan X., Xu S., Chen H., Xia H. and Zuo S., One-pot synthesis of 5-hydroxymethylfurfural from carbohydrates using an inexpensive FePO₄ catalyst. *RSC Advances* **2015**, 5 (26), 19900-19906.

[66]. Kozhevnikov I.V., Sinnema A., Jansen R.J.J., Pamin K. and Vanbekkum H., New acid catalyst comprising heteropoly acid on a mesoporous molecular-sieve MCM-41. *Catalysis Letters* **1995**, 30 (1-4), 241-252.

[67]. Margolese D., Melero J.A., Christiansen S.C., Chmelka B.F. and Stucky G.D., Direct syntheses of ordered sba-15 mesoporous silica containing sulfonic acid groups. *Chemistry of Materials* **2000**, 12 (8), 2448-2459.

[68]. Clark J.H., Solid acids for green chemistry. *Accounts of Chemical Research* **2002**, 35 (9), 791-797.

[69]. Katryniok B., Paul S., Capron M., Royer S., Lancelot C., Jalowiecki-Duhamel L., Bellière-Baca V., Rey P. and Dumeignil F., Synthesis and characterization of zirconia-grafted SBA-15 nanocomposites. *Journal of Materials Chemistry* **2011**, 21 (22), 8159.

- [70]. Osatiashtiani A., Lee A.F., Granollers M., Brown D.R., Olivi L., Morales G., Melero J.A. and Wilson K., Hydrothermally stable, conformal, sulfated zirconia monolayer catalysts for glucose conversion to 5-HMF. *ACS Catalysis* **2015**, 5 (7), 4345-4352.
- [71]. Chang B., Fu J., Tian Y. et al., Mesoporous solid acid catalysts of sulfated zirconia/SBA-15 derived from a vapor-induced hydrolysis route. *Applied Catalysis A: General* **2012**, 437-438, 149-154..
- [72]. Zhu L., Fu X., Hu Y. and Hu C., Controlling the reaction networks for efficient conversion of glucose into 5-hydroxymethylfurfural. *ChemSusChem* **2020**.
- [73]. Li L.C., Yue H.Q., Zhang S.Y., Huang Y.B., Zhang W.N., Wu P., Ji Y.X. and Huo F.W., Solving the water hypersensitive challenge of sulfated solid superacid in acid-catalyzed reactions. *ACS Applied Materials & Interfaces* **2019**, 11 (10), 9919-9924.
- [74]. Murayama T., Nakajima K., Hirata J. et al., Hydrothermal synthesis of a layered-type W–Ti–O mixed metal oxide and its solid acid activity. *Catalysis Science & Technology* **2017**, 7 (1), 243-250.
- [75]. Noma R., Nakajima K., Kamata K. et al., Formation of 5-(hydroxymethyl)furfural by stepwise dehydration over TiO₂ with water-tolerant Lewis acid sites. *The Journal of Physical Chemistry C* **2015**, 119 (30), 17117-17125.
- [76]. Anastas P. and Eghbali N., Green chemistry: Principles and practice. *Chemical Society Review* **2010**, 39 (1), 301-312.
- [77]. Vasudevan V. and Mushrif S.H., Insights into the solvation of glucose in water, dimethyl sulfoxide (DMSO), tetrahydrofuran (THF) and n,n-dimethylformamide (DMF) and its possible implications on the conversion of glucose to platform chemicals. *RSC Advances* **2015**, 5 (27), 20756-20763.
- [78]. Garcés D., Díaz E. and Ordóñez S., Aqueous phase conversion of hexoses into 5-hydroxymethylfurfural and levulinic acid in the presence of hydrochloric acid: Mechanism and kinetics. *Industrial & Engineering Chemistry Research* **2017**, 56, , 5221–5230.
- [79]. Datta R., Tsai S.-P., Bonsignore P., Moon S.-H. and Frank J.R., Technological and economic potential of poly(lactic acid) and lactic acid derivatives. *FEMS Microbiology Reviews* **1995**, 16 (2-3), 221-231.
- [80]. Xia X. and Stone A.T., Mandelic acid and phenyllactic acid “reaction sets” for exploring the kinetics and mechanism of oxidations by hydrous manganese oxide (hmo). *Environmental Science: Processes & Impacts* **2019**, 21 (6), 1038-1051.
- [81]. Njiojob C.N., Rhinehart J.L., Bozell J.J. and Long B.K., Synthesis of enantiomerically pure lignin dimer models for catalytic selectivity studies. *The Journal of Organic Chemistry* **2015**, 80 (3), 1771-1780.
- [82]. Baciocchi E., Gerini M.F., Lanzalunga O. and Mancinelli S., Lignin peroxidase catalysed oxidation of 4-methoxymandelic acid. The role of mediator structure. *Tetrahedron* **2002**, 58 (40), 8087-8093.
- [83]. Berthold F., Lindgren C.T. and Lindstrom M.E., Formation of (4-hydroxy-3-methoxyphenyl)-glyoxylic acid and (4-hydroxy-3,5-dimethoxyphenyl)-glyoxylic acid during polysulfide treatment of softwood and hardwood. *Holzforschung* **1998**, 52 (2), 197-199.

- [84]. Narayanan N., Roychoudhury P.K. and Srivastava A., (+) Lactic acid fermentation and its product polymerization. *Electronic Journal of Biotechnology* **2004**, 7 (2), 167-U2.
- [85]. Dusselier M., Van Wouwe P., Dewaele A., Makshina E. and Sels B.F., Lactic acid as a platform chemical in the biobased economy: The role of chemocatalysis. *Energy & Environmental Science* **2013**, 6 (5), 1415.
- [86]. Holm M.S., Saravanamurugan S. and Taarning E., Conversion of sugars to lactic acid derivatives using heterogeneous zeotype catalysts. *Science* **2010**, 328 (5978), 602-605.
- [87]. Onda A., Ochi T., Kajiyoshi K. and Yanagisawa K., Lactic acid production from glucose over activated hydrotalcites as solid base catalysts in water. *Catalysis Communications* **2008**, 9 (6), 1050-1053.
- [88]. Onda A., Ochi T., Kajiyoshi K. and Yanagisawa K., A new chemical process for catalytic conversion of D-glucose into lactic acid and gluconic acid. *Applied Catalysis A: General* **2008**, 343 (1-2), 49-54.
- [89]. Kong L., Li G., Wang H., He W. and Ling F., Hydrothermal catalytic conversion of biomass for lactic acid production. *Journal of Chemical Technology & Biotechnology* **2008**, 83 (3), 383-388.
- [90]. Long Y.-D. and Fang Z., Hydrothermal conversion of glycerol to chemicals and hydrogen: Review and perspective. *Biofuels, Bioproducts and Biorefining* **2012**, 6 (6), 686-702.
- [91]. West R.M., Holm M.S., Saravanamurugan S., Xiong J., Beversdorf Z., Taarning E. and Christensen C.H., Zeolite h-usy for the production of lactic acid and methyl lactate from C3-sugars. *Journal of Catalysis* **2010**, 269 (1), 122-130.
- [92]. Pescarmona P.P., Janssen K.P.F., Delaet C., Stroobants C., Houthoofd K., Philippaerts A., De Jonghe C., Paul J.S., Jacobs P.A. et al., Zeolite-catalysed conversion of C3 sugars to alkyl lactates. *Green Chemistry* **2010**, 12 (6), 1083.
- [93]. Taarning E., Saravanamurugan S., Spangenberg Holm M., Xiong J., West R.M. and Christensen C.H., Zeolite-catalyzed isomerization of triose sugars. *ChemSusChem* **2009**, 2 (7), 625-627.
- [94]. Rasrendra C.B., Fachri B.A., Makertihartha I., Adisasmito S. and Heeres H.J., Catalytic conversion of dihydroxyacetone to lactic acid using metal salts in water. *Chemsuschem* **2011**, 4 (6), 768-777.
- [95]. Miranda B.C., Chimentão R.J., Santos J.B.O. et al., Conversion of glycerol over 10%Ni/ γ -Al₂O₃ catalyst. *Applied Catalysis B: Environmental* **2014**, 147, 464-480.
- [96]. Lari G.M., Garcia-Muelas R., Mondelli C., Lopez N. and Perez-Ramirez J., Glycerol oxidehydration to pyruvaldehyde over silver-based catalysts for improved lactic acid production. *Green Chemistry* **2016**, 18 (17), 4682-4692.
- [97]. Ciriminna R., Pina C.D., Rossi M. and Pagliaro M., Understanding the glycerol market. *European Journal of Lipid Science and Technology* **2014**, 116 (10), 1432-1439.
- [98]. Tao M.L., Yi X.H., Delidovich I., Palkovits R., Shi J.Y. and Wang X.H., Hetropolyacid-catalyzed oxidation of glycerol into lactic acid under mild base-free conditions. *Chemsuschem* **2015**, 8 (24), 4195-4201.
- [99]. Ftouni J., Villandier N., Auneau F., Besson M., Djakovitch L. and Pinel C., From

glycerol to lactic acid under inert conditions in the presence of platinum-based catalysts: The influence of support. *Catalysis Today* **2015**, 257, 267-273.

[100]. Jiang Z., Zhang Z., Wu T., Zhang P., Song J., Xie C. and Han B., Efficient generation of lactic acid from glycerol over a Ru-Zn-CuI/hydroxyapatite catalyst. *Chemistry - An Asian Journal* **2017**, 12 (13), 1598-1604.

[101]. Yang G.-Y., Ke Y.-H., Ren H.-F., Liu C.-L., Yang R.-Z. and Dong W.-S., The conversion of glycerol to lactic acid catalyzed by zro2-supported cuo catalysts. *Chemical Engineering Journal* **2016**, 283, 759-767.

[102]. Purushothaman R.K.P., Van Haveren J., Van Es D.S., Melián-Cabrera I., Meeldijk J.D. and Heeres H.J., An efficient one pot conversion of glycerol to lactic acid using bimetallic gold-platinum catalysts on a nanocrystalline CeO₂ support. *Applied Catalysis B: Environmental* **2014**, 147, 92-100.

[103]. Wang X.C., Song Y.J., Huang L., Wang H., Huang C.P. and Li C.Q., Tin modified nb2o5 as an efficient solid acid catalyst for the catalytic conversion of triose sugars to lactic acid. *Catalysis Science & Technology* **2019**, 9 (7), 1669-1679.

[104]. Sun Y.Y., Shi L., Wang H., Miao G., Kong L.Z., Li S.G. and Sun Y.H., Efficient production of lactic acid from sugars over sn-beta zeolite in water: Catalytic performance and mechanistic insights. *Sustainable Energy & Fuels* **2019**, 3 (5), 1163-1171.

[105]. Wang J., Masui Y. and Onaka M., Conversion of triose sugars with alcohols to alkyl lactates catalyzed by Brønsted acid tin ion-exchanged montmorillonite. *Applied Catalysis B: Environmental* **2011**, 107 (1-2), 135-139.

[106]. Kim K.D., Wang Z.C., Jiang Y.J., Hunger M. and Huang J., The cooperative effect of lewis and Brønsted acid sites on Sn-MCM-41 catalysts for the conversion of 1,3-dihydroxyacetone to ethyl lactate. *Green Chemistry* **2019**, 21 (12), 3383-3393.

[107]. De Clippel F., Dusselier M., Van Rompaey R., Vanelderen P., Dijkmans J., Makshina E., Giebler L., Oswald S., Baron G.V. et al., Fast and selective sugar conversion to alkyl lactate and lactic acid with bifunctional carbon-silica catalysts. *Journal of the American Chemical Society* **2012**, 134 (24), 10089-10101.

[108]. Wang X.C., Song Y.J., Huang C.P. and Wang B., Crystalline niobium phosphates with water-tolerant and adjustable lewis acid sites for the production of lactic acid from triose sugars. *Sustainable Energy & Fuels* **2018**, 2 (7), 1530-1541.

[109]. Guo Q., Fan F., Pidko E.A., Van Der Graaff W.N.P., Feng Z., Li C. and Hensen E.J.M., Highly active and recyclable Sn-MWW zeolite catalyst for sugar conversion to methyl lactate and lactic acid. *ChemSusChem* **2013**, 6 (8), 1352-1356.

[110]. Morales M., Dapsens P.Y., Giovinazzo I., Witte J., Mondelli C., Papadokostantakis S., Hungerbühler K. and Pérez-Ramírez J., Environmental and economic assessment of lactic acid production from glycerol using cascade bio- and chemocatalysis. *Energy & Environmental Science* **2015**, 8 (2), 558-567.

[111]. Wang X., Liang F., Huang C., Li Y. and Chen B., Highly active tin(iv) phosphate phase transfer catalysts for the production of lactic acid from triose sugars. *Catalysis Science & Technology* **2015**, 5 (9), 4410-4421.

[112]. Razali N. and Abdullah A.Z., Production of lactic acid from glycerol via chemical conversion using solid catalyst: A review. *Applied Catalysis A: General* **2017**,

543, 234-246.

- [113]. Saleh S.N.M. and Abdullah A.Z., Zirconium-cerium oxides supported on SBA-15 as catalyst for shape-selective synthesis of lactic acid from glycerol. *Waste and Biomass Valorization* **2020**, 1877-2641.
- [114]. Santos K.M.A., Albuquerque E.M., Innocenti G., Borges L.E.P., Sievers C. and Fraga M.A., The role of Brønsted and water-tolerant Lewis acid sites in the cascade aqueous-phase reaction of triose to lactic acid. *Chemcatchem* **2019**, 11 (13), 3054-3063.
- [115]. Mäki-Arvela P., Simakova I.L., Salmi T. and Murzin D.Y., Production of lactic acid/lactates from biomass and their catalytic transformations to commodities. *Chemical Reviews* **2014**, 114 (3), 1909-1971.
- [116]. Albuquerque E.M., Borges L.E.P. and Fraga M.A., Lactic acid production from hydroxyacetone on dual metal/base heterogeneous catalytic systems. *Green Chemistry* **2015**, 17 (7), 3889-3899.
- [117]. Abaee M.S., Sharifi R. and Mojtahedi M.M., Room-temperature cannizzaro reaction under mild conditions facilitated by magnesium bromide ethyl etherate and triethylamine. *Organic Letters* **2005**, 7 (26), 5893-5895.
- [118]. Russell A.E., Miller S.P. and Morken J.P., Efficient lewis acid catalyzed intramolecular cannizzaro reaction. *The Journal of Organic Chemistry* **2000**, 65 (24), 8381-8383.
- [119]. Curini M., Epifano F., Genovese S., Marcotullio M.C. and Rosati O., Ytterbium triflate-promoted tandem one-pot oxidation–cannizzaro reaction of aryl methyl ketones. *Organic Letters* **2005**, 7 (7), 1331-1333.
- [120]. Wang Z., Jiang Y., Baiker A. and Huang J., Efficient acid-catalyzed conversion of phenylglyoxal to mandelates on flame-derived silica/alumina. *ACS Catalysis* **2013**, 3 (7), 1573-1577.
- [121]. Wang Z., Jiang Y., Rachwalik R., Liu Z., Shi J., Hunger M. and Huang J., One-step room-temperature synthesis of [Al]MCM-41 materials for the catalytic conversion of phenylglyoxal to ethylmandelate. *ChemCatChem* **2013**, 5 (12), 3889-3896.
- [122]. Xu H., Wang Z., Miao Z., Zhu Y., Marianov A., Wang L., Castignolles P., Gaborieau M., Huang J. et al., Correlation between acidity and catalytic performance of mesoporous zirconium oxophosphate in phenylglyoxal conversion. *ACS Sustainable Chemistry & Engineering* **2019**, 7 (9), 8931-8942.
- [123]. Ishihara K., Yano T. and Fushimi M., Asymmetric intramolecular cannizzaro reaction of anhydrous phenylglyoxal. *Journal of Fluorine Chemistry* **2008**, 129 (10), 994-997.
- [124]. Wang Z., Jiang Y., Hunger M., Baiker A. and Huang J., Catalytic performance of brønsted and lewis acid sites in phenylglyoxal conversion on flame-derived silica-zirconia. *ChemCatChem* **2014**, 6 (10), 2970-2975.
- [125]. Valange S. and Vedrine J.C., General and prospective views on oxidation reactions in heterogeneous catalysis. *Catalysts* **2018**, 8 (10).
- [126]. Heyns K. and Paulsen H., Selective catalytic oxidation of carbohydrates, employing platinum catalysts. *Advances in Carbohydrate Chemistry and Biochemistry* **1962**, 17, 169-221.
- [127]. Gallezot P., Selective oxidation with air on metal catalysts. *Catalysis Today* **1997**,

37 (4), 405-418.

[128]. Besson M. and Gallezot P., Selective oxidation of alcohols and aldehydes on metal catalysts. *Catalysis Today* **2000**, 57 (1-2), 127-141.

[129]. Biella S., Prati L. and Rossi M., Selective oxidation of D-glucose on gold catalyst. *Journal of Catalysis* **2002**, 206 (2), 242-247.

[130]. Comotti M., Della Pina C., Falletta E. and Rossi M., Aerobic oxidation of glucose with gold catalyst: Hydrogen peroxide as intermediate and reagent. *Advanced Synthesis & Catalysis* **2006**, 348 (3), 313-316.

[131]. Cattaneo S., Stucchi M., Villa A. and Prati L., Gold catalysts for the selective oxidation of biomass-derived products. *Chemcatchem* **2019**, 11 (1), 309-323.

[132]. Saliger R., Decker N. and Prüße U., D-glucose oxidation with H₂O₂ on an Au/Al₂O₃ catalyst. **2011**, 102 (3-4), 584-589.

[133]. Zhang J., Li Z., Huang J., Liu C., Hong F., Zheng K. and Li G., Size dependence of gold clusters with precise numbers of atoms in aerobic oxidation of D-glucose. *Nanoscale* **2017**, 9 (43), 16879-16886.

[134]. Ishida T., Kinoshita N., Okatsu H., Akita T., Takei T. and Haruta M., Influence of the support and the size of gold clusters on catalytic activity for glucose oxidation. *Angewandte Chemie International Edition* **2008**, 47 (48), 9265-9268.

[135]. Comotti M., Della Pina C., Matarrese R. and Rossi M., The catalytic activity of "Naked" Gold particles. *Angewandte Chemie International Edition* **2004**, 43 (43), 5812-5815.

[136]. Wang Y., Van De Vyver S., Sharma K.K. and Román-Leshkov Y., Insights into the stability of gold nanoparticles supported on metal oxides for the base-free oxidation of glucose to gluconic acid. *Green Chemistry* **2014**, 16 (2), 719-726.

[137]. Megías-Sayago C., Bobadilla L.F., Ivanova S., Penkova A., Centeno M.A. and Odriozola J.A., Gold catalyst recycling study in base-free glucose oxidation reaction. *Catalysis Today* **2018**, 301, 72-77.

[138]. Delidovich I., Taran O., Matvienko G., Simonov A., Simakova I., Bobrovskaya A. and Parmon V., Selective oxidation of glucose over carbon-supported Pd and Pt catalysts. *Catalysis Letters* **2010**, 140, 14-21.

[139]. Jin X., Zhao M., Vora M., Shen J., Zeng C., Yan W., Thapa P.S., Subramaniam B. and Chaudhari R.V., Synergistic effects of bimetallic PtPd/TiO₂ nanocatalysts in oxidation of glucose to glucaric acid: Structure dependent activity and selectivity. *Industrial & Engineering Chemistry Research* **2016**, 55 (11), 2932-2945.

[139]. Jin X., Zhao M., Vora M. et al., Synergistic effects of bimetallic Pt-Pd/TiO₂ nanocatalysts in oxidation of glucose to glucaric acid: Structure dependent activity and selectivity. *Industrial & Engineering Chemistry Research* **2016**, 55 (11), 2932-2945.

[140]. Bönemann H., Brijoux W., Brinkmann R. et al., Selective oxidation of glucose on bismuth-promoted Pd-Pt/C catalysts prepared from NOct₄Cl-stabilized Pd-Pt colloids. *Inorganica Chimica Acta* **1998**, 270 (1-2), 95-110.

[141]. Hermans S., Devillers M., On the role of ruthenium associated with Pd and/or Bi in carbon-supported catalysts for the partial oxidation of glucose. *Applied Catalysis A-General* **2002**, 235 (1-2), 253-264.

- [142]. Wenkin M., Ruiz P., Delmon B. et al., The role of bismuth as promoter in Pd-Bi catalysts for the selective oxidation of glucose to gluconate. *Journal of Molecular Catalysis A-Chemical* **2002**, 180 (1-2), 141-159.
- [143]. Karski S., Activity and selectivity of Pd-Bi/SiO₂ catalysts in the light of mutual interaction between Pd and Bi. *Journal of Molecular Catalysis A-Chemical* **2006**, 253 (1-2), 147-154.
- [144]. Bian R.B., Shen J., Synthesis of sodium gluconate by Bi promoted Pd/C catalyst. *Materials Transactions* **2007**, 48 (8), 2252-2254.
- [145]. Besson M., Lahmer F., Gallezot P., Fuertes P. and Fleche G., Catalytic-oxidation of glucose on bismuth-promoted palladium catalysts. *Journal of Catalysis* **1995**, 152 (1), 116-121.
- [146]. Besson M., Fleche G., Fuertes P. et al., Oxidation of glucose and gluconate on Pt, Pt-Bi, and Pt-Au catalysts. *Recueil Des Travaux Chimiques Des Pays-Bas-Journal of the Royal Netherlands Chemical Society* **1996**, 115 (4), 217-&
- [147]. Witonska I., Frajtek M. and Karski S., Selective oxidation of glucose to gluconic acid over Pd-te supported catalysts. *Applied Catalysis A-General* **2011**, 401 (1-2), 73-82.
- [148]. Karski S., Paryjczak T. and Witon'Ska I., Selective oxidation of glucose to gluconic acid over bimetallic Pd-Me catalysts (Me = Bi, Tl, Sn, Co) *Kinetics and Catalysis* **2003**, 44 (5), 618-622.
- [149]. Karski S., Bismuth as an additive modifying the selectivity of palladium catalysts. *Journal of Molecular Catalysis A: Chemical* **2003**, 191 (1), 87-92.
- [150]. Li S., Deng W., Wang S., Wang P., An D., Li Y., Zhang Q. and Wang Y., Catalytic transformation of cellulose and its derivatives into functionalized organic acids. *ChemSusChem* **2018**, 11 (13), 1995-2028.
- [151]. Li C., Zhao X., Wang A., Huber G.W. and Zhang T., Catalytic transformation of lignin for the production of chemicals and fuels. *Chemical Reviews* **2015**, 115 (21), 11559-11624.
- [152]. Liu W.-J., Li W.-W., Jiang H. and Yu H.-Q., Fates of chemical elements in biomass during its pyrolysis. *Chemical Reviews* **2017**, 117 (9), 6367-6398.
- [153]. Yoon T.P., Ischay M.A. and Du J., Visible light photocatalysis as a greener approach to photochemical synthesis. *Nature Chemistry* **2010**, 2 (7), 527-532.
- [154]. Schultz D.M. and Yoon T.P., Solar synthesis: Prospects in visible light photocatalysis. *Science* **2014**, 343 (6174), 1239176-1239176.
- [155]. Yu P.Y. and Cardona M., Fundamentals of semiconductors: Physics and materials properties, fourth edition. In *Fundamentals of semiconductors: Physics and materials properties, fourth edition*, 2010; pp 1-775.
- [156]. Photocatalytic semiconductors: Synthesis, Characterization, and Environmental Applications. Editors: Hernández-Ramírez A. and Medina-Ramírez I., *Springer*: **2015**.
- [157]. Colmenares J.C. and Luque R., Heterogeneous photocatalytic nanomaterials: Prospects and challenges in selective transformations of biomass-derived compounds. *Chemical Society Review* **2014**, 43 (3), 765-778.
- [158]. Fagnoni M., Dondi D., Ravelli D. and Albini A., Photocatalysis for the formation

- of the C–C bond. *Chemical Reviews* **2007**, 107 (6), 2725-2756.
- [159]. Qu Y. and Duan X., Progress, challenge and perspective of heterogeneous photocatalysts. *Chem. Soc. Rev.* **2013**, 42 (7), 2568-2580.
- [160]. Kisch H., Semiconductor photocatalysis-mechanistic and synthetic aspects. *Angewandte Chemie International Edition* **2013**, 52 (3), 812-847.
- [161]. Fujishima A., Rao T.N. and Tryk D.A., Titanium dioxide photocatalysis. *Journal of Photochemistry and Photobiology C: Photochemistry Reviews* **2000**, 1 (1), 1-21.
- [162]. Bozell J.J. and Petersen G.R., Technology development for the production of biobased products from biorefinery carbohydrates-the us department of energy's "top 10" revisited. *Green Chemistry* **2010**, 12 (4), 539.
- [163]. Skoog E., Shin J.H., Saez-Jimenez V., Mapelli V. and Olsson L., Biobased adipic acid – the challenge of developing the production host. *Biotechnology Advances* **2018**, 36 (8), 2248-2263.
- [164]. Omri M., Sauvage F., Golonu S., Wadouachi A. and Pourceau G., Photocatalyzed transformation of free carbohydrates. *Catalysts* **2018**, 8 (12), 672.
- [165]. Colmenares J.C., Magdziarz A. and Bielejewska A., High-value chemicals obtained from selective photo-oxidation of glucose in the presence of nanostructured titanium photocatalysts. *Bioresource Technology* **2011**, 102 (24), 11254-11257.
- [166]. Colmenares J.C. and Magdziarz A., Room temperature versatile conversion of biomass-derived compounds by means of supported TiO_2 photocatalysts. *Journal of Molecular Catalysis A: Chemical* **2013**, 366, 156-162.
- [167]. Da Vià L., Recchi C., Gonzalez-Yañez E.O., Davies T.E. and Lopez-Sanchez J.A., Visible light selective photocatalytic conversion of glucose by TiO_2 . *Applied Catalysis B: Environmental* **2017**, 202, 281-288.
- [168]. Colmenares J.C., Magdziarz A., Chernyayeva O., Lisovytskiy D., Kurzydowski K. and Grzonka J., Sonication-assisted low-temperature routes for the synthesis of supported Fe- TiO_2 nanomaterials: Partial photooxidation of glucose and phenol aqueous degradation. *Chemcatchem* **2013**, 5 (8), 2270-2277.
- [169]. Park H., Kim H.-I., Moon G.-H. and Choi W., Photoinduced charge transfer processes in solar photocatalysis based on modified TiO_2 . *Energy & Environmental Science* **2016**, 9 (2), 411-433.
- [170]. Da Vià L., Recchi C., Davies T.E., Greeves N. and Lopez-Sanchez J.A., Visible-light-controlled oxidation of glucose using titania-supported silver photocatalysts. *ChemCatChem* **2016**, 8 (22), 3475-3483.
- [171]. Zhou B., Song J., Zhang Z., Jiang Z., Zhang P. and Han B., Highly selective photocatalytic oxidation of biomass-derived chemicals to carboxyl compounds over Au/TiO_2 . *Green Chemistry* **2017**, 19 (4), 1075-1081.
- [172]. Omri M., Sauvage F., Busby Y., Becuwe M., Pourceau G. and Wadouachi A., Gold catalysis and photoactivation: A fast and selective procedure for the oxidation of free sugars. *ACS Catalysis* **2018**, 8 (3), 1635-1639.
- [173]. Shiraishi Y., Morishita M. and Hirai T., Acetonitrile-assisted highly selective photocatalytic epoxidation of olefins on Ti-containing silica with molecular oxygen. *Chemical Communications* **2005**, (48), 5977.

- [174]. De S., Dutta S. and Saha B., Critical design of heterogeneous catalysts for biomass valorization: Current thrust and emerging prospects. *Catalysis Science & Technology* **2016**, 6 (20), 7364-7385.
- [175]. Cerdan K., Ouyang W.Y., Colmenares J.C., Munoz-Batista M.J., Luque R. and Balu A.M., Facile mechanochemical modification of g-C₃N₄ for selective photo-oxidation of benzyl alcohol. *Chemical Engineering Science* **2019**, 194, 78-84.
- [176]. Colmenares J.C., Ouyang W.Y., Ojeda M., Kuna E., Chernyayeva O., Lisovytskiy D., De S., Luque R. and Balu A.M., Mild ultrasound-assisted synthesis of TiO₂ supported on magnetic nanocomposites for selective photo-oxidation of benzyl alcohol. *Applied Catalysis B-Environmental* **2016**, 183, 107-112.
- [177]. Magdziarz A., Colmenares J.C., Chernyayeva O., Kurzydowski K. and Grzonka J., Iron-containing titania photocatalyst prepared by the sonophotodeposition method for the oxidation of benzyl alcohol. *Chemcatchem* **2016**, 8 (3), 536-539.
- [178]. Magdziarz A., Colmenares J.C., Chernyayeva O., Lisovytskiy D., Grzonka J., Kurzydowski K., Freindl K. and Korecki J., Insight into the synthesis procedure of Fe³⁺/TiO₂-based photocatalyst applied in the selective photo-oxidation of benzyl alcohol under sun-imitating lamp. *Ultrasonics Sonochemistry* **2017**, 38, 189-196.
- [179]. Nair V., Colmenares J.C. and Lisovytskiy D., Ultrasound assisted zno coating in a microflow based photoreactor for selective oxidation of benzyl alcohol to benzaldehyde. *Green Chemistry* **2019**, 21 (6), 1241-1246.
- [180]. Ouyang W.Y., Kuna E., Yopez A., Balu A.M., Romero A.A., Colmenares J.C. and Luque R., Mechanochemical synthesis of TiO₂ nanocomposites as photocatalysts for benzyl alcohol photo-oxidation. *Nanomaterials* **2016**, 6 (5).
- [181]. Higashimoto S., Kitao N., Yoshida N., Sakura T., Azuma M., Ohue H. and Sakata Y., Selective photocatalytic oxidation of benzyl alcohol and its derivatives into corresponding aldehydes by molecular oxygen on titanium dioxide under visible light irradiation. *Journal of Catalysis* **2009**, 266 (2), 279-285.
- [182]. Liang S., Wen L., Lin S., Bi J., Feng P., Fu X. and Wu L., Monolayer h-BN for selective photocatalytic oxidation of benzylic alcohols with visible light response. *Angewandte Chemie International Edition* **2014**, 53 (11), 2951-2955.
- [183]. Lin Q., Li L., Liang S., Liu M., Bi J. and Wu L., Efficient synthesis of monolayer carbon nitride 2d nanosheet with tunable concentration and enhanced visible-light photocatalytic activities. *Applied Catalysis B: Environmental* **2015**, 163, 135-142.
- [184]. Jing K., Xiong J., Qin N. et al., Development and photocatalytic mechanism of monolayer Bi₂MoO₆ nanosheets for the selective oxidation of benzylic alcohols. *Chemical Communications* **2017**, 53 (61), 8604-8607.
- [185]. Tanaka A., Hashimoto K., Kominami H., Preparation of Au/CeO₂ exhibiting strong surface plasmon resonance effective for selective or chemoselective oxidation of alcohols to aldehydes or ketones in aqueous suspensions under irradiation by green light. *Journal of the American Chemical Society* **2012**, 134 (35), 14526-14533.
- [186]. Tsukamoto D., Shiraishi Y., Sugano Y. et al., Gold nanoparticles located at the interface of anatase/rutile TiO₂ particles as active plasmonic photocatalysts for aerobic oxidation. *Journal of the American Chemical Society* **2012**, 134 (14), 6309-6315.
- [187]. Zhang N., Liu S., Fu X. et al., A simple strategy for fabrication of "plum-pudding"

type Pd@CeO₂ semiconductor nanocomposite as a visible-light-driven photocatalyst for selective oxidation. *The Journal of Physical Chemistry C* **2011**, 115 (46), 22901-22909.

[188]. Zhang N., Fu X. and Xu Y.-J., A facile and green approach to synthesize Pd@CeO₂ nanocomposite with tunable core-shell and yolk-shell structure and its application as a visible light photocatalyst. *Journal of Materials Chemistry* **2011**, 21 (22), 8152.

[189]. Zhang N., Liu S. and Xu Y.-J., Recent progress on metal core@semiconductor shell nanocomposites as a promising type of photocatalyst. *Nanoscale* **2012**, 4 (7), 2227.

[190]. Staveness D., Bosque I. and Stephenson C.R.J., Free radical chemistry enabled by visible light-induced electron transfer. *Accounts of Chemical Research* **2016**, 49 (10), 2295-2306.

[191]. Zhou B., Song J., Zhou H., Wu T. and Han B., Using the hydrogen and oxygen in water directly for hydrogenation reactions and glucose oxidation by photocatalysis. *Chemical Science* **2016**, 7 (1), 463-468.

[192]. Da Vià L., Recchi C., Davies T.E., Greeves N. and Lopez-Sanchez J.A., Visible-light-controlled oxidation of glucose using titania-supported silver photocatalysts. *ChemCatChem* **2016**, 8 (22), 3475-3483.

[193]. Ravelli D., Dondi D., Fagnoni M. and Albini A., Photocatalysis. A multi-faceted concept for green chemistry. *Chemical Society Reviews* **2009**, 38 (7), 1999.

Chapter 3. Lewis-promoted glucose conversion into HMF catalyzed by metal exchanged phosphotungstic acid confined into MCM-41

3.1 Introduction

Carbon-neutral manufacturing from renewable biomass to replace fossil fuel is considered as a major route for the sustainable production of chemicals and fuels.¹ Glucose is an abundant and low-cost biomass feedstock, which recently attracts great interest in producing HMF.^{2,3} HMF, containing an aldehyde and a hydroxymethyl group, is an important precursor to synthesize a variety of value-added chemicals such as levulinic acid (LA), 2,5-dimethyltetrahydrofuran (DMTHF), γ -valerolactone (GVL) and so on.^{4,5} Meanwhile, HMF also can be further converted into a series of high-quality fuels such as 2, 5-dimethylfuran (DMF). and 5-ethoxymethylfurfural (EMF).⁶

A tandem reaction mechanism by the cooperativity of Lewis and Brønsted acid sites has been widely accepted as glucose isomerization to fructose on LAS and fructose further dehydration to HMF on BAS.^{7,8} Combining inorganic Brønsted acids (such as H_2SO_4 and HCl) with homogeneous Lewis acidic metal chloride salts (i.e., AlCl_3 ,⁹ CrCl_3 ¹⁰ and SnCl_4 ¹¹) or Lewis acidic zeolites¹² has been previously used in HMF production widely. However, this catalytic process causes serious problems in recycling and eco-friendliness due to the toxic and corrosive nature of inorganic acids. Moreover, although low-cost zeolites¹² are the most extensively used, increasing Lewis acidity in zeolites by dealumination or ion-exchange often results in decreasing the density of BAS.^{13,14} And these extra-framework metal ions are easily dissolved or leaching out from zeolites in liquid-phase reactions.³ Thus, the design of solid acids with high

stability and enhanced dual Brønsted-Lewis acidic properties has attracted great interest in the efficient production of HMF from glucose.

Heteropoly acids (HPAs) have received much attention due to their inherent characteristics of strong acidity, stability and high proton mobility.^{15, 16} Particularly, phosphotungstic acid with stable Keggin anion structures ($\text{H}_3\text{PW}_{12}\text{O}_{40}$, HPW) possesses superior Brønsted acidity¹⁷ and showed high performance in fructose conversion into HMF.¹⁸ And its Lewis acidity could be manipulated easily through exchange H^+ with various metals on HPW. These metal-exchanged HPWs possess LAS originated from the metal cations as electron-pair acceptors, as well as BAS generated from the dissociation of coordinated water via the polarization of the cations,^{19, 20} which could remarkably promote glucose dehydration into HMF.

It was reported that metal exchanged HPWs were efficient catalysts in the hydrolysis of cellulose.²¹ However, the application of metal exchanged HPWs is hindered by the low surface area and high solubility in organic solvents.²² Separating these catalysts from products is not feasible, which requires some auxiliary separation processes and terminal waste treatment. Confining metal exchanged HPWs inside nanoporous materials is a promising approach to improve their catalytic activity and stability in reactions. Because the porous structure could offer spatial confinement to control the growth of nanoparticles and prevent nanoparticles from aggregation.²³⁻²⁵ Up to now, several acidic or neutral materials including silica,^{26, 27} activated-carbon²⁸ and metallic oxides,²⁹ have been employed to confine HPW catalysts. Compared to microporous supports, mesoporous supports are favorable in confining HPWs due to their high specific surface area, large pore size, high adsorption capacity, high thermal stability and non-toxicity.³⁰ Moreover, mesoporous materials are also emphasized for the facile immobilization of nanocomposites and for rapid mass transfer in the reaction of large

molecules.^{24, 31} For example, in xylose dehydration reaction, HPW confined inside mesoporous siliceous MCM-41 (HPW/MCM) shows high stability and excellent activity comparable to H₂SO₄.^{30, 32}

Therefore, to achieve a high HMF yield from glucose conversion, an efficient and stable bi-functional heteropoly acid is required to be confined inside nanopores. In the present work, we designed a number of metal (Fe³⁺, Cu²⁺, Zn²⁺ and Sn⁴⁺) exchanged HPW catalysts that were confined inside mesoporous siliceous MCM-41 support as the bi-acidic catalysts (MPW/MCM) with both BAS and LAS. The application of these catalysts in glucose dehydration to HMF shows the effect of different Lewis acid metals on the catalytic performance of glucose conversion into HMF. To further investigate the role of different acid sites on glucose dehydration reaction, the comparison samples HPW/MCM and Sn(IV)PW/MCM with elevating pre-treatment temperatures were synthesized. The acidic properties of these catalysts were characterized by ammonia temperature-programmed desorption (NH₃-TPD) and Fourier transform infrared (FT-IR) spectroscopy using pyridine as a probe molecule. Combined their acidity and catalytic activity, the roles of the total acid sites, BAS and LAS (density and strength) on HMF catalytic production were elucidated.

3.2 Experimental

3.2.1 Materials and reagents

Ammonia aqueous (NH₄OH, 25%), tetraethyl orthosilicate (TEOS, 100%), hexadecyl trimethylammonium chloride solution (CTACl, 25%), Keggin-type 12-tungstophosphoric acid (H₃PW₁₂O₄₀·xH₂O, HPW), tin (IV) chloride (SnCl₄, 98%), iron (III) chloride hexahydrate (FeCl₃·6H₂O, 97%), copper (II) nitrate trihydrate

($\text{Cu}(\text{NO}_3)_2 \cdot 3\text{H}_2\text{O}$) and zinc acetate dihydrate ($\text{Zn}(\text{CH}_3\text{COO})_2 \cdot 2\text{H}_2\text{O}$, 98%) were used for the synthesis of materials. Glucose (as a substrate), dimethyl sulfoxide (DMSO, as the reaction solvent), dimethylformamide (DMF), N-methyl-2-pyrrolidone (NMP) fructose (as a standard sample) and 5-hydroxymethylfurfural (HMF, as a standard sample) and methanol (HPLC grade) were obtained from Sigma-Aldrich. $\text{H}_3\text{PW}_{12}\text{O}_{40} \cdot x\text{H}_2\text{O}$ was dried in an oven at 100 °C for 6 h before use. All reagents were used as supplied without further purification.

3.2.2 Catalyst preparation

Mesoporous siliceous MCM-41 (denoted as MCM-41) was prepared as described in our earlier work.³¹ For the typical synthesis procedure, NH_4OH (25 wt%), CTACl (25%), TEOS in a volume of 18.3 mL, 22.65 mL and 24.3 mL, respectively, were added to 500 mL of deionized water and completely mixed under magnetic stirring at room temperature. After sonicating for 1 h, the resulting solid was collected by filtration, washed, and then dried in an oven at 80 °C. The final material was obtained after the as-synthesized product calcined at 500 °C for 6 h in static air.

Metal-exchanged HPW (MPW) were prepared from an aqueous solution of HPW (0.05 mol/L, 10 mL) by dropwise addition of stoichiometric quantities of the aqueous solution of metal salts (0.375-0.75 mmol) under vigorous stirring at room temperature. The mixture was continuously stirred for another 1 h, followed by evaporation under reduced pressure. Then the white precipitate was formed and dried at 100 °C overnight. This preparation method ensures the composition of metal (M^{n+}) exchanged $\text{PW}_{12}\text{O}_{40}^{3-}$ as $\text{M}_{3/n}\text{PW}_{12}\text{O}_{40}$. For example, Sn^{4+} salts of $\text{PW}_{12}\text{O}_{40}^{3-}$ as $\text{Sn}_{3/4}\text{PW}_{12}\text{O}_{40}$, is denoted Sn(IV)PW.

The confinement of MPW into MCM-41 was conducted via a wet impregnation method

as reported.³³ Similarly, the appropriate amount of MPW was dissolved in 60 mL of water at 100°C. Then the stoichiometric quantity of MCM-41 was added into the solution. The mixture was stirred for 4 h, and the water was removed by centrifugation. The resulting solid was dried at 100°C overnight and calcined at 350 °C for 3 h in the static air. Then the collected solid was washed with hot distilled water for several times to remove the unsupported MPW. Afterwards, it was dried and calcined at 350 °C for 3 h in the air. The obtained catalyst is denoted as xMPW/MCM, where x stands for the mass ratio of MPW to MPW/MCM), For comparing, xHPW/MCM catalysts were synthesized following the same procedure but without metal exchange.

3.2.3 Catalyst characterization

Microwave plasma atomic emission spectroscopy (MP AES) was carried out on the Agilent 4100 MP AES instrument for the analysis of principal elements (metal elements, Si and P). Working solutions were prepared by dissolving appropriate amounts of samples in diluted HCl (dissolving MPW) and NaOH (dissolving MPW/MCM) solutions. Fourier transform infrared (FT-IR) spectra were recorded on a Nicolet 6700 spectrometer (Thermo Fisher Scientific) in the wave number range of 600-4000 cm⁻¹. Powder X-ray diffraction (XRD) patterns were recorded on a PANalytical X'Pert PRO Multipurpose Diffractometer at 40 kV voltage and 20 mA current via Cu K α ($\lambda=1.5406$ Å). Measurements were conducted at a step size of 0.0167° and count time of 5.08 s for low-angle XRD, and step size of 0.0334° and count time of 60.33 s for high-angle XRD. Nitrogen adsorption/desorption isotherms were recorded on a TriStar II 3020 Autosorb-iQ analyzer at -196 °C. Prior to the measurements, the samples were degassed at 80 °C under vacuum overnight. High resolution transmission electron microscopy (HRTEM) images were recorded on a JEOL 2100 TEM operated at a voltage of 200 kV. Scanning

electron microscopy (SEM) with energy dispersive X-ray spectroscopy (EDS) measurements were operated on Zeiss's ULTRA Plus at an electron high tension of 15 kV. Temperature programmed desorption of ammonia (NH₃-TPD) was carried out on a Quantachrome instrument with a thermal conductivity detector (TCD). Using pyridine as a molecule, Fourier transform infrared spectroscopy (FTIR) was performed on an FTIR-650 spectrometer. In a home-made vacuum infrared cell with CaF₂ windows, a self-supported wafer of the sample (about 10 mg) was initially dried under vacuum at 400 °C for 1 h and then cooled down to 50 °C. During the cooling process, the reference spectra were recorded at 350, 250, 150 and 50 °C, respectively. Afterwards, the wafer was saturated with about 25 mbar of pyridine vapor at 50 °C for 30 min and then evacuated again for 30 min to completely remove physisorbed pyridine. Finally, the evacuated sample containing chemisorbed pyridine was subjected to TPD at 150, 250 and 350 °C for 30 min with a heating rate of 10 °C/min and the IR spectra were recorded in situ at these temperatures. The amounts of acid sites were determined from the integral intensity of characteristic bands (1450 cm⁻¹ for LAS, and 1540 cm⁻¹ for BAS) using the molar extinction coefficients of Emeis.³⁴

3.2.4 Catalytic reaction

In a typical experiment of glucose conversion, 50 mg of catalyst and 1 mL of glucose solution (0.1 g/mL in solvent) were transferred into a 15 mL glass reactor which was then closed tightly and placed into an oil bath at a given temperature. At a certain interval of time, the reactor was quenched by submerging the reactor into an ice-water bath. The solution was separated from solid catalysts by centrifugation and then analyzed by high-performance liquid chromatography (HPLC). The HMF was analyzed by an Agilent 1260 system equipped with a reversed-phase C18 column (Agilent

Eclipse Plus Columns, 250 × 4.6 mm, 5 μm) and a multi-wavelength detector at 284 nm. The mobile phase was 20 % (v/v) methanol aqueous solution at a flow rate of 0.6 mL/min. Substrate (glucose) and the by-product (fructose) were analyzed using an Agilent 1290 system equipped with a Biorad Aminex HPX-87H column (300 × 7.8 mm, 9 μm) and a refractive index detector (RID). 0.005 M H₂SO₄ aqueous solution was used as the mobile phase at a flow rate: 0.60 ml/min. The temperatures of column and RID were maintained at 60 °C and 50 °C, respectively. To confirm the other by-products of glucose conversion, the solution after reaction was analyzed by a gas chromatography-mass spectrometry (GC-MS; PerkinElmer, Clarus SQ 8) equipped with a capillary column, TC-1701 (GL Sciences, length 60 m, i.d. 0.25 μm, and film thickness 0.25 μm). A high-performance liquid chromatography-mass spectrometry (LC-MS; Agilent 1260 HPLC system) coupled to an Agilent 6130 MS detector equipped with an electrospray ionisation (ESI) was operated in both positive and negative ionization mode. The conversion of glucose and the yield of HMF and fructose were calculated according to the following equations:

The conversion of glucose (%) = the molar of glucose converted *100 / the molar of initial glucose; The yield of HMF/fructose (%) = the molar of HMF/fructose produced *100 / the molar of initial glucose; The selectivity of HMF/fructose (%) = the molar of HMF/fructose produced *100 / the molar of glucose converted.

3.2.5 Recycling experiment of catalyst

To investigate the reusability of the catalyst, the catalyst was recycled and tested under the identical reaction conditions. The catalyst was recovered by centrifugation, washed with 10 mL water three times, and dried at 60 °C overnight for the next experiment.

3.2.6 Dehydration experiments

The synthesized catalyst was pre-treated at a given temperature of 50, 150, 250 and 350 °C, for 2 h under N₂ (50 mL/min). The pre-treated sample was then cooled to room temperature and transferred to the reactor in a glove box (Ar, O₂ pressure < 0.3 ppm, moisture < 0.3 ppm) ready for the kinetics experiments.

3.3 Results and discussion

3.3.1 Textural and morphological characteristics

The compositions of MPW and MPW/MCM composite catalysts were determined by the MP-AES analysis of metals, P and Si (Table 3.1). The exchanged metal contents in MPW samples are very close to the theoretical values, indicating that these metals were introduced into the MPW successfully and the H⁺ was exchanged almost completely. In addition, for all MPW/MCM composites, the concentrations of MPW are as expected, indicating that the contents of MPW in the MPW/MCM samples could be accurately controlled by adding stoichiometric quantities of MPW at ca. 40%. As shown in Figure 3.1, the optimal loading amount of MPW and HPW are 40% and 20%, respectively. The structural properties of the MPW/MCM catalysts (with 40% loading amount) in comparison with MCM-41 and HPW/MCM (with 20% loading amount) were investigated by various characterization techniques. All MPW/MCM catalysts show similar structural properties. Sn(IV)PW/MCM was used as a representative for all the MPW/MCM catalysts studied in this work.

Table 3.1 Elemental contents of MPW and MPW/MCM composite catalysts.

Samples	Metal content (mmol/g)		Metal/P molar ratio	Samples	MPW content (%)
	Actual value	Theoretical value			
Zn(II)PW	0.47	0.50	1.39	40Zn(II)PW/ MCM	39.9
Fe(III)PW	0.34	0.34	0.87	40Fe(III)PW/ MCM	40.3
Cu(II)PW	0.48	0.50	1.31	40Cu(II)PW/ MCM	37.0
Sn(IV)PW	0.25	0.25	0.75	40Sn(IV)PW/ MCM	40.8

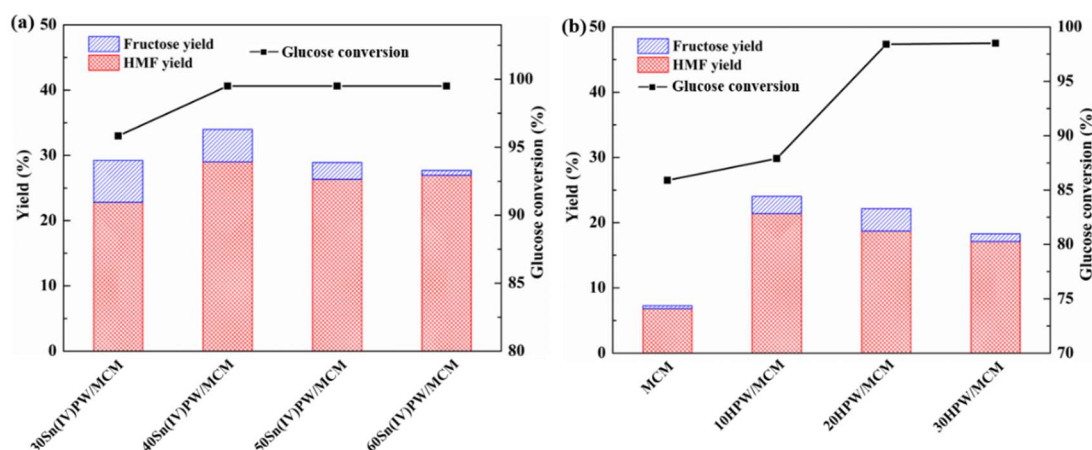


Figure 3.1 Activity comparison of different x Sn(IV)PW/MCM and y HPW/MCM catalysts for dehydration of glucose. Conditions: 100 mg glucose was dissolved in 1 mL of DMSO; the mass ratio of catalyst: glucose=1:2; 160 °C; 2 h.

Besides, the effect of solvent system on the performance of the reaction was evaluated and the results are shown in Table 3.2. HMF yields in the different solvents follow a decreasing order as DMSO > NMP > H₂O > DMF. The highest HMF selectivity of 29.8% is achieved by 40 Sn(IV)PW/MCM in DMSO solvent system. The highest yield and selectivity of HMF in DMSO solvent compared to the aqueous medium and the other

organic solvents can be ascribed to the hindrance of the side reactions in DMSO system and also to the catalytic capability of DMSO in the conversion of intermediate fructose into HMF via a 5-membered cyclic mechanism.³⁵ The lowest glucose conversion in H₂O is probably attributed to the strong interaction of H₂O with the hydrogen bonds of glucose, thus reducing their tendency to interact with glucose.³⁶

Table 3.2 The effect of different solvent system on the performance of glucose conversion into HMF

Solvent	Conversion (%)	HMF yield (%)	HMF selectivity (%)
H ₂ O	77.2	6.6	8.5
DMF	97.4	2.8	2.9
NMP	99.1	25.5	25.7
DMSO	97.6	29.1	29.8

As shown in Figure 3.2a, the low-angle XRD pattern of the MCM-41 is well defined and displays the (100), (110) and (200) reflections of ordered hexagonal mesoporous lattice at 2.4, 4.0 and 4.6°, respectively.³⁷ Compared with MCM-41, the decrease in the intensity of these peaks for HPW/MCM and MPW/MCM samples confirms the successful incorporation of HPW and MPW in MCM-41. But their framework structures of mesoporous molecular sieve were not destroyed. Besides, the shift of these peaks towards a higher angle for MPW/MCM sample is evident, arising from the interaction between MPW and MCM-41. It is assumed that MPW particles were not only dispersed on the surface of the catalyst but also entered the MCM-41 framework, resulting in weak diffraction peaks and declining d-spacing values. For the high-angle XRD patterns (Figure 3.2b), MCM-41 displayed only a broad peak in the range of $2\theta = 20-30^\circ$, which can be assigned to the diffraction peaks of amorphous silica. HPW

presented a set of well-resolved sharp diffraction peaks, particularly at $2\theta = 25.5, 35.7, 55.6$ and 60.0° , an index of the typical secondary cubic structure of Keggin anions of HPW crystal.³⁸ The same diffraction peaks with lower intensity were observed for MPW samples. Compared to bulk HPW and MPW, the supported catalysts only show a similar broad peak at $2\theta = 20\text{--}30^\circ$ with that of MCM-41 support, indicating that HPW and MPW were finely dispersed on MCM-41.

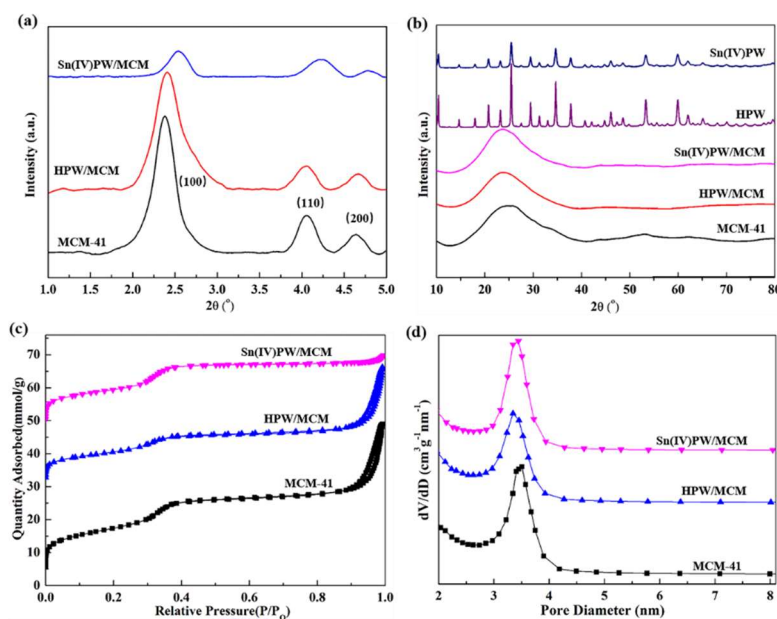


Figure 3.2 The low-angle (a) and high-angle (b) XRD patterns, N₂ adsorption-desorption isotherms (c) and pore diameter distributions (d) of MCM-41, HPW/MCM and Sn(IV)PW/MCM.

The characteristics of the Type IV profile of mesoporous MCM-41 with a sharp inflection at $P/P_0 = 0.3\text{--}0.4$ was observed in the N₂ adsorption-desorption isotherms of all samples (Figure 3.2c), indicating the capillary condensation mesoporous structure with a uniform size. The average pore size distribution (Figure 3.2d) is narrow for all materials and is centered at 3.5 nm (Table 3.3) with a pore volume of $1.0 \text{ cm}^3/\text{g}$ for MCM-41 and 3.3 nm with a pore volume of $0.7 \text{ cm}^3/\text{g}$ for both HPW/MCM and

MPW/MCM samples. All these mesoporous materials exhibit high BET specific surface areas as shown in Table 3.3. However, compared to MCM-41 (1053.0 m²/g), after loading HPW and MPW, the specific surface areas were reduced to 752.4 and 835.4 m²/g, respectively. A similar trend was observed on the pore volume and pore size of these supported catalysts. This could be explained that HPW and MPW were deposited inside the mesoporous channels of the MCM-41 support.

Table 3.3 Textural properties of MCM-41, HPW/MCM and Sn(IV)PW/MCM samples.

Catalyst	Surface area (m ² /g)	Pore volume (cm ³ /g)	Pore size (nm)
MCM-41	1053	1	3.5
HPW/MCM	752.4	0.7	3.3
Sn(IV)PW/MCM	835.4	0.7	3.3

The specific surface area is calculated by the BET method.

Total pore volume is determined by N₂ adsorption at a relative pressure of 0.99.

The average pore diameter is obtained from the adsorption isotherm by the BJH method.

MCM-41 depicts hexagonal pores with a typical ordered mesoporous structure.³¹ After impregnation of HPW and MPW, the nanocomposite maintained the same morphology. As shown in Figure 3.3a, the crystallite structure of HPW with the d-spacing of around 0.266 nm was observed on the HRTEM images of HPW/MCM (insert). It is shown that a small amount of HPW was located on the surface of MCM-41. The ordered mesoporous channel structure of (001) and (110) lattice planes are visible, as shown in HRTEM images in Figure 3.3b-d. The lattice space of (001) planes on MPW/MCM materials (3.47 nm) as shown in Figure 3.3d is smaller than that of bare MCM-41 observed from SXRD (3.68 nm), indicating that MPW particles were embedded in

mesoporous channels in MCM matrix. Elemental mapping by energy-dispersive X-ray (EDX) spectroscopy confirms the existence of P, W, and Sn on Sn(IV)PW/MCM, demonstrating the uniform distribution of all elements (Figure 3.3e). It is worth mentioning that after supported with HPW and MPW nanoparticles, mesoporous channels still exist in MCM-41, which ensures facile infiltration of the substrate into the mesopores during the reaction process.

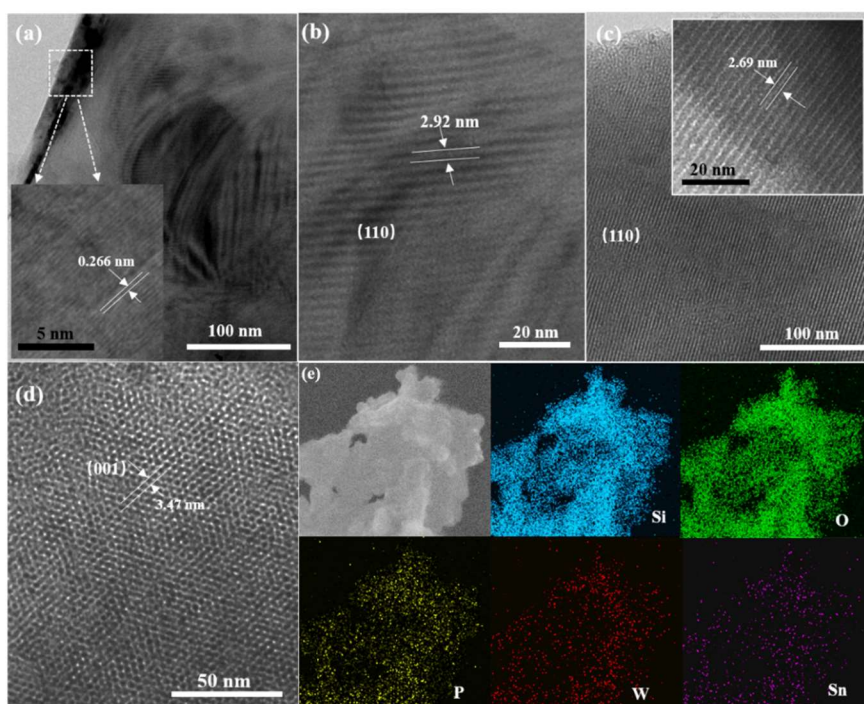


Figure 3.3 HRTEM images of HPW/MCM (a-b) and Sn(IV)PW/MCM(c-d); SEM-EDS elemental mapping images of Sn(IV)PW/MCM (e).

3.3.2 Effect of Lewis acid metals of MPW/MCM catalysts on glucose conversion

The activities of MPW/MCM samples with various LAS metals on the production of HMF from glucose were evaluated under identical reaction conditions (Figure 3.4a). All the MPW/MCM catalysts showed efficient catalytic activity on glucose conversion

to HMF. Noticeably, the HMF yield mainly depends on the strength of Lewis acidity of metals as follows: Sn(IV)PW/MCM > Fe(III)PW/MCM > Zn(II)PW/MCM > Cu(II)PW/MCM. To better elucidate the effect of metals, HMF yields over these MPW/MCM catalysts were plotted as a function of the ratio of charge and ionic radius (e/r) (Figure 3.4b). The e/r value reflects the electron-withdrawing ability of metal cations and has been used as an approximate measure for Lewis acidity of metal cations.^{21, 39} The reaction activity was increased for metal cations with an ascending e/r ratio. The highest HMF yield (23.3%) was observed for the catalyst (Sn(IV)PW/MCM) with the strongest LAS. Hence, it is concluded that a strong LAS of the MPW/MCM catalyst is more favorable for the conversion of glucose into HMF. It could be understood that the strong LAS would strongly interact with the oxygen atoms of the hydroxyl groups in glucose, leading to a subsequent reaction. Sn(IV)PW/MCM is the best LAS metal catalyst studied in this work for one-pot glucose conversion to HMF.

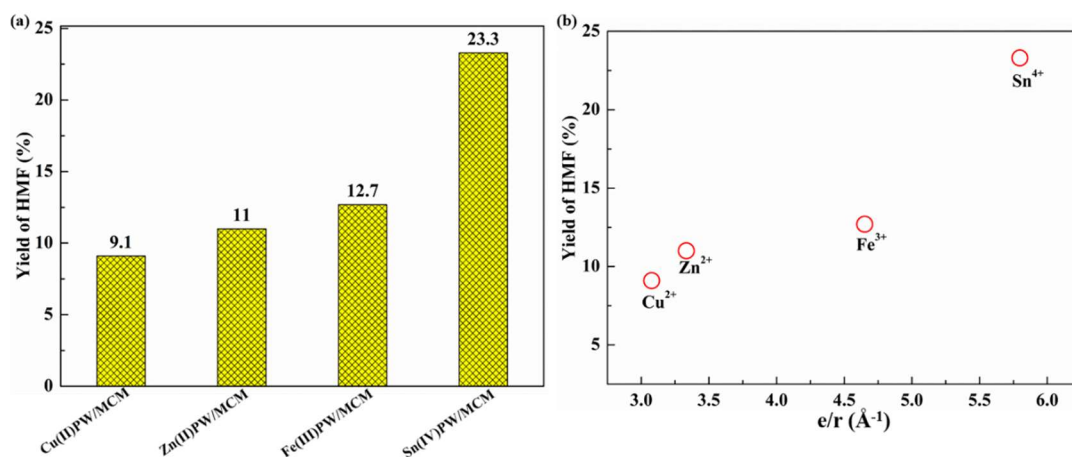


Figure 3.4 Effect of the Lewis metal for MPW/MCM catalysts on HMF yield. Reaction conditions: 100 mg glucose was dissolved in 1 mL of DMSO; the mass ratio of catalyst: glucose=1:2; 140 °C; 3 h.

3.3.3 Acidity characterization

The NH_3 -TPD was used to characterize the total acidity of catalysts. As shown in Figure 3.5, the wide desorption peaks of NH_3 on weak acid sites was observed at 215 °C and 280 °C for HPW/MCM and Sn(IV)PW/MCM samples, respectively. These weak acid sites may be due to the presence of weak LAS resulting from the interaction between MPW and the framework MCM-41.⁴⁰ The TPD profile of HPW/MCM also shows a wide desorption peak of NH_3 at around 725 °C due to the strong BAS from P-OH groups. Likewise, a sharp peak centered at 600 °C observed on Sn(IV)PW/MCM is ascribed to the strong LAS generated from Sn^{4+} .¹⁰ The amount of total acid sites is given in Table 3.4. It shows that Sn(IV)PW/MCM has a higher density of total acid sites and LAS than HPW/MCM.

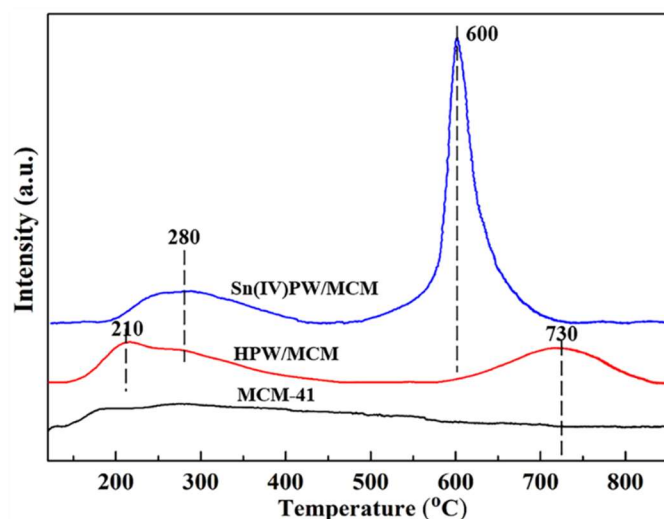


Figure 3.5 NH_3 -TPD profiles of HPW/MCM and Sn(IV)PW/MCM samples.

Table 3.4 Acidities of HPW/MCM and Sn(IV)PW/MCM samples.

Catalyst	Total acid sites ($\mu\text{mol}_{\text{NH}_3}/\text{g}_{\text{cat}}$)	BAS ($\mu\text{mol}_{\text{NH}_3}/\text{g}_{\text{cat}}$)	LAS ($\mu\text{mol}_{\text{NH}_3}/\text{g}_{\text{cat}}$)	L/B
HPW/MCM	185.8	143.0	42.8	0.3
Sn(IV)PW/MCM	304.2	101.4	202.8	2.0

The amount of acid sites was calculated by quantifying the desorbed NH_3 from NH_3 -TPD.

The ratio of different acid sites was determined by quantifying the desorbed pyridine from - FTIR of pyridine desorption at the desorption temperature of 150 °C.

FT-IR spectroscopy was used to quantitatively evaluate BAS and LAS on catalysts upon adsorption and desorption of pyridine as a probe molecule (Figure 3.6). The spectra depict the effect of the desorption temperature on the distribution of acid sites for HPW/MCM and Sn(IV)PW/MCM. The bands at 1540 and 1635 cm^{-1} bands are attributed to the pyridinium ion formed on the BAS.⁴¹ The bands at 1445 and 1609 cm^{-1} correspond to the pyridine coordinatively bonded to LAS.^{42, 43} These results confirm the coexistence of BAS and LAS on both samples. In addition, the band observed at 1595 cm^{-1} is ascribed to the hydrogen-bonded pyridine obtained by intermolecular interactions of pyridine via the nitrogen lone pair electrons.⁴⁴ The hydrogen-bonded pyridine can be removed easily at an elevated desorption temperature as it is noted that this band disappeared completely at 150 °C for HPW/MCM and 250 °C for Sn(IV)PW/MCM. It is noteworthy that the band at 1445 cm^{-1} showed a decreased intensity with an increased desorption temperature, assigned to the desorption of pyridine adsorbed mainly on weak LAS,⁴³ which could be mainly generated from the interaction between HPW or Sn(IV)PW with the framework MCM-41.⁴⁰

Compared with HPW/MCM, the spectra of Sn(IV)PW/MCM reveal a relatively weak absorption band at 1540 cm^{-1} and a strong band at 1445 cm^{-1} , suggesting the lower ratio

of BAS to LAS. Therefore, we can conclude that introducing Sn in HPW/MCM contributes to the increase of the ratio of LAS to BAS as shown in Table 3.4. In Figure 3.6b, it is also observed that the intensity of the band at 1445 cm^{-1} attributed to pyridine mainly adsorbed on weak LAS decreased, and eventually disappeared at a higher desorption temperature of $350\text{ }^{\circ}\text{C}$. A new peak at 1450 cm^{-1} appeared, which is attributed to these pyridine molecules adsorbed onto the strong LAS generated by tin ions.^{37, 46} As we know, the desorption procedure of absorbed pyridine molecules directly leads to the exposure of acid sites (LAS and BAS) on catalysts. With the increase of the desorption temperature from 50 to $350\text{ }^{\circ}\text{C}$, the peak area of pyridine adsorbed at 1445 cm^{-1} decreased more significantly than that absorbed at 1540 cm^{-1} as shown in Table 3.5, corresponding to a more significantly increased of LAS than BAS exposed on Sn(IV)PW/MCM. Besides, the Sn(IV)PW/MCM sample pre-treated at 250 and $350\text{ }^{\circ}\text{C}$ showed the strong LAS evidenced by the observation of a new peak at 1450 cm^{-1} . And the density of strong LAS exposed on Sn(IV)PW/MCM increased with the increased desorption temperature from 250 to $350\text{ }^{\circ}\text{C}$.

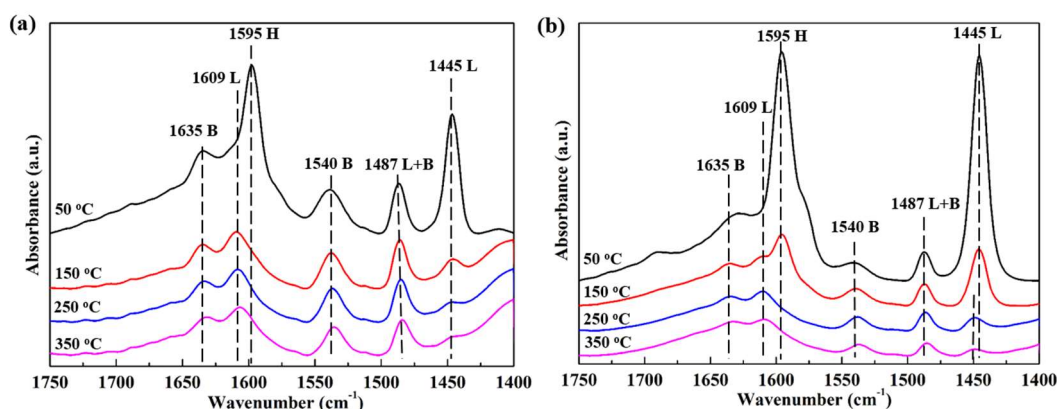


Figure 3.6 FT-IR spectra of pyridine adsorbed on HPW/MCM (a) and Sn(IV)PW/MCM samples (b). Recorded after desorption at $50\text{ }^{\circ}\text{C}$, $150\text{ }^{\circ}\text{C}$, $250\text{ }^{\circ}\text{C}$ and $350\text{ }^{\circ}\text{C}$. [B: pyridine molecules bound to BAS; L: pyridine molecules bound to LAS; H: hydrogen-bonded pyridine molecules].

Table 3.5 The peak area of pyridine adsorbed on LAS and BAS of Sn(IV)PW/MCM at different desorption temperature.

Desorption temperature	LAS peak area at 1445-1450 cm^{-1}	BAS peak area at 1540 cm^{-1}
50 °C	8.86 ^a	1.17
150 °C	2.08 ^a	1.06
250 °C	1.11 ^b	0.71
350 °C	0.78 ^b	0.63

^aAccording to the peak area at 1445 cm^{-1} .

^bAccording to the peak area at 1450 cm^{-1} .

3.3.4 Catalytic performance of HPW/MCM and Sn(IV)PW/MCM in glucose conversion

To study the role of the total acid sites in the glucose dehydration to HMF over Sn(IV)PW/MCM, several controlled experiments with different ratios of catalyst to glucose were conducted at the identical reaction time and temperature (160 °C; 2 h). The total acid sites were calculated based on the mass of the catalyst and the density of total acid sites determined by NH_3 -TPD. The HMF yield was plotted against the molar ratio of total acid sites to glucose as shown in Figure 3.7a. The HMF yield was increased dramatically with the increase of the total acid sites/glucose ratio when the ratio was below 0.028. Further increasing the ratio resulted in a significantly decreased HMF yield. This could be explained that the excessive total acid sites lead to a subsequent formation of secondary products from HMF, including polymers, humins and HMF derivatives.⁴⁷ A proper ratio of total acid sites to glucose at around 0.028 contributes to a better yield to HMF. Therefore, the optimal ratio of total acid sites to glucose was set

as around 0.028, equivalent to 1/2 mass ratio of catalyst/glucose in the following experiments.

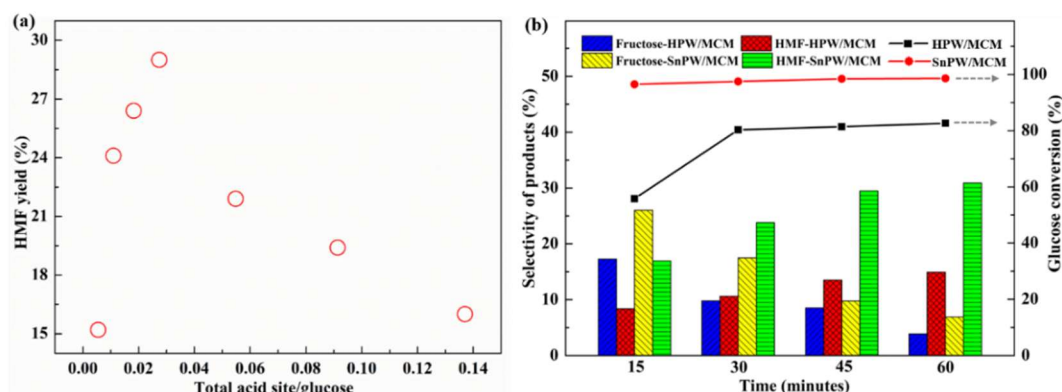


Figure 3.7 Effect of the molar ratio of total acid sites to glucose on HMF yield over Sn(IV)PW/MCM catalyst (a) and a typical time course of glucose conversion and the selectivity to HMF and fructose on HPW/MCM and Sn(IV)PW/MCM (b). Reaction conditions (a): 1 mL DMSO, 160 °C, 2 h; (b): 1 mL DMSO; the mass ratio of catalyst: glucose=1:2; 160 °C.

To understand the contribution of BAS and LAS on glucose conversion, the activities of HPW/MCM (BAS dominated) and Sn(IV)PW/MCM (LAS dominated) were examined under identical reaction conditions. A typical time course of glucose conversion and the selectivity to HMF and fructose is shown in Figure 3.7b. Sn(IV)PW/MCM with a similar mesoporous structure to HPW/MCM, exhibited superior catalytic performance both in terms of glucose conversion and fructose and HMF selectivity. Within 15 min of reaction, the glucose conversion was up to 96.5% on Sn(IV)PW/MCM, and 55.8% on 20HPW/MCM. The improvement factor of glucose conversion (ca. 1.7 times) aligns very well with the increase of total acidity (ca. 1.6 times). After 15 min of reaction, a selectivity to fructose of 26.0% and HMF of 16.9%

was achieved on Sn(IV)PW/MCM, while HPW/MCM afforded 17.3% and 8.4%, respectively. The differences in fructose selectivity could be due to the larger amount of LAS in Sn(IV)PW/MCM compared to HPW/MCM (Table 3.4). However, it is worth noting that as the reaction time passed, the selectivity to fructose gradually decreased for all catalysts, while the glucose conversion and HMF selectivity remained increased for all samples (Figure 3.7b). Over 99% of glucose conversion and 32.8% of HMF selectivity were obtained on Sn(IV)PW/MCM after 60 min. The decline of fructose selectivity corresponding to the ascending HMF selectivity verifies that the glucose conversion into HMF occurred through intermediate fructose. This suggests that the LAS in MPW/MCM catalysts could show a beneficial effect on the reaction of glucose conversion into HMF, which was consistent with the conclusion reported.⁵³ The better selectivity to HMF achieved on Sn(IV)PW/MCM might be attributed to the dehydration of fructose into HMF induced by the high concentration of fructose formed than HPW/MCM.

The reaction effluent obtained on Sn(IV)PW/MCM was analyzed by HPLC-MS (Figure 3.8) and GC-MS (Table 3.6) to identify the by-products. Some main by-products, such as HMF derivatives including 2,5-dihydromethyl furan, 5-formyl-2-furancarboxylic acid, furan-2,5-dicarboxylic acid, 1, 4-pentanediol and γ -valerolactone, were detected. The result partly agrees with an earlier report where LAS in zeolites⁴⁶ adversely affected xylose dehydration into furfural derivatives directly. Levoglucosan and disaccharides originated from glucose were also identified. The other by-products could be oligomers and intramolecular dehydration products.^{49, 50} Besides, a high density of total acid sites could also lead to the formation of soluble polymers, various

intermediates and parallel by-products with HMF from glucose and fructose.^{51, 52} Based on the HPLC-MS and GC-MS analysis, reaction pathways of glucose conversion are proposed in Scheme 3.1. There are two main pathways for HMF production and four main HMF-derived by-products.

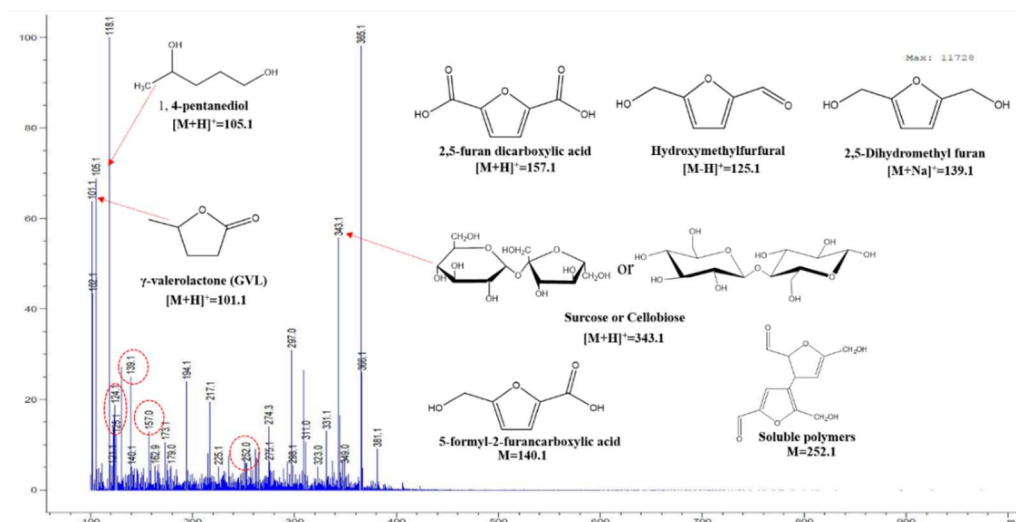


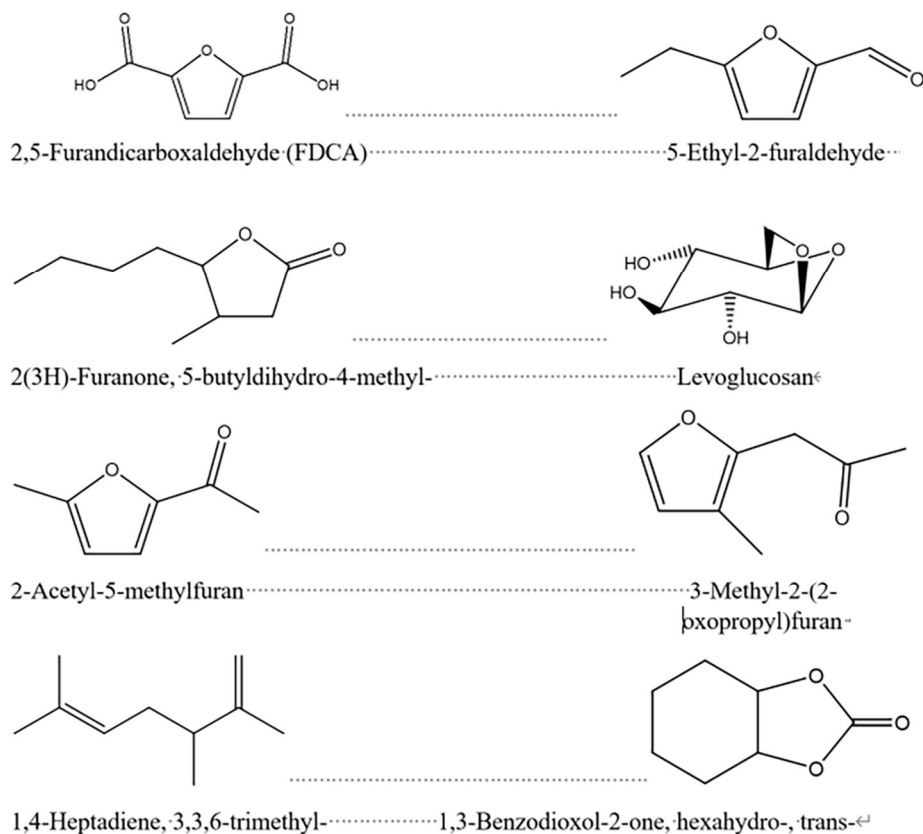
Figure 3.8 The positive LC-MS spectrum of the solution after reaction using SnPW/MCM solvent (160 °C, 2h) and the proposal by-products. Mobile phase: water/acetonitrile = 80/20 (V/V); Column flow rate: 0.5 ml/min; Column temperature: 30 °C.

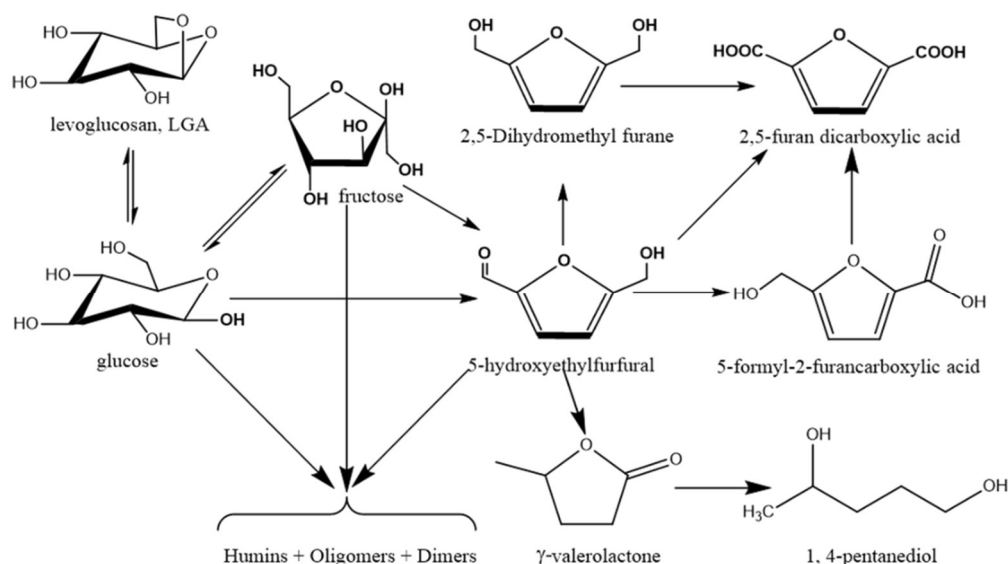
Table 3.6 The proposed by-products from glucose conversion on Sn(IV)PW/MCM obtained by GC-MS results.

Name	Formula	Score	Mass (DB)	Base Peak	Area
2,5-Furandicarboxaldehyde	C ₆ H ₄ O ₃	50.66	124	124	6089
5-(Hydroxymethyl)-2-(dimethoxymethyl)furan	C ₈ H ₁₂ O ₄	79.34	172.1	141.1	9299318
5-Ethyl-2-furaldehyde	C ₇ H ₈ O ₂	0.16	124	124	1765702

2(3H)-Furanone, 5-butyl-4-methyl-	C ₉ H ₁₆ O ₂	1.93	156	100	564107
Levoglucosan	C ₆ H ₁₀ O ₅	63.42	162.1	60	167542
2-Acetyl-5-methylfuran	C ₇ H ₈ O ₂	46.57	124	109	38698
2-Butyn-1-ol, 4-methoxy-	C ₅ H ₈ O ₂	41.28	100	57	14502
3-Methyl-2-(2-oxopropyl)furan	C ₈ H ₁₀ O ₂	59.84	138	57	6778
1,4-Heptadiene, 3,3,6-trimethyl-	C ₁₀ H ₁₈	52.59	138	55	3017
3-Methyl-2-(2-oxopropyl)furan	C ₈ H ₁₀ O ₂	59.87	138	57	396
1,3-Benzodioxol-2-one, hexahydro-, trans-	C ₇ H ₁₀ O ₃	60.53	142	69	4809

Proposed by-products obtained by GC-MS:





Scheme 3.1 Possible reaction pathways of glucose conversion based on MS analysis.

3.3.5 Tuning Lewis acidity via dehydration of Sn(IV)PW/MCM for glucose conversion

The above results reveal the importance of LAS in a catalyst for effective glucose dehydration to HMF. To further illustrate the effect of LAS on catalytic activity, four controlled experiments were conducted on Sn(IV)PW/MCM pre-treated at different temperatures from 50 to 350 °C (Figure 3.9). The elevated pre-treatment temperature leads to more acid sites exposed, providing an increase in total acid sites, which contributes to a significant increase in the glucose conversion (Figure 3.9a), corroborating with our previous conclusion. According to the results of FTIR characterization using pyridine as the probe molecule, the elevated pre-treatment temperature (from 50 to 350 °C) mainly leads to the increase of LAS. The sample pre-treated at 150 °C with more LAS showed a nearly 15 times higher fructose selectivity

(23%) in comparison with the sample pre-treated at 50 °C (1.6%) in 15min (Figure 3.9b). After a longer reaction time, a maximum fructose selectivity of 35.2% and 22.1% was observed for the samples pre-treated at 150 °C and 50 °C for 30 min and 60 min, respectively. The catalytic results can be explained by the population of LAS and BAS. A relatively high density of LAS, which can act as catalytic sites for glucose isomerization into intermediate fructose, leads to a high fructose selectivity. However, the samples pre-treated at 250 and 350 °C with strong LAS showed a declined fructose selectivity of 9.4% and 5.4%, respectively. The phenomena could be due to the fast formation and dehydration of fructose on the strong LAS, so that fructose could not be detected.

The increase of LAS also leads to a significant enhancement in the selectivity to HMF (Figure 3.9c), which is attributed to the increased fructose formation over the high density of LAS. Meanwhile, the HMF selectivity on all catalysts displayed an ascending trend as the reaction time increased from 15 to 60 min. However, further prolonging the reaction time, a slight decrease of HMF selectivity was observed on all catalysts as shown in Figure 3.10, which is due to the occurrence of secondary side reactions of HMF as shown in Scheme 3.1. The highest HMF yield is attributed to the equilibrium of HMF formation and conversion. Notably, the sample pre-treated at 350 °C with a high density of strong LAS originated from the Sn^{4+} cation reached the maximum HMF selectivity within only 60 min. It indicates that strong LAS could be more favorable for accelerating the conversion of glucose. This conclusion is also certified by the high glucose conversion of Sn(IV)PW/MCM pre-treated at 350 °C, where almost 96.5% glucose was converted within only 15min (Figure 3.9a).

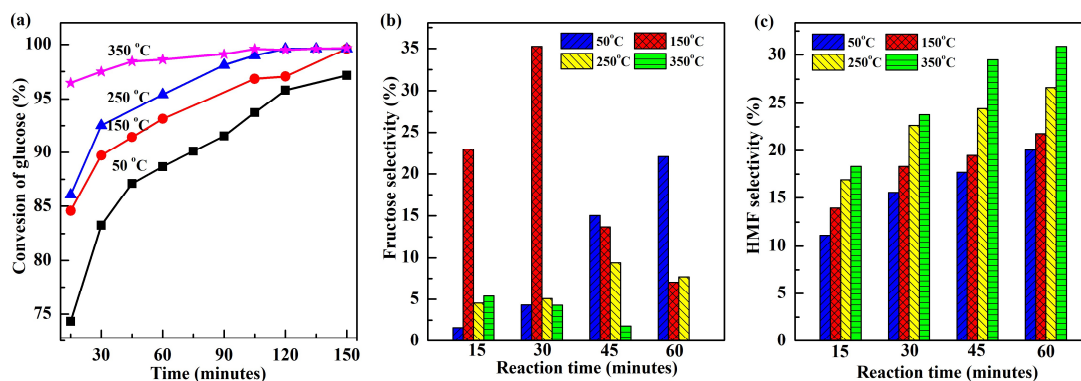


Figure 3.9 Time course of glucose conversion (a) and the selectivity to fructose (b) and HMF (c) on Sn(IV)PW/MCM catalysts at different pre-treatment temperatures.

Conditions: 100 mg glucose was dissolved in 1 mL of DMSO; the mass ratio of catalyst: glucose = 1:2; 160 °C.

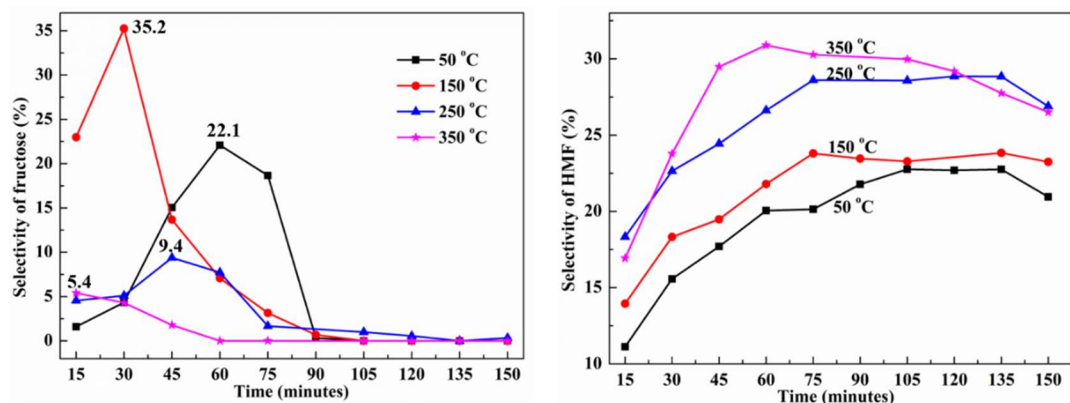


Figure 3.10 Time course of fructose (a) and HMF selectivity (b) with Sn(IV)PW/MCM catalysts pre-treated under different temperatures. Conditions: 100 mg glucose was dissolved in 1 mL of DMSO; the mass ratio of catalyst: glucose = 1:2; 160 °C.

3.3.6 LAS accelerates fructose production at a lower temperature.

To understand how strong LAS accelerates the conversion of glucose, a series of glucose conversion reactions at low temperatures was performed using Sn(IV)PW/MCM pre-treated at 350 °C as the catalyst. As shown in Figure 3.11a-b, the

glucose isomerization to fructose is dominant at the initial stage of the reaction within 15 min. At a low temperature of 120 °C, the highest selectivity to fructose reached 52.5% at a low glucose conversion of 16%. With prolonging reaction time to 60 min, around 75% fructose selectivity was obtained at 30.4% glucose conversion. It indicates that the strong LAS on Sn(IV)PW/MCM catalyst can initiate glucose isomerization into fructose at a relatively low temperature, where the secondary reaction of fructose was slow, leading to a large amount of fructose accumulated. With the increase of reaction temperature or reaction time, the selectivity to fructose decreased but the glucose conversion increased. These results confirm that a large amount of fructose formed at a high glucose conversion was accompanied by the faster dehydration of fructose into HMF and/or fructose condensation into humins or other polymers.^{54, 55}

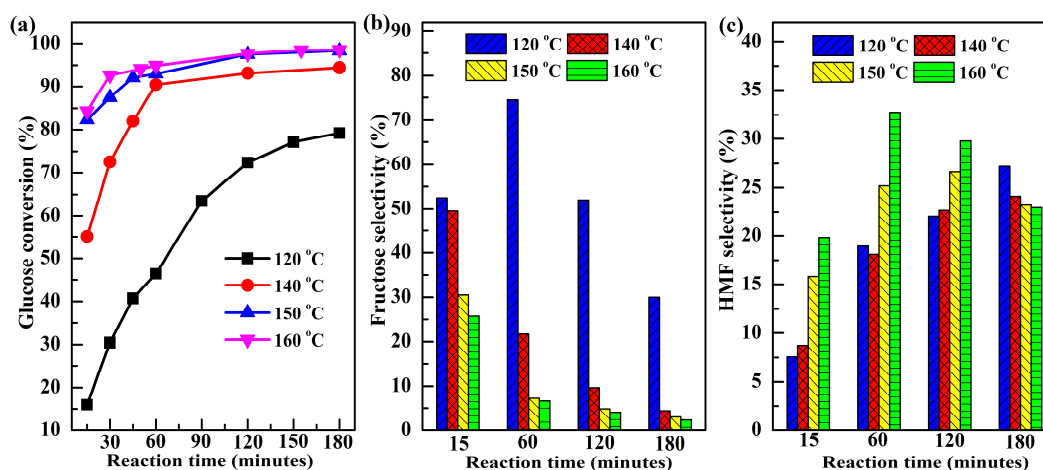


Figure 3.11 Time course of glucose conversion (a) and the selectivity to fructose (b) and HMF (c) on Sn(IV)PW/MCM at different reaction temperatures. Conditions: 100 mg glucose was dissolved in 1 mL of DMSO; the mass ratio of catalyst: glucose = 1:2.

Figure 3.11c show a similar profile of the selectivity to HMF at low temperature (120-140 °C) within the reaction time of 2 h. In contrast, A high HMF selectivity was achieved at the high temperature of 150-170 °C, suggesting that the conversion of

glucose to HMF needs a relatively high temperature than glucose conversion to fructose. It has been reported that the production of furan compounds occurred at a high temperature because of the endothermic nature of the fructose conversion.⁵⁶ The HMF selectivity reached the maximum value of 32.8% at a high temperature of 160 °C in 60 min. However, further prolonging the reaction time to 180 min led to the fast decrease of HMF selectivity to around 23% at 150 and 160 °C, which is caused by the degradation and condensation of HMF in good agreement with the literature.⁹ It is deduced that HMF could be produced faster at high temperature but converted to other by-products rapidly as well. This observation reinforces that the isomerization of glucose to fructose is an essential step in this reaction. And the reaction rate of glucose isomerization into fructose is higher than that of fructose dehydration at a low glucose conversion, leading to the accumulation of fructose. Afterward, a high concentration of fructose at a high glucose conversion accelerates fructose dehydration into HMF.

Based on the above-mentioned discussion, the reaction pathway involves the first step of glucose isomerization to fructose on LAS, followed by the dehydration of fructose to HMF on LAS⁵⁷ and/or BAS⁵⁸. Metal cation acting as an electrophile LAS activates the open-ring of glucose^{11, 35} Sn⁴⁺ with strongest Lewis acidity showed the highest activity due to strongly interact with the oxygen atoms of the hydroxyl groups in glucose leading to subsequent reaction. The one-pot reactor adjusted the equilibrium-limited glucose to fructose isomerization leading to high glucose conversion through dehydration of the accumulated fructose to HMF.

In last, to further explore the catalytic feature of Sn(IV)PW/MCM pre-treated at 350 °C, an apparent activation energy barrier (E_a) of glucose transformation in DMSO was estimated according to the Arrhenius law. The glucose concentration versus time was plotted at different temperatures (120-140 °C) assuming a first-order reaction in glucose

conversion, a good fit for the experimental data ($R^2 > 0.98$ for all series) (Figure 3.12a).⁵⁹ Then the rate constants at different temperatures were obtained and plotted versus the reciprocal of temperature in Figure 3.12b. The apparent activation energy of glucose conversion (79.7 kJ/mol) obtained on Sn(IV)PW/MCM is considerably lower than that (138 kJ/mol) on aluminum triflate reported by Rasrendra et al.⁵⁹ using the same reaction solvent.

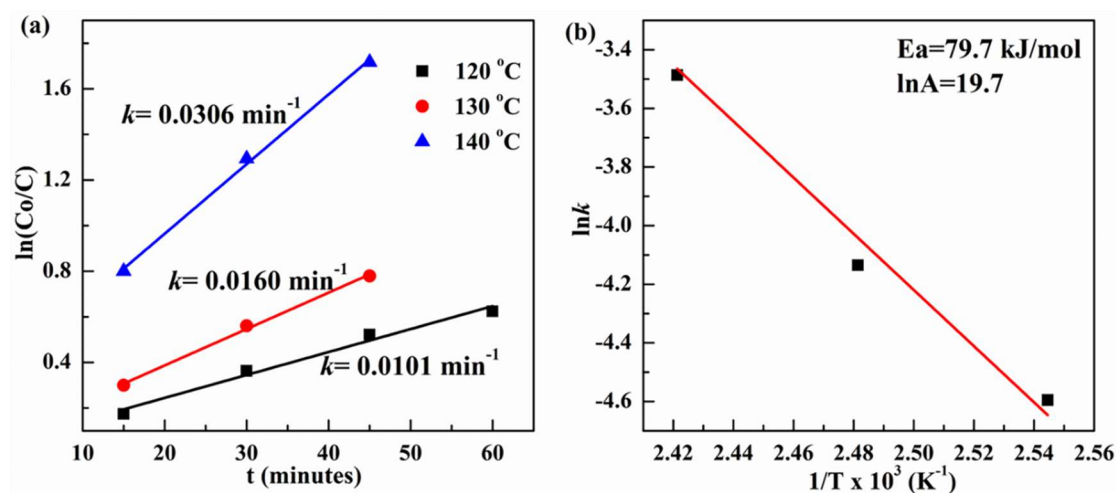


Figure 3.12 First-order fitting in glucose conversion with different temperatures (a) and the Arrhenius plot for glucose conversion in DMSO using Sn(IV)PW/MCM as the catalyst (b). (C_0 is the concentration of glucose at the beginning of the reaction, C is the concentration of glucose at the time t , and k is the rate constant, T is the absolute temperature (in kelvins), A is the pre-exponential factor, E_a is the activation energy for the reaction.)

3.3.7 Stability and reusability

Another important advantage of heterogeneous acid catalyst is the stability against the leaching of acid sites during the process of the reaction. MPW showed efficient activity in glucose conversion (Table 3.7), however, we found that these catalysts were partially

dissolved in DMSO after the reaction. To investigate the confinement effect of mesoporous MCM-41, the catalytic stability of MPW/MCM was evaluated by choosing the most active Sn(IV)PW/MCM as the representative sample. Its catalytic performance has proceeded for four consecutive runs under the same condition. After each catalytic run, the catalyst was recovered by centrifugation, and then washed with water three times. After being dried at 60 °C for 2 h, the catalyst was weighed and applied to the next run. It is worth mentioning that a small amount of catalyst could be lost during the recycling process. To overcome this problem, we repeated the first run seven times, ensuring that the total amount of collected catalyst was enough for the second run for six times, and so on.

Table 3.7 Conversion glucose to HMF using various metal exchanged HPWs in DMSO.

Catalysts	Condition	The yield of HMF (%)
Fe(III)PW	140 °C; 3 h	13.6
Sn(IV)PW	140 °C; 3 h	32.7
Cu(II)PW	140 °C; 3 h	18.3
Zn(II)PW	140 °C; 3 h	20.5

Conditions: 100 mg glucose was dissolved in 1 mL of DMSO; the mass ratio of catalyst: glucose = 1:2.

As shown in Figure 3.13, the HMF yield slightly decreased from 29% to 25.8% after four consecutive runs. The possible reason is that a small amount of highly active by-products generated during the reaction can be strongly adsorbed on the catalyst surface.⁶⁰ They will occupy a small amount of the surface-active sites to hinder the reaction process, which reduces the catalytic performance of catalysts. It was also observed that the color of the spent catalysts gradually changed from white to pale yellow with increasing cycle number. The catalyst after the fourth run could be

effectively regenerated after calcination, exhibiting a 30.3% HMF yield. This indicates mesoporous MCM-41 support could provide high resistance of Sn(IV)PW from leaching and dissolving in a polar solvent, leading to good reusability of Sn(IV)PW/MCM catalyst.

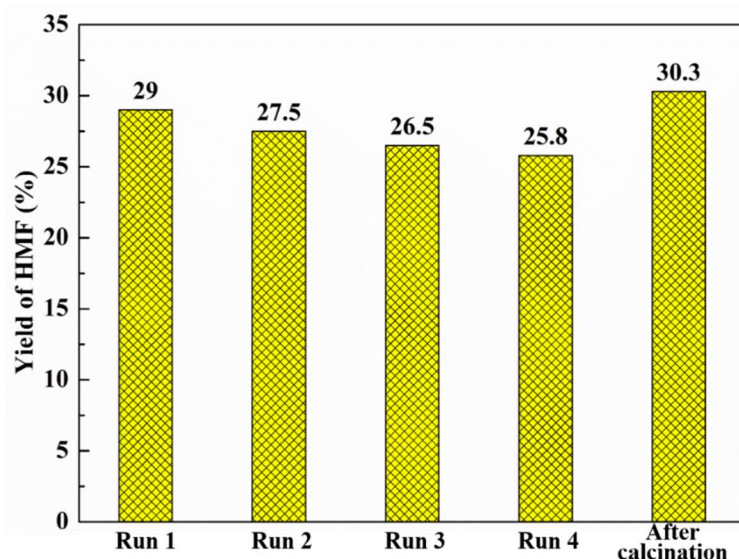


Figure 3.13 Catalyst recycling and regeneration experiments of Sn(IV)PW/MCM for converting glucose into HMF. Conditions: 100 mg glucose was dissolved in 1 mL of DMSO; the mass ratio of catalyst: glucose=1:2; 160 °C; 2 h.

3.4 Conclusions

In this work, a series of acidic catalysts HPW/MCM and MPW/MCM were synthesized for glucose conversion. The introduction of different metal cations varied Lewis and Brønsted acidity on MPW/MCMs, which governed the catalytic activities. Sn(IV)PW/MCM with the strongest LAS was found to be more efficient in glucose conversion into HMF, with 32.8% HMF selectivity and nearly 99% glucose conversion obtained at 160 °C for 1 h in DMSO. The catalyst could be reused several times without significant loss of activity. Based on the comparable activity in glucose conversion over

HPW/MCM and Sn(IV)PW/MCM, it is concluded that the Lewis acidities play an important role in promoting the glucose dehydration reaction. Four controlled experiments using Sn(IV)PW/MCM pre-treated at different temperatures from 50 to 350 °C further elucidated the significant role of LAS. It is found that the selectivity of HMF depends on the density of LAS and shows a gradual increase with the increased ratio of LAS/BAS in Sn(IV)PW/MCM. And the strong LAS could promote glucose isomerization into fructose at a lower reaction temperature, showing apparent activation energy of 79.7 kJ/mol for glucose conversion using Sn(IV)PW/MCM pre-treated at 350 °C. The work could aid the rational design of the acid catalytic system for glucose dehydration reaction in the future.

References

- [1]. Clark J.H., Budarin V., Deswarte F.E.I. et al., Green chemistry and the biorefinery: A partnership for a sustainable future. *Green Chemistry* **2006**, 8 (10), 853-860.
- [2]. Wang T.F., Nolte M.W., Shanks B.H., Catalytic dehydration of C-6 carbohydrates for the production of hydroxymethylfurfural (HMF) as a versatile platform chemical. *Green Chemistry* **2014**, 16 (2), 548-572.
- [3]. Wang Z.C., Li T., Jiang Y.J. et al., Acidity enhancement through synergy of penta- and tetra-coordinated aluminum species in amorphous silica networks. *Nature Communication* **2020**, 11 (1).
- [4]. Rosatella A.A., Simeonov S.P., Frade R.F.M. et al., 5-hydroxymethylfurfural (HMF) as a building block platform: Biological properties, synthesis and synthetic applications. *Green Chemistry* **2011**, 13 (4), 754-793.
- [5]. Van Putten R.J., Van Der Waal J.C., De Jong E. et al., Hydroxymethylfurfural, a versatile platform chemical made from renewable resources. *Chemical Reviews* **2013**, 113 (3), 1499-1597.
- [6]. Wang H.Y., Zhu C.H., Li D. et al., Recent advances in catalytic conversion of biomass to 5-hydroxymethylfurfural and 2, 5-dimethylfuran. *Renewable & Sustainable Energy Reviews* **2019**, 103, 227-247.
- [7]. Ranoux A., Djanashvili K., Arends I. et al., 5-hydroxymethylfurfural synthesis from hexoses is autocatalytic. *ACS Catalysis* **2013**, 3 (4), 760-763.
- [8]. Wang Z.C., Huang J., Brønsted-Lewis acids for efficient conversion of renewables. *Production of biofuels and chemicals with bifunctional catalysts*, **2017**; 99-135.
- [9]. Pagan-Torres Y.J., Wang T.F., Gallo J.M.R. et al., Production of hydroxymethylfurfural from glucose using a combination of Lewis and Brønsted acid catalysts in water in a biphasic reactor with an alkylphenol solvent. *ACS Catalysis* **2012**,

2 (6), 930-934.

[10]. Choudhary V., Mushrif S.H., Ho C. et al., Insights into the interplay of Lewis and Brønsted acid catalysts in glucose and fructose conversion to 5-(hydroxymethyl)furfural and levulinic acid in aqueous media. *Journal of the American Chemical Society* **2013**, 135 (10), 3997-4006.

[11]. Hu S.Q., Zhang Z.F., Song J.L. et al., Efficient conversion of glucose into 5-hydroxymethylfurfural catalyzed by a common Lewis acid SnCl₄ in an ionic liquid. *Green Chemistry* **2009**, 11 (11), 1746-1749.

[12]. Nikolla E., Roman-Leshkov Y., Moliner M. et al., "One-pot" synthesis of 5-(hydroxymethyl)furfural from carbohydrates using tin-beta zeolite. *ACS Catalysis* **2011**, 1 (4), 408-410.

[13]. Huang J., Jiang Y.J., Marthala V.R.R. et al., Characterization and acidic properties of aluminum-exchanged zeolites x and y. *Journal of Physical Chemistry C* **2008**, 112 (10), 3811-3818.

[14]. Jiang Y.J., Huang J., Dai W. et al., Solid-state nuclear magnetic resonance investigations of the nature, property, and activity of acid sites on solid catalysts. *Solid State Nuclear Magnetic Resonance* **2011**, 39 (3-4), 116-141.

[15]. Misono M., Heterogeneous catalysis by heteropoly compounds of molybdenum and tungsten. *Catalysis Reviews-Science and Engineering* **1987**, 29 (2-3), 269-321.

[16]. Guo F., Fang Z., Xu C.C. et al., Solid acid mediated hydrolysis of biomass for producing biofuels. *Progress in Energy and Combustion Science* **2012**, 38 (5), 672-690.

[17]. Misono M., Mizuno N., Katamura K. et al., Catalysis by heteropoly compounds .3. The structure and properties of 12-heteropolyacids of molybdenum and tungsten (H₃PMo_{12-x}W_xO₄₀) and their salts pertinent to heterogeneous catalysis. *Bulletin of the Chemical Society of Japan* **1982**, 55 (2), 400-406.

[18]. Gomes F., Mendes F.M.T., Souza M., Synthesis of 5-hydroxymethylfurfural from fructose catalyzed by phosphotungstic acid. *Catalysis Today* **2017**, 279, 296-304.

[19]. Ghosh A.K., Moffat J.B., Acidity of heteropoly compounds. *Journal of Catalysis* **1986**, 101 (2), 238-245.

[20]. Baba T., Watanabe H., Ono Y., Generation of acidic sites in metal-salts of heteropolyacids. *Journal of Physical Chemistry* **1983**, 87 (13), 2406-2411.

[21]. Shimizu K., Furukawa H., Kobayashi N. et al., Effects of Brønsted and Lewis acidities on activity and selectivity of heteropolyacid-based catalysts for hydrolysis of cellobiose and cellulose. *Green Chemistry* **2009**, 11 (10), 1627-1632.

[22]. Rana S., Mallick S., Rath D. et al., Characterization of novel Cs and K substituted phosphotungstic acid modified MCM-41 catalyst and its catalytic activity towards acetylation of aromatic alcohols. *Journal of Chemical Sciences* **2012**, 124 (5), 1117-1125.

[23]. Pan X.L., Bao X.H., The effects of confinement inside carbon nanotubes on catalysis. *Accounts of Chemical Research* **2011**, 44 (8), 553-562.

[24]. Sun J.M., Bao X.H., Textural manipulation of mesoporous materials for hosting of metallic nanocatalysts. *Chemistry-A European Journal* **2008**, 14 (25), 7478-7488.

[25]. Wang Z.C., Kim K.-D., Zhou C.F. et al., Influence of support acidity on the performance of size-confined Pt nanoparticles in the chemoselective hydrogenation of acetophenone. *Catalysis Science & Technology* **2015**, 5 (5), 2788-2797.

[26]. Kozhevnikov I.V., Kloetstra K.R., Sinnema A. et al., Study of catalysts comprising

heteropoly acid $\text{H}_3\text{PW}_{12}\text{O}_{40}$ supported on MCM-41 molecular sieve and amorphous silica. *Journal of Molecular Catalysis A-Chemical* **1996**, *114* (1-3), 287-298.

[27]. Guo Y.H., Li K.X., Yu X.D. et al., Mesoporous $\text{H}_3\text{PW}_{12}\text{O}_{40}$ -silica composite: Efficient and reusable solid acid catalyst for the synthesis of diphenolic acid from levulinic acid. *Applied Catalysis B-Environmental* **2008**, *81* (3-4), 182-191.

[28]. Wang Z.H., Yang Z.L., Wu S.M. et al., A study on the production of isophthalic acid from m-xylene under the catalysis of cobalt and $\text{H}_3\text{PW}_{12}\text{O}_{40}$ /carbon modified by HNO_3 solution. *International Journal of Chemical Reactor Engineering* **2015**, *13* (3), 413-425.

[29]. An S., Song D.Y., Sun Y.N. et al., Design of highly ordered mesoporous Nb_2O_5 -based hybrid catalysts bifunctionalized by the keggin-type heteropoly acid and phenyl-bridged organosilica moieties for the synthesis of methyl levulinate. *Microporous and Mesoporous Materials* **2016**, *226*, 396-405.

[30]. Dias A.S., Pillinger M., Valente A.A., Mesoporous silica-supported 12-tungstophosphoric acid catalysts for the liquid phase dehydration of D-xylose. *Microporous and Mesoporous Materials* **2006**, *94* (1-3), 214-225.

[31]. Wang Z.C., Jiang Y.J., Rachwalik R. et al., One-step room-temperature synthesis of Al MCM-41 materials for the catalytic conversion of phenylglyoxal to ethylmandelate. *ChemCatChem* **2013**, *5* (12), 3889-3896.

[32]. Liu A.Q., Zhang Z.H., Fang Z.F. et al., Synthesis of 5-ethoxymethylfurfural from 5-hydroxymethylfurfural and fructose in ethanol catalyzed by MCM-41 supported phosphotungstic acid. *Journal of Industrial and Engineering Chemistry* **2014**, *20* (4), 1977-1984.

[33]. Sheng X.L., Kong J., Zhou Y.M. et al., Direct synthesis, characterization and catalytic application of SBA-15 mesoporous silica with heteropolyacid incorporated into their framework. *Microporous and Mesoporous Materials* **2014**, *187*, 7-13.

[34]. Emeis C.A., Determination of integrated molar extinction coefficients for infrared-absorption bands of pyridine adsorbed on solid acid catalysts. *Journal of Catalysis* **1993**, *141* (2), 347-354.

[35]. De S., Dutta S., Saha B., Microwave assisted conversion of carbohydrates and biopolymers to 5-hydroxymethylfurfural with aluminium chloride catalyst in water. *Green Chemistry* **2011**, *13* (10), 2859-2868.

[36]. Brandt A., Gräsvik J., Hallett J.P. and Welton T., Deconstruction of lignocellulosic biomass with ionic liquids. *Green Chemistry* **2013**, *15* (3), 550-583.

[37]. Li L., Stroobants C., Lin K.F. et al., Selective conversion of trioses to lactates over Lewis acid heterogeneous catalysts. *Green Chemistry* **2011**, *13* (5), 1175-1181.

[38]. Zhao P.P., Zhang Y.Y., Wang Y. et al., Conversion of glucose into 5-hydroxymethylfurfural catalyzed by acid-base bifunctional heteropolyacid-based ionic hybrids. *Green Chemistry* **2018**, *20* (7), 1551-1559.

[39]. Penzien J., Haeßner C., Jentys A. et al., Heterogeneous catalysts for hydroamination reactions: Structure-activity relationship. *Journal of Catalysis* **2004**, *221* (2), 302-312.

[40]. Xia Q.H., Wee C.H., Hidajat K. et al., $\text{H}_3\text{PW}_{12}\text{O}_{40}$ -supported MCM-41 acid catalyst for the gas-phase synthesis of MTBE. In *Studies in surface science and catalysis* **2004**, *154*, 2915-2922.

[41]. Hemmann F., Agirrezabal-Telleria I., Jaeger C. et al., Quantification of acidic sites of nanoscopic hydroxylated magnesium fluorides by FTIR and ^{15}N MAS NMR

- spectroscopy. *RSC Advances* **2015**, 5 (109), 89659-89668.
- [42]. Rajagopal S., Marzari J.A., Miranda R., Silica-alumina-supported Mo oxide catalysts - genesis and demise of Brønsted-Lewis acidity. *Journal of Catalysis* **1995**, 151 (1), 192-203.
- [43]. Benaliouche F., Boucheffa Y., Ayrault P. et al., NH₃-TPD and FTIR spectroscopy of pyridine adsorption studies for characterization of Ag- and Cu-exchanged x zeolites. *Microporous and Mesoporous Materials* **2008**, 111 (1-3), 80-88.
- [44]. Kung M.C., Kung H.H., IR studies of NH₃, pyridine, CO, and NO adsorbed on transition metal oxides. **1985**, 27 (3), 425-460.
- [45]. Srinivas D., Srivastava R., Ratnasamy P., Transesterifications over titanasilicate molecular sieves. *Catalysis Today* **2004**, 96 (3), 127-133.
- [46]. Barzetti T., Selli E., Moscotti D. et al., Pyridine and ammonia as probes for FTIR analysis of solid acid catalysts. *Journal of the Chemical Society, Faraday Transactions* **1996**, 92 (8), 1401.
- [47]. Dutta A., Patra A.K., Dutta S. et al., Hierarchically porous titanium phosphate nanoparticles: An efficient solid acid catalyst for microwave assisted conversion of biomass and carbohydrates into 5-hydroxymethylfurfural. *Journal of Materials Chemistry* **2012**, 22 (28), 14094-14100.
- [48]. O'Neill R., Ahmad M.N., Vanoye L. et al., Kinetics of aqueous phase dehydration of xylose into furfural catalyzed by ZSM-5 zeolite. *Industrial & Engineering Chemistry Research* **2009**, 48 (9), 4300-4306.
- [49]. Jia S.Y., He X.J., Ma J. et al., Efficient synthesis of 5-hydroxymethylfurfural from mannose with a reusable MCM-41-supported tin catalyst. *Catalysis Science & Technology* **2018**, 8 (21), 5526-5534.
- [50]. Pilath H.M., Nimlos M.R., Mittal A. et al., Glucose reversion reaction kinetics. *Journal of Agricultural and Food Chemistry* **2010**, 58 (10), 6131-6140.
- [51]. Patil S.K.R., Heltzel J., Lund C.R.F., Comparison of structural features of humins formed catalytically from glucose, fructose, and 5-hydroxymethylfurfuraldehyde. *Energy & Fuels* **2012**, 26 (8), 5281-5293.
- [52]. Horvat J., Klaic B., Metelko B. et al., Mechanism of levulinic acid formation in acid-catalyzed hydrolysis of 2-hydroxymethylfuran and 5-hydroxymethylfuran-2-carbaldehyde. *Croatica Chemica Acta* **1986**, 59 (2), 429-438.
- [53]. Ordonsky V., Sushkevich V.L., Schouten J.C. et al., Glucose dehydration to 5-hydroxymethylfurfural over phosphate catalysts. *Journal of Catalysis* **2013**, 300, 37-46.
- [54]. Mazzotta M.G., Gupta D., Saha B. et al., Efficient solid acid catalyst containing Lewis and Brønsted acid sites for the production of furfurals. *ChemSuschem* **2014**, 7 (8), 2342-2350.
- [55]. Liu J., Li H., Liu Y.-C. et al., Catalytic conversion of glucose to 5-hydroxymethylfurfural over nano-sized mesoporous Al₂O₃-B₂O₃ solid acids. *Catalysis Communications* **2015**, 62, 19-23.
- [56]. Okano T., Qiao K., Bao Q. et al., Dehydration of fructose to 5-hydroxymethylfurfural (HMF) in an aqueous acetonitrile biphasic system in the presence of acidic ionic liquids. *Applied Catalysis A: General* **2013**, 451, 1-5.
- [57]. Qi X., Watanabe M., Aida T.M. et al., Sulfated zirconia as a solid acid catalyst for the dehydration of fructose to 5-hydroxymethylfurfural. *Catalysis Communications*

2009, *10* (13), 1771-1775.

[58]. Perez G.P., Mukherjee A., Dumont M.J., Insights into HMF catalysis. *Journal of Industrial and Engineering Chemistry* **2019**, *70*, 1-34.

[59]. Rasrendra C.B., Soetedjo J.N.M., Makertihartha I.G.B.N. et al., The catalytic conversion of D-glucose to 5-hydroxymethylfurfural in dmso using metal salts. *Topics in Catalysis* **2012**, *55* (7), 543-549.

[60]. Xu H.M., Miao Z.C., Zhao H.H. et al., Dehydration of fructose into 5-hydroxymethylfurfural by high stable ordered mesoporous zirconium phosphate. *Fuel* **2015**, *145*, 234-240.

Chapter 4. Correlation between acidity and catalytic performance of mesoporous zirconium oxophosphate in phenylglyoxal conversion

4.1 Introduction

The synthesis of α -hydroxycarboxylic acids (such as lactic acid and mandelic acid) and their derivatives from biomass resources is a process of great appeal in the areas of renewable biomass conversion and green chemistry. These versatile derivatives are considered as key platform molecules in the synthesis of pharmaceuticals and fine chemicals.¹⁻³ Rapid progress in developing efficient synthesis methods for these compounds, such as bio-fermentation,⁴ and chemical routes,³ has been witnessed over recent years. The direct conversion of α -keto aldehydes to α -hydroxycarboxylic acids and their derivatives via chemical routes has attracted much interest recently. It is generally known in carbohydrate chemistry that these compounds could be generated via base-catalyzed isomerization reactions. However, it requires high reaction temperatures of 250-300 °C and provides a moderate yield of α -hydroxycarboxylic acid.⁵ On the contrary, by using Lewis acids, α -hydroxycarboxylic acids and their derivatives can be produced under milder conditions via an intramolecular Cannizzaro reaction^{6, 7} or a Meerwein-Ponndorf-Verley-Oppenauer (MPVO) redox reaction.^{8, 9} Recently, various Lewis acid heterogeneous catalysts, such as zeolites^{8, 10} and mesoporous materials,^{9, 11-14} have been applied widely in this reaction due to the advantages of easy separation and recycling, aiming a greener chemical process. Pescarmona et al.¹⁰ reported the selectivity towards the desired ethyl lactate and

mandelate on zeolite USY CBV 600 catalyst was due to the presence of Lewis acid sites (LAS) in the form of extra-framework aluminum species, which catalyze the 1,2-hydride shift leading to the rearrangement. Moreover, it was reported that the Brønsted acid sites (BAS) on silica-alumina catalysts showed a beneficial effect on the reaction, wherein mandelates were produced with high yield when the catalyst exhibited only Brønsted acidity.¹³ Furthermore, compared to zirconium dioxide (ZrO_2), only possessing LAS, silica–zirconia materials with both BAS and LAS showed higher performance in PG conversion.¹⁴ Therefore, the individual role of BAS and LAS in this reaction remains a matter of debate. LAS and BAS may collaborate to promote the reaction process.

Among numerous solid acid catalysts, ordered mesoporous materials have attracted extensive attention because of their high thermal stability, uniform pore sizes as well as large pore volumes.^{15,16} Especially, ordered mesoporous zirconium oxophosphate (ZrPO), possessing both LAS and BAS, has been applied in many acid-catalyzed reactions.^{17, 18} The Lewis acidity of this material originates zirconium atoms and Brønsted acidity from the bridging or terminal hydroxyl groups of P-OH. Since each component bears one type of acid, the population of LAS and BAS can be tuned by varying the ratio of P/Zr and the preparation conditions.

To date, the synthesis of mesoporous ZrPO were reported mostly via a two-step procedure with cationic surfactants as structure-directing agents and post-treatment with phosphoric source.¹⁹⁻²¹ By changing the times of post-treatment, P/Zr ratios could be adjusted.²² In addition, by using different kinds of cationic surfactants, the structure of mesoporous ZrPO such as hexagonal and cubic symmetries could also be designed.^{23,}²⁴ However, the mesoporous ZrPO obtained from this method has a small pore size and the P/Zr ratios cannot be controlled accurately. Recently, the synthesis of mesoporous

ZrPO via a facile one-pot evaporation-induced self-assembly (EISA) strategy by employing nonionic surfactants as structure-directing agents was explored.^{17, 25} It is reported that the mesoporous ZrPO prepared using EISA method shows large specific surface area, big volume, uniform pore size distribution and high thermal stability.²³

Besides, the pre-treatment procedure is also critical to control the density of BAS and LAS on solid-acid catalysts.²⁶ The main objective of pre-treatment is to remove water absorbed on the catalyst surface due to the detrimental effects induced by water on acid sites.²⁰ However, some authors suggested that moderate water content is necessary for the catalyst to reach its maximum activity.^{26, 28} It was reported that a decrease in water content resulted in a decrease in Brønsted acidity with a concurrent increase in Lewis acidity. The most active catalyst possesses a moderate amount of Brønsted acidity. Therefore, a systematic investigation of the effect of water absorbed on the active catalytic sites is of great interest.

Herein, we fabricated ZrPO catalysts and manipulated the acidity by varying ratios of P/Zr from 0 to 1.25 and calcination temperatures from 300 to 900 °C. The catalytic performance in phenylglyoxal (PG) conversion to ethyl mandelate (EM) as a model reaction was evaluated. A correlation between the acidity of ZrPO and its catalytic activity is established. A reaction mechanism is therefore proposed. We also combined reaction kinetics studies of the PG reaction and water desorption/adsorption experiments to examine the effect of water on the catalytic activity, further gaining a deep insight into the role of active catalytic sites on the catalytic performance.

4.2 Experimental section

4.2.1 Chemicals

Triblock copolymer poly (ethylene glycol)-*b*-(propylene glycol)-*b*-(ethylene glycol) (Pluronic F127, the average molecular weight of 12600, Sigma Aldrich) was used as a structure-directing agent. Zirconyl chloride octahydrate ($\text{ZrOCl}_2 \cdot 8\text{H}_2\text{O}$, 99%, Sigma-Aldrich) and trimethyl phosphate ($\text{PO}(\text{OCH}_3)_3$, 99%, Sigma-Aldrich) were used as a zirconium and phosphorus precursors in all experiments. Phenylglyoxal hydrate ($\text{C}_6\text{H}_5\text{COCHO} \cdot \text{H}_2\text{O}$, 97%), as a substrate, was purchased from Sigma-Aldrich. Ethyl mandelate ($\text{C}_6\text{H}_5\text{CH}(\text{OH})\text{CO}_2\text{C}_2\text{H}_5$, 97%), as a standard sample, was purchased from Thermo Fisher. All chemicals were used without further purification.

4.2.2 Catalyst synthesis

A series of ordered mesoporous ZrPO catalysts were prepared by a one-pot evaporation-induced self-assembly (EISA) method as reported by Miao et al.¹⁷ In a typical procedure, 1.2 g of F127 was first suspended in 15 mL of anhydrous ethanol at room temperature. A nominal molar ratio of $\text{ZrOCl}_2 \cdot 8\text{H}_2\text{O}$ and $\text{PO}(\text{OCH}_3)_3$ was then added to the above suspension under vigorous stirring and kept stirring overnight. The mixture was placed inside the oven at 60 °C for 48 h, then at 100 °C for 24 h. Finally, the obtained colorless and transparent xerogel was calcined in static air at a given temperature for 5 h. The catalysts were denoted as ZrPO-*x*-*y*, where *x* refers to the molar ratio of P/Zr (0, 0.25, 0.50, 0.75, 1.00 and 1.25) and *y* to the calcination temperature (300, 400, 500, 600, 700, 800 and 900°C).

4.2.3 Characterizations

Powder X-ray diffraction (XRD) patterns were recorded on a PANalytical X'Pert PRO Multipurpose Diffractometer at 40 kV voltage and 20 mA current via Cu K α ($\lambda=1.5406$ Å). Nitrogen adsorption/desorption isotherms were recorded on a TriStar II 3020 Autosorb-iQ analyzer at -196 °C. Before the measurements, the samples were degassed at 120 °C under vacuum overnight. High resolution scanning electron microscopy (HRSEM) were operated on Zeiss's ULTRA Plus equipped with Schottky field-emission source for high resolution and beam current at 15 kV and energy dispersive X-Ray spectroscopy (EDS) on Oxford Instruments AZtec integrated EDS system with X-Max 20mm² silicon drift EDS detector. Transmission electron microscopy (TEM) images were recorded on a Philips CM10 TEM operated at a voltage of 100 kV. Fourier transform infrared (FT-IR) spectra were recorded between 550 to 4000 cm⁻¹ on a Nicolet 6700 spectrometer (Thermo Fisher Scientific).

Temperature programmed desorption of ammonia (NH₃-TPD) was carried out on a Quantachrome instrument with a thermal conductivity detector (TCD). Before the TPD measurements, approximately 100 mg of the sample was pre-treated at 300 °C for 2 h under helium (He, 50 mL/min) and subsequently cooled to 100 °C. The sample was then saturated with NH₃ (5 % NH₃-He for 1 h at 50 mL/min). Physisorbed NH₃ molecules were removed by purging the sample with He (50 mL/min) at 100 °C for 1 h; then the sample was heated to 800 °C at a heating rate of 10 °C/min.

Single-pulse excitation magic-angle spinning nuclear magnetic resonance (SPE MAS NMR) spectra were recorded on a Bruker DRX300 spectrometer at resonance frequencies of 300 MHz and 121.5 MHz for ¹H and ³¹P, respectively. Typically, free-induction-decay (FID) signals were accumulated using a single pulse sequence with a

recycle delay of 10 s, 4 mm zirconium oxide rotors and a sample spinning frequency of 14 kHz. The number of scans per acquisition was set at 32 and 128 times for ^1H and ^{31}P , respectively. The ^{31}P chemical shift scale was referenced externally using a solution of trimethyl phosphate in CDCl_3 at $\delta = 3.0$ ppm.²² Prior to NMR measurements, samples were dehydrated at 300 °C under evacuation conditions overnight. The dehydrated catalysts (approximately 100 mg) were then mixed with trimethyl phosphine oxide (TMPO, approximately 10 mg) in a glovebox inside a 4-mm zirconium oxide rotor, which was sealed with an O-ring-containing Macor-cap. The sealed sample rotor was finally subjected to thermal treatment at 160 °C for 2 h. The total acidity was determined according to the NH_3 -TPD profiles; The BAS and LAS were obtained from the ^{31}P MAS NMR results. The density of BAS, strong LAS and weak LAS were calculated according to the peak area of signals at $\delta_{31\text{P}} = 62.0, 42.0$ and 38.8 ppm, respectively.

4.2.4 Catalytic activity testing

In a typical catalytic test of PG conversion, 50 mg catalyst was suspended in 1.25 mL of PG ethanol solution (0.4 M) and transferred into a glass vessel. Then the glass vessel was closed tightly and placed into an oil bath at 90 °C. The mixture was allowed to react for 6 h under continuous magnetic stirring. For the kinetic experiments, samples were taken at intervals over 6 h. After the reaction, the reactants and products were separated and analyzed by a gas chromatograph (Shimadzu GC2014) equipped with a capillary column (Rtx-5 column, $30\text{ m} \times 0.25\text{ mm} \times 3\text{ }\mu\text{m}$) and flame ionization detector (FID). The main products were identified from known standards and by a gas chromatography-mass spectrometry (Shimadzu GCMS-QP2010 Ultra, Rtx-5 MS column, $30\text{ m} \times 0.25\text{ mm} \times 0.25\text{ }\mu\text{m}$).

To investigate the reusability of the material, catalysts were recycled under the same reaction conditions. The catalyst was recovered by centrifugal separation, washed with 5 mL ethanol three times and dried at 80 °C for 2 h. Then, it was directly used for the recycling experiment. It is worth noting that a little amount of catalysts could be lost during the recycling process. To overcome this problem, we duplicated the first run seven times, ensuring that the total amount of collected catalyst was enough for a duplicated second run for six runs, and so on.

4.2.5 Dehydration and rehydration experiments

Experiments were performed to study the effect of water content on the catalytic activity. The as-synthesized catalysts were pre-treated at a given temperature (25, 100, 150, 250, 350 and 450 °C) for 2 h under N₂ (50 mL/min). The pre-treated samples were then cooled to room temperature and transferred to a reactor in a glove box (Ar, O₂ pressure <0.3 ppm; moisture<0.3 ppm) ready for the kinetics experiments. The rehydration experiments were conducted as reported by Kobe et al.²¹ 50 mg catalyst was firstly pre-treated at 500 °C as described above. After being cooled to room temperature, the flask was evacuated using a vacuum manifold, and water vapor was dosed onto the samples (2, 15, 23, 61 and 176 μmol). After equilibration for 30 minutes, the rehydrated sample was transferred to a reactor in a glove box (Ar, O₂ pressure < 0.3 ppm; moisture < 0.3 ppm) for the subsequent kinetics experiments.

4.3 Results and discussion

4.3.1 Textural and morphological properties

The low-angle XRD patterns (Figure 4.1a and b) show that all the samples displayed an intense diffraction peak at around 0.69-0.85° and a poorly resolved diffraction peak

at around 1.2° , which are indexed as (100) and (110) reflections of $p6mm$ two-dimensional hexagonal structure, respectively.³⁰ These diffraction peaks indicate the existence of a mesoporous structure and correspond to the maximum nearest-neighbor pore-center to the pore-center distance of 11.2 nm using Bragg's law.³¹ The high-angle XRD patterns (Figure 4.2a and b) show that the nanocrystalline nature of ZrO_2 was observed in $ZrPO-0-500$. The diffractions at $2\theta = 30.2^\circ, 35.0^\circ, 50.3^\circ, 60.2^\circ, 62.8^\circ$ and 74.8° are ascribed to the tetragonal phase of ZrO_2 (t- ZrO_2).³² The weak diffraction peaks at $2\theta = 24.1^\circ$ and 28.3° correspond to the monoclinic phase of ZrO_2 (m- ZrO_2).³³ The incorporation of P disturbed the ZrO_2 crystal structure with all samples exhibited two very broad peaks in the 2θ range of $20-40^\circ$ and $40-65^\circ$.^{17, 34} Notably, the sample calcined at 900°C showed several small and sharp peaks at around $2\theta = 30^\circ, 50^\circ$ and 60° (Figure 4.2b), suggesting that crystalline frameworks are observed upon high calcination temperature. This may be because the ordered mesostructured start to collapse when $ZrPO$ was calcined at 900°C even if the mesoporous still exists (as shown in Figure 4.1b).

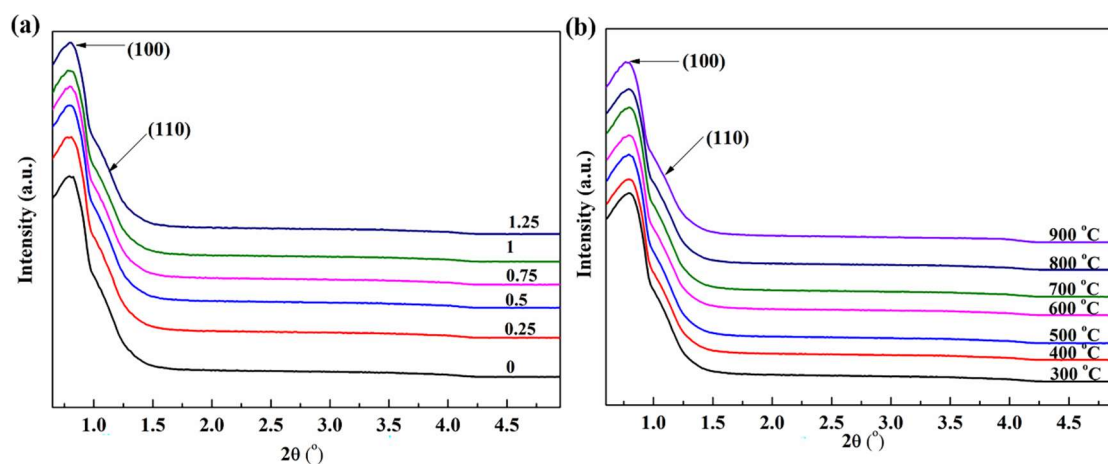


Figure 4.1 Low-angle XRD patterns of $ZrPO-x-500$ with different P/Zr ratios (a) and $ZrPO-0.75-y$ calcined at different temperatures (b).

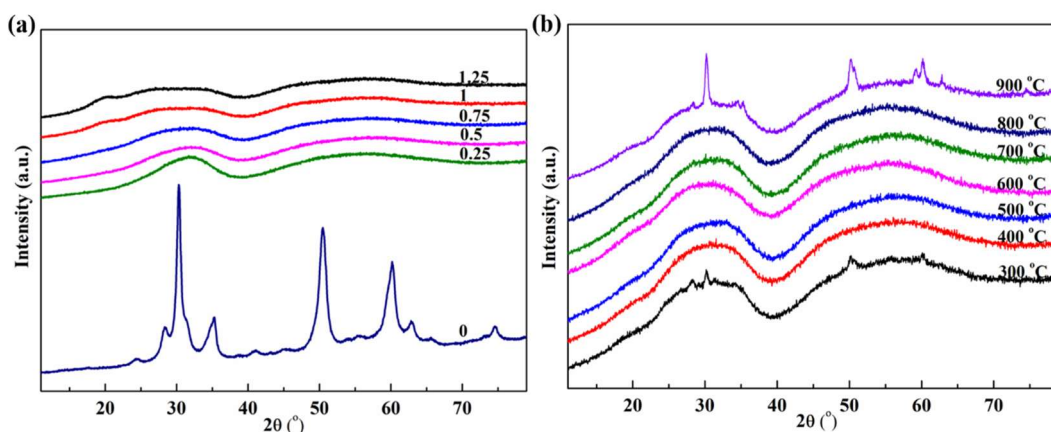


Figure 4.2 High-angle XRD patterns of ZrPO-x-500 with different P/Zr ratios (a) and ZrPO-0.75-y calcined at different temperatures (b).

The textural properties of the ZrPO were characterized by N₂ adsorption-desorption measurement. The pronounced desorption hysteresis, the steep condensation steps and BJH pore size distribution of ZrPO curves (Figure 4.3) suggest the existence of a mesoporous structure in these materials.³⁵ The hysteresis of ZrO₂ (Figure 4.3a) is a typical H4-type hysteresis loop, revealing the presence of narrow slit-like pores. Upon addition of P, the isotherms for all samples are in between the H1-shaped and H2-shaped hysteresis loops, indicating the occurrence of well-defined capillary condensation. This shape of isotherm also reflects the presence of uniform mesopores.¹⁸ BET specific surface area (SSA), average pore diameter, and pore volume for ZrPO samples are summarized in Table 4.1. With an increase in P/Zr from 0 to 0.75, the SSA became larger (from 50.7 to 151.8 m²/g). Similar trends were also observed in the changes in average pore size (from 3.7 to 4.8 nm) and pore volume (from 0.08 to 0.20 cm³/g). Further increasing the P/Zr up to 1, the average pore size and pore volume further increased, while the SSA decreased. A dramatic decrease in the pore volume and SSA was observed after adding more P into the structure (P/Zr = 1.25). However, with the

increase in calcination temperature from 300 to 800 °C, the average pore size of the samples has nearly no significant change (between 4.6 and 4.8 nm). On the other hand, the SSA and pore volume depend on the calcination temperature. Notably, the sample calcined at 300 °C showed high SSA (130.8 m²/g), which could be due to the partial crystalline structure as shown in Figure 4.2b.

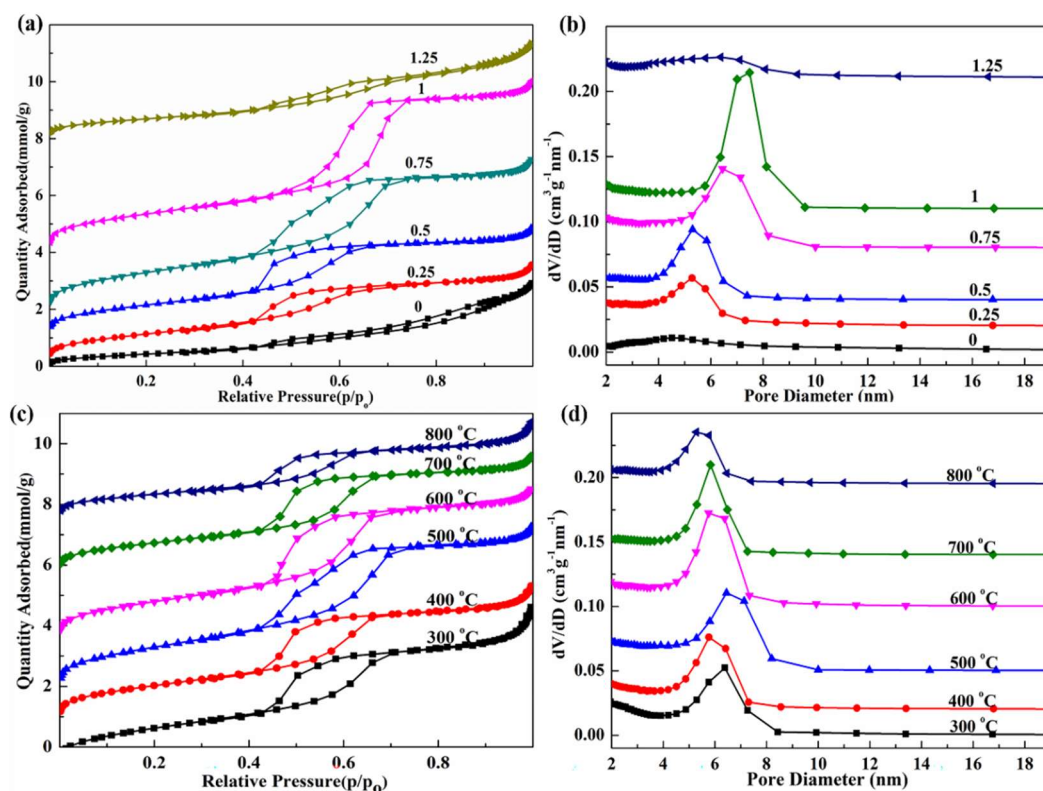


Figure 4.3 N₂ adsorption-desorption isotherms and BJH pore size distributions of ZrPO-x-500 with different P/Zr ratios (a and b) and ZrPO-0.75-y calcined at different temperatures (c and d).

With the increase in calcination temperature from 400 to 500 °C, the SSA and pore volume showed an increasing trend. They reached maximum values at the calcination temperature of 500 °C. Continuing to increase the calcination temperature to 800 °C, the specific surface area decreased significantly. This indicating the mesoporous structure suffered some damage during the increasing of treating

temperature from 500 to 800 °C. When the temperature is at 900 °C, no the pronounced desorption hysteresis and narrow pore size distribution could be observed, showing the severe damage of the mesostructure on ZrPO-0.75-900 (not shown here), in good agreement with the results reported by Miao¹⁷ and Das.¹⁸

Table 4.1 Textural properties of different ZrPO materials.

Samples	Specific surface area (m ² /g)	average Pore size (nm)	Pore volume (cm ³ /g)
ZrPO-0-500	50.7	3.7	0.08
ZrPO-0.25-500	107.4	4.3	0.12
ZrPO-0.50-500	116.8	4.4	0.14
ZrPO-0.75-500	151.8	4.8	0.20
ZrPO-1.0-500	139.8	5.5	0.22
ZrPO-1.25-500	71.7	5.1	0.10
ZrPO-0.75-300	130.8	4.6	0.17
ZrPO-0.75-400	122.0	4.6	0.16
ZrPO-0.75-600	135.9	4.8	0.19
ZrPO-0.75-700	99.4	4.8	0.14
ZrPO-0.75-800	75.4	4.6	0.10

To confirm the morphology of ZrPO, the selected samples were analyzed by HRSEM and TEM (Figure 4.4). For all the samples, the HRSEM images (Figure 4.4a-e) show a typical ordered mesoporous morphology, agreeing well with XRD and BET results. The alignment of cylindrical pores along [110] direction and the ordered hexagonal arrangement of pores along [001] direction was distinctly observed for all samples. The TEM image of a representative sample of ZrPO-0.75-500 sample is shown in Figure

4.4f, which provides further information about the detailed morphology and lattice structure of ZrPO. It also shows two different nearest-neighbor pore-center to pore-center correlation distance of 8.1 and 9.7 nm, respectively, which includes pore dimensions as well as wall thickness.³⁶ To investigate the distribution of metals, the representative sample (ZrPO-0.75-500) was evaluated using the SEM image (Figure 4.4g) coupled with elemental mapping (Figure 4.4h-k). The results demonstrate the uniform distribution of Zr, P and O in the frameworks. The elemental analysis (Figure 4.4l) reveals the exclusive peaks of Zr, P and O elements, implying that all the elements were successfully introduced into the wall of the pores. The atomic ratio of P/Zr (0.80) obtained from the elemental analysis is close to the theoretical value (0.75).

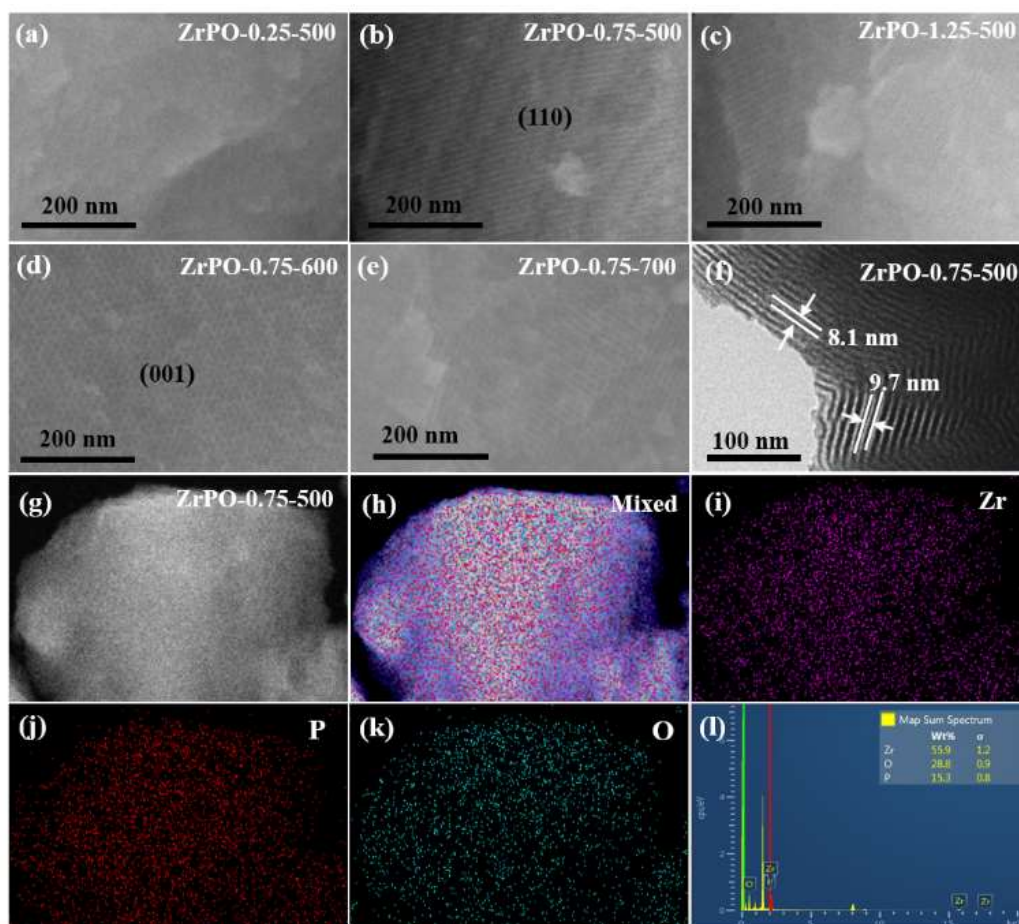


Figure 4.4 (a-e) HRSEM images of ZrPO samples with different P/Zr ratios and calcination temperatures; (f) TEM image of ZrPO-0.75-500; (g-k) SEM-EDS elemental

mapping images and (l) elemental analysis of ZrPO-0.75-500.

4.3.2 Coordination states of phosphate

^{31}P MAS NMR spectroscopy was used to characterize the local environment of phosphorus in the hexagonal ZrPO. As shown in Figure 4.5a, ^{31}P MAS NMR spectrum of the ZrPO-0.25-500 sample showed a low-intensity signal at $\delta_{31\text{P}} = -10.1$ ppm, assigned to tetrahedral phosphates connected with two zirconium atoms $[(\text{OH})_2\text{P}(\text{OZr})_2]$.³⁷ When P/Zr ratio increased to 0.75, the signal of the ^{31}P MAS NMR spectrum was shifted to $\delta_{31\text{P}} = -16.7$ ppm (assigned to $[(\text{OH})\text{P}(\text{OZr})_3]$) and the intensity increased significantly. Further incorporation of phosphorus into the mesoporous structure, signals at the higher magnetic field were observed. The dominant signal at -26.1 ppm indicates the formation of P-O-P bonds due to the condensation of phosphate groups.³⁸ The shoulder at approximately -20.2 ppm indicates that ZrPO-1.25 also contained a large amount of $[\text{P}(\text{OZr})_4]$ bonds.³⁷ It appears that with the increasing of P ratio, more P atoms were incorporated into the ZrO_2 network, facilitating the formation of P-O-Zr bonds. However, excessive P led to the condensation of phosphate groups.³⁹ This indicates that the coordination state of phosphorus atoms could be varied by different preparation conditions, making possible for modulating their acidity. In contrast, calcination temperature had no significant influence on the coordination state of phosphorus (Figure 4.5b). All ZrPO-0.75 samples calcined from 500 to 700 °C showed a dominant signal at around $\delta_{31\text{P}} = -16.7$ ppm, revealing the presence of large amounts of phosphate with $[(\text{OH})\text{P}(\text{OZr})_3]$ bonds.

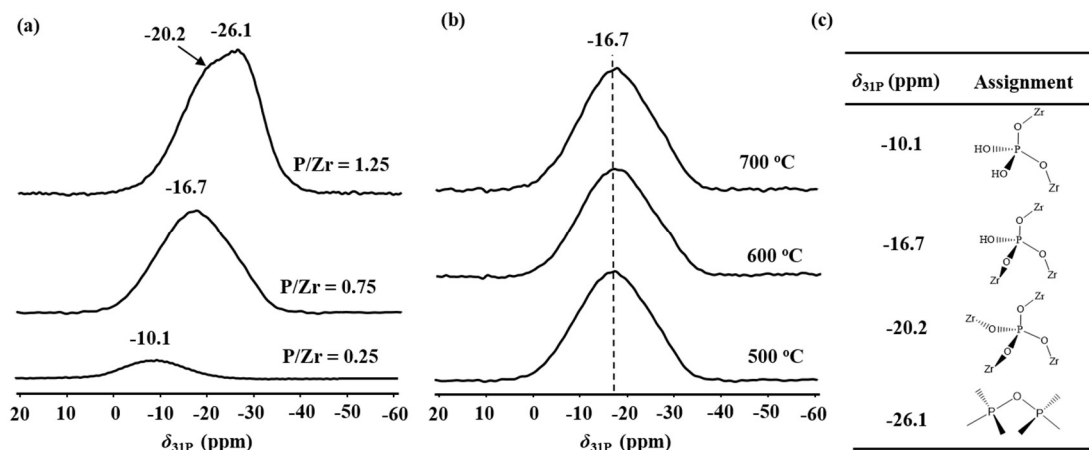


Figure 4.5 ^{31}P MAS NMR spectra of ZrPO-x-500 with different P/Zr ratios (a) and ZrPO-0.75-y calcined at different temperatures (b); Signal assignment (c).

4.3.3 Acidic properties

NH_3 -TPD was carried out to evaluate the acidic properties of the selected ZrPO samples (Figure 4.6). The peak area of the desorbed NH_3 corresponds to the number of acid sites whereas the position of the peak indicates the strength of the acid sites.⁴⁰ For all the samples, the desorption of NH_3 commenced at approximately 200 °C and ended over 750 °C, assigned to the presence of weak, medium and strong acid sites.^{33, 40} The desorbed NH_3 molecules are derived from those bound to BAS from bridging or terminal hydroxyl (O-H) groups and LAS from the metal (Zr) sites.⁴¹ As shown in Figure 4.6a, it is notable that ZrPO-0.25-500 displayed significant desorption of NH_3 at higher temperatures from 650 to 750 °C, which might be due to interface defects and positive charges (Zr^{4+} and/or Zr^{2+}) induced by oxygen vacancies. Such defects were also observed on Si doping ZrO_2 .⁴² An increase in the P/Zr ratio led to a decrease of Zr^{4+} and/or Zr^{2+} , consequently, reducing the density of strong acid sites. However, the intensity of the peak at around 280 °C, ascribed to the weak acid sites, increased with the increased P/Zr ratio. It could be understood that the increase in P content was

accompanied by an increase in surface P-OH sites.^{18, 34} However, it is worth mentioning that the density of medium acid sites (400 °C to 650 °C) was decreased when the ratio of P/Zr increases from 0.25 to 0.75. It indicates that a high P content led to a decrease in the number of medium acid sites. Further addition of phosphate content decreased the number of medium acid sites but enhanced their strength. It could be explained that the formation of P-O-P bonds on ZrPO-1.25 (as discussed in the section of 3.2.) leads to decreasing the electron density on the nearest-neighbor Zr atoms significantly due to the high electro-negativity of P compared with Zr.⁴³ A lower electron density of the Zr core increases the ability to accept electrons, improving the acidic strength. As shown in Figure 4.6b, the increase in the calcination temperature from 500 to 600 °C was accompanied by the decrease of NH₃ desorption amounts on weak, medium and strong acid sites. This may be attributed to the fact that a higher calcination temperature led to the polymerization of the surface P-OH groups and Zr cations. It is also noted that a gradual shift of the NH₃-desorption peak from 510 °C to 570 °C was observed, suggesting an increase in acidic strength (medium acid sites) at elevated calcination temperature. Further increasing the calcination temperature to 700 °C, strong acid sites with desorption peak at around 650 °C was shown. It indicates that a higher calcination temperature may lead to the bond breaking of Zr-O-P, resulting in the formation of strong acid sites. The phenomenon is similar to that observed for sulfated hydrous zirconia (SZ), wherein compared with uncalcined SZ, strong LAS was formed during the calcination process and increased by a high calcination temperature.⁴⁴

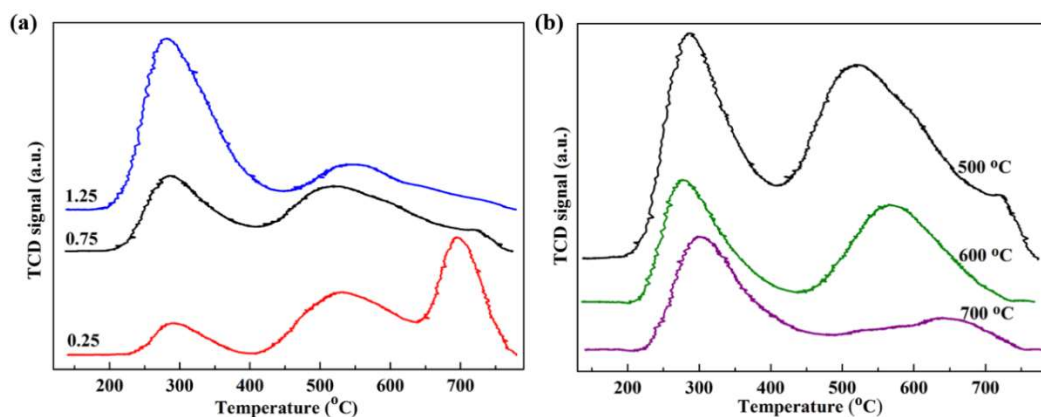


Figure 4.6 NH₃-TPD profiles of the ZrPO-x-500 with different P/Zr ratios (a) and ZrPO-0.75-y calcined at different temperatures (b).

The acid features were further investigated by ³¹P MAS NMR spectroscopies using TMPO as a probe molecule (Figure 4.7 a).⁴¹ The signal at $\delta_{31\text{P}} = 62.0$ ppm (Figure 7a and b), is typical of TMPO adsorbed on strong BAS.^{45, 46} The signals at $\delta_{31\text{P}} = 42.0$ and 38.8 ppm are due to TMPO adsorbed on two types of LAS with different acid strengths.^{45, 47-49} The previous studies revealed that the ³¹P chemical shift of adsorbed TMPO moved down-field with increased acid strength.^{41, 48} Thus, the signal at $\delta_{31\text{P}} = 42.0$ ppm corresponds to strong LAS, and 38.8 ppm to weak LAS. In addition, physisorbed TMPO ($\delta_{31\text{P}} = 46$ ppm)³⁹ and excessive crystalline TMPO ($\delta_{31\text{P}} = 41$ ppm)⁵⁰ were not observed for all the samples. For ZrPO-0.25-500, no resonance at 38.8 ppm assigned to TMPO interacting with weak LAS was visible in the ³¹P MAS NMR spectrum. This is probably due to the signal of weak LAS was covered by the signal of strong LAS due to a large number of Zr cations, which corresponds well with the NH₃-TPD results. The relative intensity of these signals at $\delta_{31\text{P}} = 62.0$ and 38.8 ppm increased with increasing P/Zr ratio from 0.25 to 1.25 (Figure 4.7a), implying the corresponding increase in the concentration of strong BAS and weak LAS on ZrPO materials. In contrast, the intensities of these two signals on ZrPO-0.75-y decreased at elevated

calcined temperatures (Figure 4.7b). However, it is notable that the signal at $\delta_{31\text{P}} = 42.0$ ppm ascribed to strong LAS became dominant on ZrPO calcined at a higher temperature (700 °C), agreeing well with the NH_3 -TPD results.

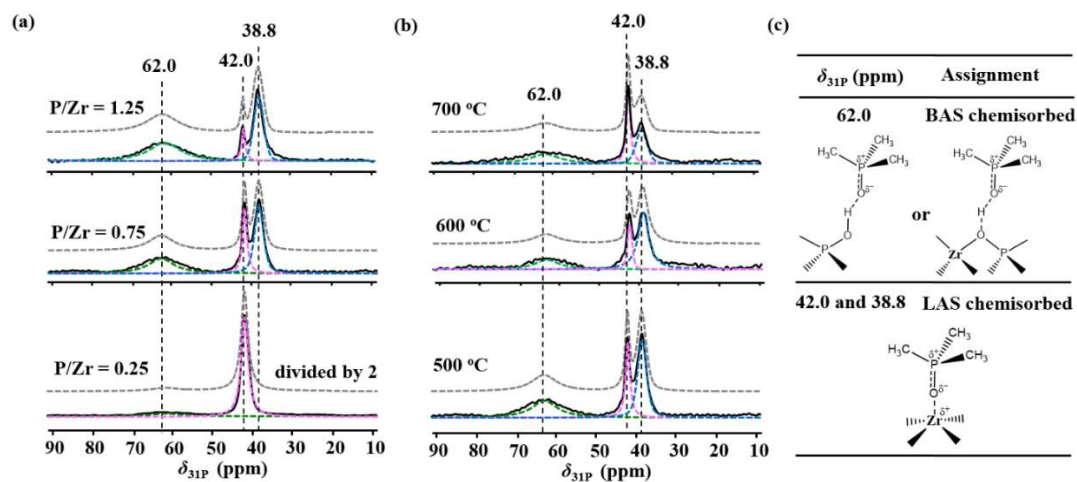


Figure 4.7 ^{31}P MAS NMR spectra of ZrPO-x-500 with different P/Zr ratios (a); ZrPO-0.75-y calcined at different temperatures (b) using TMPO as the probe molecule; Signal assignment (c). Experimental NMR spectra are shown as black lines (lower traces), while the simulated spectra are shown as dashed lines. The dashed lines indicate the main resonance positions with corresponding Gaussian curves.

Quantitative evaluation of acid sites on the ZrPO catalysts by ^{31}P MAS NMR combined with the NH_3 -TPD profiles provides the densities of LAS, BAS and total acid sites, summarized in Table 4.2. This result suggests that the total acidity for the mesoporous ZrPO increased gradually with the increased P/Zr ratio, which agrees well with the reported results.¹⁸ It could be attributed to the increase in surface area and the enhanced concentration of P-OH and P-O-Zr groups in the frameworks.^{18, 51, 52} On the other hand, the total acid sites decrease at higher calcination temperatures. Likewise, this may be due to the decrease in surface area and the formation of polyphosphate.⁵² The LAS density (15.9 $\mu\text{mol/g}$) is 5.5-times-higher than that of BAS in the ZrPO-0.25-500 sample. When P loadings increased to 1.25, the density of LAS decreased along with

an increase in BAS. Almost equal LAS and BAS were achieved on ZrPO-1.25-500. However, both LAS and BAS decreased with the increase in the calcination temperature.

Table 4.2 The acidity and the catalytic performance of ZrPO catalysts on PG conversion^[a].

Catalysts	BAS ($\mu\text{mol/g}$)	LAS ($\mu\text{mol/g}$)			Total acid sites ($\mu\text{mol/g}$)	LAS/ BAS	C_{PG} (%)	Y_{EM} (%)
		Strong	Weak	Total				
ZrPO-0.25-500	2.9	15.9	0	15.9	18.8	5.5	61.8	42.9
ZrPO-0.75-500	6.9	5.2	9.1	14.3	21.2	2.1	73.0	56.6
ZrPO-1.25-500	11.5	2.4	9.4	11.8	23.3	1.0	47.7	27.2
ZrPO-0.75-600	2.8	1.5	4.9	6.4	9.2	2.3	54.3	47.6
ZrPO-0.75-700	2.1	2.1	2.7	4.8	6.9	2.3	55.6	50.5

^[a]Conversion of PG (0.4M) in ethanol (1.25 mL) using 50 mg catalyst at 90 °C for 6 h in a batch reactor. C_{PG} = conversion of PG; Y_{EM} = yield of EM. The total acidity was determined according to the NH_3 -TPD profiles; The BAS and LAS were obtained from the ^{31}P MAS NMR results. The density of BAS, strong LAS and weak LAS were calculated according to the peak area of signals at $\delta_{31\text{P}} = 62.0, 42.0$ and 38.8 ppm, respectively.

Based on the characterization results discussed above, our materials, ZrPO catalysts, contained a tetrahedral zirconium framework, which is connected to P atoms through the Zr-O-P bonds. There are different coordination states of phosphorus bonding to zirconia (two, three, or four) or phosphorus atoms on ZrPO with different P/Zr ratios. The LAS of ZrPO catalysts is originated from the Zr atoms and the BAS from the bridging or terminal O-H groups. It is inferred that the combination of the P-OH protons with adjacent LAS is responsible for the strong BAS. When some P species are incorporated into the ZrO_2 network, the negatively charged defect sites generated by

electronegativity difference between Zr and P component⁵³ can be counter-balanced by the presence of a proton, which also affords the BAS.⁵⁴ Upon calcination at high temperature, the P-OH groups acting as strong BAS are favorable to be converted into polyphosphates, resulting in a decrease of strong BAS. With further calcination at a higher temperature, the BAS is further decreased, while strong LAS may be formed due to the bond breaking of Zr-O-P.

4.3.4 Catalytic performance in PG conversion to EM

The catalytic performance of mesoporous ZrPO catalysts was evaluated using PG conversion to EM as a model reaction. As shown in Figure 4.8, the PG conversion and EM yield were plotted as a function of the reaction time. The catalytic performance of ZrPO strongly depended on the P content (Figure 4.8a and b). The pure ZrO₂ catalysts with only LAS no BAS¹⁶ showed minor catalytic activity, reaching only 42.3% PG conversion and 18.5% EM yield after 6 h, indicating that low catalytic performance was obtained in Lewis acid catalytic system. While doping the ZrO₂ with only a small quantity of P (P/Zr ratio is 0.25), the PG conversion was increased dramatically up to 61.8% with an EM yield of 42.9% (Table 4.2), which may be contributed by the synergistic effect of BAS and LAS in ZrPO catalyst. The activity achieved its maximum values at the P/Zr ratio of 0.75 with LAS/BAS ratio of 2.1. Interestingly, only 27.2% EM yield was obtained when the P/Zr ratio was increased further to 1.25 with a further increase of BAS. It indicates that the introduction of BAS into the ZrO₂ matrix improved the catalytic activity, while more BAS on ZrPO catalysts did not show a beneficial effect on the reaction.

The effect of calcination temperature on the catalytic performance was also investigated as shown in Figure 4.8c and d. Keeping the optimum P/Zr ratio of 0.75, increasing the

calcination temperature from 300 to 500 °C induced a gradual increase in PG conversion to reach a maximum of 72%. A further increase in calcination temperature resulted in a lower conversion of PG. However, these catalysts calcined from 300 to 700 °C presented a similar performance concerning EM yield, which could be due to the similar LAS/BAS ratio shown in Table 4.2. It is worth pointing out that when the calcination temperature was 900 °C, the catalytic activity of ZrPO was very poor, which may be because the mesoporous structure is damaged at a calcination temperature of 900 °C. It has been proved by the XRD and BET result of ZrPO-0.75-900.

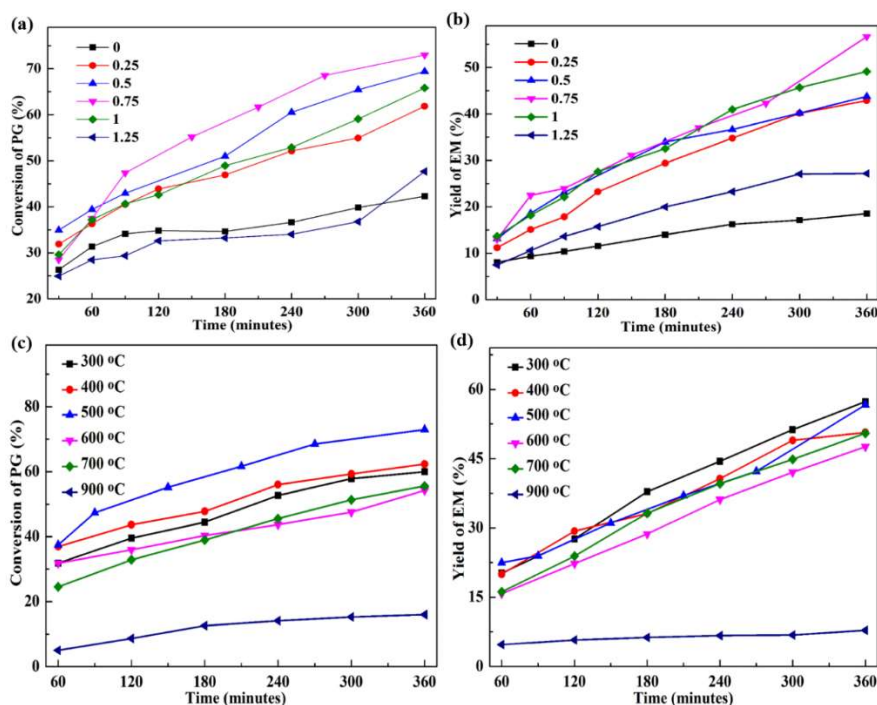


Figure 4.8 Kinetic plots of PG conversion and EM yield over ZrPO-x-500 with different P/Zr ratios (a and b) and ZrPO-0.75-y calcined at different temperatures (c and d).

The catalytic results of ZrPO possessing different density of LAS and BAS are summarized in Table 4.2. PG conversion and EM yield plotted against the density of acid sites on the catalysts are summarized in Figure 4.9. The EM yield and PG conversion were not correlated to the total amount of acid sites. (Figure 4.9a). The PG

conversion and EM yield vs. the ratio of LAS/BAS exhibited a volcano-type curve (Figure 4.9b), which indicated that there is a balance of LAS and BAS for the PG conversion to EM and that a suitable LAS/BAS (ranging between 2-2.5) corresponds to a better yield to EM. The maximum EM yield (57 %) and PG conversion (73 %) were achieved at LAS/BAS = 2.1. Excess of LAS and BAS on the catalyst led to a decrease in catalytic activity. That is probably because excessive BAS could promote the formation of phenylglyoxal diethyl acetal detected by GC-MS and excessive LAS might suppress PG conversion. Therefore, we propose that the LAS/BAS ratio on ZrPO played a dominant role in PG conversion to EM.

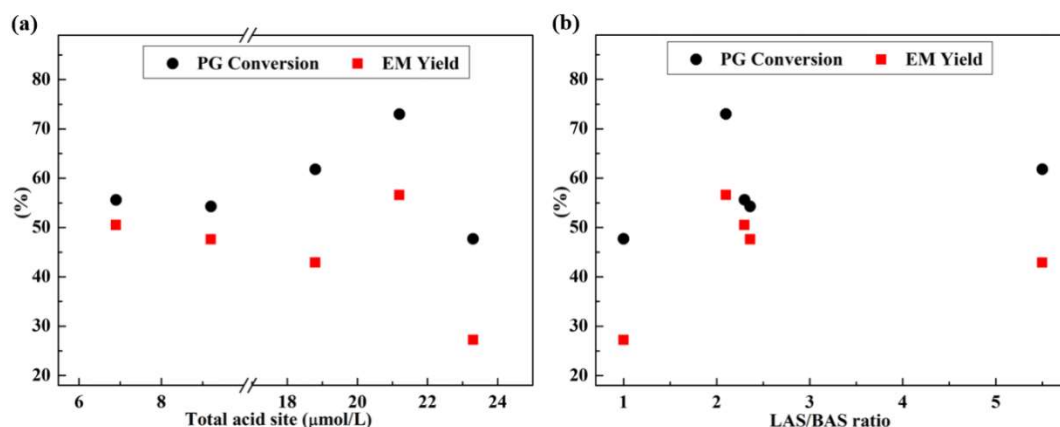
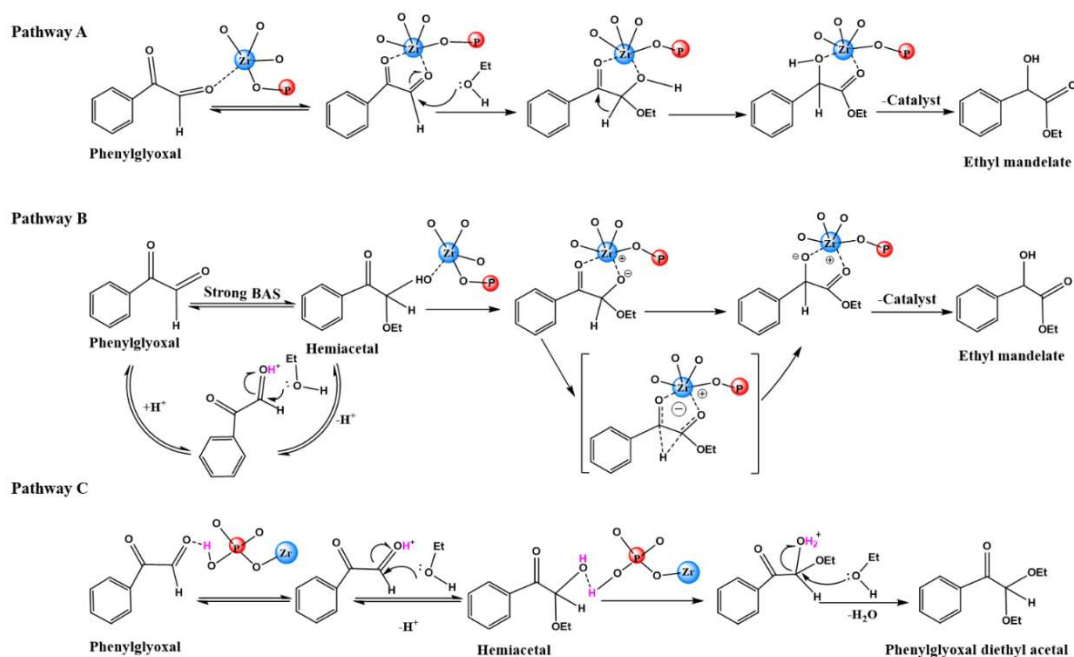


Figure 4.9 Effect of total acid sites (a) and LAS/BAS ratio (b) of catalysts on the catalytic performance.

4.3.5 Reaction pathways of PG conversion on ZrPO

Based on the above-mentioned catalytic results of ZrPO, it has been demonstrated that either strong BAS combined with LAS or only LAS can be employed as effective catalysts for the PG conversion to EM. The possible reaction pathways of PG conversion occurring on ZrPO are illustrated in Scheme 4.1. For pathway A, PG is converted into EM through the synthetic effect of strong BAS and LAS where

intermediate hemiacetal is formed on the strong BAS and further transformed to the desired EM on the LAS.⁷⁻¹⁰ The initiation of the reaction proceeds through the protonation of the carbonyl groups by the phosphorus hydroxyl (P-OH) group of the catalysts, resulting in the formation of carbocation species. The species is then bound to the alcoholic oxygen and subsequently yields the intermediate product hemiacetal. In the alcoholic media, the hemiacetal can react to EM via an intramolecular Cannizzaro reaction.⁶ The isomerization step involves a formal 1,2-hydride shift between the hydrogen donor and the carbonyl group, which involves the coordination and activation of the carbonyl group by Zr ions acting as LAS. The attack of the nucleophile and the isomerization reaction can also occur on only LAS via intramolecular Cannizzaro reaction. PG is firstly adsorbed on the active Zr sites of the catalyst; then the carbonyl group is coordinated and stabilized by LAS. A hydride shift (the aldehyde H of the terminal CHO of PG shifts to the adjacent carbon atom) also occurs via the formation of a cyclic five-membered transition state similar to the Pathway A, giving EM as the product. It is noteworthy that PG can also incorporate two alcohol molecules catalyzed by strong BAS, forming an undesirable by-product phenylglyoxal diethyl acetal, which has been confirmed by GC-MS (Pathway C).³



Scheme 4.1 Possible reaction pathways of PG conversion on ZrPO catalyst in ethanol solution.

4.3.6 Effect of water content on catalytic activity

The catalytic performance of ZrPO-0.75-500 pre-treated at various temperatures was evaluated (Figure 4.10a). The PG conversion, EM yield, and selectivity increased with elevated pre-treatment temperatures from 25 to 150 °C and then decreased at higher temperatures. At the optimum pre-treatment temperature of 150 °C, the maximum PG conversion of 75% was achieved. The EM yield and selectivity showed the same trends as that of PG conversion. It indicates that a moderate pre-treatment temperature of catalysts led to high catalytic performance, which is consistent with the reports from Song et al.²⁶ and Kobe et al.²⁸

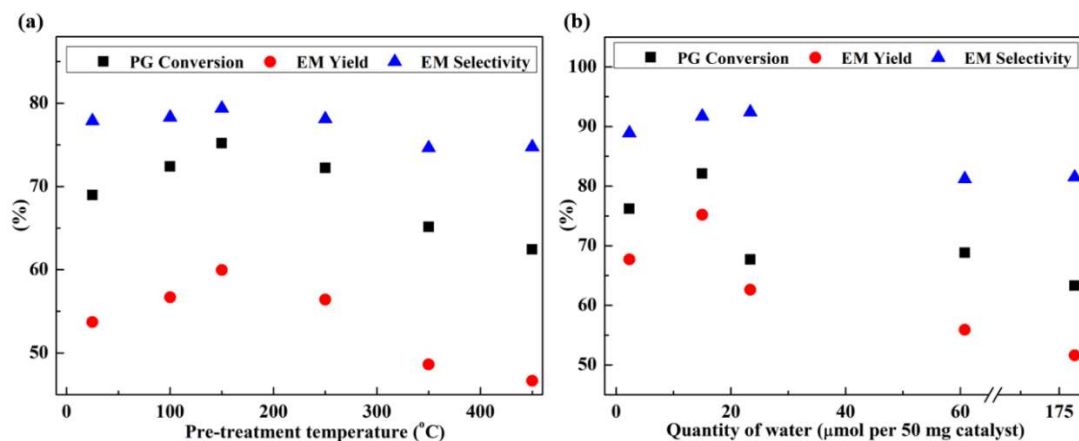


Figure 4.10 The catalytic conversion of PG over ZrPO-0.75-500 with different pre-treatment temperatures (a) and rehydrated with different quantities of water (b).

The change of pre-treatment temperatures resulted in the change of water content adsorbed on the surface of ZrPO catalysts, which affects catalytically active sites.⁵⁵ To further investigate the role of water, different amounts of water vapor were dosed onto the ZrPO-0.75-500 catalyst. The corresponding catalytic performance is shown in Figure 4.10b. Similarly, the catalytic performance as the function of the content of water adsorbed on catalysts exhibited a volcano-type curve, and the maximum value was observed with 15 μmol water dosed on 50 mg catalyst, corresponding to about 92% of EM selectivity. From both the dehydration and rehydration studies, it is concluded that moderate water content promoted the catalytic activity, while the presence of excessive water had a detrimental effect on the catalytic performance.

4.3.7 Stability and Recyclability Evaluation

One of the most important advantages of heterogeneous acid catalysts is their stability against leaching of the acid sites during the process of the reaction. To evaluate the catalytic stability and recycle ability, the most active ZrPO-0.75-500 was selected for the recycling experiment. The catalytic performance was carried out for five

consecutive runs under the same reaction conditions (90 °C for 6 h). ZrPO-0.75-500 was simply recovered by centrifugation and then washed with ethanol several times. After being dried at 150 °C for 2 h to remove the absorbed water and ethanol, it was subsequently used for the next reaction under identical conditions. As shown in Figure 4.11, the catalyst maintained 77–82% conversion of PG and 54–59% yield of EM after five cycles. The fluctuation of catalytic activity was in the range of $\pm 5\%$, indicating good stability and reusability of the catalyst, which probably can be attributed to the high structural stability of the catalyst.⁵⁶

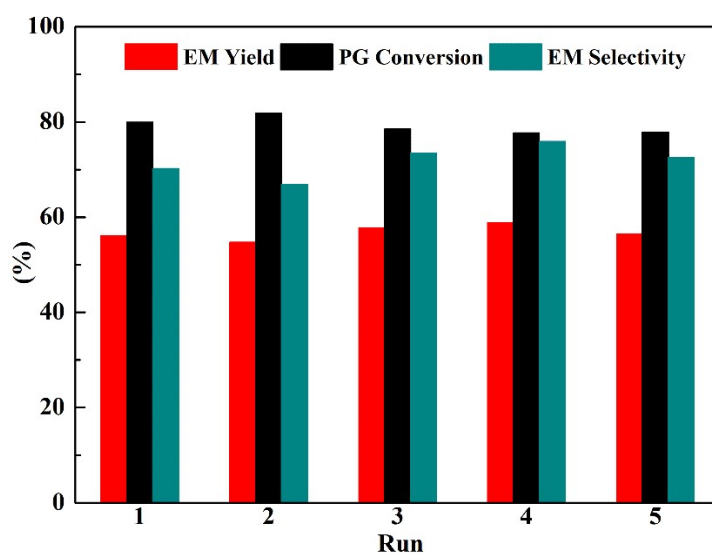


Figure 4.11 Recycling experiments of the ZrPO-0.75-500 for the PG conversion.

4.4 Conclusions

In this work, the ordered mesoporous ZrPO catalysts were synthesized by an EISA method. The structure and acidity properties of these materials could be readily tuned by varying P/Zr ratios and calcination temperatures. XRD, N₂ physisorption, SEM and TEM analysis confirmed the ordered mesoporous structure of materials. ³¹P MAS NMR spectroscopy was used to investigate the local environment of phosphorus in ZrPO. The

nature of acid sites in terms of the types, strength and density was quantitatively evaluated by ^{31}P MAS NMR and ^1H MAS NMR spectroscopy using TMPO as a probe molecule combined with NH_3 -TPD. This work demonstrates that the LAS/strong BAS ratio was primarily responsible for the PG conversion to EM and the superior catalytic performance of ZrPO was achieved when the LAS/BAS ratio was around 2 due to the synergistic effect of these two acid sites. In addition, ZrPO shows good stability and reusability in this reaction, which may probably be attributed to the high structural stability of the catalyst. The reaction mechanisms for the PG conversion on the ZrPO catalyst are therefore proposed. Finally, the effect of water on the catalytic activity was studied, which further confirms that the interplay of LAS and BAS on the ZrPO is of critical importance to accelerate the catalytic conversion of PG to EM. A moderate content of water-induced either by catalyst pre-treatment at the proper temperature or deliberately dosed on the ZrPO materials achieved a maximum catalytic activity.

References

- [1]. Corma, A.; Iborra, S.; Velty, A., Chemical routes for the transformation of biomass into chemicals. *Chemical Reviews* **2007**, *107* (6), 2412-2423.
- [2]. King, J. B.; Winters, C.; Stickler, D. J., An invitro assessment of mandelic-acid as a bladder washout solution. *Medecine Et Maladies Infectieuses* **1992**, *22*, 614-620.
- [3]. Dusselier, M.; Van Wouwe, P.; Dewaele, A.; Makshina, E.; Sels, B. F., Lactic acid as a platform chemical in the biobased economy: the role of chemocatalysis. *Energy & Environmental Science* **2013**, *6* (5), 1415-1442.
- [4]. Abdel-Rahman, M. A.; Tashiro, Y.; Zendo, T.; Sonomoto, K., Effective (+)-lactic acid production by co-fermentation of mixed sugars. *Journal of Biotechnology* **2010**, *150*, S347-S348.
- [5]. Kishida, H.; Jin, F. M.; Yan, X. Y.; Moriya, T.; Enomoto, H., Formation of lactic acid from glycolaldehyde by alkaline hydrothermal reaction. *Carbohydrate Research* **2006**, *341* (15), 2619-2623.
- [6]. Wang, P.; Tao, W. J.; Sun, X. L.; Liao, S. H.; Tang, Y., A highly efficient and enantioselective intramolecular Cannizzaro reaction under TOX/Cu(II) catalysis. *Journal of the American Chemical Society* **2013**, *135* (45), 16849-16852.
- [7]. Russell, A. E.; Miller, S. P.; Morken, J. P., Efficient Lewis acid catalyzed

intramolecular Cannizzaro reaction. *Journal of Organic Chemistry* **2000**, 65 (24), 8381-8383.

[8]. Taarning, E.; Saravanamurugan, S.; Holm, M. S.; Xiong, J. M.; West, R. M.; Christensen, C. H., Zeolite-catalyzed isomerization of triose sugars. *ChemSusChem* **2009**, 2 (7), 625-627.

[9]. De Clippel, F.; Dusselier, M.; Van Rompaey, R.; Vanelderen, P.; Dijkmans, J.; Makshina, E.; Giebel, L.; Oswald, S.; Baron, G. V.; Denayer, J. F. M.; Pescarmona, P. P.; Jacobs, P. A.; Sels, B. F., Fast and selective sugar conversion to alkyl lactate and lactic acid with bifunctional carbon-silica catalysts. *Journal of the American Chemical Society* **2012**, 134 (24), 10089-10101.

[10]. Pescarmona, P. P.; Janssen, K. P. F.; Delaet, C.; Stroobants, C.; Houthoofd, K.; Philippaerts, A.; De Jonghe, C.; Paul, J. S.; Jacobs, P. A.; Sels, B. F., Zeolite-catalysed conversion of C-3 sugars to alkyl lactates. *Green Chemistry* **2010**, 12 (6), 1083-1089.

[11]. Wang, Z. C.; Jiang, Y. J.; Baiker, A.; Huang, J., Efficient Acid-catalyzed conversion of phenylglyoxal to mandelates on flame-derived silica/alumina. *ACS Catalysis* **2013**, 3 (7), 1573-1577.

[12]. Li, L.; Stroobants, C.; Lin, K. F.; Jacobs, P. A.; Sels, B. F.; Pescarmona, P. P., Selective conversion of trioses to lactates over Lewis acid heterogeneous catalysts. *Green Chemistry* **2011**, 13 (5), 1175-1181.

[13]. Wang, Z. C.; Jiang, Y. J.; Rachwalik, R.; Liu, Z. W.; Shi, J.; Hunger, M.; Huang, J., One-step room-temperature synthesis of Al MCM-41 materials for the catalytic conversion of phenylglyoxal to ethylmandelate. *ChemCatChem* **2013**, 5 (12), 3889-3896.

[14]. Wang, Z. C.; Jiang, Y. J.; Hunger, M.; Baiker, A.; Huang, J., Catalytic performance of Brønsted and Lewis acid sites in phenylglyoxal conversion on flame-derived silica-zirconia. *ChemCatChem* **2014**, 6 (10), 2970-2975.

[15]. Tan, H. B.; Li, Y. Q.; Jiang, X. F.; Tang, J.; Wang, Z. L.; Qian, H. Y.; Mei, P.; Malgras, V.; Bando, Y.; Yamauchi, Y., Perfectly ordered mesoporous iron-nitrogen doped carbon as highly efficient catalyst for oxygen reduction reaction in both alkaline and acidic electrolytes. *Nano Energy* **2017**, 36, 286-294.

[16]. Guo, Y. N.; Tang, J.; Henzie, J.; Jiang, B.; Qian, H. Y.; Wang, Z. L.; Tan, H. B.; Bando, Y.; Yamauchi, Y., Assembly of hollow mesoporous nanoarchitectures composed of ultrafine Mo₂C nanoparticles on N-doped carbon nanosheets for efficient electrocatalytic reduction of oxygen. *Materials Horizons* **2017**, 4 (6), 1171-1177.

[17]. Miao, Z. C.; Xu, L. L.; Song, H. L.; Zhao, H. H.; Chou, L. J., One-pot synthesis of ordered mesoporous zirconium oxophosphate with high thermostability and acidic properties. *Catalysis Science & Technology* **2013**, 3 (8), 1942-1954.

[18]. Das, S. K.; Bhunia, M. K.; Sinha, A. K.; Bhaumik, A., Synthesis, characterization, and biofuel application of mesoporous zirconium oxophosphates. *ACS Catalysis* **2011**, 1 (5), 493-501.

[19]. Riley A.E., Tolbert S.H., Synthesis of periodic hexagonal surfactant templated platinum tin tellurides: Narrow band gap inorganic/organic composites. *Journal of the American Chemical Society* **2003**, 125 (15), 4551-4559.

[20]. Ciesla U., Fröba M., Stucky G. et al., Highly ordered porous zirconias from

surfactant-controlled syntheses: Zirconium oxide–sulfate and zirconium oxo phosphate. *Chemistry of Materials* **1999**, *11* (2), 227-234.

[21]. Carenco S., Hu Y., Florea I. et al., Metal-dependent interplay between crystallization and phosphorus diffusion during the synthesis of metal phosphide nanoparticles. *Chemistry of Materials* **2012**, *24* (21), 4134-4145.

[22]. Wu P., Liu Y., He M. et al., Postsynthesis of hexagonally packed porous zirconium phosphate through a novel anion exchange between zirconium oxide mesophase and phosphoric acid. *Chemistry of Materials* **2005**, *17* (15), 3921-3928.

[23]. Yu J.C., Zhang L., Zheng Z. et al., Synthesis and characterization of phosphated mesoporous titanium dioxide with high photocatalytic activity. *Chemistry of Materials* **2003**, *15* (11), 2280-2286.

[24]. Zhang Y., Li Y., Sakamoto Y. et al., Structure and thermal stability of mesostructured zirconium oxophosphates. *Microporous and Mesoporous Materials* **2007**, *100* (1), 295-301.

[25]. Tian B., Liu X., Tu B. et al., Self-adjusted synthesis of ordered stable mesoporous minerals by acid-base pairs. *Nat Mater* **2003**, *2* (3), 159-63.

[26]. Song, S. X.; Kydd, R. A., Activation of sulfated zirconia catalysts - Effect of water content on their activity in n-butane isomerization. *Journal of the Chemical Society-Faraday Transactions* **1998**, *94* (9), 1333-1338.

[27]. Yaluris, G.; Larson, R. B.; Kobe, J. M.; Gonzalez, M. R.; Fogash, K. B.; Dumesic, J. A., Selective poisoning and deactivation of acid sites on sulfated zirconia catalysts for n-butane isomerization. *Journal of Catalysis* **1996**, *158* (1), 336-342.

[28]. Kobe, J. M.; Gonzalez, M. R.; Fogash, K. B.; Dumesic, J. A., Effects of water on the performance of sulfated zirconia catalysts for butane isomerization. *Journal of Catalysis* **1996**, *164* (2), 459-466.

[29]. Streck, R.; Barnes, A. J., Solvent effects on infrared, C-13 and P-31 NMR spectra of trimethyl phosphate - Part 2. Binary solvent systems. *Spectrochimica Acta Part a-Molecular and Biomolecular Spectroscopy* **1999**, *55* (5), 1059-1076.

[30]. Zhao, D. Y.; Feng, J. L.; Huo, Q. S.; Melosh, N.; Fredrickson, G. H.; Chmelka, B. F.; Stucky, G. D., Triblock copolymer syntheses of mesoporous silica with periodic 50 to 300 angstrom pores. *Science* **1998**, *279* (5350), 548-552.

[31]. Paul, M.; Pal, N.; Rana, B. S.; Sinha, A. K.; Bhaumik, A., New mesoporous titanium-phosphorus mixed oxides having bifunctional catalytic activity. *Catalysis Communications* **2009**, *10* (15), 2041-2045.

[32]. Pazhani, R.; Padma Kumar, H.; Varghese, A.; Moses Ezhil Raj, A.; Solomon, S.; Thomas, J. K., Synthesis, vacuum sintering and dielectric characterization of zirconia (t-ZrO₂) nanopowder. *Journal of Alloys and Compounds* **2011**, *509* (24), 6819-6823.

[33]. Miao, Z. C.; Zhao, H. H.; Yang, J.; Zhao, J.; Song, H. L.; Chou, L. J., Mesoporous Mn-Zr composite oxides with a crystalline wall: synthesis, characterization and application. *Dalton Transactions* **2015**, *44* (7), 2997-3001.

[34]. Zhang, Y.; Wang, J. J.; Ren, J. W.; Liu, X. H.; Li, X. C.; Xia, Y. J.; Lu, G. Z.; Wang, Y. Q., Mesoporous niobium phosphate: an excellent solid acid for the dehydration of fructose to 5-hydroxymethylfurfural in water. *Catalysis Science & Technology* **2012**, *2* (12), 2485-2491.

- [35]. Kruk, M.; Jaroniec, M., Gas adsorption characterization of ordered organic-inorganic nanocomposite materials. *Chemistry of Materials* **2001**, *13* (10), 3169-3183.
- [36]. Boissiere, C.; Larbot, A.; Van der Lee, A.; Kooyman, P. J.; Prouzet, E., A new synthesis of mesoporous MSU-X silica controlled by a two-step pathway. *Chemistry of Materials* **2000**, *12* (10), 2902-2913.
- [37]. Jones, D. J.; Aptel, G.; Brandhorst, M.; Jacquin, M.; Jimenez-Jimenez, J.; Jimenez-Lopez, A.; Maireles-Torres, P.; Piwonski, I.; Rodriguez-Castellon, E.; Zajac, J.; Roziere, J., High surface area mesoporous titanium phosphate: Synthesis and surface acidity determination. *Journal of Materials Chemistry* **2000**, *10* (8), 1957-1963.
- [38]. Sun, Y.; Afanasiev, P.; Vrinat, M.; Coudurier, G., Porous zirconium phosphates prepared by surfactant-assisted precipitation. *Journal of Materials Chemistry* **2000**, *10* (10), 2320-2324.
- [39]. Li, F. K.; France, L. J.; Cai, Z. P.; Li, Y. W.; Liu, S. J.; Lou, H. M.; Long, J. X.; Li, X. H., Catalytic transfer hydrogenation of butyl levulinate to gamma-valerolactone over zirconium phosphates with adjustable Lewis and Brønsted acid sites. *Applied Catalysis B-Environmental* **2017**, *214*, 67-77.
- [40]. Zhang, J. N.; Ma, Z.; Jiao, J.; Yin, H. F.; Yan, W. F.; Hagaman, E. W.; Yu, J. H.; Dai, S., Surface functionalization of mesoporous silica SBA-15 by liquid-phase grafting of zirconium phosphate. *Microporous and Mesoporous Materials* **2010**, *129* (1-2), 200-209.
- [41]. Zheng, A. M.; Huang, S. J.; Liu, S. B.; Deng, F., Acid properties of solid acid catalysts characterized by solid-state P-31 NMR of adsorbed phosphorous probe molecules. *Physical Chemistry Chemical Physics* **2011**, *13* (33), 14889-14901.
- [42]. Pruneda, J. M.; Artacho, E., Energetics of intrinsic point defects in ZrSiO₄. *Physical Review B* **2005**, *71* (9), 094113, 1-7.
- [43]. Opila, R. L.; Wilk, G. D.; Alam, M. A.; van Dover, R. B.; Busch, B. W., Photoemission study of Zr- and Hf-silicates for use as high-kappa oxides: Role of second nearest neighbors and interface charge. *Applied Physics Letters* **2002**, *81* (10), 1788-1790.
- [44]. Clearfield, A.; Serrette, G. P. D.; Khazisyed, A. H., Nature of hydrous zirconia and sulfated hydrous zirconia. *Catalysis Today* **1994**, *20* (2), 295-312.
- [45]. Hu, W.; Luo, Q.; Su, Y.; Chen, L.; Yue, Y.; Ye, C.; Deng, F., Acid sites in mesoporous Al-SBA-15 material as revealed by solid-state NMR spectroscopy. *Microporous and Mesoporous Materials* **2006**, *92* (1-3), 22-30.
- [46]. Jiang, Y.; Huang, J.; Dai, W.; Hunger, M., Solid-state nuclear magnetic resonance investigations of the nature, property, and activity of acid sites on solid catalysts. *Solid State Nuclear Magnetic Resonance* **2011**, *39* (3-4), 116-141.
- [47]. Li, S.; Zhou, H.; Han, B.; Deng, F.; Liu, X.; Xiao, L.; Fan, J., Hydrogenated mesoporous TiO₂-SiO₂ with increased moderate strong Brønsted acidic sites for Friedel-Crafts alkylation reaction. *Catalysis Science & Technology* **2012**, *2* (4), 719-721.
- [48]. Rakiewicz, E. F.; Peters, A. W.; Wormsbecher, R. F.; Sutovich, K. J.; Mueller, K. T., Characterization of acid sites in zeolitic and other inorganic systems using solid-state ³¹P NMR of the probe molecule trimethylphosphine oxide. *The Journal of*

Physical Chemistry B **1998**, 102 (16), 2890-2896.

[49]. Zhao, Q.; Chen, W. H.; Huang, S. J.; Wu, Y. C.; Lee, H. K.; Liu, S. B., Discernment and quantification of internal and external acid sites on zeolites. *Journal of Physical Chemistry B* **2002**, 106 (17), 4462-4469.

[50]. Karra, M. D.; Sutovich, K. J.; Mueller, K. T., NMR characterization of Brønsted acid sites in faujasitic zeolites with use of perdeuterated trimethylphosphine oxide. *Journal of the American Chemical Society* **2002**, 124 (6), 902-903.

[51]. Sinhamahapatra, A.; Sutradhar, N.; Roy, B.; Tarafdar, A.; Bajaj, H. C.; Panda, A. B., Mesoporous zirconium phosphate catalyzed reactions: Synthesis of industrially important chemicals in solvent-free conditions. *Applied Catalysis a-General* **2010**, 385 (1-2), 22-30.

[52]. Sinhamahapatra, A.; Sutradhar, N.; Pahari, S.; Bajaj, H. C.; Panda, A. B., Mesoporous Zirconium Phosphate: An efficient catalyst for the synthesis of coumarin derivatives through pechmann condensation reaction. *Applied Catalysis a-General* **2011**, 394 (1-2), 93-100.

[53]. Sastre, G.; Lewis, D. W., Modelling of Brønsted acidity in AFI and CHA zeotypes. *Journal of the Chemical Society-Faraday Transactions* **1998**, 94 (19), 3049-3058.

[54]. Shah, R.; Gale, J. D.; Payne, M. C., Comparing the acidities of zeolites and SAPOs from first principles. *Chemical Communications* **1997**, (1), 131-132.

[55]. Loveless, B. T.; Gyanani, A.; Muggli, D. S., Discrepancy between TPD- and FTIR-based measurements of Brønsted and Lewis acidity for sulfated zirconia. *Applied Catalysis B-Environmental* **2008**, 84 (3-4), 591-597.

[56]. Xu, H. M.; Miao, Z. C.; Zhao, H. H.; Yang, J.; Zhao, J.; Song, H. L.; Liang, N.; Chou, L. J., Dehydration of fructose into 5-hydroxymethylfurfural by high stable ordered mesoporous zirconium phosphate. *Fuel* **2015**, 145, 234-240

Chapter 5. Pt single sites on Bi-TiO₂ for selective photocatalytic oxidation of alcohols into aldehydes

5.1 Introduction

The selective oxidation of alcohols to their corresponding aldehydes is one of the most important functional group transformations in organic synthesis and chemistry since aldehydes and their derivatives are important building blocks for producing fine chemicals.¹ Various catalysis processes have been developed for aldehydes production from alcohols.

Photocatalysis is based on the use of photons to drive chemical reactions thus featuring several advantages simultaneously.²⁻⁵ Firstly, the photo-excited charge carriers or photogenerated reactive species can drive reduction or oxidation reactions without consuming additional reagents, enabling the environmentally benign transformations. Stoichiometric oxidants (e.g., H₂O₂) are usually required in thermal catalysis. Secondly, by using solar energy rather than thermal energy, the oxidation reaction can be carried out at lower temperature. Since radical species can generally be produced by the photoredox approach under mild conditions, whereas the conventional generation of radicals typically requires high temperatures. Furthermore, by using a selective photocatalyst, some chemicals or functional groups in the system may remain intact during the photocatalytic reaction. Thus, photocatalysis has the potential to perform selective transformation of selected reactants.

Therefore, the catalytic transformations of alcohols using solar energy have attracted much attention, because of unique reactive species and reaction patterns as well as mild reaction conditions, which may enable selective functionalization of specific functional groups further enabling the precise production of target chemicals. Particularly, photocatalytic oxidation with environmentally benign oxidants, such as molecular oxygen, is a promising route to produce the key intermediates, aldehydes or ketones.⁶ Among numerous semiconductor photocatalysts, titanium dioxide (TiO₂) has been extensively studied as one of the most ideal candidates for the selective oxidation of alcohols owing to its nontoxicity, strong oxidation ability, comparatively high efficiency and stability.⁷ Particularly, the mesoporous TiO₂ possesses large surface areas and well-ordered channels or pores that can increase surface active sites and facilitate mass diffusion within frameworks.^{8, 9} However, photocatalytic selective oxidation of alcohols to the corresponding aldehydes over TiO₂ semiconductor remains a great challenge because of the limited light absorption¹⁰ and the rapid recombination rate of photoexcited electrons and holes on TiO₂. Besides, the high oxidation potential of TiO₂ (2.7 eV) makes hydroxyl radicals (OH[•]) easy to generate and often causes over-oxidation of alcohols to produce by-products, such as acids or CO₂, thus leading to a low selectivity of aldehydes.¹¹ Numerous strategies have been implemented to solve these problem, such as anion doping, metal ion doping,¹² sensitization by visible light-responsive sensitizers (such as dyes),¹³ hybrid semiconductors having wide and narrow bandgap energies,¹⁴ and so on. So far, cocatalyst loading has been proven as an effective approach to boost the photocatalytic efficiency. Metals, especially noble metals such as

Pt, Pd and Au,^{15, 16} are the most often used cocatalysts to enhance the photocatalytic activity of TiO₂, and endow greater promotional properties on the photocatalytic oxidation in the visible-light region.¹⁷ As the photoinduced electrons are transferred from photocatalysts to metal nanoparticles and then be trapped, the surface modification using metal nanoparticles can speed up the separation of photoinduced electron-hole pairs and thus improve the photocatalytic activity.¹⁸ Meanwhile, the deposited metals may promote the adsorption and activation of oxygen (O₂), which is favored by the catalytic processes involving O₂.¹⁹ For instance, the doping of Pt nanoparticles into TiO₂ could improve the visible-light harvesting, charge-separation, and electron-transport of the resultant catalyst, leading to the enhanced photocatalytic activity.²⁰ It was demonstrated that the Pt modified TiO₂ nanocomposite is a promising catalyst for alcohol oxidation.^{21,22} Besides, Mondelli et al. reported that the presence of metal promoter Bi largely hindered the formation of carboxylates from benzaldehyde oxidation by controlling the supply of O₂ to the noble metal under aerobic conditions.²³ The Bi-Pt bimetallic catalysts could be used to improve the performance and lifetime of the TiO₂ catalyst and modulate the product distribution of aromatic alcohols oxidation, thereby strongly influencing aldehydes or ketones selectivity.

Conventional metal-deposited catalysts usually contain metal nanoparticles with a broad size distribution. It has been well established that small size distribution of metal catalysts would to some extent contribute to high selectivity.^{24, 25} Single-atom or single-site metal catalysts offer a promising way to utilize precious noble metal elements more effectively, providing that they are sufficiently stable and catalytically active.^{26, 27} Much

work has been done to synthesize single-atom or single site noble metals anchored on supports by using various strategies, such as the in-situ method²⁸ and post-synthesis method.²⁹ The single-atom or single-site metals could be firmly anchored on the internal surface of supports by the in-situ method, which exhibits enhanced stability and performance.²⁸ This chapter reports the synthesis of Pt single sites deposited on the mesoporous Bi-TiO₂ nanocomposites by the in-situ method. The size effect of Pt single sites, subnano clusters, and nanoparticles on the photocatalytic activity of benzyl alcohol oxidation as a model reaction was evaluated. Comparative studies on the morphological, structural properties and electrochemical properties were undertaken to explore the origin of the enhanced photocatalytic performance.

5.2 Experimental section

5.2.1 Catalyst fabrication

5.2.1.1 Mesoporous TiO₂

The mesoporous TiO₂ material was fabricated via modified evaporation-induced self-assembly (EISA) method according to the literature.³⁰ Typically, 1.5 g of triblock copolymer Pluronic F127 (EO₁₀₆PO₇₀EO₁₀₆, from Sigma Aldrich) as a structure-directing agent was dissolved in 20 mL of anhydrous ethanol (EtOH), stirred for 0.5 h at room temperature and then sonicated for 10 min. Meanwhile, 238 μ L of concentrated hydrochloric acid was added dropwise to 3055 μ L of titanium isopropoxide (TTIP) solution. After magnetic stirring for 0.5 h, the above solution was added to a mixture of F127/EtOH under vigorous stirring for overnight. The resulting sol solution was aged

in an open petri dish at 30 °C for 24 h, then at 100 °C for 8 h. Finally, the obtained colorless and transparent xerogel was calcined in static air at 500 °C for 3 h.

5.2.1.2 One-pot synthesis of xPt-0.8Bi-TiO₂

A series of Pt–Bi bimetallic deposited on mesoporous TiO₂ catalysts were prepared using the same method. In a typical procedure, 1.5 g of triblock copolymer F127 was first suspended in 20 mL of anhydrous ethanol at room temperature which was stirring for 0.5 h at room temperature. Next, a nominal weight ratio of TTIPO, chloroplatinic acid hexahydrate (H₂PtCl₆·6H₂O, ≥37.50% Pt basis, Sigma-Aldrich) and bismuth(III) nitrate pentahydrate (Bi(NO₃)₃·5H₂O, ≥98.0%, Sigma-Aldrich) were successively added to the above suspension under vigorous stirring and kept for overnight. The mixture was then placed inside the oven at 30 °C for 24 h, then at 100 °C for 8 h. Finally, the obtained transparent xerogel was calcined in static air at 500 °C for 3 h. The catalysts were denoted as xPt-0.8Bi-TiO₂, where x refers to the weight concentration of Pt. The reduction material was prepared by hydrogen reduction at 500 °C for 2 h under an H₂ flow (15 ml/min, H₂:N₂ = 1:1) and denoted as xPt-0.8Bi-TiO₂-H₂. For comparison, 0.15Pt-TiO₂ and 0.8Bi-TiO₂ without H₂ reduction also were synthesized using the same method.

5.2.1.3 0.15Pt-0.8Bi-TiO₂-imp

The Pt–Bi bimetallic deposited on TiO₂ catalyst with the Bi loading of 0.8 wt% and Pt loading of 0.15 wt% were also synthesized by a sequential wet impregnation method.

Firstly, 0.398 mg $\text{H}_2\text{PtCl}_6 \cdot 6\text{H}_2\text{O}$ was dissolved in Milli-Q water and added dropwise to 100 mg TiO_2 slurry, under stirring at room temperature for 8 h. Then the collected sample named 0.15Pt- TiO_2 -imp was dried at 100°C overnight followed by calcination at 500°C for 3 h. Next, a nominal weight ratio of $\text{Bi}(\text{NO}_3)_3 \cdot 5\text{H}_2\text{O}$ was dissolved in the HNO_3 solution (pH=5–6) and added dropwise to the above 60 mg 0.15Pt- TiO_2 -imp. The obtained catalysts were dried overnight at 100°C and calcined at 500°C for 3 h. The sample was denoted as 0.15Pt-0.8Bi- TiO_2 -imp. For comparison, the reduction material denoted 0.15Pt-0.8Bi- TiO_2 -imp- H_2 was prepared by hydrogen reduction at 500 °C for 3 h under an H_2 flow (15 ml/min, $\text{H}_2:\text{N}_2 = 1:1$).

5.2.2 Characterization

Powder X-ray diffraction (XRD) patterns were recorded on a PANalytical X'Pert PRO Multipurpose Diffractometer at 40 kV voltage and 20 mA current via $\text{Cu K}\alpha$ ($\lambda=1.5406$ Å). Nitrogen adsorption/desorption isotherms were recorded on a TriStar II 3020 Autosorb-iQ analyses at -196 °C. Before the measurements, the samples were degassed at 80 °C under vacuum overnight. High-resolution transmission electron microscopy (HRTEM) and high-angle annular dark field-scanning transmission electron microscopy (HAADF-STEM) images were acquired using a FEI Themis-Z Double-corrected 60-300 kV STEM operated at 300 kV. The convergence and collection angle under the HAADF-STEM mode is 17.9 mrad and 50- 200 mrad, respectively. The point resolution of Themis-Z under the STEM mode is around 0.6 Å (operated at 300 kV). The HAADF-STEM imaging mode combined with EDS was used to obtain atomic

resolution elemental mapping data. X-ray photoelectron spectra (XPS) were recorded on an ESCALAB 250Xi spectrometer (Thermo Scientific). The binding energy of adventitious carbon (C 1s) at 284.8 eV was used to correct the charging effect of samples. Ultraviolet-visible (UV-vis) diffuse reflectance spectra were obtained on a Shimadzu UV-3600 Plus spectrophotometer with ISR-603 sample base plate integrating sphere Set.

The H₂ temperature-programmed reduction (H₂-TPR) and H₂-O₂ titration were carried out on a Quantachrome instrument with a thermal conductivity detector (TCD). For H₂-TPR measurement, samples (50 mg) were first pretreated with pure He at 350°C for 1 h (15 mL/min). After cooling to room temperature and purging with the 20% H₂/N₂ reducing gas (15 mL/min), the H₂-TPR was performed at a rate of 5°C/min from 30 to 700°C. The H₂ consumption was recorded using a TCD detector. For the H₂-O₂ titration experiment, 50 mg sample was first pretreated under 350°C with He for 1 h and then reduced under 500°C with 20% H₂/N₂ for 2 h. After purged with pure N₂ for another 1h until the temperature down to 120°C, H₂ adsorbed on the surface of the catalyst was titrated by O₂ pulses until full saturation, and then the physically adsorbed O₂ was purged fully using pure N₂ until the signal being stable. Next, the resulting monolayer of adsorbed O₂ on Pt was titrated using H₂ pulses until the equal areas of eluted peaks were observed. The Pt dispersion (D) was calculated from the volume of H₂ titrated by the following equation:

$$D = \frac{2VM}{22414 \times 3 \times W \times P}$$

Where V is the volume of H₂ used for the titration of O₂ (mL), W is the catalyst mass

(g), P is the Pt mass fraction in the tested catalyst (%), M is the atomic mass of Pt (g/mol).

To study the mechanism of photocatalytic oxidation, the photoelectrochemical measurements were performed on a potentiostat (SP-300, BioLogic Science Instruments) in a conventional three-electrode configuration with an Ag/AgCl (in saturated KCl) and Pt-wire as a reference electrode and counter electrode, respectively. The catalyst suspension was deposited onto Ti foil to form the working electrode. The photocurrent measurements were carried out at a constant potential of +1.0 V, and a 300 W Xenon lamp (OPS-A500, Oriel instruments) was served as a light source. The electrochemical impedance spectra (EIS) were recorded under an AC perturbation signal of 10 mV over the frequency range of 1 Hz - 100 kHz at 2V. The Mott-Schottky measurement was made at 1 kHz under dark conditions in 0.5 M Na₂SO₃.

5.2.3 Photocatalytic oxidation of alcohols

For each photocatalytic experiment, 10 mg of catalyst was suspended in 1 ml of the 50 mmol/L alcohol solution with acetonitrile as a solvent, which was saturated with pure molecular oxygen. Next, the reaction mixture was stirred for 15 min in dark to reach an adsorption equilibrium. Then the photocatalytic oxidation was carried out under the irradiation of 300 W xenon lamp (OPS-A500, Oriel instruments) with a UV-cut off filter (≥ 420 nm). To ensure sufficient interaction between the sample surface and the alcohol molecules, the solution was held under constant magnetic stirring conditions during the whole photocatalytic process. After the photocatalytic oxidation, the catalysts were

separated from the reaction mixture by centrifugation at 16,000 rpm rate and the products were analyzed by gas chromatography (Shimadzu GC2014) equipped with flame ionization detector (FID) using chlorobenzene as an internal standard.

$$\text{conversion of alcohols (\%)} = \frac{\text{molar of alcohols converted} \times 100}{\text{molar of initial alcohols}}$$

$$\text{yield of aldehydes (\%)} = \frac{\text{molar of aldehyde produced} \times 100}{\text{molar of initial alcohols}}$$

$$\text{selectivity of aldehydes (\%)} = \frac{\text{molar of aldehydes produced} \times 100}{\text{molar of alcohols converted}}$$

5.3 Results and discussion

5.3.1 Characterization

5.3.1.1 XRD

The wide-angle XRD patterns of the prepared TiO₂-based photocatalysts are displayed in Figure 5.1a. These high-intensity crystal peaks at around $2\theta = 25.2, 37.7, 48.1, 54.0, 55.3$ and 62.8° are attributed to the (101), (004), (200), (105), (211) and (204) of nanocrystalline anatase TiO₂ (JCPDS, No. 21-1272). These diffraction peaks were also observed for all Pt and Bi doping samples, indicating that the typical structure of anatase TiO₂ did not alter upon surface modification with Pt and Bi metals. However, a slight shift of peak at 25° was observed for all the modified TiO₂ (Figure 5.1b). This slight shift might be explained by the interaction of metals with the TiO₂ support; The deposition of metals (Pt or Bi) onto the crystalline structure of TiO₂ led to decreased crystal size. When Pt loading increased to 0.35% and 1%, a slight change in crystalline

structure was observed on (105) and (211) planes due to a broad peak at 55° observed. It is noted that no diffraction peak of Pt and Bi was detected in the XRD patterns of all the samples, which implies that the fine Pt were highly dispersed on the support. In addition, it also shows that the Pt loading at up to 1% content did not cause any morphological or textural changes of TiO_2 .³¹ However, a small diffraction peak at 27.3° was observed on 0.15Pt-0.8Bi- TiO_2 sample after reduction with H_2 , which could be ascribed to Bi (012) plane, indicating the formation of metallic Bi nanoparticles on the TiO_2 after the H_2 reduction process.³²

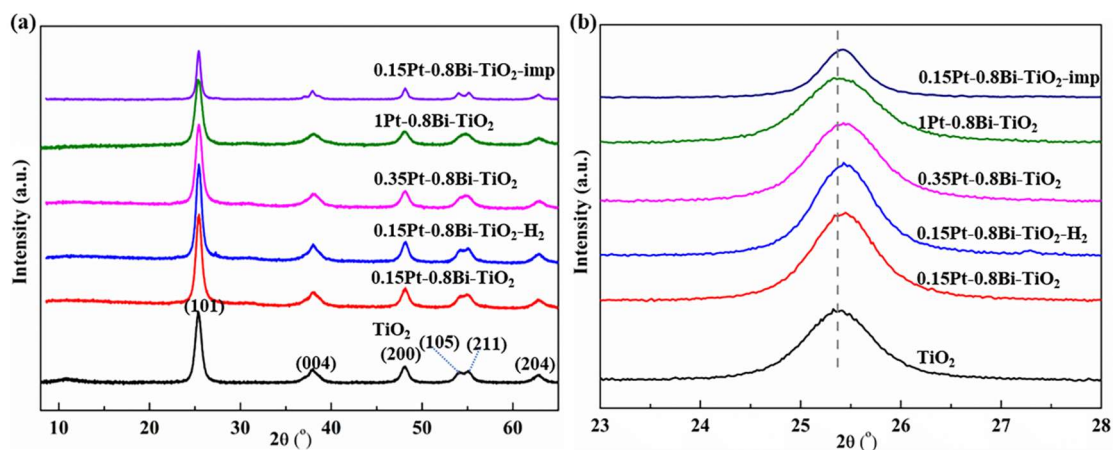


Figure 5.1 XRD patterns of different TiO_2 -based samples.

5.3.1.2 BET

As shown in Figure 5.2, the N_2 adsorption/desorption isotherms of the TiO_2 and xPt-0.8Bi- TiO_2 materials both show typical type IV curves with a sharp capillary condensation step at $P/P_0 = 0.7$ – 0.9 and an H1-type hysteresis loop, which is typical of large-pore mesoporous materials with cylindrical channels. The Brunauer–Emmett–Teller (BET) surface area and pore volume of the TiO_2 materials

were calculated to be $\sim 86.3 \text{ m}^2 \text{ g}^{-1}$ and $0.202 \text{ cm}^3 \text{ g}^{-1}$, respectively (Table 5.1). The pore size of TiO_2 derived from the desorption branches of the isotherms by using the Barrett-Joyner-Halenda (BJH) method is about 8.0 nm with a narrow distribution. For 0.15Pt-0.8Bi- TiO_2 powder, a large peak was observed in the range of 5 to 7 nm and 8 to 14 nm, and the average pore size is 8.9 nm. For 0.35% and 1% Pt samples, a high-intensity peak was observed at the center of around 10.0 and 7.0 nm, respectively. The BET surface areas increase from 86.3 to 96.4, 104.4 and $102.1 \text{ m}^2 \text{ g}^{-1}$ for 0.15Pt-0.8Bi- TiO_2 , 0.35Pt-0.8Bi- TiO_2 and 1Pt-0.8Bi- TiO_2 . However, the decrease pore size, surface area and pore volume of the 1Pt sample were observed compared to the 0.35Pt sample. This could be due to the increased nanoparticle size of Pt with increased Pt loading.

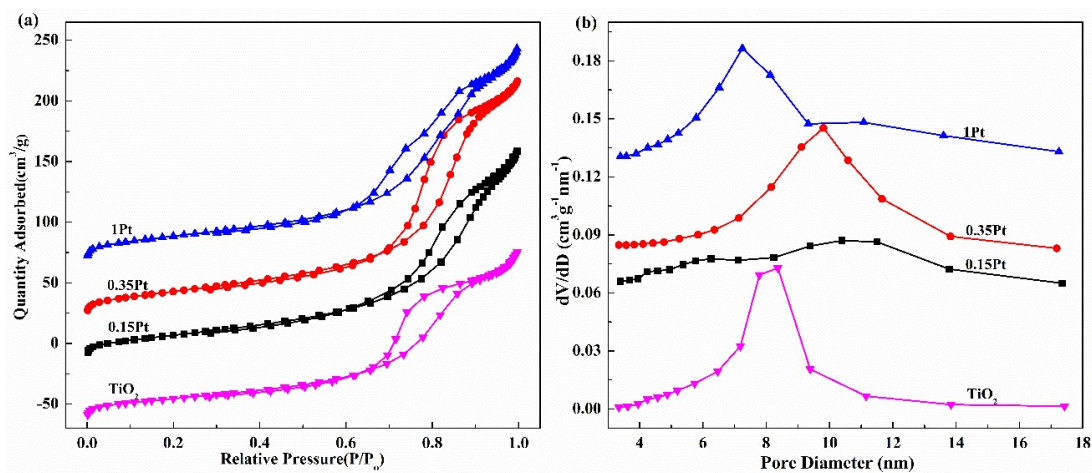


Figure 5.2 N_2 adsorption/desorption isotherms (a) and BJH pore size distributions (b) of TiO_2 and xPt-0.8Bi- TiO_2 samples.

Table 5.1. Textural properties of different TiO₂-based samples.

Sample	BET Surface Area (m ² /g)	Pore Size (nm)	Pore Volume (cm ³ /g)
TiO ₂	86.3	8.0	0.202
0.15Pt-0.8Bi-TiO ₂	96.4	8.9	0.236
0.35Pt-0.8Bi-TiO ₂	104.4	9.2	0.295
1Pt-0.8Bi-TiO ₂	102.1	8.4	0.256

5.3.1.3 TEM

As shown in Figure 5.3, the HRTEM image of 0.15Pt-0.8Bi-TiO₂-H₂ shows the TiO₂ lattice structure without visible Pt nanoparticles. The observed lattice spacing of 0.351 nm, 0.231 nm and 0.146 nm can be ascribed to the (101), (004) and (204) crystal planes of TiO₂, respectively. This indicates that the crystalline structure of TiO₂ can be well retained during the treatment, consistent with the XRD results discussed above.

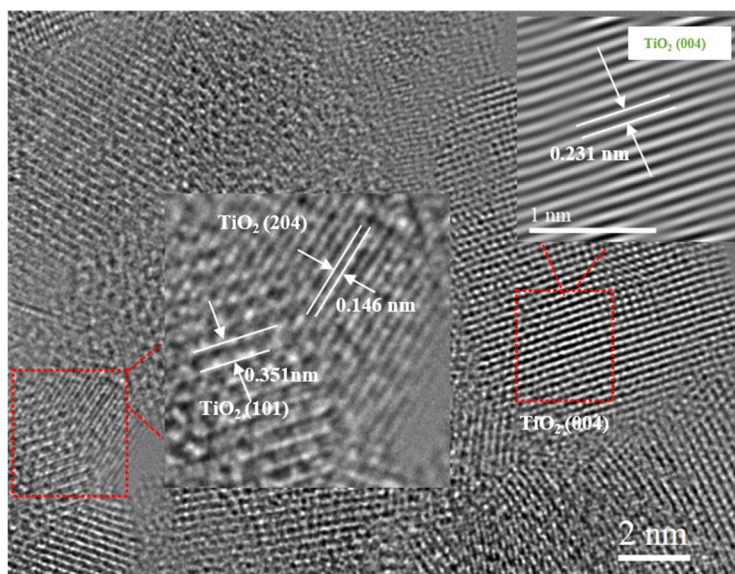


Figure 5.3 HRTEM image of 0.15Pt-0.8Bi-TiO₂-H₂.

The HAADF-STEM image of 0.15Pt-0.8Bi-TiO₂-H₂ demonstrates the existence of isolated Pt and/or Bi single sites: (marked with red circles in Figure 5.4a) with high density according to the Z-contrast difference between the light Ti, O and the heavier Pt and Bi atoms. Apart from the dominant single sites, a few subnano clusters were also observed (shown in the yellow rectangle in Figure 5.4a). The size distribution (Figure 5.4b) shows that Pt and/or Bi single sites with ultrasmall sizes between 0.1 and 0.4 nm. The HAADF-STEM and element mapping images reveal that Pt and Bi were uniformly dispersed throughout the sample (Figure 5.4c-g). The compositional line-scanning profile (Figure 5.4h) through the metal particle along the direction shown in Figure 5.4c further indicates the presence of isolated Pt and Bi single sites. In addition, the overlapping of Pt and Bi was observed as well, which indicates that Pt-Bi ensembles exist as a solid solution.³¹

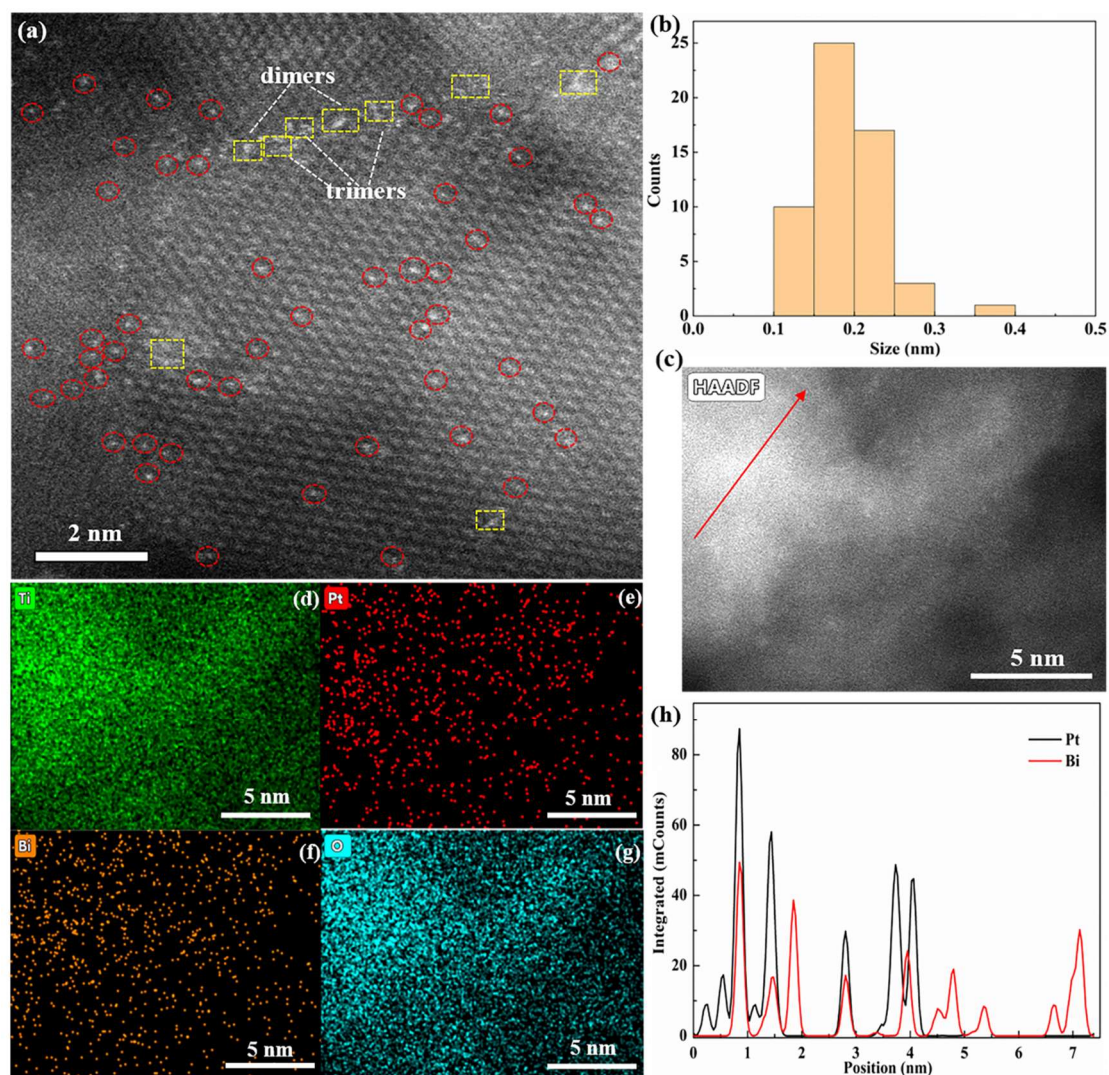


Figure 5.4 Morphology of the 0.15Pt-0.8Bi-TiO₂-H₂. (a) Aberration-correct HAADF-STEM images. (b) The size distribution of Pt and/or Bi presented in (a). (c-g) HAADF-STEM and EDS scan images of Ti, Pt, Bi and O. (h) The compositional EDX-line-scanning profile of the selected area (c) along the red arrow.

The abundant metal (Pt and/or Bi) single sites were also observed on the HAADF-STEM image of 0.35Pt-0.8Bi-TiO₂-H₂ (Figure 5.5a, shown in red circles). In addition, a large amount of subnano clusters composed of loose and random ensembles of several to tens of atoms, with dimensions < 0.6 nm as shown in Figure 5.5f, were observed in Figure 5.5a, (shown in yellow rectangles). Similar to 0.15Pt loading

sample, the distribution of Pt and Bi atoms was evenly (Figure 5.5b-e). The compositional line-scan profile (Figure 5.5g) indicates that the Pt-Bi ensembles exist as a solid solution of arbitrary composition and the content of Pt is similar to that of Bi along the green line shown in Figure 5.5a. For 1Pt-0.8Bi/TiO₂-H₂ shown in Figure 5.6a, the highlighted dots (shown in green circles) can be ascribed to small Pt nanoparticles with a size of around 0.5~2.5 nm as shown in the size distribution inserted in Figure 5.6a. In the STEM-mapping images of Pt and Bi elements ((Figure 5.6b-d), the partially aggregated Pt nanoparticles were found due to a high concentration of Pt. It seems that the Bi atoms preferred to be aggregated around Pt nanoparticles. Based on the brightness variations of these nanoparticles in HAADF images and by comparing their intensities with those of the single sites and subnano clusters, we concluded that most of these nanoparticles possessed a three-dimensional (3D) morphology while subnano clusters possessed a two-dimensional (2D) raft-like morphology.³³

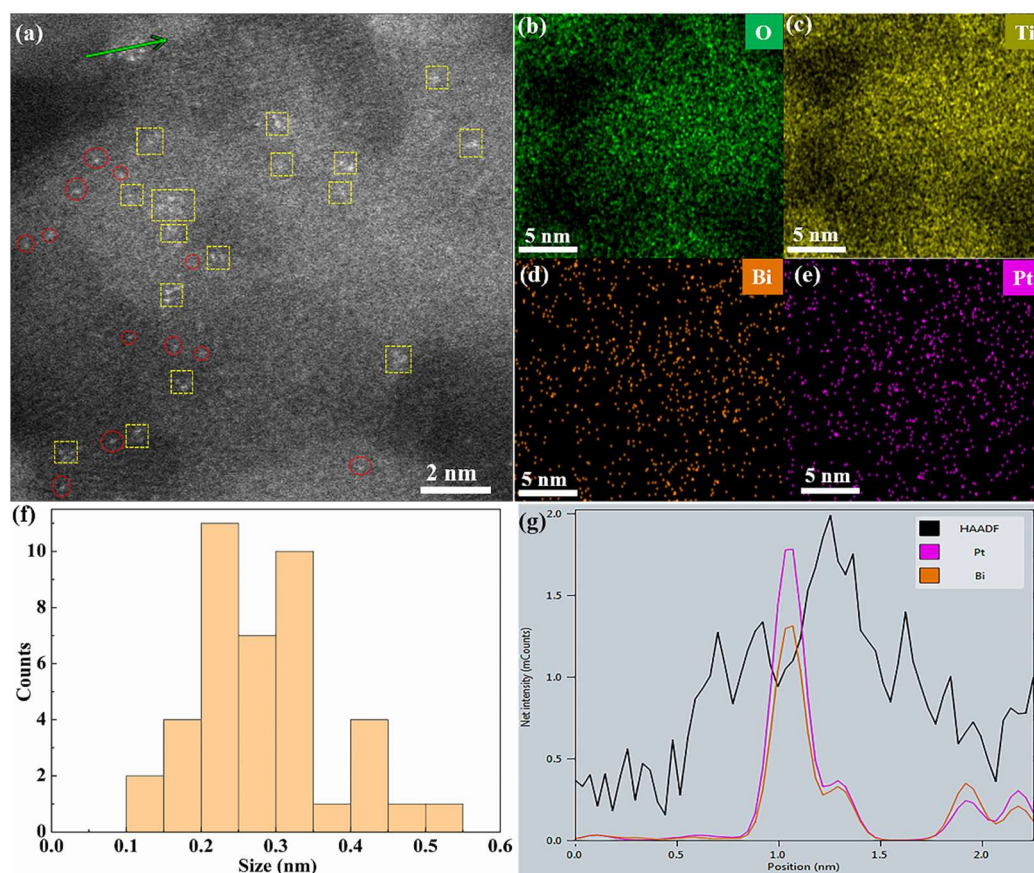


Figure 5.5 Morphology of the 0.35Pt-0.8Bi-TiO₂-H₂. (a) Aberration-correct HAADF-STEM images. (b-e) EDS scan images of Ti, Pt, Bi and O. (f) The size distribution of Pt and/or Bi presented in (a). (g) The composition-line-scanning profile of the selected highlighted area presented in (a) along with the green arrow.

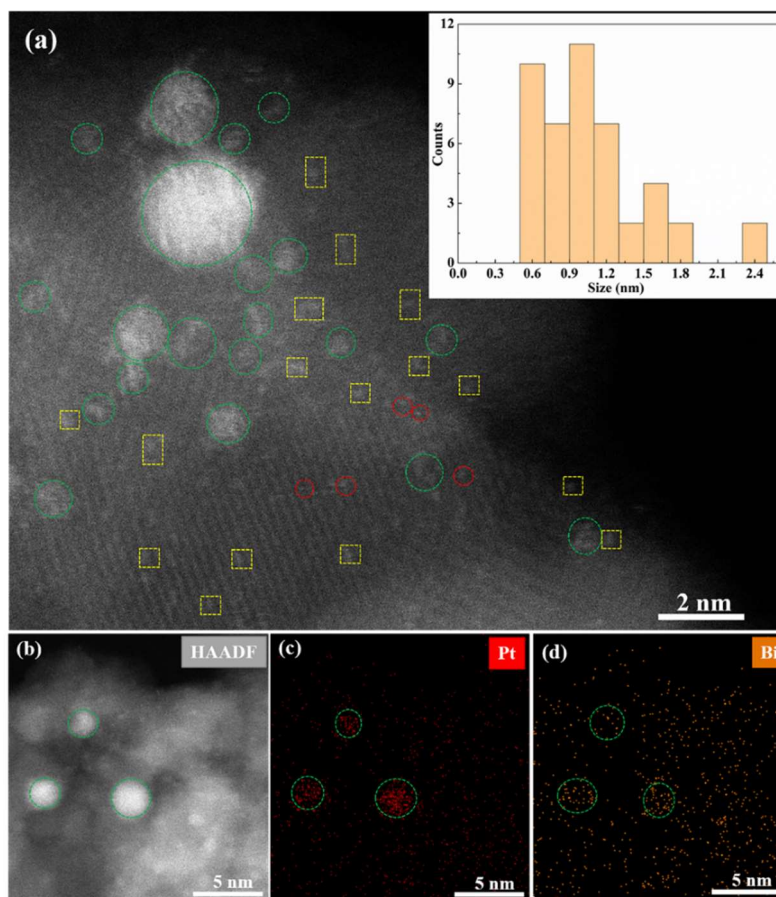


Figure 5.6 Morphology of the 1Pt-0.8Bi-TiO₂-H₂. (a) Aberration-correct HAADF-STEM images. The size distribution of Pt and/or Bi presented insert in (a). (b-d) HAADF-STEM and EDS scan images of Ti, Pt, Bi and O.

5.3.1.4 H₂-TPR

The reductive behavior of TiO₂ based samples over H₂ was determined from their temperature-programmed reduction (TPR) profiles. The reduction of bare TiO₂ requires a relatively high temperature of 560 °C (Figure 5.7a). For 0.8Bi-TiO₂, a broad peak from 100 to 400 °C, which could be ascribed to the reduction of Bi₂O₃ species anchored into TiO₂ or supported on the surface.³⁴ The peak around 480 °C is ascribed to the partial reduction of TiO₂.³⁵ The lower reduction temperature of Ti⁴⁺ on 0.8Bi-TiO₂ compared

to the bare TiO_2 could be explained that the hydrogen spillover occurs from Bi_2O_3 nanoparticles most likely to the surface of TiO_2 , resulting in the low reduction temperature of Ti^{4+} .³⁶ For the 0.15Pt-0.8Bi- TiO_2 sample, the reduction peak centered at around 320 °C could be attributed to the reduction of PtO_x single sites which interacted with the support or the Pt- TiO_x interface site. The last reduction peak at 580°C could be related to the reduction of TiO_2 interacted with PtO_x single sites.³⁵ Compared to the bare one, the Pt-loaded catalysts showed higher reduction temperature for the TiO_x species, suggesting a stronger Pt- TiO_2 interaction.³⁵ Different with Pt-Bi bimetallic catalysts, The TPR profile of 0.15Pt- TiO_2 shows several reduction peaks. The peaks at around 110°C and 180 °C could be attributed to the reduction of PtO_x nanoparticles and subnano clusters to metallic Pt.³⁵ A new reduction peak of TiO_2 presented around 450 °C, which is ascribed to the hydrogen spillover occurs from PtO_2 nanoparticles to the surface of TiO_2 . This phenomenon illustrates that the addition of Bi promotes the dispersion of Pt, benefiting the formation of Pt single sites. The peak corresponding to the reduction of TiO_x species is also shifted to a lower temperature (450 °C) for the impregnation-made catalyst, similar to that of 0.15Pt- TiO_2 , confirming the formation of Pt or Bi nanoparticles. A broad peak from 50 to 300 °C is probably due to the formation of PtO_2 nanoparticles or subnano cluster by this method.

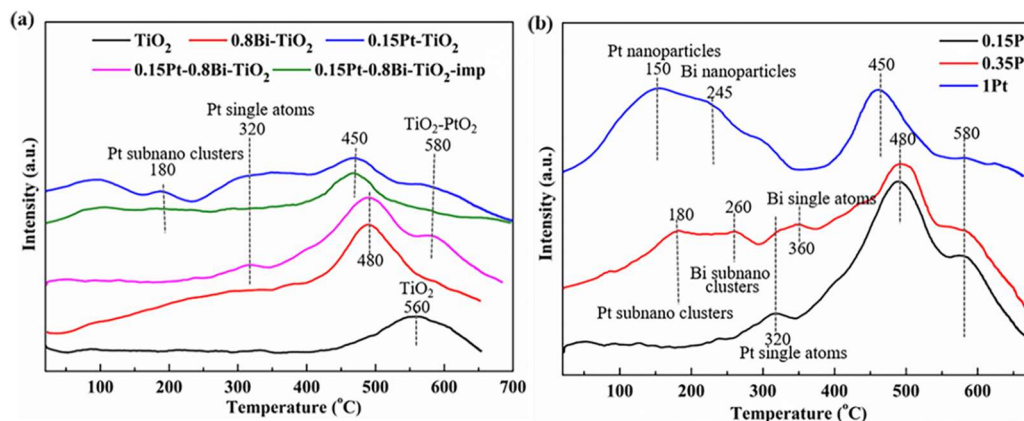


Figure 5.7 H₂-TPR profiles for TiO₂-based samples prepared using EISA method and 0.15Pt-0.8Bi-TiO₂ prepared using the impregnation method (a), and xPt-0.8Bi-TiO₂ prepared using EISA method (b).

Figure 5.7b shows the TPR profiles of the xPt-0.8Bi-TiO₂ catalysts prepared using the EISA method. Compared to 0.15Pt-0.8Bi-TiO₂, the reduction peaks of 0.35Pt-0.8Bi-TiO₂ at around 180 °C and 260 °C have attributed the reduction of PtO₂ and Bi₂O₃ subnano clusters to metallic Pt and Bi, respectively. The phenomenon further demonstrates that 0.35Pt-0.8Bi-TiO₂ is dominated by Pt and Bi subnano clusters. With the increase of Pt doping from 0.35% to 1%, the intensity of PtO_x nanoparticle reduction peak at 150 °C increased, indicating that the majority of PtO_x aggregated to form the nanoparticles which could be reduced to metallic Pt under low temperature. In addition, the reduction peak at 580 °C ascribed to Pt-TiO_x species disappeared on 1% Pt-loading sample, suggesting a weaker metal-support interaction due to the presence of Pt nanoparticles. This result corroborates with the HAADF-STEM analysis that most Pt nanoparticles presented in the 1Pt-0.8Bi-TiO₂ sample were anchored on the surface of TiO₂ support.

5.3.1.5 XPS

The chemical composition and valence state of the elements in the TiO₂-based composites were analyzed by XPS. As shown in Figure 5.8a, the peaks at 458.6 and 464.3 eV are consistent with Ti⁴⁺ valence state on lattice oxygen.³⁷ Compared to the XPS spectra taken from 0.15Pt-0.8Bi-TiO₂ without reduction, the Ti 2p binding energies were slightly shifted toward lower binding energy region centered at 458.3 eV and 464.1 eV after reduction, which could be due to the removal of lattice oxygen atoms around Ti⁴⁺ to form Ti³⁺, resulting in the lower binding energies.^{35,38} Figure 5.8b shows the O 1s spectra of these samples. All the catalysts exhibit two main peaks centered at 529.8 eV and 531.5 eV, which are assigned to the lattice oxygen (Ti-O, Bi-O and Pt-O) and oxygen defect sites, respectively.³⁸

The Pt in the 0.15Pt-TiO₂ and 0.15Pt-0.8Bi-TiO₂ samples exist in oxidation states, as indicated by the Pt 4f spectra (Figure 5.8c). In Figure 5.8d, the Bi oxide species were observed on all the samples evidenced by the typical characteristic peaks of oxidation state Bi 4f 7/2 and Bi 4f 5/2 doublets centered at 164.2 and 158.9 eV. In addition, the other two peaks centered at around 162.3 and 157.1 eV, which arise from Bi 4f 7/2 and Bi 4f 5/2 doublets of Bi metallic state, respectively.³⁹ This indicates that Bi species exist in both metallic and oxidation states. Moreover, compared to 0.8Bi-TiO₂ material, the intensity of metallic Bi 4f peaks slightly increased on 0.15Pt-0.8Bi-TiO₂, suggesting the effect of Pt doping on Bi valence states. Furthermore, after reduction, all Bi 4f peaks of 0.15Pt-0.8Bi-TiO₂ samples were shifted to lower binding energy due to the increase of lattice oxygen vacancy sites around Bi. Similarly, a loss of surface lattice oxygen

atoms removed from Bi_2O_3 can affect the Bi^{3+} ions, which receive electrons from lattice oxygen, resulting in lower binding energies.

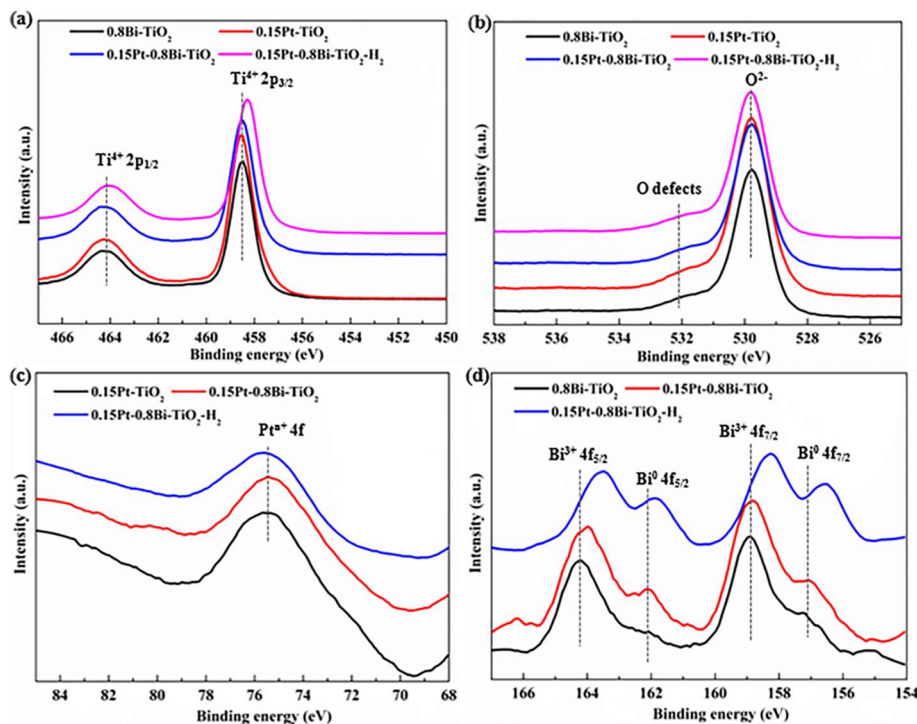


Figure 5.8 XPS of TiO_2 -based samples. (a) Ti 2p spectra; (b) O 1s spectra; (c) Pt 4f spectra. (d) Bi 4f spectra.

As shown in Figure 5.9a, all the reduced xPt-0.8Bi- TiO_2 - H_2 samples show the peaks at 457.6 and 463.2 eV assigned to the Ti 2p $3/2$ and Ti 2p $1/2$ orbitals of Ti^{3+} , respectively,³⁷ indicating that reduction at 500 °C removed a small portion of lattice oxygen from the TiO_2 support and possibly leading to the generation of oxygen vacancies.⁴⁰ As shown in Figure 5.9b, for all the xPt-0.8Bi- TiO_2 - H_2 catalysts, there are the characteristic peaks of lattice oxygen (529.8 eV) and surface oxygen defects (531.5 eV).³⁸ In Figure 5.9c, the characteristic peaks of Pt^0 4f doublets were observed at around 70.5 eV ($4f_{7/2}$) and 73.8 eV ($4f_{5/2}$), respectively.⁴¹ And the peaks found at 74.4 and 77.7 eV are attributed to the $4f_{7/2}$ and $4f_{5/2}$ of Pt^{4+} , respectively.⁴² It seems that the

oxidized Pt species are predominant in the 0.15Pt-0.8Bi-TiO₂-H₂. However, in the 1Pt-0.8Bi/TiO₂-H₂ materials, the metallic Pt was detected as the main species along with a small amount of oxidized Pt species. A large increase of metallic Pt sites with the Pt doping amount from 0.15 to 1% could be due to the low reduction temperature of surface Pt subnano clusters and nanoparticles, which is consistent with the results of HAADF-STEM and H₂-TPR.

Noteworthy, for the three bimetallic xPt-0.8Bi-TiO₂-H₂ samples, the binding energies of Bi 4f orbitals were slightly shifted to higher binding energy with the increase of Pt loading amount while the binding energies of Pt 4f orbitals shifted to lower values as shown in Table 5.2 and Table 5.3. This phenomenon could be due to an interaction between Bi and Pt on high concentration Pt catalysts. This conclusion is consistent with the phenomenon demonstrated in HAADF-STEM, where the Bi atoms preferred to be aggregated around Pt nanoparticles.

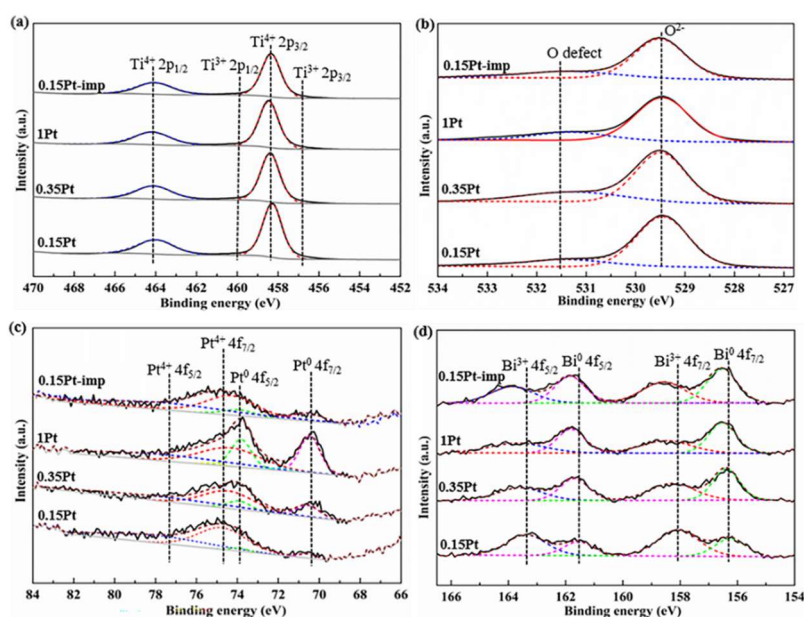


Figure 5.9 XPS of xPt-0.8Bi-TiO₂-H₂ samples. (a) Ti 2p spectra; (b) O 1 s spectra; (c) Pt 4f spectra. (d) Bi 4f spectra.

The percentage of each metal species was estimated by the areas of the corresponding XPS peaks. As provided in Table 5.2, the quantitative analysis of Pt 4f XPS results illustrates that the metallic and oxidation species of Bi and Pt coexist in the xPt-0.8Bi/TiO₂-H₂ sample. There is a low ratio of Pt⁰/Ptⁿ⁺ (0.17) in 0.15 wt% Pt catalyst even after 2h H₂ reduction at 500 °C, suggesting that the Pt single sites have strong interaction with the support, leading to a high reduction temperature, in good agreement with the H₂-TPR results. The phenomenon was also observed by Wei et al.³³ They reported the presence of positively charged Pt centers on Pt single atoms and pseudo-single atoms dominant Pt/FeO_x sample. The ratio of Pt⁰/Ptⁿ⁺ in the 0.35Pt-0.8Bi-TiO₂ (0.36) and 1Pt-0.8Bi-TiO₂ (0.7) catalyst increased by about 2 and 4 times as a consequence of increasing Pt subnano clusters and nanoparticles. In conclusion, the lower Pt loading (0.15%) results in a high percentage of Pt single-atoms showing strong interaction with TiO₂.³³ As a consequence, the 0.15Pt-0.8Bi-TiO₂ showed a high reduction temperature of PtO_x species at 320 °C as shown in Figure 5.7b, resulting in a high concentration of positively charged Pt centers as shown in Figure 5.9c.

As depicted in Figure 5.9d and Table 5.3, the ratio of Bi⁰/Bi³⁺ is increased from 0.5 to 1.1 with the increase of Pt concentration (from 0.15% to 1%). This could be the reason that the Bi species tend to be aggregated into subnano clusters and/or nanoparticles with the increasing of Pt loading amount as shown in the HAADF-STEM results. These Bi species could be reduced to metallic Bi easily.

Table 5.2 The binding energies and peak areas of the Pt 4f XPS spectra.

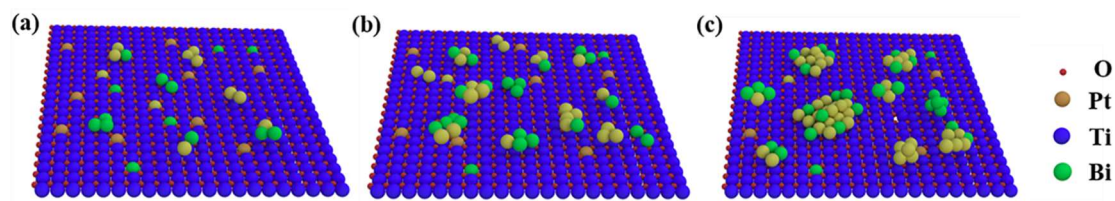
Catalyst	Pt 4f 7/2		Pt 4f 5/2		Pt ⁰ /Pt ⁿ⁺
	Pt ⁰ (eV)	Pt ⁿ⁺ (eV)	Pt ⁰ (eV)	Pt ⁿ⁺ (eV)	
0.15Pt-0.8Bi-TiO ₂	206.05 (70.6)	1196.7 (73.9)	154.5 (74.8)	897.5 (78.1)	0.17
0.35Pt-0.8Bi-TiO ₂	381.3 (70.6)	1053.2 (73.9)	286 (74.5)	789.9 (77.8)	0.36
1Pt-0.8Bi-TiO ₂	943.6 (70.5)	1354.9 (73.8)	707.7 (74.4)	1016.1 (77.7)	0.70
0.15Pt-0.8Bi-TiO ₂ -imp	301.6 (70.6)	1074.7 (73.9)	226.2 (74.9)	806 (78.4)	0.28

Table 5.3 The binding energies and peak areas of the Bi 4f XPS spectra.

Catalyst	Bi 4f 7/2		Bi 4f 5/2		Bi ⁰ /Bi ³⁺
	Bi ⁰ (eV)	Bi ³⁺ (eV)	Bi ⁰ (eV)	Bi ³⁺ (eV)	
0.15Pt-0.8Bi-TiO ₂	816.4	1756.1	612.3	1317.1	0.5
	(156.2)	(158.02)	(161.5)	(163.3)	
0.35Pt-0.8Bi-TiO ₂	902.9	1432.2	677.2	1073.8	0.6
	(156.5)	(158.2)	(161.6)	(163.5)	
1Pt-0.8Bi-TiO ₂	1286.7	1147.7	965	860.1	1.1
	(156.5)	(158.5)	(161.8)	(163.6)	
0.15Pt-0.8Bi-TiO ₂ -imp	1677.1	1470.9	1257.8	1103	1.1
	(156.4)	(158.5)	(161.8)	(163.8)	

Based on the above characterization results of xPt-0.8Bi-TiO₂-H₂, a schematic illustration of the various types of Pt and/or Bi single sites, subnano clusters and nanoparticles on the TiO₂ surfaces is presented in Scheme 5.1. A large amount of

isolated Pt and Bi single sites were observed on 0.15Pt-0.8Bi-TiO₂-H₂ sample. For 0.35Pt-0.8Bi-TiO₂-H₂ sample, highly disordered or amorphous-like 2D subnano clusters, as well as metal single sites, coexist on the support surface (Scheme 5.1b). Beside amorphous-like subnano clusters, Pt and/or Bi nanoparticles were also observed on 1Pt-0.8Bi-TiO₂-H₂ as shown in the HAADF-STEM results.



Scheme 5.1 Schematic illustration of various types of metal single sites, subnano clusters, and nanoparticles dispersed onto the TiO₂ surface. (a) 0.15Pt-0.8Bi-TiO₂-H₂ dominantly by Pt and/or Bi single sites (b) 0.35Pt-0.8Bi-TiO₂-H₂ dominantly by Pt and/or Bi subnano clusters (c) 1Pt-0.8Bi-TiO₂-H₂ dominantly by Pt and/or Bi nanoparticles.

5.3.1.6 UV-Vis spectra

The UV-Vis diffuse reflectance spectra (DRS) are shown in Figure 5.10 and Figure 5.11. The characteristic absorption edge of TiO₂ is at around 400 nm (Figure 5.10a). The spectra of Pt and/or Bi modified TiO₂ samples shifted to a longer wavelength from UV to visible light, revealing a decrease in the bandgap from 2.96 eV to 2.85 and 2.80 eV, respectively, as shown in Figure 5.10b. Compared to the Pt deposited TiO₂, the Bi deposited TiO₂ shows a higher absorption of visible light. Besides, we found that the absorbance in the visible range of the reduced sample 0.15Pt-0.8Bi-TiO₂-H₂ is strongly enhanced compared to the unreduced one, providing a low bandgap of 2.60 eV.

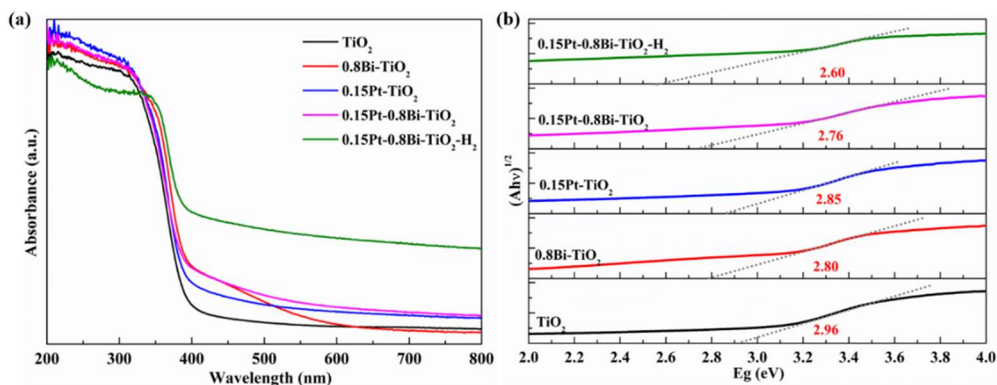


Figure 5.10. UV-Vis diffuse reflectance spectra (DRS) of TiO₂-based samples.

As shown in Figure 5.11a, the DRS profile illustrates that the 0.15Pt-0.8Bi-TiO₂-H₂ sample shows the best absorption of visible light, which could be attributed to the high density of Pt single sites at the low Pt concentration. However, the bandgap is decreased with the increase of Pt loading (Figure 5.11b). Besides, the visible-light absorption of 0.15Pt-0.8Bi-TiO₂-imp is lower than that prepared by the EISA method.

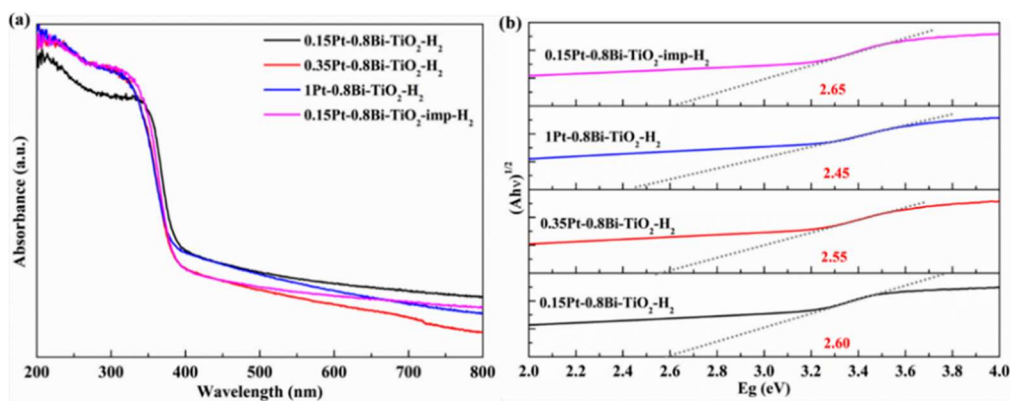


Figure 5.11 UV-Vis diffuse reflectance spectra of xPt-0.8Bi-TiO₂-H₂ and 0.15Pt-0.8Bi-TiO₂-imp-H₂ composites.

5.3.1.7 Electrochemical measurements

The electrochemical measurements were performed to investigate the electron-hole separation and charge transfer performance. As shown in Figure 5.12a and 5.13a, the

transient photocurrent responses of the samples were investigated by several on-off cycles of intermittently visible-light irradiation (>420 nm). TiO_2 has a negligible photocurrent under visible-light irradiation (Figure 5.12a). The deposition of Pt enhanced the photocurrent intensity for TiO_2 under visible-light irradiation. A further enhancement in the photocurrent was observed after adding Bi on 0.15Pt- TiO_2 sample, about 2.5 times as high as that of 0.15Pt- TiO_2 . The increasing photocurrent indicates a more efficient separation of the photoexcited electron-hole pairs, which is mainly due to the transfer of the photogenerated electrons from TiO_2 to the co-catalyst Pt. However, the Bi deposited on TiO_2 has a negligible effect on the separation of electro-hole pairs. This indicates that Bi acts as a promoter, which promotes the charge carrier transformation from TiO_2 to Pt. After the reduction of 0.15Pt-0.8Bi- TiO_2 sample by H_2 , the resulted electrode achieves the highest photocurrent, indicating that the reduced Pt and Bi species can efficiently trap photogenerated electrons of excited TiO_2 . It is worth noting that the photocurrent value of 0.15Pt-0.8Bi- TiO_2 - H_2 was about 3 times higher than that of the sample prepared using the impregnation method.

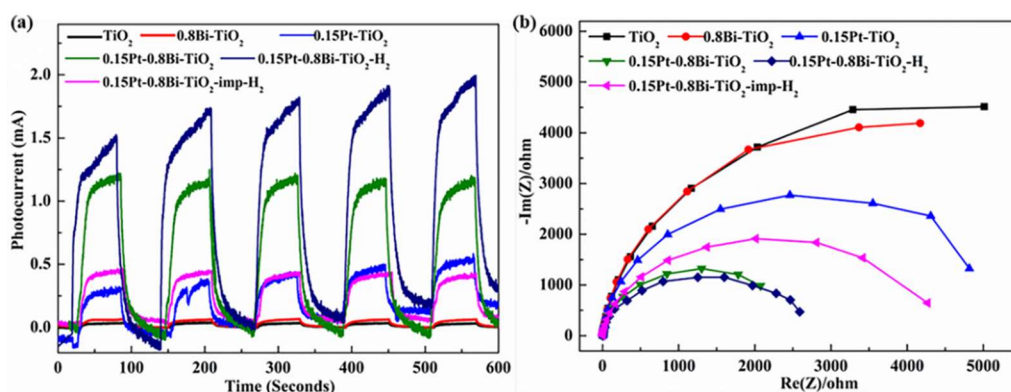


Figure 5.12 The photocurrent plot (a) and EIS Nyquist plots profiles (b) of TiO_2 -based composites in 0.5 M Na_2SO_3 (pH=7).

However, with Pt atoms aggregating into subnano clusters and nanoparticles induced by the increasing Pt concentration, a lower electron separation was observed (Figure 5.13a). Therefore, it is concluded that a more efficient charge separation could be obtained over metal single-sites than over subnano clusters and nanoparticles, allowing more charge carriers to take part in photocatalytic reaction.

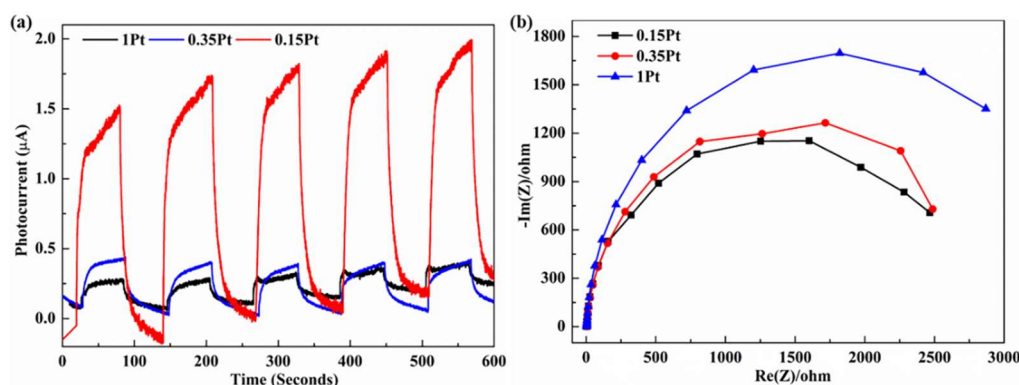


Figure 5.13 The photocurrent plot (a) and EIS Nyquist plots profiles (b) of xPt-0.8Bi-TiO₂-onepot-H₂ composites in 0.5 M Na₂SO₃ (pH=7).

The charge separation characteristics of the photoelectrodes can also be probed by electrochemical impedance spectroscopy (EIS). The Nyquist plot has been extensively used to evaluate the charge transport characteristics of an electrode-electrolyte interface. The semicircle in the high-frequency region reflects the charge transfer resistance (R_{ct}) of the respective electrodes. A low R_{ct} value with a smaller semicircle signifies lower charge transfer resistance.⁴³ Consistent with the results of the photocurrent test, the presence of Pt and Bi both lower the charge transfer resistance, improving the interfacial charge transfer (Figure 5.12b). In addition, the separation efficiency of the electron-hole pair on 0.15Pt-0.8Bi-TiO₂ was better than that of 0.15Pt-0.8Bi-TiO₂-imp. Moreover, the Pt loading amounts remarkably affect the EIS Nyquist plots. As shown

figure 5.13b, a smaller semicircle of 0.15Pt-0.8Bi-TiO₂-H₂ means that the interfacial charge transfer to the electron donor/electron acceptor on Pt single-sites dominant catalyst is faster than Pt subnano clusters and nanoparticles dominant nanocomposites. As the Pt loading increased, the captured carrier would recombine with the photon generated on surface Pt subnano clusters or nanoparticles, which could become a carrier recombination center.

5.3.1.8 Mott-Schottky

The Mott-Schottky plots of the various TiO₂-based samples were recorded from electrochemical impedance spectroscopy to verify the flat band potentials (E_{fb}), as shown in Figure 5.14 and Figure 5.15. The positive slope of the Mott-Schottky plot indicates that all the samples are n-type semiconductors. The conduction band potential (CB) for n-type semiconductors is very close to the flat-band potential value (to be 0.1 eV more negative than E_{fb}).⁴⁴ For example, the flat band potential of TiO₂ at -0.62 eV versus Ag/AgCl (equivalent to -0.42 eV vs normalized hydrogen electrode (NHE)), the CB value is estimated to be -0.52 eV. The xPt-0.8Bi-TiO₂-H₂ showed around -0.60, -0.73 and -1.00 eV of E_{fb} versus Ag/AgCl for 0.15, 0.35 and 1% Pt modified samples, respectively (equivalent to -0.40, -0.53 eV and -0.80 eV vs NHE), as the result, giving the CB of -0.50, -0.63 eV and -0.90 eV, respectively. With the assistance of the Tauc plot, the valence band (VB) values of 0.15Pt-0.8Bi-TiO₂-H₂, 0.35Pt-0.8Bi-TiO₂-H₂ and 1Pt-0.8Bi-TiO₂-H₂ were then calculated to be 2.10, 1.92 V and 1.55 eV, respectively. The bandgap, CB and VB of all the TiO₂ based catalysts are summarized in Table 5.4.

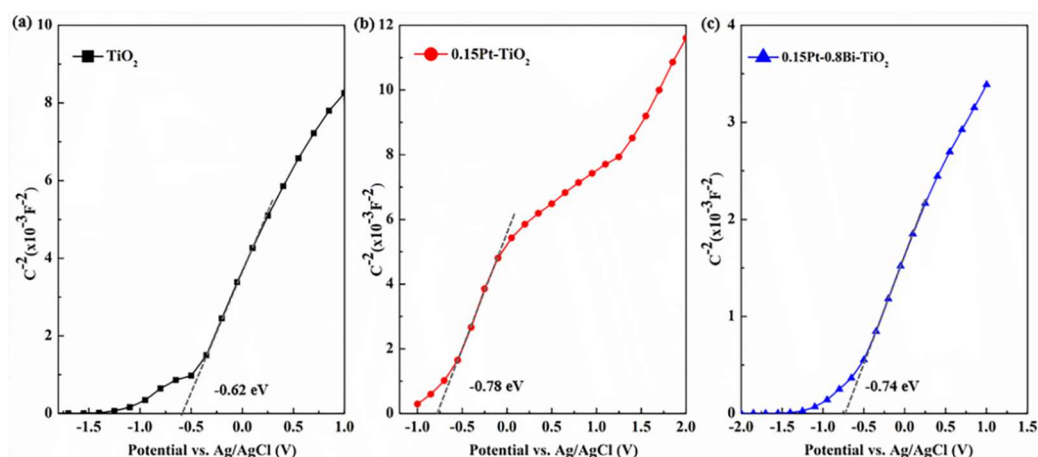


Figure 5.14. The Mott-Schottky plots of TiO_2 -based samples with a frequency of 1 kHz in the dark.

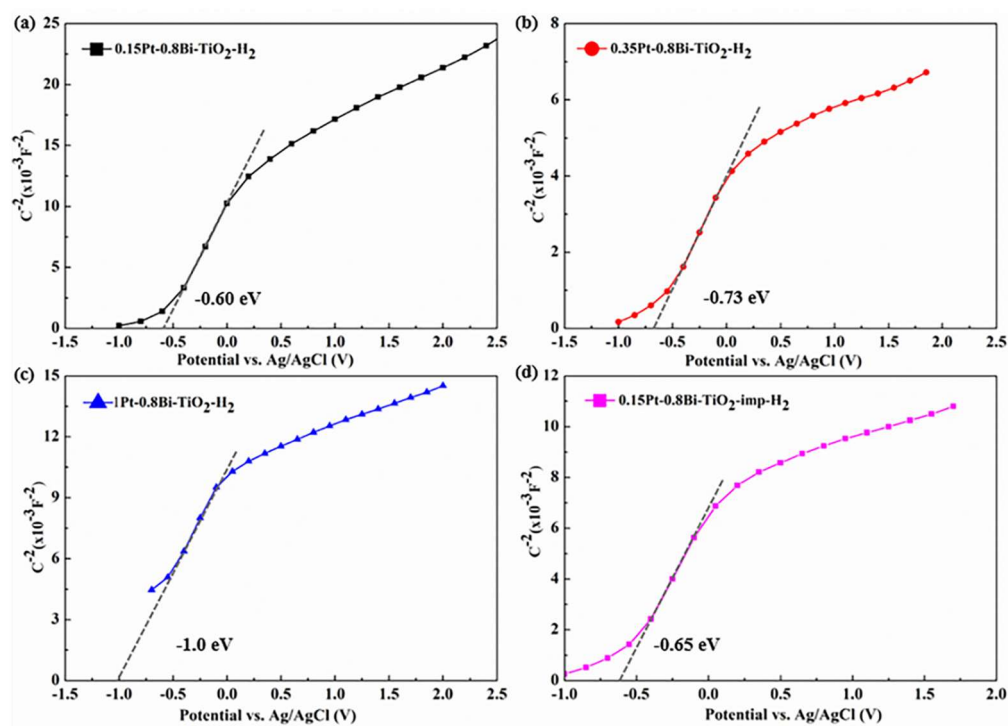


Figure 5.15 The Mott-Schottky plots of $x\text{Pt}-0.8\text{Bi}-\text{TiO}_2\text{-H}_2$ with a frequency of 1 kHz in the darkness.

Table 5.4 Bandgap, conduction band, and valence band of all the TiO₂-based catalysts.

Catalyst	Bandgap (eV)	Valence band (eV)	Conduction band (eV)
TiO ₂	2.96	2.44	-0.52
0.15Pt-TiO ₂	2.85	2.17	-0.68
0.15Pt-0.8Bi-TiO ₂	2.76	2.12	-0.64
0.15Pt-0.8Bi-TiO ₂ -H ₂	2.60	2.10	-0.50
0.35Pt-0.8Bi-TiO ₂ -H ₂	2.55	1.92	-0.63
1Pt-0.8Bi-TiO ₂ -H ₂	2.45	1.55	-0.90
0.15Pt-0.8Bi-TiO ₂ -imp-H ₂	2.65	2.10	-0.55

5.3.2 Photocatalytic performance

The photocatalytic performance of benzyl alcohol oxidation was evaluated using O₂ as an electron acceptor under visible-light irradiation ($\lambda > 420$ nm). The yield of benzaldehyde is only 11.3% over TiO₂ due to almost no absorption of visible light (Figure 5.16a). With the addition of Pt (0.15%), the yield of benzaldehyde increased to 26.5%. The Pt and Bi bimetallic loading TiO₂ catalyst demonstrated remarkable conversion of benzyl alcohol under mild conditions, affording a benzaldehyde yield of 44.8%. The activity is more than 1.7 times and 4 times higher than that of only Pt loaded catalyst and bare TiO₂. The Pt-loaded cocatalyst and promoter Bi on TiO₂ is beneficial for improving light absorption, promoting the photo-generated electron-hole pairs separation, thus enhancing the activities of photocatalysis.⁴⁵ Upon H₂ reduction of 0.15Pt-0.8Bi-TiO₂, the activity over the H₂-reduced sample was further increased to

65.3% of benzaldehyde yield.

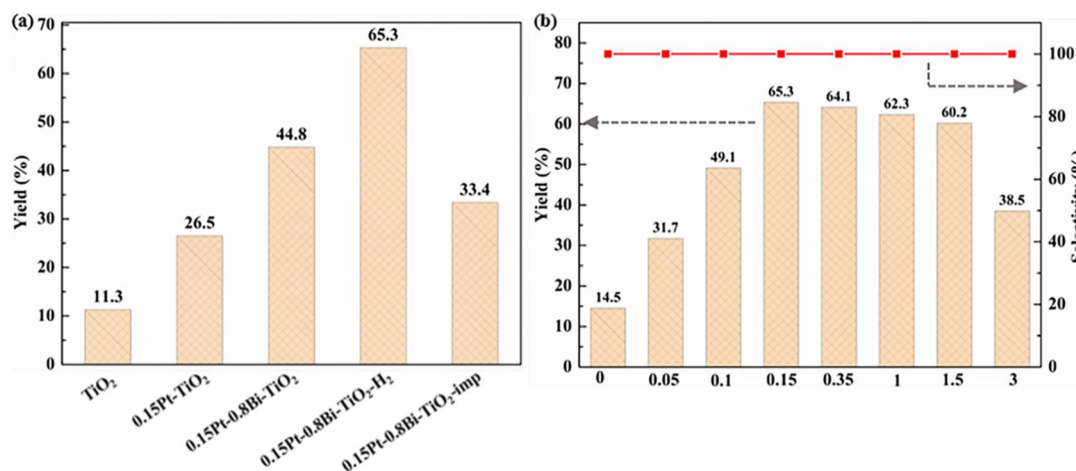


Figure 5.16 The photocatalytic activity of TiO₂-based catalysts (a) and xPt-0.8Bi-TiO₂-H₂ with different Pt loading amounts (b) for benzyl alcohol oxidation. Reaction condition: 10 mg catalyst in 1 mL of 50 mmol/L benzyl alcohol in acetonitrile solution and visible-light irradiation (> 420 nm) for 8 h.

The photocatalytic performance of xPt-0.8Bi-TiO₂ catalysts with different contents of Pt (0-3 wt%) on benzyl alcohol oxidation under visible-light irradiation (Figure 5.16b). A volcano-type curve of benzaldehyde production depending on the Pt content is observed. The deposition of Pt onto the mesoporous TiO₂ enhanced the activity of the catalyst. When the Pt amount is below 0.15 wt%, the increasing factor of the benzaldehyde yield aligns well with the increasing of Pt content, as shown in Figure 5.17. It could be deduced that at a low loading amount below 0.15%, the Pt single sites could be the dominant active sites. With the increase of loading amount over 0.15%, the aggregation of single Pt sites into subnano clusters and nanoparticles was observed, leading to a similar activity (60-70% yield for 0.15-1.5% Pt loading samples). The maximum benzaldehyde yield of 65.3% was observed on 0.15%Pt-0.8Bi-TiO₂-H₂, ca.

4 times high than that on the bare TiO_2 . An excessive amount of Pt doping (3%) leads to a decrease of the benzyl alcohol oxidation activity, which could be ascribed to the suppression of transfer of photoinduced carriers caused by the increased size of Pt nanoparticles.

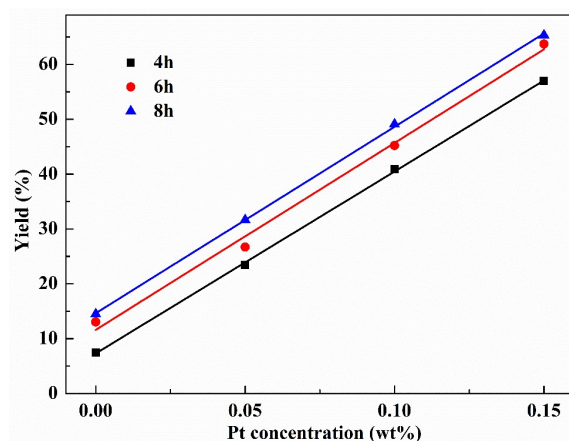


Figure 5.17 The effect of Pt loading amounts on the photocatalytic oxidation benzyl alcohol. Reaction condition: 10 mg catalyst in 1 mL of 50 mmol/L benzyl alcohol in acetonitrile solution and visible-light irradiation (> 420 nm).

Almost no reaction occurred without the presence of any catalyst (Entry 1, Table 5.5). The possible benzyl alcohol itself-reaction has been experimentally excluded. In addition, there was also no product without visible light irradiation (Entry 2) and benzaldehyde production begins with the onset of irradiation (Entry 3-6), indicating that the oxidation reaction over the $x\text{Pt}-0.8\text{Bi}-\text{TiO}_2-\text{H}_2$ catalysts is entirely due to a photocatalytic process. $0.15\text{Pt}-0.8\text{Bi}-\text{TiO}_2-\text{H}_2$ showed 59% conversion and 95.2% selectivity under the irradiation of UV-Vis light after 2h (Entry 3). With the increase of reaction time to 4h, the conversion of benzyl alcohol increased to 80.7%, however, the selectivity of benzaldehyde decreased significantly (67.8%, Entry 4), which could be

ascribed to the occurrence of subsequent benzaldehyde oxidation reaction under UV-vis light. However, almost 100% selectivity to benzaldehyde was achieved under the illumination of visible light at the same conditions (Entry 5). The ^{13}C NMR results (Figure 5.19) verify no formation of benzoic acid in the reaction system, which is consistent with the GC results where the selectivity to benzaldehyde is 100%.

The TOF for benzaldehyde formation on Pt single-sites dominant catalyst (0.15% Pt) is 372.2 h^{-1} , higher than those of Pt subnano clusters and nanoparticles dominant catalysts, i.e., 300 h^{-1} for 0.35% Pt and 95.9 h^{-1} for 1% Pt, respectively, under the identical conditions (Entry 5-7). Noteworthy, all the xPt-0.8Bi-TiO₂ catalysts showed 100% selectivity to benzaldehyde.

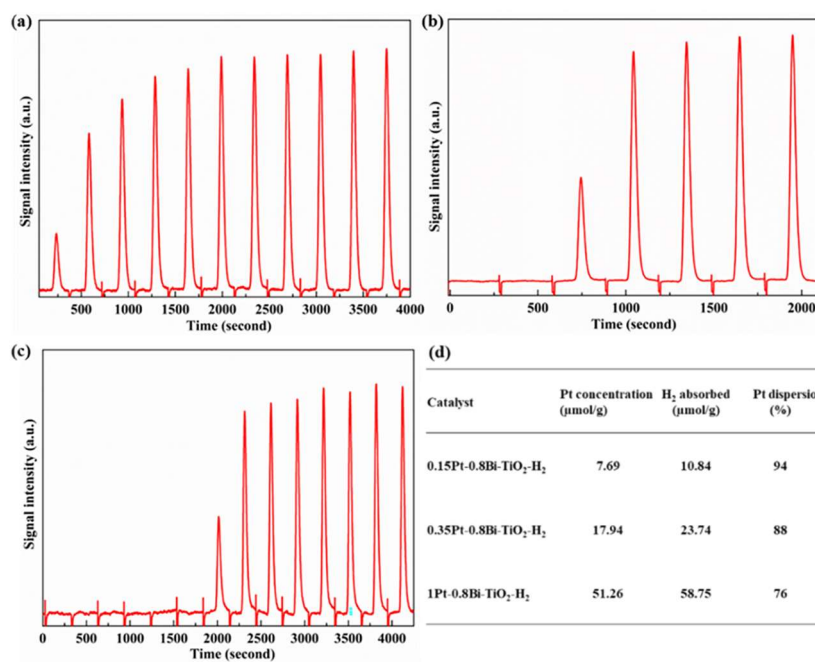


Figure 5.18 H₂-O₂ titration curves (a-c) and properties (d) of xPt-0.8Bi-TiO₂-H₂. (a) 50 mg 0.15Pt-0.8Bi-TiO₂-H₂, (b) 50 mg 0.35Pt-0.8Bi-TiO₂-H₂, (c) 50 mg 1Pt-0.8Bi-TiO₂-H₂.

Table 5.5 Photocatalytic oxidation of benzyl alcohols on xPt-0.8Bi-TiO₂-H₂ under different reaction conditions.

Entry	Substrate	Catalyst	Yield (%)	Selectivity of benzaldehyde (%)	TOF (h ⁻¹)
1	Benzyl alcohol	-	Trace	Trace	-
2 ^a	Benzyl alcohol	0.15Pt-0.8Bi-TiO ₂ -H ₂	Trace	Trace	-
3 ^{b, c}	Benzyl alcohol	0.15Pt-0.8Bi-TiO ₂ -H ₂	59.0	95.2	-
4 ^{b, d}	Benzyl alcohol	0.15Pt-0.8Bi-TiO ₂ -H ₂	80.7	67.8	-
5	Benzyl alcohol	0.15Pt-0.8Bi-TiO ₂ -H ₂	65.3	>99	372.2
6	Benzyl alcohol	0.35Pt-0.8Bi-TiO ₂ -H ₂	64.1	>99	300
7	Benzyl alcohol	1Pt-0.8Bi-TiO ₂ -H ₂	62.3	>99	95.9

Reaction conditions: $\lambda > 420$ nm, catalyst 10 mg, substrate 50 mM, CH₃CN 1mL, oxygen 1 atm, reaction temperature 25 °C, reaction time 8h. ^a In the dark. ^b Under UV-Vis light illumination. ^c Reaction time of 2 h. ^d Reaction time of 4 h. TOF = Moles of substrate consumed/ (moles of Pt active sites*time of reaction); The TOF was calculated based on the conversion of these aromatic alcohols and active sites listed in Table 5.6. Here the active sites were calculated based on the loading concentration and the dispersion of Pt on catalysts obtained using the H₂-O₂ titration method (Figure 5.18). The consumed substrates (μmol) = 50 * conversion of corresponding substrates.

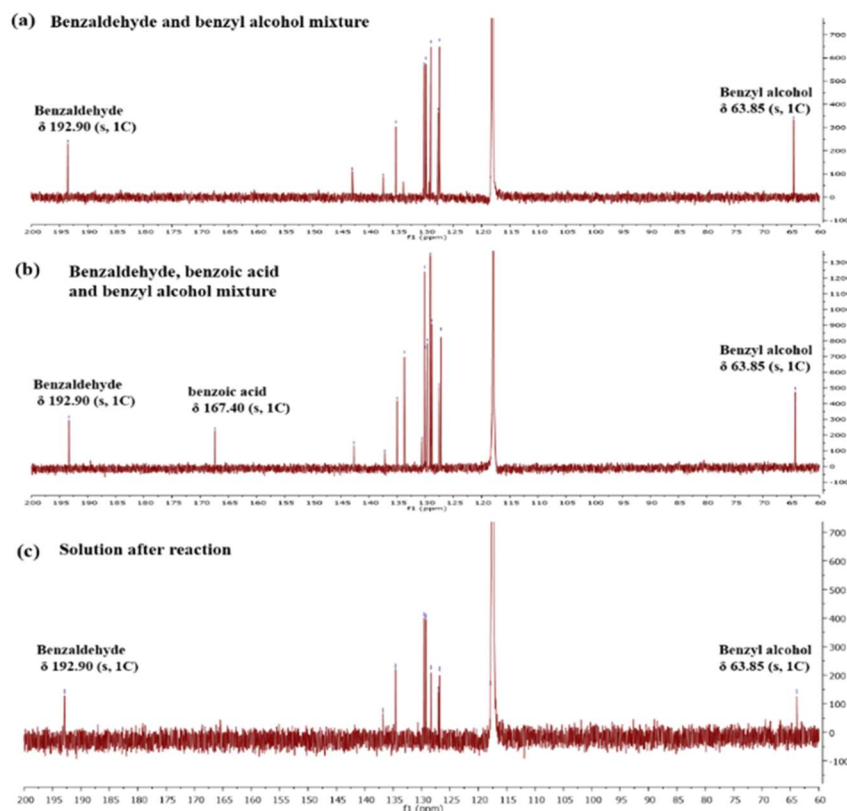


Figure 5.19 ^{13}C NMR (400 MHz, CDCl_3) of standard solution (a, b) and solvent after reaction over 0.15Pt-0.8Bi- $\text{TiO}_2\text{-H}_2$ for 8h (c).

To investigate the general applicability of Pt and Bi bimetallic TiO_2 catalyst for selective oxidation of alcohols, the photocatalytic oxidation of other aromatic alcohols including cinnamyl alcohol over Pt single-sites dominant catalyst (0.15%) was investigated in the presence of O_2 (Table 5.6). Aromatic alcohols can be easily oxidized with high selectivity. In both cases, nearly 100% selectivity to the corresponding aldehydes was obtained. The electron-donating substituents (such as $-\text{CH}_3$ and $-\text{OCH}_3$) improve the rate of the aldehyde formation; for instance, the conversion of 4-methoxybenzyl alcohol is up to 81.1% after 4 h reaction. However, electron-withdrawing substituents (such as $-\text{F}$ and $-\text{C}=\text{C}$) retard that slightly. For alkyl alcohols, the oxidation reaction exhibits low activities. Cyclohexanol and 1-butanol were

oxidized at the conversion of 7.0% and 8.8%, respectively.

Table 5.6 Photocatalytic oxidation of various alcohols on 0.15Pt-0.8Bi-TiO₂-H₂.

Entry	Substrate	Yield of Correspondi ng aldehyde (%)	Selectivity of Corresponding aldehyde (%)	TOF (h ⁻¹)
1	2-methoxybenzyl alcohol	60.1	>99	386.1
2	3-methoxybenzyl alcohol	76.4	>99	686.1
3	4-methoxybenzyl alcohol	81.1	>99	572.2
4	4-methylbenzyl alcohol	74.5	>99	541.7
5	4-chlorobenzyl alcohol	89.4	>99	786.1
6	4-Fluorobenzyl alcohol	55.6	>99	-
7	Benzyl alcohol	57.0	>99	372.2
8	Cinnamyl alcohol	55.6	>99	-
9	Cyclohexanol	7.0 ^a	-	68.1
10	1-Butanol	8.8 ^a	-	54.2

Reaction conditions: $\lambda > 420$ nm, catalyst 10 mg, substrate 50 mM, CH₃CN 1mL, oxygen 1 atm, reaction temperature 25 °C, reaction time 4h. ^a Conversion of alcohol. TOF = Moles of substrate consumed/ (moles of Pt active sites*time of reaction); The TOF was calculated based on the conversion of these aromatic alcohols.

Taken together, it is confirmed that Pt single sites favor the interaction between TiO₂ support and Pt co-catalyst, leading to forming positively charged Pt even if at high reduction temperature (500 °C). The unique Ptⁿ⁺-O-Ti enhances the photo-electrochemical properties of the catalyst, improving its activities on alcohol oxidation.

5.4 Conclusion

In conclusion, a facile synthetic strategy to disperse Pt single sites into a Bi-TiO₂ was developed. A strong interaction between the bimetallic and TiO₂ support has been evidenced. The characterization results reveal that the introduction of Pt single sites onto Bi-TiO₂ enhances better electron-hole separation and transfer than the Pt subnano clusters and nanoparticles dominant catalysts, leading to the improved photocatalytic activity. The 0.15Pt-0.8Bi-TiO₂-H₂ exhibited the best photocatalytic activity of benzyl alcohol oxidation toward a 100% selectivity to benzaldehyde at a high yield of 65.3%, roughly 2.5 and 5.8 times higher than that of 0.15Pt-TiO₂ and bare TiO₂, respectively, as well as higher than that of 0.15Pt-0.8Bi-TiO₂ composites prepared using impregnation method. The achieved TOF value on the 0.15Pt-0.8Bi-TiO₂ is around 1.2 and 3.9 times as high as that of Pt subnano clusters and nanoparticles on a per-Pt-atom basis.

Reference

- [1]. Hudlicky M., Oxidations in organic chemistry. *Analytical Chemistry* **1991**, 63 (17), 837A-837A.
- [2]. Ravelli D., Dondi D., Fagnoni M. et al., Photocatalysis. A multi-faceted concept for green chemistry. *Chemical Society Reviews* **2009**, 38 (7), 1999.
- [3]. Schultz D.M., Yoon T.P., Solar synthesis: Prospects in visible light photocatalysis. *Science* **2014**, 343 (6174), 1239176-1239176.
- [4]. Yoon T.P., Ischay M.A., Du J., Visible light photocatalysis as a greener approach to photochemical synthesis. *Nature Chemistry* **2010**, 2 (7), 527-532.
- [5]. Wu X., Luo N., Xie S. et al., Photocatalytic transformations of lignocellulosic biomass into chemicals. *Chemical Society Reviews* **2020**, 49 (17), 6198-6223.
- [6]. Lang X., Chen X., Zhao J., Heterogeneous visible light photocatalysis for selective organic transformations. *Chemical Society Review* **2014**, 43 (1), 473-486.
- [7]. Mills A., LeHunte S., An overview of semiconductor photocatalysis. *Journal of*

Photochemistry and Photobiology A-Chemistry **1997**, 108 (1), 1-35.

- [8]. Zhang Z., Zuo F., Feng P., Hard template synthesis of crystalline mesoporous anatase TiO₂ for photocatalytic hydrogen evolution. *Journal of Materials Chemistry* **2010**, 20 (11), 2206.
- [9]. Zhou W., Sun F.F., Pan K. et al., Well-ordered large-pore mesoporous anatase TiO₂ with remarkably high thermal stability and improved crystallinity: Preparation, characterization, and photocatalytic performance. *Advanced Functional Materials* **2011**, 21 (10), 1922-1930.
- [10]. Dette C., Pérez-Osorio M.A., Kley C.S. et al., TiO₂ anatase with a bandgap in the visible region. *Nano Letters* **2014**, 14 (11), 6533-6538.
- [11]. Zhang Z., Luo Z., Yang Z. et al., Band-gap tuning of n-doped TiO₂ photocatalysts for visible-light-driven selective oxidation of alcohols to aldehydes in water. *RSC Advances* **2013**, 3 (20), 7215.
- [12]. Kumaravel V., Mathew S., Bartlett J. et al., Photocatalytic hydrogen production using metal doped TiO₂: A review of recent advances. *Applied Catalysis B: Environmental* **2019**, 244, 1021-1064.
- [13]. Diaz-Angulo J., Gomez-Bonilla I., Jimenez-Tohapanta C. et al., Visible-light activation of TiO₂ by dye-sensitization for degradation of pharmaceutical compounds. *Photochemical & Photobiological Sciences* **2019**, 18 (4), 897-904.
- [14]. Humayun M., Raziq F., Khan A. et al., Modification strategies of TiO₂ for potential applications in photocatalysis: A critical review. *Green Chemistry Letters and Reviews* **2018**, 11 (2), 86-102.
- [15]. Feng W., Wu G., Li L. et al., Solvent-free selective photocatalytic oxidation of benzyl alcohol over modified TiO₂. *Green Chemistry* **2011**, 13 (11), 3265.
- [16]. Zheng Z., Huang B., Qin X. et al., Facile in situ synthesis of visible-light plasmonic photocatalysts m@TiO₂ (m = Au, Pt, Ag) and evaluation of their photocatalytic oxidation of benzene to phenol. *Journal of Materials Chemistry* **2011**, 21 (25), 9079.
- [17]. Subramanian V., Wolf E.E., Kamat P.V., Catalysis with TiO₂/gold nanocomposites. Effect of metal particle size on the fermi level equilibration. *Journal of the American Chemical Society* **2004**, 126 (15), 4943-4950.
- [18]. Ran J., Jaroniec M., Qiao S.-Z., Cocatalysts in semiconductor-based photocatalytic CO₂ reduction: Achievements, challenges, and opportunities. *Advanced Materials* **2018**, 30 (7), 1704649.
- [19]. Kou J., Lu C., Wang J. et al., Selectivity enhancement in heterogeneous photocatalytic transformations. *Chemical Reviews* **2017**, 117 (3), 1445-1514.
- [20]. Song H., Liu Z., Wang Y. et al., Template-free synthesis of hollow TiO₂ nanospheres supported Pt for selective photocatalytic oxidation of benzyl alcohol to benzaldehyde. *Green Energy & Environment* **2019**, 4 (3), 278-286.
- [21]. Hua H., Hu C., Zhao Z. et al., Pt nanoparticles supported on submicrometer-sized TiO₂ spheres for effective methanol and ethanol oxidation. **2013**, 105, 130-136.
- [22]. Zhai W.Y., Xue S.J., Zhu A.W. et al., Plasmon-driven selective oxidation of aromatic alcohols to aldehydes in water with recyclable Pt/TiO₂ nanocomposites. *Chemcatchem* **2011**, 3 (1), 127-130.

- [23]. Mondelli C., Ferri D., Grunwaldt J.D. et al., Combined liquid-phase atr-ir and xas study of the bi-promotion in the aerobic oxidation of benzyl alcohol over Pd/Al₂O₃. *Journal of Catalysis* **2007**, 252 (1), 77-87.
- [24]. Corma A., Concepción P., Boronat M. et al., Exceptional oxidation activity with size-controlled supported gold clusters of low atomicity. *Nature Chemistry* **2013**, 5 (9), 775-781.
- [25]. Liu Y., Tsunoyama H., Akita T. et al., Aerobic oxidation of cyclohexane catalyzed by size-controlled au clusters on hydroxyapatite: Size effect in the sub-2 nm regime. *ACS Catalysis* **2011**, 1 (1), 2-6.
- [26]. Yang X.F., Wang A.Q., Qiao B.T. et al., Single-atom catalysts: A new frontier in heterogeneous catalysis. *Accounts of Chemical Research* **2013**, 46 (8), 1740-1748.
- [27]. Wang A.Q., Li J., Zhang T., Heterogeneous single-atom catalysis. *Nature Reviews Chemistry* **2018**, 2 (6), 65-81.
- [28]. Zhang Z., Zhu Y., Asakura H. et al., Thermally stable single atom Pt/m-Al₂O₃ for selective hydrogenation and co oxidation. *Nature Communications* **2017**, 8 (1), 16100.
- [29]. Chen Y., Ji S., Chen C. et al., Single-atom catalysts: Synthetic strategies and electrochemical applications. *Joule* **2018**, 2 (7), 1242-1264.
- [30]. Zhou W., Li W., Wang J.Q. et al., Ordered mesoporous black TiO₂ as highly efficient hydrogen evolution photocatalyst. *Journal of the American Chemical Society* **2014**, 136 (26), 9280-9283.
- [31]. Wang F., Jiang Y., Wen X. et al., Confined au-pd ensembles in mesoporous TiO₂ spheres for the photocatalytic oxidation of acetaldehyde. *ChemCatChem* **2013**, 5 (12), 3557-3561.
- [32]. Ahila M., Malligavathy M., Subramanian E. et al., Effect of anodization time on the growth of twinned pyramid crystals of bismite from polyhedral bismuth particle by facile electrolysis-based oxidation. *Particulate Science and Technology* **2018**, 36 (6), 655-659.
- [33]. Wei H., Liu X., Wang A. et al., Feox-supported platinum single-atom and pseudo-single-atom catalysts for chemoselective hydrogenation of functionalized nitroarenes. *Nature Communications* **2014**, 5 (1), 5634.
- [34]. Lu T., Du Z., Liu J. et al., Aerobic oxidation of primary aliphatic alcohols over bismuth oxide supported platinum catalysts in water. *Green Chemistry* **2013**, 15 (8), 2215.
- [35]. Kuhaudomlap S., Mekasuwandumrong O., Praserttham P. et al., The H₂-treated TiO₂ supported pt catalysts prepared by strong electrostatic adsorption for liquid-phase selective hydrogenation. *Catalysts* **2018**, 8 (2), 87.
- [36]. Lan M., Zhang B., Cheng H. et al., Chemoselective hydrogenation of 3-nitrostyrene to 3-aminostyrene over Pt-Bi/TiO₂ catalysts. *Molecular Catalysis* **2017**, 432, 23-30.
- [37]. Yang Y., Gao P., Ren X. et al., Massive Ti³⁺ self-doped by the injected electrons from external Pt and the efficient photocatalytic hydrogen production under visible-light. *Applied Catalysis B: Environmental* **2017**, 218, 751-757.
- [38]. Mekasuwandumrong O., Chaitaworn S., Panpranot J. et al., Photocatalytic liquid-phase selective hydrogenation of 3-nitrostyrene to 3-vinylaniline of various treated-

TiO₂ without use of reducing gas. *Catalysts* **2019**, 9 (4), 329.

[39]. Young C., Lim T.M., Chiang K. et al., Photocatalytic oxidation of toluene and trichloroethylene in the gas-phase by metallised (Pt, Ag) titanium dioxide. *Applied Catalysis B: Environmental* **2008**, 78 (1-2), 1-10.

[40]. Xu T., Zheng H., Zhang P., Isolated pt single atomic sites anchored on nanoporous TiO₂ film for highly efficient photocatalytic degradation of low concentration toluene. *Journal of Hazardous Materials* **2020**, 388, 121746.

[41]. Qiao B., Wang A., Yang X. et al., Single-atom catalysis of co oxidation using Pt₁/FeO_x. *Nature Chemistry* **2011**, 3 (8), 634-641.

[42]. Wang F., Jiang Y., Lawes D.J. et al., Analysis of the promoted activity and molecular mechanism of hydrogen production over fine Au–Pt alloyed TiO₂ photocatalysts. *ACS Catalysis* **2015**, 5 (7), 3924-3931.

[43]. Roy N., Park Y., Sohn Y. et al., Green synthesis of anatase TiO₂ nanocrystals with diverse shapes and their exposed facets-dependent photoredox activity. *ACS Applied Materials & Interfaces* **2014**, 6 (19), 16498-16507.

[44]. Yu L., Zhang X., Li G. et al., Highly efficient Bi₂O₂CO₃/BiOCl photocatalyst based on heterojunction with enhanced dye-sensitization under visible light. *Applied Catalysis B: Environmental* **2016**, 187, 301-309.

[45]. Yang J.H., Wang D.G., Han H.X. et al., Roles of cocatalysts in photocatalysis and photoelectrocatalysis. *Accounts of Chemical Research* **2013**, 46 (8), 1900-1909.

Chapter 6. Pt-deposited hierarchical flower-like Bi₂WO₆ microspheres for the selective photooxidation of benzyl alcohol

6.1 Introduction

Solar energy-driven photocatalytic alcohols oxidation is one of the most attractive green technologies in the field of aldehydes production, which is a fundamentally important process due to the high value of aldehydes as intermediates in the perfume industry.¹⁻³ In the photocatalytic process, TiO₂ has been extensively studied owing to its advantages of low cost, non-toxicity, and stability.⁴⁻⁶ However, the practical application of TiO₂ is still limited due to low quantum efficiency and its large bandgap.⁴ Graphitic carbon nitride, like g-C₃N₄, is an extensively studied photocatalyst due to its lower bandgap (~2.8 eV), and the abundance of surface groups that enable coupling to other photocatalysts.^{7, 8} However, g-C₃N₄ has inferior chemical stability⁹ because it can be susceptible to degradation by hydroxyl radicals.¹⁰ It can also exhibit high recombination rates, low conductivity, insufficient visible-light absorption, and low solvent-accessible surface area.¹¹ Therefore, tremendous efforts have been made to develop other novel semiconductor photocatalysts.

In recent years, naturally abundant and non-toxic bismuth-based oxides (BiOX, X=Cl, Br, I, W, or Mo), have emerged as potential visible-light-driven photocatalysts due to their strong visible light absorption ($\lambda > 400$ nm).¹²⁻¹⁴ Particularly, bismuth-based oxides are most evaluated in photocatalytic oxidation reaction. For example, Fu et al¹⁵ reported that bismuth tungstate (Bi₂WO₆) synthesized by a hydrothermal crystallization

process showed a good photooxidation capability due to its sufficiently positive valence band (VB) position. The potential of its VB (+2.94 V vs NHE at pH = 7) is more positive than the oxidation potential of H₂O (OH•/H₂O = +2.38 V vs NHE at pH = 7)¹⁶. The OH• formed from H₂O oxidation is proven to be an important oxidant for the photocatalytic oxidation reactions. Therefore, Bi₂WO₆, as a promising photooxidation catalyst, has received great attention and has been applied in various oxidation reactions.¹⁷⁻¹⁹ Besides, Mondelli et al. reported that the presence of metal promoter Bi largely hindered the formation of carboxylates from benzaldehyde oxidation.²⁰ Thus, BiOW composites have been chosen here for selective conversion of benzyl alcohols into benzaldehyde.

Studies have reported that the photo-catalytic performance of Bi₂WO₆, a kind of multicomponent oxide, is largely dependent on its structure, morphology and components.^{8, 18-19, 21-29} For example, Fu's group found that Bi_{3.84}W_{0.16}O_{6.24}/Bi₂WO₆ composite exhibited an enhanced photocatalytic activity on the degradation of methylene blue compared with either Bi₂WO₆ or Bi_{3.84}W_{0.16}O_{6.24} due to the suppressed photoexcited electron-hole recombination.²⁶ Moreover, the shape-associated visible-light-driven activities of Bi₂WO₆ on the degradation of Rhodamine B has also been reported and flower-like Bi₂WO₆ showed the best activity.¹⁹ However, how the morphologies and components would affect the activities of bismuth tungsten-based composites has not been studied systemically.

In this chapter, various BiOW composites were fabricated via a facile, template-free hydrothermal method. Their structure and Bi/W ratios were manipulated via changing pH values of the precursor suspension solution. The photocatalytic oxidation of benzyl alcohol was chosen as a model reaction to investigate the effects of structure and component. However, Bi₂WO₆ with a relatively positive conduction band (+0.24 V)¹⁵

hinders the efficient consumption of photoexcited electrons and weakens the activity of Bi_2WO_6 . It was demonstrated that the Pt modified bismuth-based oxides nanocomposite is a promising catalyst for alcohol oxidation.¹⁴ The doping of Pt nanoparticles into photocatalysts could improve the visible-light harvesting, charge-separation, and electron-transport of the resultant catalyst, leading to the enhanced photocatalytic activity.²⁷ Therefore, to further improve the charge separation efficiency, the reductive Pt cocatalyst was loaded onto the surface of Bi_2WO_6 . It turns out to be an effective way to enhance the photocatalytic performance in benzyl alcohol oxidation.

6.2 Experimental

6.2.1 Preparation of samples

The procedure for Bi_2WO_6 synthesis is based on a modified hydrothermal approach.²³ Typically, 0.98 g of $\text{Bi}(\text{NO}_3)_3 \cdot 5\text{H}_2\text{O}$ was ultrasonicated in 40 mL of 0.3 M HNO_3 aqueous solution for complete dissolution. Then, 20 mL of 0.05 M Na_2WO_4 solution was added under vigorous stirring and the white precipitate was formed. Subsequently, a certain amount of 0.2 M NaOH solution was added to adjust the pH value to 0.9, 7, 9, 11 and 13, respectively. and the mixing solution was kept under stirring for 24 h. After that, it was transferred to 100 mL Teflon-sealed autoclave and maintained at 433 K for 8 h. The resulting samples were recovered by filtration, washed by water, and fully dried at 333 K in the oven to afford the final samples denoted as BiOW-n (n is the pH value).

The 0.1wt%Pt/BiOW-0.9 sample was synthesized by the photo-deposition method.¹⁴ BiOW-0.9 sample was dispersed in methanol aqueous solution (50 vol%) containing a stoichiometry of chloroplatinic acid under vacuum. The mixture was illuminated by a 300W Xenon arc lamp (CX-04E) for 2 h under magnetic stirring in a water bath at 283

K and then afforded Pt-loaded BiOW-0.9.

6.2.2 Characterization

The steady-state photoluminescence (PL) spectra were recorded on a Jasco FP-8500 fluorescence spectrophotometer at an excitation wavelength of 330 nm. Scanning electron microscopy (SEM) with energy-dispersive X-ray spectroscopy (EDX) was performed on a JEOL 7100F-field emission scanning electron microscope at an accelerating voltage of 15 kV. Electrochemical impedance spectra (EIS) were recorded under an AC perturbation signal of 10 mV over the frequency range of 1 Hz-100 kHz at 3V. The Mott-Schottky measurement was performed at 1 kHz under dark conditions in 0.5 M Na₂SO₃. The method introduction of XRD, BET and UV-Vis characterizations and photocurrent measurements refers to Chapter 5.2.2.

6.2.3 Photocatalytic oxidation of benzyl alcohol

The detail about the photocatalytic experiment and production analysis refer to Chapter 5.2.3.

6.3 Results and discussion

6.3.1 Structure characterization

A series of BiOW-n under different pH of precursor suspension solutions was synthesized via a simple hydrothermal route. The crystallinity and phase purity of the catalysts were confirmed by XRD analysis. As shown in Figure 6.1, the XRD pattern of BiOW-0.9 could be well indexed to the orthorhombic phase of Bi₂WO₆ (JCPDS No. 39-0256), with (113) as the preferred orientation, along with (006), (206), (119) and (226) reflections. No impurity peak was observed, indicating the high purity of the

prepared sample. When the pH was increased to 7 and 9, the predominant phases of Bi_2WO_6 were observed as well. Compared with BiOW-0.9, BiOW-7 and BiOW-9 exhibited the enhanced intensity of peaks, indicating the high crystallinity of the Bi_2WO_6 phase.²⁸ BiOW-11 consists of two mixed phases of Bi_2WO_6 (JCPDS No. 39-0256) and $\text{Bi}_{3.84}\text{W}_{0.16}\text{O}_{6.24}$ (JCPDS No. 43-0047, labeled with red stars). In the pattern of BOW-13 composite, there are obvious characteristic peaks of B_2O_3 (JCPDS No. 41-1449). This phenomenon can be explained by the factor that the alkaline solution promotes the hydrolysis of the Bi^{3+} . As a result, the rate of Bi_2WO_6 nucleation is then depressed due to the greatly reduced concentration of Bi^{3+} ions during the hydrothermal process, leading to a high ratio of Bi/W on the sample.²⁸ The XRD data reveal that the components of the BiOW composites are affected by the pH value of the synthesis solution, while the Pt loading did not alter the crystal structure of BiOW-0.9. It is noted that no diffraction peak of Pt was detected in the XRD patterns of Pt/BiOW-0.9 sample, which implies that the fine Pt were highly dispersed on the BiOW-0.9 support.

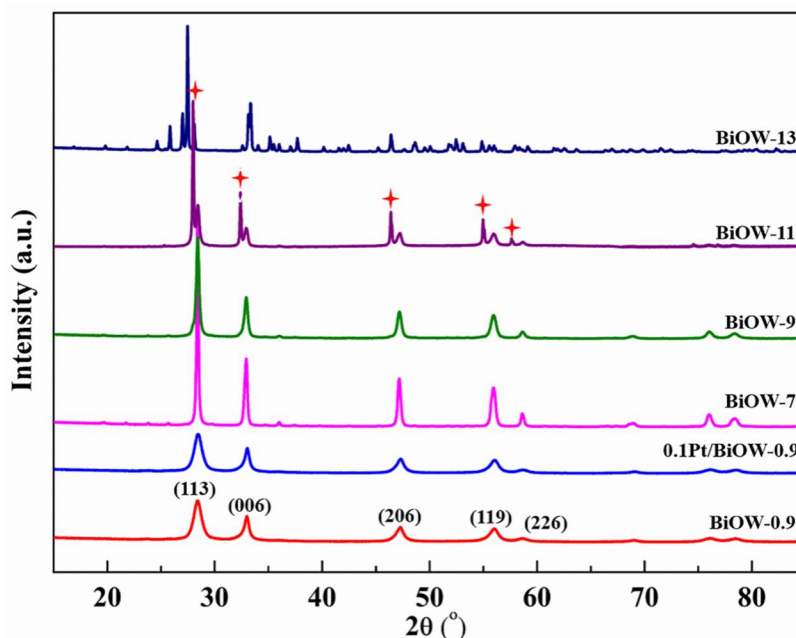


Figure 6.1 XRD patterns of different Bi_2WO_6 samples.

To study the effects of pH value on the morphology of BiOW-n samples, the SEM images of BiOW-n samples are displayed in Figure 6.2. BiOW-0.9 possesses hierarchical flower-like microspheres composed of regularly aligned nanosheets (Figure 6.2a-b). These nanosheets are aligned to the spherical surface at a specific angle with clearly oriented layers. Abundant pores with varying diameters were formed, which may serve as transport channels for small molecules. BiOW-7 consists of random single nanosheets (Figure 6.2c), while the morphology of BiOW-9 (Figure 6.2d) changed to nanoplate which was made up of stacked nanosheets. This is because the hydrolysis of Bi^{3+} is accelerated with increasing pH value, leading to the concentration of Bi^{3+} is greatly reduced. The rate of Bi_2WO_6 nucleation is then depressed slowing down the aggregation of Bi_2WO_6 nuclei before the intrinsic anisotropic growth of Bi_2WO_6 . Sheet-like Bi_2WO_6 structures instead of flower-like superstructures are formed under high pH condition. These results therefore show a pH-dependent evolution of morphology from 3D flower-like superstructures to 2D nanosheet-like structures.²⁸ BiOW-11 composite ($\text{Bi}_2\text{WO}_6/\text{Bi}_{3.84}\text{W}_{0.16}\text{O}_{6.24}$, Figure 6.2e) and BiOW-13 (Bi_2O_3 , Figure 6.2f) exhibit a block-like morphology with different diameter and thickness. It is concluded that the change of pH can greatly affect the morphology of the BiOW composites. As shown in Table 6.1, it seems that the pH value also affects the surface areas determined by the BET measurements. BiOW-0.9 with a hierarchical structure has a larger surface area ($35 \text{ m}^2/\text{g}$) than BiOW-7 with nanosheet-like structure ($3.3 \text{ m}^2/\text{g}$) and BiOW-9 with nanoplate-like structure ($1.7 \text{ m}^2/\text{g}$). The higher BET surface area of the BiOW-0.9 sample than that of the BiOW-7 and BiOW-9 samples

could be due to the poor crystalline phase of the BiOW-0.9 sample, as shown in XRD analysis.

SEM characterization was also conducted on the Pt loaded BiOW-0.9 (Figure 6.3). The morphology is identical to that of the well-distributed flower-like BiOW-0.9 (Figure 6.3a-b). The EDS analysis (Figure 6.3b) reveals the existence of Bi, W, O, Pt elements and the uniform distribution indicates the fine distribution of Pt on BiOW-0.9 composite. The Pt deposition onto BiOW-0.9 did not make a significant difference in the surface area ($33.8 \text{ m}^2/\text{g}$ for 0.1Pt/ BiOW-0.9 and $35 \text{ m}^2/\text{g}$ for BiOW-0.9, respectively) since the morphological structure remains as revealed in SEM.

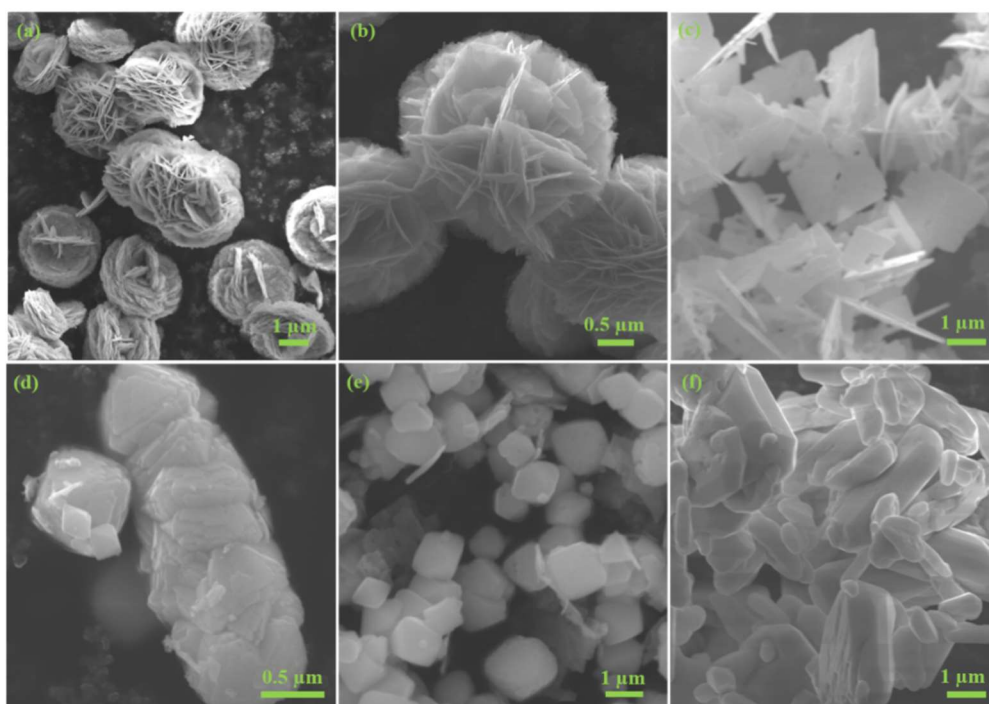


Figure 6.2 SEM images of (a-b) BiOW-0.9, (c) BiOW-7, (d) BiOW-9, (e) BiOW-11 and (f) BiOW-13 composites.

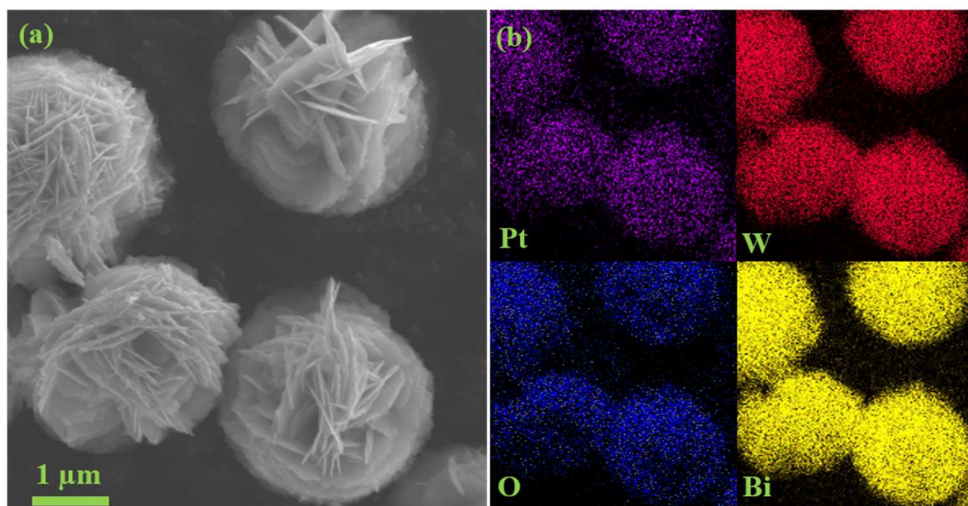


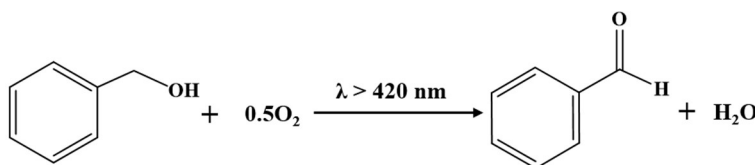
Figure 6.3 SEM image (a) and EDX mapping images (b) of 0.1Pt/BiOW-0.9.

6.3.2 Photocatalytic performance

The photocatalytic performance of various BiOW-*n* samples under identical conditions was evaluated using benzyl alcohol oxidation as a model reaction. As shown in Table 6.1, the blank test without any catalyst reveals that benzyl alcohol is stable under visible light illumination. The nanosheet-like BiOW-7 and nanoplate-like BiOW-9 produced benzaldehyde at lower reaction rates compared to BiOW-0.9. It indicates that the photocatalytic performance of these Bi₂WO₆ samples strongly depends on their morphological structure. Several previous studies^{28, 29} also have shown that the photocatalytic activities of Bi₂WO₆ are strongly dependent on their shape, size, and structure under visible-light irradiation. Interestingly, Bi₂WO₆/Bi_{3.84}W_{0.16}O_{6.24} composite (BiOW-11) and Bi₂O₃ (BiOW-13) were inactive. This finding is different from the results obtained by Fu et al²⁶. They reported that the formation of Bi_{3.84}W_{0.16}O_{6.24}/Bi₂WO₆ significantly improved photocatalytic efficiency than bulk Bi_{3.84}W_{0.16}O_{6.24} and Bi₂WO₆. This could be related to their low surface area. The low BET surface area of the BiOW-11 and BiOW-13 samples results in a decrease of adsorption percentages of benzyl alcohol and O₂ molecules.

With cocatalyst loading, the photocatalytic activity of 0.1Pt/BiOW-0.9 composite on benzyl alcohol oxidation is further enhanced (Table 6.1). The flower-like 0.1Pt/BiOW-0.9 achieved the highest activity with benzaldehyde production at a rate of 46.2 mmol/g/h. As shown in Figure 6.4, 0.1Pt/BiOW-0.9 reached a conversion of 70% with 100% selectivity after 24 h irradiation. Some studies have demonstrated that loading suitable cocatalysts on semiconductors is beneficial for the strong light absorbance and can also provide more trapping sites for the photogenerated charges, promoting the photo-generated electron-hole pairs separation, thus enhancing the photocatalytic activity.³⁰

Table 6.1 Oxidation of benzyl alcohol over various photocatalysts.



Catalysts	S_{BET} (m^2/g)	Activity (mmol/ h/g)	Conversion (%)	Selectivity (%)
None	/	trace	trace	/
BiOW-0.9	36.0	28.9	23.1	>99
BiOW-7	3.3	10.9	8.7	>99
BiOW-9	1.7	8.6	6.9	>99
BiOW-11	trace	trace	trace	/
BiOW-13	trace	trace	trace	/
0.1Pt/ BiOW-0.9	33.8	46.2	36.9	>99

Reaction conditions: $\lambda > 420 \text{ nm}$, catalyst 10 mg, benzyl alcohol 50 mM, visible-light irradiation time: 4 h, oxygen 1 atm.

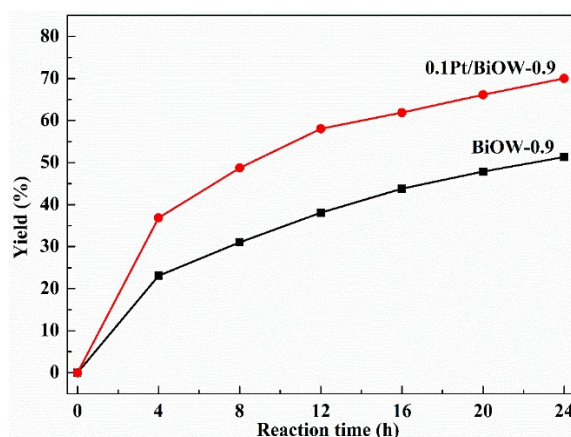


Figure 6.4 Time-online of photocatalytic oxidation of benzyl alcohol on BiOW-0.9 and 0.1Pt/ BiOW-0.9. Reaction conditions: $\lambda > 420$ nm, catalyst 30 mg, benzyl alcohol 50 mM, CH_3CN 1 mL, reaction temperature 25 °C, oxygen 0.1 MPa.

6.3.3 Photoelectrochemical performance

To explain the mechanism governing the pH effect of the precursor suspensions and co-catalyst Pt on the photocatalytic activity, the energy level alignment of BiOW-n and 0.1Pt/BiOW-0.9 were studied. As depicted in Figure 6.5, the optical absorption properties of BiOW-n (0.9, 7 and 9) measured using a UV-vis spectrometer are nearly identical, and these samples display photo-absorption from the ultraviolet region to visible light as far as a wavelength up to 450 nm. All the samples exhibit a significant light absorption in the wavelengths lower than about 450 nm. The bandgap energy (E_g) of flower-like BiOW-0.9 (Bi_2WO_6) is estimated to be around 2.52 eV based on the absorption spectrum and the $(A_{\text{hv}}) = K(h\nu - E_g)^{n/2}$ formula ($n = 1$ for direct absorption), in agreement with previous results.³¹ The UV-vis diffuse reflectance spectrum of BiOW-11 and BiOW-13 referring to $\text{Bi}_{3.84}\text{W}_{0.16}\text{O}_{6.24}/\text{Bi}_2\text{WO}_6$ and Bi_2O_3 exhibited an absorption edge at about 430 to 450 nm corresponding to E_g of 2.55 and 2.62 eV, respectively. For comparison, the same measurement was conducted for 0.1Pt/BiOW-0.9, providing an enhanced photo-absorption with the narrower bandgap of 2.50 V than

the bare BiOW-0.9. In this work, the different of the bandgap is observed for the BiOW composite with different component. Bi₂O₃ exhibited the widest bandgap (2.62 eV). Interestingly, it is found that the shape and structure of the Bi₂WO₆ (BiOW-0.9, BiOW-7 and BiOW-9) do not affect the optical absorption and bandgap energy, which is different with the conclusions obtained by Zhang et al.²⁸ However, the photocatalytic activities of Bi₂WO₆ on benzyl alcohol oxidation activity are dependent on their structure and shape. And flower-like Bi₂WO₆ (BiOW-0.9) showed the best activity. This could be due to these emanative pores in the flower-like BiOW-0.9 sample allowing light waves to penetrate deep inside the photocatalyst, leading to high mobility of charge,^{32, 33} which greatly promotes its photocatalytic performance. In addition, the high BET surface area with the formation of pore in flower-like BiOW-0.9 sample also benefits the absorption of benzyl alcohol and O₂ molecular, thus enhancing the photocatalytic activity of Bi₂WO₆.^{24, 34}

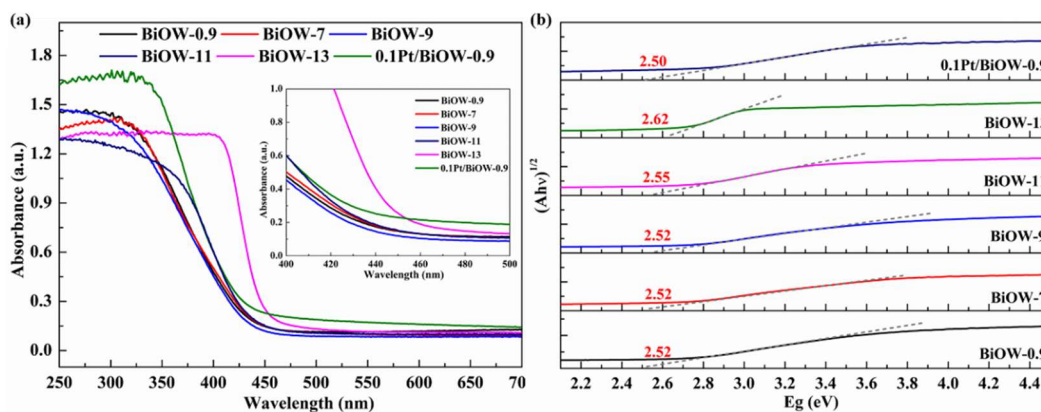


Figure 6.5 UV-vis diffuse reflectance spectra (a) and the corresponding $(Ah\nu)^{1/2}$ versus photon energy plot (b) of BiOW-n and 0.1Pt/BiOW-0.9.

The flat-band potentials of 0.1Pt/BiOW-0.9 and BiOW-n were further determined by the Mott-Schottky plots in a Na₂SO₃ aqueous solution (Figure 6.6a). All the samples show a positive slope as expected for n-type semiconductors (Figure 6.6a). The flat band of BiOW-0.9 was measured to be -0.70 eV (vs Ag/AgCl) according to the Mott-

Schottky equation ($C^{-2} = 2(V_a - V_{fb} - kT/e)/e\epsilon\epsilon_0 N_d$, when $C^{-2} = 0$, $V_{fb} = V_a - kT/e = V_a - 0.02$ V), corresponding to -0.50 eV (vs NHE pH=7). The flat-band potential is located just below the conduction band minimum ($E_{CB} = E_{fb} - 0.1$ eV = -0.60 eV)³⁵. Its valence band (VB) was estimated to be $+1.92$ eV using its bandgap (2.52 eV). All the Bi_2WO_6 samples with different structures provide a comparable flat band and both show more negative CB (around -0.60 eV) than O_2 reduction potential ($\text{O}_2/\text{O}_2^{\bullet-} = -0.16$ eV vs. NHE at pH = 7), implying activated oxygen could be formed on the surface of these materials. The flat-band potential of $0.1\text{Pt}/\text{BiOW-0.9}$ is -0.80 eV (vs Ag/AgCl), corresponding to -0.60 eV (vs NHE at pH = 7) and its CB and VB are -0.70 and 1.80 eV, respectively. The obtained band structures of flower-like BiOW-0.9 and $0.1\text{Pt}/\text{BiOW-0.9}$, BiOW-11 ($\text{Bi}_{3.84}\text{W}_{0.16}\text{O}_{6.24}/\text{Bi}_2\text{WO}_6$) and BiOW-13 (Bi_2O_3) are presented in Figure 6.6b. Since $\text{O}_2/\text{O}_2^{\bullet-}$ display a standard redox potential (vs. NHE) of -0.16 eV is below the redox capability of the flower-like BiOW-0.9. Hence, in theory, BiOW-0.9 can accelerate the reduction of O_2 to $\text{O}_2^{\bullet-}$ by transferring photo-generated electrons from BiOW-0.9 to O_2 on the catalyst surface.

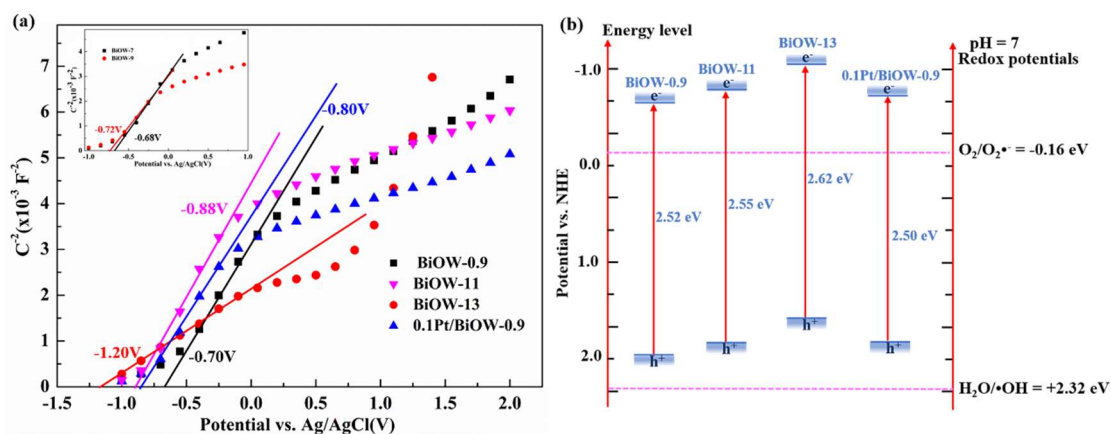


Figure 6.6 (a) Mott-Schottky plots of $0.1\text{Pt}/\text{BiOW-0.9}$ and BiOW-n collected at a frequency of 1 kHz and (b) their band gaps compared with redox potentials of hydroxyl and superoxide radicals.

The process of electron-hole separation and charge migration on 0.1Pt/BiOW-0.9 and BiOW-n samples were further studied by the photoelectrochemical measurements. As shown in Figure 6.7a, the transient photocurrent responses of the samples were investigated by several on-off cycles of intermittently visible light irradiation (>420 nm). It was observed that the Pt loading with 0.1wt% could enhance the photocurrent of BiOW-0.9 significantly, about 2 times as high as that of the bare BiOW-0.9 sample. Besides, the results show that more effective electron-hole separation of flower-like BiOW-0.9 electrode in comparison with nanosheet BiOW-7 and nanoplate BiOW-9 electrodes. However, from Table 6.1 and Figure 6.7a, the flower-like BiOW-0.9 exhibits enhanced photocatalytic activity (28.9 mmol/h/g) compared with that of the plate-like BiOW-7 (10.9 mmol/h/g), although they have similar photocurrent intensity. The various photocatalytic activities of these two samples should be due to the difference in structure and the BET surface areas resulting from their distinct morphologies.

As shown in Figure 6.7b, the 0.1Pt/BiOW-0.9 exhibits the smallest semicircle in Nyquist plots, corresponding to the lowest charge transfer resistance, which indicates the fastest electron transfer rate.³⁶ This could be mainly due to the diffusion of the photo-generated electrons from Bi_2WO_6 to the co-catalyst Pt. Combined with the results of photocurrent and EIS, we conclude that the flower-like BiOW-0.9 facilitates more fast separation and transport of photogenerated electron-hole pairs than nanosheet BiOW-7 and nanoplate BiOW-9. This could be related to acidic precursor suspensions leading to the formation of smaller crystalline grains. The small crystalline grains could reduce the opportunity of electron-hole recombination and the charge carriers can more easily transfer to the surface of samples.²⁹ The rapid electron-hole separation and electron migration are beneficial to the improvement of the photocatalytic activity. The nanosheet BiOW-7 and nanoplate BiOW-9 show a similar profile of charge separation

and transfer, which could be ascribed to their similar nanostructure.

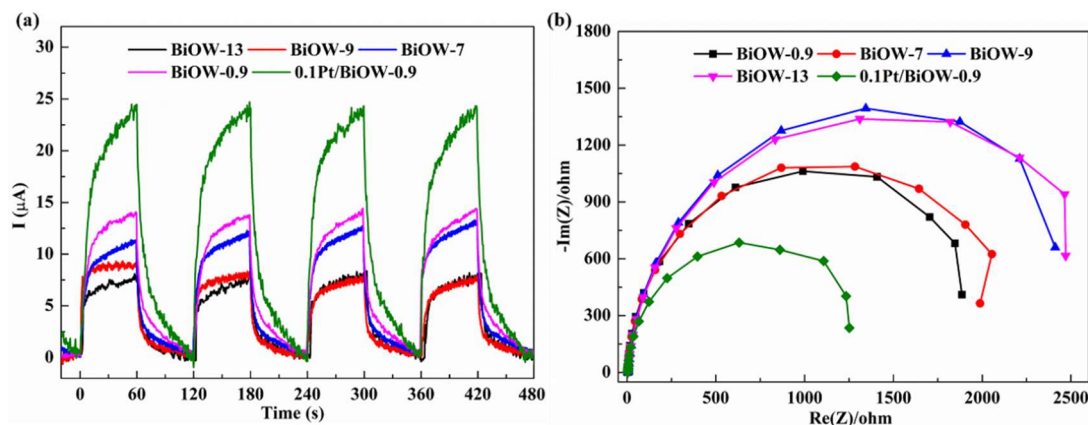


Figure 6.7 The photocurrent plot (a) and EIS Nyquist plots profiles (b) of 0.1Pt/BiOW-0.9 and BiOW-n composites in 0.5 M Na_2SO_3 (pH=7).

To investigate the recombination rate of photo-induced electrons and holes, the photoluminescence (PL) spectra of the prepared samples were measured and shown in Figure 6.8. The measurements were carried out under the exciting wavelength of 350 nm. All Bi_2WO_6 based samples exhibit two PL peaks located at ~ 430 nm (~ 2.88 eV) and ~ 470 nm (~ 2.64 eV), which could be originated from the main emission of bandgap transition as well as recombination of free carriers. The peak presented at 2.64 eV indicates the existence of a shallow defect level in the bandgap of BiOW-n composite.³⁷ The peak position of ~ 2.88 eV demonstrates that a deep defect level which was introduced into BiOW-n.³⁷ The PL processes are known to be related to the free exciton recombination process. And this process is strongly affected by some factors, such as particle sizes³⁸, surface areas³⁹, defects⁴⁰, and impurities⁴¹. 0.1Pt/BOW-0.9 shows the lowest PL intensity, suggesting the lowest recombination efficiency of photo-induced electrons and holes. The pore in nanoflowers-like nanostructure of BiOW-0.9 could provide more channels for the charge transfer, promoting the charge transfer, which results in the efficient inhibition of the electron-hole recombination rate.

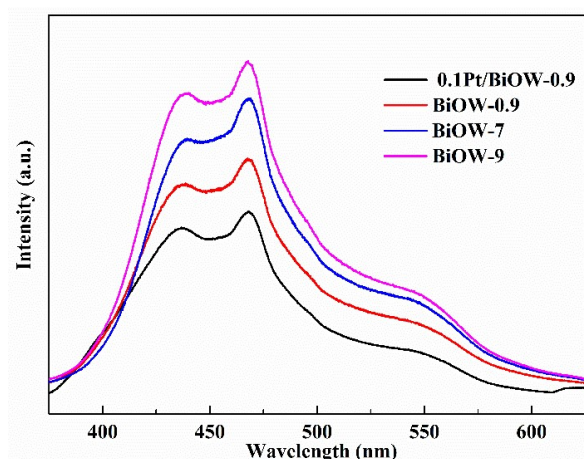


Figure 6.8 photoluminescence (PL) emission spectra of 0.1Pt/BiOW-0.9 and BiOW-n composites.

6.3.4 The proposed mechanism

Based on the above-discussed results, the possible mechanism of photocatalytic oxidation of benzyl alcohol on flower-like 0.1Pt/BOW-0.9 hybrid nanocomposite is proposed and shown schematically in Figure 6.9.

From the above-calculated results, the edge potential E_{CB} for 0.1Pt/BOW-0.9 is -0.70 eV vs. NHE (pH = 7) which is more negative than the O_2 reduction potential ($O_2/O_2^{\bullet-} = -0.16$ eV)³⁵. Therefore, it is thermodynamically permissible for photogenerated electrons to migrate to the adsorbed O_2 , forming the $O_2^{\bullet-}$ radicals.

Initially, the flower-like Bi_2WO_6 semiconductor is excited under visible-light irradiation to produce carriers. The excited electrons migrate from Bi_2WO_6 to co-catalyst Pt nanoparticles. Both flower-like Bi_2WO_6 with abundant pores and small crystalline grains and co-catalyst Pt nanoparticles significantly promote the electron-hole separation and transfer and decrease the electron-hole recombination, hence improving the photocatalytic efficiency. The electrons then react with adsorbed O_2 to produce $O_2^{\bullet-}$. The adsorbed benzyl alcohol on the catalyst surface is oxidized by the

positive holes and/or $\text{O}_2^{\bullet-}$ to produce the target product benzaldehyde.

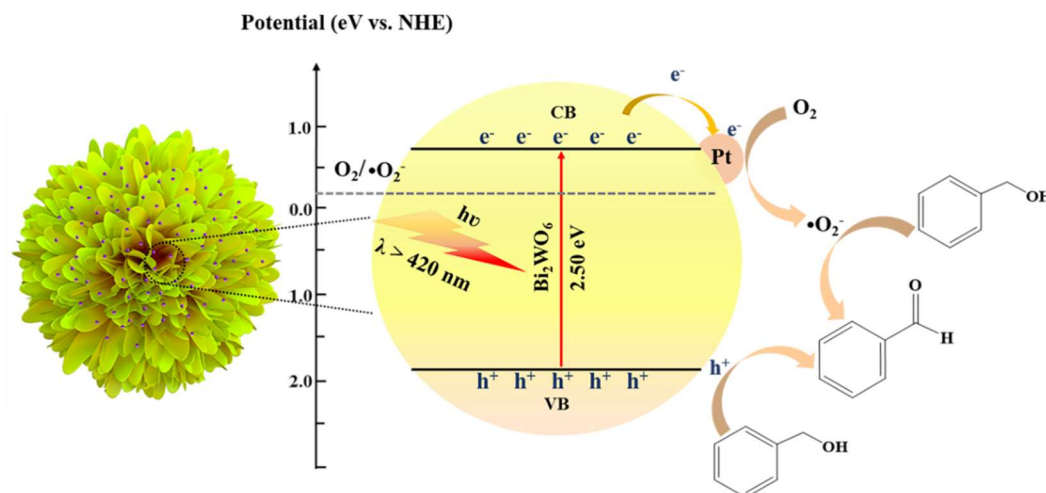


Figure 6.9 Proposed mechanism for selective oxidation of benzyl alcohol to benzaldehyde over the flower-like Pt/Bi₂WO₆ catalyst under visible-light irradiation.

6.4 Conclusions

This work developed a facile hydrothermal approach to prepare various BiOW composites with different morphology structures and component via changing the pH value of precursor suspension. The XRD and SEM results reveal that the sample synthesized under pH=0.9 possesses a hierarchical flower-like Bi₂WO₆ microsphere assembled with nanosheets. However, the sample prepared under neutral solution consists of more irregular nanosheets but with same component. With the increase of pH into 9, the sample is dominated by the nanoplate structure. In contrast, a more basic solution (pH=11 and 13) promotes the hydrolysis of the Bi³⁺, leading to the formation of bismuth-rich BiOW composites (Bi₂WO₆/Bi_{3.84}W_{0.16}O_{6.24} composite and Bi₂O₃). The UV-Vis diffuse reflectance spectra and Mott–Schottky analysis explore their difference in electronic band structure; Bismuth-rich BiOW composites display relatively broad bandgap and low photocatalytic oxidation activity. The high photo-oxidative capability of flower-like BiOW-0.9 consisting of Bi₂WO₆ for benzyl alcohol oxidation under

visible-light irradiations could be ascribed to the abundant pore reduced by its hierarchical flower-like structure and its high surface area, which promotes the charge-separation and transfer efficiency and affording abundant catalytically active sites. Besides, a further enhanced photocatalytic performance of BiOW-0.9 was achieved by loading co-catalyst Pt on the bare sample. In last, the underlying photocatalytic mechanism is proposed based on the band structure analysis and different redox position of chemicals. The finding accounts for the shape-controlled synthesis of nanostructured BiOW materials to improve their physical and chemical properties and illustrate the use of structural engineering to promote the photocatalytic performance.

References

- [1]. Leite T.O.C., Benzaldehyde (CAS 100-52-7). *Revista Virtual De Quimica* **2020**, 12 (1), 183-195.
- [2]. Chen B., Wang L.Y., Gao S., Recent advances in aerobic oxidation of alcohols and amines to imines. *ACS Catalysis* **2015**, 5 (10), 5851-5876.
- [3]. Vannucci A.K., Hull J.F., Chen Z. et al., Water oxidation intermediates applied to catalysis: Benzyl alcohol oxidation. *Journal of the American Chemical Society* **2012**, 134 (9), 3972-3975.
- [4]. Gupta S., Tripathi M., A review of TiO₂ nanoparticles. *Chinese Science Bulletin* **2011**, 56 (16), 1639-1657.
- [5]. Yang M.Q., Zhang N., Xu Y.J., Synthesis of fullerene-, carbon nanotube-, and graphene-TiO₂ nanocomposite photocatalysts for selective oxidation: A comparative study. *ACS Applied Materials & Interfaces* **2013**, 5 (3), 1156-1164.
- [6]. Li C.J., Xu G.R., Zhang B.H. et al., High selectivity in visible-light-driven partial photocatalytic oxidation of benzyl alcohol into benzaldehyde over single-crystalline rutile TiO₂ nanorods. *Applied Catalysis B-Environmental* **2012**, 115, 201-208.
- [7]. Di T.M., Zhu B.C., Cheng B. et al., A direct z-scheme g-C₃N₄/SnS₂ photocatalyst with superior visible-light CO₂ reduction performance. *Journal of Catalysis* **2017**, 352, 532-541.
- [8]. Jiang W., Luo W., Wang J. et al., Enhancement of catalytic activity and oxidative ability for graphitic carbon nitride. *Journal of Photochemistry and Photobiology C: Photochemistry Reviews* **2016**, 28, 87-115.
- [9]. Loeb S.K., Alvarez P.J.J., Brame J.A. et al., The technology horizon for photocatalytic water treatment: Sunrise or sunset? *Environ Sci Technol* **2019**, 53 (6), 2937-2947.

- [10]. Xiao J., Han Q., Xie Y. et al., Is C_3N_4 chemically stable toward reactive oxygen species in sunlight-driven water treatment? *Environmental Science & Technology* **2017**, *51* (22), 13380-13387.
- [11]. Wu C., Han Q., Qu L., Functional group defect design in polymeric carbon nitride for photocatalytic application. *APL Materials* **2020**, *8* (12), 120703.
- [12]. Meng X.C., Zhang Z.S., Bismuth-based photocatalytic semiconductors: Introduction, challenges and possible approaches. *Journal of Molecular Catalysis A-Chemical* **2016**, *423*, 533-549.
- [13]. Zhang N., Ciriminna R., Pagliaro M. et al., Nanochemistry-derived Bi_2WO_6 nanostructures: Towards production of sustainable chemicals and fuels induced by visible light. *Chemical Society Reviews* **2014**, *43* (15), 5276-5287.
- [14]. Zhang B., Li J., Gao Y. et al., To boost photocatalytic activity in selective oxidation of alcohols on ultrathin Bi_2MoO_6 nanoplates with Pt nanoparticles as cocatalyst. *Journal of Catalysis* **2017**, *345*, 96-103.
- [15]. Fu H.B., Zhang L.W., Yao W.Q. et al., Photocatalytic properties of nanosized Bi_2WO_6 catalysts synthesized via a hydrothermal process. *Applied Catalysis B-Environmental* **2006**, *66* (1-2), 100-110.
- [16]. He W.W., Kim H.K., Warner W.G. et al., Photogenerated charge carriers and reactive oxygen species in ZnO/Au hybrid nanostructures with enhanced photocatalytic and antibacterial activity. *Journal of the American Chemical Society* **2014**, *136* (2), 750-757.
- [17]. Lops C., Ancona A., Di Cesare K. et al., Sonophotocatalytic degradation mechanisms of rhodamine b dye via radicals generation by micro- and nano-particles of ZnO . *Applied Catalysis B-Environmental* **2019**, *243*, 629-640.
- [18]. Liu Y., Chen L., Yuan Q. et al., A green and efficient photocatalytic route for the highly-selective oxidation of saturated alpha-carbon C-H bonds in aromatic alkanes over flower-like Bi_2WO_6 . *Chemical Communications* **2016**, *52* (6), 1274-1277.
- [19]. Yuan B., Zhang B., Wang Z. et al., Photocatalytic aerobic oxidation of toluene and its derivatives to aldehydes on Pd/Bi_2WO_6 . *Chinese Journal of Catalysis* **2017**, *38* (3), 440-446.
- [20]. Mondelli C., Ferri D., Grunwaldt J.-D. et al., Combined liquid-phase ATR-IR and XAS study of the bi-promotion in the aerobic oxidation of benzyl alcohol over Pd/Al_2O_3 . *Journal of Catalysis* **2007**, *252* (1), 77-87.
- [21]. Zhang L., Wang H., Chen Z. et al., Bi_2WO_6 micro/nano-structures: Synthesis, modifications and visible-light-driven photocatalytic applications. *Applied Catalysis B: Environmental* **2011**, *106* (1), 1-13.
- [22]. Fu H., Pan C., Yao W. et al., Visible-light-induced degradation of rhodamine b by nanosized Bi_2WO_6 . *The Journal of Physical Chemistry B* **2005**, *109* (47), 22432-22439.
- [23]. Zhang Y.H., Zhang N., Tang Z.R. et al., Identification of Bi_2WO_6 as a highly selective visible-light photocatalyst toward oxidation of glycerol to dihydroxyacetone in water. *Chemical Science* **2013**, *4* (4), 1820-1824.
- [24]. Zhang C., Zhu Y., Synthesis of square Bi_2WO_6 nanoplates as high-activity visible-light-driven photocatalysts. *Chemistry of Materials* **2005**, *17* (13), 3537-3545.
- [25]. Yu J., Xiong J., Cheng B. et al., Hydrothermal preparation and visible-light

- photocatalytic activity of Bi_2WO_6 powders. *Journal of Solid State Chemistry* **2005**, 178 (6), 1968-1972.
- [26]. Chen S.F., Tang W.M., Hu Y.F. et al., The preparation and characterization of composite bismuth tungsten oxide with enhanced visible light photocatalytic activity. *Crystengcomm* **2013**, 15 (39), 7943-7950.
- [27]. Song H., Liu Z., Wang Y. et al., Template-free synthesis of hollow TiO_2 nanospheres supported Pt for selective photocatalytic oxidation of benzyl alcohol to benzaldehyde. *Green Energy & Environment* **2019**, 4 (3), 278-286.
- [28]. Zhang L.S., Wang W.Z., Zhou L. et al., Bi_2WO_6 nano- and microstructures: Shape control and associated visible-light-driven photocatalytic activities. *Small* **2007**, 3 (9), 1618-1625.
- [29]. Amano F., Nogami K., Ohtani B., Visible light-responsive bismuth tungstate photocatalysts: Effects of hierarchical architecture on photocatalytic activity. *Journal of Physical Chemistry C* **2009**, 113 (4), 1536-1542.
- [30]. Yang J.H., Wang D.G., Han H.X. et al., Roles of cocatalysts in photocatalysis and photoelectrocatalysis. *Accounts of Chemical Research* **2013**, 46 (8), 1900-1909.
- [31]. Radha R., Srinivasan A., Manimuthu P. et al., Tailored sunlight driven nano-photocatalyst: Bismuth iron tungstate (Bi_2FeWO_6). *Journal of Materials Chemistry C* **2015**, 3 (39), 10285-10292.
- [32]. Wang X., Yu J.C., Ho C. et al., Photocatalytic activity of a hierarchically macro/mesoporous titania. *Langmuir* **2005**, 21 (6), 2552-2559.
- [33]. Zhang L.Z., Yu J.C., A sonochemical approach to hierarchical porous titania spheres with enhanced photocatalytic activity. *Chemical Communications* **2003**, 17 (13), 2078-2079.
- [34]. Fu H.B., Zhang L.W., Yao W.Q. et al., Photocatalytic properties of nanosized Bi_2WO_6 catalysts synthesized via a hydrothermal process. *Applied Catalysis B-Environmental* **2006**, 66 (1-2), 100-110.
- [35]. Kheradmand A., Zhu Y.X., Zhang W.W. et al., Cobalt oxide on mesoporous carbon nitride for improved photocatalytic hydrogen production under visible light irradiation. *International Journal of Hydrogen Energy* **2019**, 44 (33), 17930-17942.
- [36]. Jin Z.L., Liu Y., Hao X.Q., Self-assembly of zinc cadmium sulfide nanorods into nanoflowers with enhanced photocatalytic hydrogen production activity. *Journal of Colloid and Interface Science* **2020**, 567, 357-368.
- [37]. Gandhi A.C., Wu S.Y., Strong deep-level-emission photoluminescence in NiO nanoparticles. *Nanomaterials* **2017**, 7 (8).
- [38]. Chung P.H., Perevedentseva E., Cheng C.L., The particle size-dependent photoluminescence of nanodiamonds. *Surface Science* **2007**, 601 (18), 3866-3870.
- [39]. Talukdar S., Mandal D., Mandal K., Surface modification of cobalt ferrite nanohollowspheres for inherent multiple photoluminescence and enhanced photocatalytic activities. *Chemical Physics Letters* **2017**, 672, 57-62.
- [40]. Yan J.Q., Wu G.J., Guan N.J. et al., Understanding the effect of surface/bulk defects on the photocatalytic activity of TiO_2 : Anatase versus rutile. *Physical Chemistry Chemical Physics* **2013**, 15 (26), 10978-10988.

- [41]. Gaubas E., Ceponis T., Deveikis L. et al., Room-temperature infrared photoluminescence in gan doped with various impurities. *Optical Materials* **2019**, 94, 266-271.

Chapter 7 Conclusions and further work

7.1 Conclusions

In this thesis, various multifunctional catalysts were designed and applied in making these processes of biomass-derived carbohydrates transformation more productive and sustainable. Several valorization processes of biomass-derived substrates including HMF production from glucose, EM production from PG and photocatalytic alcohols oxidation into aldehydes were investigated. Moreover, this thesis provides an in-depth understanding of how these catalysts accelerate biomass conversion.

In the conventional thermal catalytic processes, stable multifunctional solid acid catalysts including metal oxides (ZrPO) and heteropoly-acids (MPW/MCM) were fabricated. Their structural features and acidities towards intrinsic activity and selectivity in the transformation of biomass-derived glucose and PG via dehydration and the Cannizzaro reactions were discussed. In last, the roles of acidity (density, strength, and types of acid sites) were elucidated, and the reaction mechanisms were therefore proposed. These findings could aid the rational design of acid catalytic system in performing multistep cascade processes in one-pot catalytic biomass conversion in the future.

In the sustainable photocatalytic processes, the Pt-Bi bimetallic modified TiO₂ and BiOW composites were fabricated and used for the oxidation of benzyl alcohol, a lignin model compound under visible-light irradiations using green O₂ as the oxidant. A fundamental understanding of surface and interface characteristics as well as photoelectrochemical properties were achieved. For the Pt-Bi bimetallic modified TiO₂

catalyst, the effect of Pt size (single sites, subnano clusters, and nanoparticles) on photoelectrochemical properties and photocatalytic activity was investigated. It is concluded that the strong interaction between Pt single sites and TiO_2 favors the formation of high density of positively charged platinum which could play an important role in promoting the charge carrier transition and separation, and improving the absorption of visible light, further enhancing the photocatalyst activity. For the BiOW composites, the nature of the photogenerated charge carriers and how the morphologies would affect the activities of bismuth tungstate were studied. In last, the underlying photocatalytic mechanism is proposed based on the band structure analysis and different redox position of chemicals. The finding accounts for the shape-controlled synthesis of nanostructured semiconductors to improve their photoelectrochemical properties and thus promoting the photocatalytic performance.

7.2 Future work

The energy crisis could be considered as one of the major challenges for today's society and future generations. Heterogeneous catalysis plays a crucial role in the valorization of biomass with efficient activity and high chemo-selectivity. According to the review of the recent research work on the catalytic valorization of biomass, in some cases excellent catalyst activity and selectivity were demonstrated. However, there are many challenges need to be addressed. Although some significant studies are carried out in this thesis based on some of these challenges, more efforts need to be devoted to solving these challenges in the future. To name a few:

(1) Efficient and selective transformation of biomass-derived carbohydrates to value-added chemicals is an important topic in the field of biomass valorization. In this thesis,

although various multifunctional catalysts were designed and applied in this transformation. However, the production of chemicals directly from renewable biomass is more costly than the conventional approaches from hydrocarbons, thus making bio-based chemicals not cost-competitive. One-step conversion of raw biomass feedstock such as cellulose and lignin to bio-based products directly has greater economic benefits, which could accelerate the industrial development of chemicals greatly. Therefore, a more economically and environmentally sustainable one-pot conversion of these biomass waste to value-added platform chemicals is required to achieve in the future. Particularly, new catalytic systems using cheap and non-toxic materials need to be developed.

(2) Sustainable production of value-added chemicals from biomass-derived carbohydrates strongly relies on the selectivity of catalytic systems. Therefore, the molecular-level understanding of the operation of a catalytic system, the identification and characterization of key intermediates of the catalytic cycle is fundamentally important and could help to improve the performance of existing processes. A better understanding of reaction mechanisms of biomass conversion by spectroscopic studies would be of great importance for improving the efficiency and selectivity. In the thesis, some crucial insights into the roles of catalyst acidity on the activity are explored to understand the reactions of biomass conversion. These studies could help to understand the insightful reaction mechanisms and design better catalysts. However, it is far from enough to provide deeper insights. A series of molecular-level studies will be required via carrying out more in situ spectroscopic characterizations combined with isotope

labelling techniques.

(3) Since several outstanding catalysts were fabricated and evaluated for biomass-derived carbohydrates conversion in desirable reaction media in this thesis, the economically feasible and scale-up production becomes very crucial. The catalytic performance of catalysts could be affected by reaction solvents and/or other auxiliary materials. Hence, the development of catalytic systems should focus on reducing solvent needs and robust catalysts. Moreover, the solvents could be readily available and cheap to achieve economically and technically feasible processes. In these cases, the efficient recycling of solvent in an integrated biorefinery or the subsequent exploitation of solvents in the technology need to be developed, which could significantly reduce the production of generated waste as well as the environmental factor. Besides, extensive efforts in the development of emerging technologies are required to reduce the operational costs. Moreover, biomass transformation processes achieved in one or a few steps without separation of intermediates are certainly more appealing in terms of waste minimization and biomass utilization on a large scale than the conventional approach via platform molecules intermediates.

In conclusion, although excellent catalytic activity and high selectivity of target products were achieved in glucose conversion in some cases, the large-scale or commercial chemicals production from glucose involving solvent and catalyst recycling as well as product purification is still a great challenge in the aspect of both chemistry and engineering.

(4) The high functionality of biomass feedstock leads to the formation of various by-

products. These by-products interact with the surface of catalysts differently due to their different electronic effects, which affects the selectivity and the distribution of final products. Therefore, the systematic studies related to the by-products' analysis and the detailed analysis correlating to actual mass balances are required. Although most of papers provided the yields of the target products using chromatographic analysis, only few data were reported on the mass balances and the demonstration of product isolation, which is important for pilot and/or industrial-scale applications.

(5) How to suppress the side reactions during the reaction processes is another important issue. Two aspects may be considered for this problem. Firstly, design novel solvent systems, e.g., biphasic solvent systems and mixed solvent systems, to change the solvent nature (viscosity, polarity), which can be beneficial for the mass transfer of target products from catalyst surface to solvents. Consequently, it could decrease the contact time between the catalytic active sites and products, thus suppressing the side reactions. Secondly, modifying the catalyst surface (hydrophilicity/hydrophobicity) can tune the interaction between products and the catalyst. Proper surface nature could decrease the above-mentioned interaction, and thus hinder the side reactions.

(6) Fundamental understanding of interface and surface characteristics of catalysts is essential for the optimization or design of catalysts and co-catalysts. For example, interface characteristics of heterojunction semiconductors can influence charge carrier's generation, separation, and transportation. The effect of particle sizes of the co-catalysts and morphological structure of photocatalysts on their activity in alcohols oxidation reaction was investigated in this thesis. However, understanding of the

bonding structures between co-catalysts and semiconductors needs to be further studied that it would enable to provide better strategies to improve charge separation and transfer. Therefore, more efforts in time-resolved spectroscopic studies and theoretical calculations are needed to overcome these fundamental challenges.